Three-Dimensional Numerical Analysis for Flow Prediction in Positive Displacement Screw Machines

by

Ahmed Kovačević

Thesis submitted for the
Degree of Doctor of Philosophy
in the School of Engineering
City University London

City University London
School of Engineering
July 2002

Table of Contents

List of Tables

List of Figures

List of Examples

Acknowledgement

My wife and children supported me and gave me immeasurable help during the time I spent in bringing this thesis to fruition. I dedicate what I wrote in here to them.

My mother and father taught me how to live, learn and work. I thank them for that.

Prof Nikola Stošić, my teacher, supervisor and real friend spent a lot of time and patience in educating me in the mystic areas of the mechanical sciences. I wish to express my deep gratitude for all his enthusiasm during that difficult mission.

Prof Ian K. Smith encouraged me to finish this thesis and greatly helped in making it into this final form.

Prof Ismet Demirdžić and Dr Samir Muzaferija kindly allowed me to use COMET; for which I am very thankful to them.

I also want to thank to all my colleagues and friends who gave me advice or help.

This study was carried out between January 1999 and June 2002 at the Centre for Positive Displacement Compressor Technology of City University, London. It was funded entirely by the income from industrial contracts that the Centre was awarded in that period. I am very thankful for the time I was granted to work on it.

Abstract

A substantial proportion of all industrial compressors now produced are of the twin-screw type. These are rotary positive displacement machines, which operate at high efficiency over a wide range of speeds and pressure differences.

Currently their performance is estimated by assuming simplified one-dimensional flow through passages with dimensions that are invariant with temperature and pressure.

As manufacturing accuracy increases, clearances can be reduced and compressors thereby made smaller and more efficient. However to obtain full advantage of this at the design stage, it must be possible to estimate accurately internal fluid flow patterns, pressure and temperature distribution and their effects on the working process.

An interface has therefore been developed in order to generate a 3-D numerical grid for this purpose. This employs a procedure to produce rotor profiles and an analytical transfinite interpolation method with adaptive meshing to obtain a fully structured 3-D numerical mesh, which is directly transferable to a Computational fluid dynamics (CFD) code. Robust calculations can then be performed while allowing for moving, stretching and sliding between the rotors with large variations in the chamber shape and proportions.

Changes in the solver functions have improved convergence and increased the speed of solution. One of these is to include a means to maintain constant pressure within the inlet and outlet ports throughout the calculating procedure.

Also, the CFD procedure has been modified to enable fast calculations to be made with real working fluids and to estimate two-phase flow effects due to phase change and oil injection in the working chamber.

The interface, pre-processing code and calculating procedures have been used with a commercial CFD solver to estimate the performance of three different compressor applications. The predicted results for one of these were compared with those obtained from the author's measurement in an experimental test rig and good agreement was obtained.

Nomenclature

A	- area of the cell surface
$\mathbf{a}_1$, $\mathbf{b}_1$	- radius vectors of boundary points
A_1, A_2	- constants in the saturation temperature equation
b_1	- constant
B_1, B_2	- constants in the compressibility factor equation
c_i	- concentration of species
c_1-c_4	- tension spline coefficients
C_1, C_2	- coefficients of the orthogonalisation procedure
C_{drag}	- drag coefficient
C_p	- specific heat at constant pressure
C, σ	- constants in k-ε model of turbulence
d_i	- distance in transformed coordinate system
D_i	- mass diffusivity of the dispersed phase
d_o	- Sauther mean droplet diameter
D_1-D_4	- constants in the vapour specific heat equation
$\dot{\mathbf{D}}$	- rate of strain tensor
e_1, e_2	- cell edges maximal values in coordinate directions
$f^i(s)$	- adaptation variable
$\mathbf{f}_b$	- resultant body force
f_e	- expansion factor
f^i_k	- weight function
$F^i(s)$	- integrated adaptation variable
h_1-h_8	- blending functions of Hermite interpolation
h	- enthalpy
h_L	- enthalpy of evaporation
k	- turbulent kinetic energy
K_1-K_4	- coefficients for Hermite interpolation
k_P	- point counter
K	- number of points
m	- mass
m_o	- mass of species
m_i	- mass in the numerical cell
Δm_L	- mass of evaporated or condensed fluid
n	- rotor speed
Nu	- Nuselt number
p	- pressure
P	- production of turbulence energy
Pr	- Prandtl number
$\mathbf{q}_{ci}$	- diffusion flux of species
$\mathbf{q}_h$	- heat flux
$\mathbf{q}_k$	- diffusion flux in kinetic energy equation
$\mathbf{q}_\varepsilon$	- diffusion flux in dissipation equation
$\mathbf{q}_{\phi S}$	- flux source in the generic transport equation
$\mathbf{q}_{\phi V}$	- volume source in the generic transport equation

$\dot{Q}_{con}$ - convective heat flux

$\dot{Q}_{mass}$ - heat flux due to phase change

r - radius vector

Re - Reynolds number

R_i - grid point ratio

S - cell surface

s - transformed coordinate

s - area vector

S_{ci} - source term of species

S_h - heat source term

S - viscous part of stress tensor

t - time

T - temperature

T - stress tensor

u - displacement vector

v - fluid velocity

$\mathbf{v}_{ci}$ - velocity of the dispersed phase

v_i - Cartesian component of velocity vector

$\mathbf{v}_s$ - surface velocity

V - cell volume

V_{CM} - volume of the control mass

V_{CV} - control volume

w - weight factor

W - weight function

X_ξ - grid spacing

x, y, z - physical coordinates

X, Y, Z – points on physical boundaries

x_p, y_p - coordinates of the calculation point

y_p', y_p'' - first and second derivatives in vicinity of the point P

y^+ - dimensionless distance from the wall

z - compressibility factor

Greek symbols

α_t - linear thermal expansion coefficient

α, β - tension spline coefficients

α_1, β_1 - blending functions

δ - Kroneker delta function

δt - time step

ε - dissipation of turbulent kinetic energy

ϕ - transported property in generic transport equation

φ - interlobe angle of male rotor

Γ_ϕ - Diffusive term in generic transport equation

η, λ - Lame coefficients

κ - thermal conductivity

μ - viscosity

μ_t - turbulent viscosity

π - 3.14

ω - angular velocity

ρ - density

σ - tension spline parameter

σ_o - oil surface tension

σ_{cv} - normalised cell volume

ξ, η - computational coordinates

$\hat{\xi}_o, \hat{\xi}_1$ - one-dimensional stretching functions

$\hat{\xi}$ - multi-dimensional stretching function

Subscripts

1 - male rotor

2 - female rotor

add - injected / subtracted fluid

const - constant prescribed value

D - discharge bearings

S - suction bearings

i - dispersed phase

o - oil

v - vapour

l - liquid

L - evaporated/condensed fluid

m - mixture

s - grid values

sat - saturation

t - turbulence

S - surface

V - volume

min - minimum

max - maximum

ref - reference value

Superscripts

' - fluctuating components of dependent variable as a result of time averaging

" - fluctuating component of dependent variable as a result of density-weighted averages

k - number of time step

Chapter 1

Introduction

1.1 SCREW COMPRESSORS

The operating principle of screw machines, as expanders or compressors, has been known for over 100 years. Despite this, the first serious efforts to produce them were not made until the nineteen forties when *Lysholm* (1942) in Sweden showed their potential. However, it is only since the beginning of the nineteen sixties, after *Nilson* (1952) first proposed the symmetric rotor profile and numerically controlled machine tools became widely available to manufacture the special shapes required, that acceptable efficiencies and manufacturing costs became possible. Since then, great improvements have been made in performance prediction, rotor profile design and manufacturing techniques.

Screw compressors are now highly efficient, compact, simple and reliable. Consequently, they have largely replaced reciprocating machines for the majority of industrial applications and in many refrigeration systems.

1.2 PRINCIPLE OF OPERATION

The screw compressor is a positive displacement rotary machine. It consists essentially of a pair of meshing helical lobed rotors, which rotate within a fixed casing that totally

encloses them, as shown in Figure 1-1. The space between any two successive lobes of each rotor and its surrounding casing forms a separate working chamber of fixed cross sectional area. The length of this chamber varies as rotation proceeds due to displacement of the line of contact between the two rotors. It is a maximum when the entire length between the lobes is unobstructed by meshing contact with the other rotor. It has a minimum value of zero when there is full meshing contact with the second rotor at the end face. The two meshing rotors effectively form a pair of helical gear wheels with their lobes acting as teeth. These are normally described as the male or main rotor and the female or gate rotor respectively.

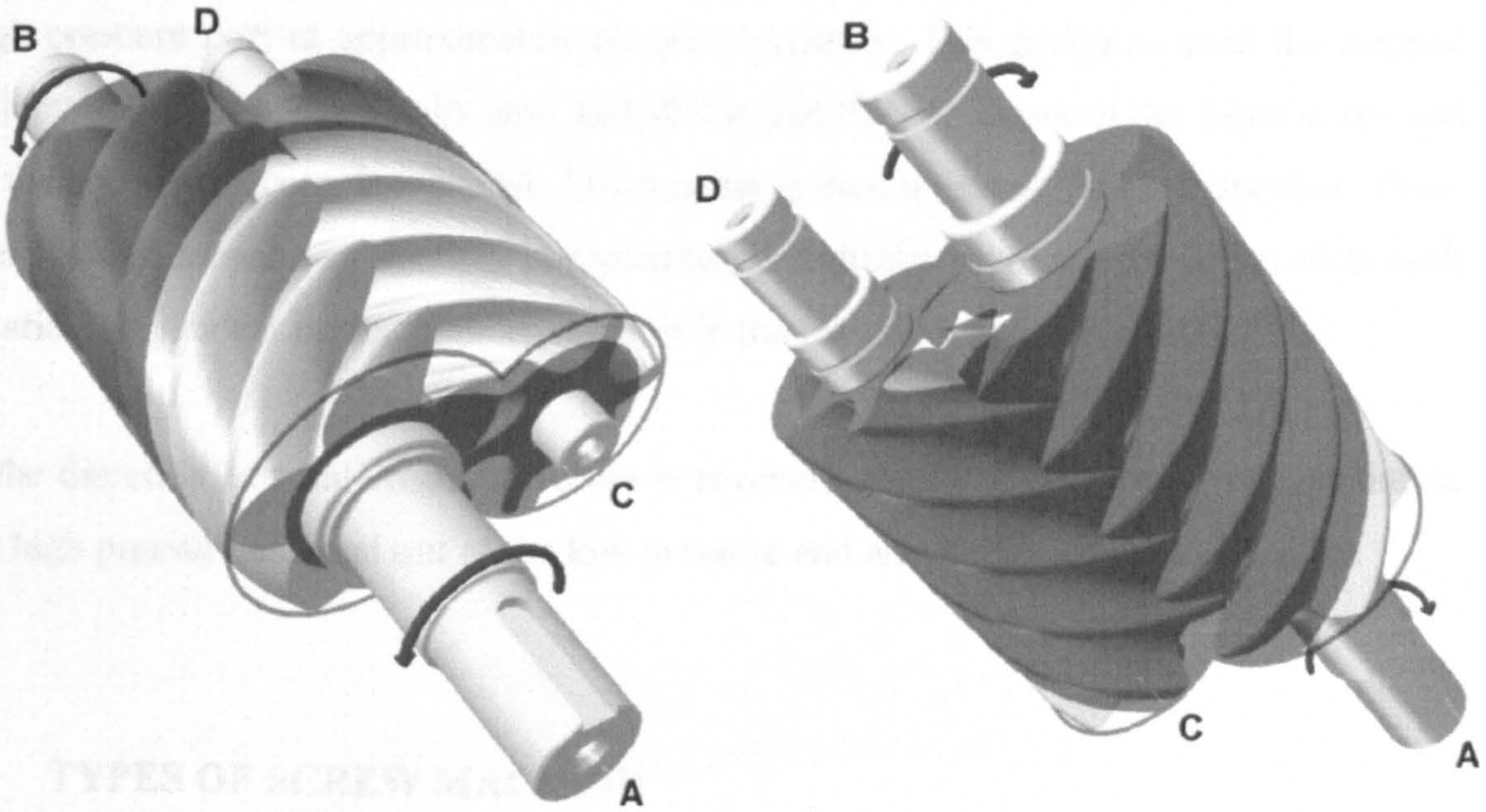

1-1 a) View from Front and Top *1-1 b) View from Bottom and Rear*

Figure 1-1Screw Compressor Main Components

As shown in Figure 1-1a), gas or vapour enters from the front and on top, through an opening, mainly in the front plane of the casing which forms the low pressure or inlet port. It thus fills the spaces between the lobes, starting from the ends corresponding to A and C in the lightly shaded area. As may be seen, the trapped volume in each chamber increases as rotation proceeds and the contact line between the rotors recedes. At the point where the maximum volume is filled, the inlet port terminates and rotation proceeds without any further fluid admission in the region corresponding to the darkly shaded area.

Viewed from Figure 1-1 b), it may be seen that the darkly shaded area begins, from the end corresponding to A and C, at the point where the male and female rotor lobes start to reengage on the underside. Thus, from that position, further rotation reduces the volume of gas or vapour trapped between the lobes and the casing. This causes the pressure to rise. At the position where the trapped volume is sufficiently reduced to achieve the required pressure rise, the ends of the rotors corresponding to D and B are exposed to an opening on the underside of the casing, which forms the high pressure or discharge port. This corresponds to the lightly shaded area at the rear end in Figure 1-1 b). Further rotation reduces the trapped volume causing the fluid to flow out through the high pressure port at approximately constant pressure. This continues until the trapped volume is reduced to virtually zero and all the gas trapped between the lobes at the end of the suction process, is expelled. The process is then repeated for each chamber. Thus, there is a succession of suction, compression and discharge processes achieved in each rotation, dependent on the number of lobes in the male and female rotors.

If the direction of rotation of the rotors is reversed, fluid will flow in to the machine at the high pressure end and out at the low pressure end and it will act as an expander.

1.3 TYPES OF SCREW MACHINE

Although screw machines can function as either expanders or compressors, their overwhelmingly common use is as compressors, of which there are two main types. These are oil flooded (or oil injected) and oil free. An example of each, with the same rotor sizes, is shown in Figure 1-2.

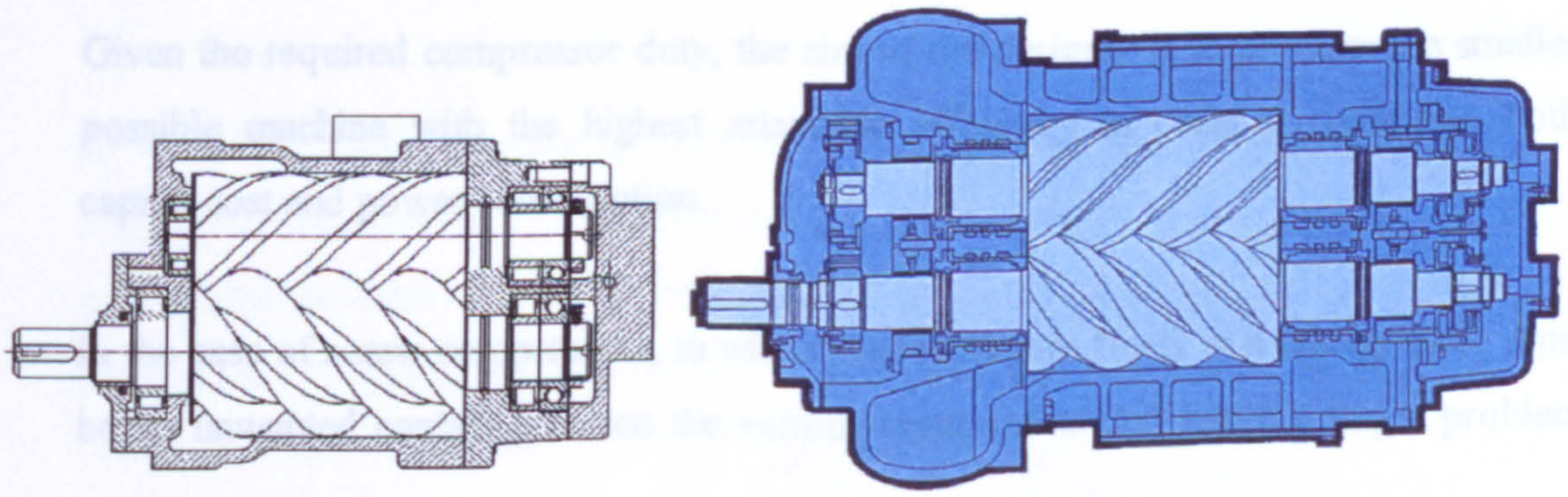

a) Oil Injected Compressor *b) Oil Free Compressor*

Figure 1-2 Types of Screw Compressor

In oil injected compressors, a relatively large mass, though a very small volume, of oil is admitted with the gas to be compressed. The oil acts as a lubricant between the contacting rotors, a sealant of any clearances between the rotors and between the rotors and the casing and as a coolant of the gas during the compression process. This cooling effect improves the compression efficiency and permits pressure ratios of up to approximately 15:1 in a single stage without an excessive temperature rise.

In oil free compressors, only gas is admitted into the working chamber. External timing gear is therefore needed, in order to prevent rotor contact, and internal shaft seals have to be located between the bearings at each end of the rotor shaft and the main body of the rotor. The shaft seals are needed to prevent oil, which is supplied to the bearings through an external lubrication system, from entering the working chamber and thereby contaminating the gas being compressed. Because there is no injected oil to cool the gas in this machine, pressure ratios are limited to approximately 3:1, depending on the type of gas being compressed. Above this value the temperature rise associated with compression creates problems associated with rotor and casing distortion.

As may be deduced from Figure 1-2, oil free compressors are bigger and more expensive to manufacture than oil injected machines but the absence of oil in the working chamber reduces the viscous drag on the rotors. Therefore, they may be rotated at higher speeds and thus an oil free compressor with a given size of rotors has a larger capacity than the corresponding oil flooded type.

1.4 PROBLEMS ASSOCIATED WITH SCREW MACHINE DESIGN

Given the required compressor duty, the aim of the designer is to produce the smallest possible machine with the highest attainable efficiency in order to minimise both, capital cost and power consumption.

In the case of screw compressors, in which the rotors turn freely in a casing, there must be no unwanted contact between the various components and hence a major problem

associated with their improvement is to minimise internal leakages through the clearances.

In recent years, solutions to this problem have been enhanced by the development of software that makes it possible to predict the thermodynamic property changes within the compressor at each stage of the compression process. Such software is based on the assumption of dimensionless or one-dimensional flow through all the passages and leakage paths and that two and three-dimensional flow patterns within the machine are not significant. Moreover, it is assumed that the dimensions of the compressor rotors and casing are unaffected by local pressure and temperature changes. Although the development of such software has brought great improvements to screw compressor design techniques, the following examples show its limitations.

A major problem in the design of oil flooded compressors is to find the best position in the casing in which to inject the oil, since its mode of distribution internally is not well understood. It is currently assumed that the oil passes through the compressor as an annular film, adhering to the casing as result of the forces on it created by the rotation of the rotors. Recent experiments by *Xing* (2001) have confirmed that this is not correct. Moreover, one industrial compressor designer informed the author that in one recent design, it took 14 months of experimental work to find the best injection position in the compressor casing.

In oil flooded compressors, the temperature rise of the working fluid is relatively small due to the huge cooling effect of the oil, whose mass can be more than four times that of the compressed gas. The effects of thermal expansion are relatively small and now that screw compressor components can be manufactured with a repeatability of the order of $\pm 5\mu$, internal clearances can be as little as 30-60μ.

In oil free compressors, the temperature rise of the compressed gas is much higher. Clearances therefore have to be much larger in order to avoid contact between the rotors or between the rotors and their casing caused by thermal distortion. It is believed that the adiabatic efficiency of oil free compressors could be increased by as much as 10%, if minimum safe clearances could be predicted accurately.

If it were possible to predict internal flow in screw compressors by 3-D methods so that the internal pressure and temperature distribution could be estimated throughout the machine, then this could be used:

i) as a basis for determining the distribution of injected oil in oil flooded machines,
ii) as a means to estimate thermal distortion within an oil free compressor,
iii) to design inlet and exit port passages with minimum flow losses.

Such a procedure would then make it possible to reduce the size of screw compressors by bringing internal leakage to a minimum, improve the adiabatic efficiency of such machines by virtue of the reduced internal losses and greatly reduce the cost of developing new products by minimising the time and cost required for experimental testing and development.

During the past twenty five years, there has been a steady growth in the use of Computational Fluid Dynamics (CFD) as a means of estimating 3-D flow patterns. It was first used mainly to estimate external flows around bodies. However, as computational procedures improved, it has been used increasingly for predicting internal flows and, today, it is widely used for estimating flow in rotating machinery and specialised codes have been developed specifically for this function.

Despite a large number of publications on CFD, little has been written on its use for the analysis of flow through screw machines. This is mainly due to the complexity of both their configuration and the flow through them. Some existing commercial CFD codes have facilities that can cope with the complex geometry of screw machines. Unfortunately, these codes need to be improved in order to give useful results. In addition, a pre-processor needs to be developed to generate a numerical mesh that describes their shape with sufficient accuracy and allows for the complex stretching and sliding motion associated with flow within them. In addition, an interface is needed to enable arbitrary screw machine geometry to be automatically mapped to discrete volumes and then used within a standard CFD code.

Accordingly, this thesis is mainly concerned with the development of grid generation methods suitable for analysis of the screw machine domain and their incorporation in existing finite volume CFD software in order to estimate both local internal flow

patterns and overall performance parameters by which screw compressor designs are evaluated.

Chapter 2

Review of previous work

2.1 INTRODUCTION

Despite the widespread usage of screw compressors, there are surprisingly few publications describing the scientific basis of their functioning. The most probable reason for this is that nearly every stage of their development was covered by patents, filed mainly by one company, Svenska Rotor Maskiner (SRM) in Sweden. Hence, any analysis of their mode of operation was maintained as proprietary information and most of the manufacturers of these machines were licensees, who were content to direct their energies to problems of manufacture, testing and reliability.

This situation began to change in the nineteen sixties when Russian industry sought to produce such machines without licensing and Soviet academics started to examine their mode of operation from first principles. The result of this was the excellent textbooks of *Sakun* (1960), *Andreev* (1961) and *Golovinstov* (1964). Regrettably, these were not translated into English and engineers with no knowledge of Russian only became aware of their existence during the last ten years. A further Russian textbook by *Amosov* (1977) revealed the basis of SRM's "A" rotor profile to the general public for the first time.

Rinder (1979) wrote a textbook in German showing how to use gear theory to produce rotor profiles. A further German textbook by *Konka* (1988) gave useful information on some engineering aspects of screw compressor design.

There are only two textbooks in English, both of relatively recent publication; namely those of *O'Neill* (1993) and *Arbon* (1994) both of which are more of a descriptive than an analytic nature.

During the past few years the screw compressor industry has grown rapidly in the far East where much research and development work continues in Japan, Korea and China. Thus, the most recent textbook by *Xing* (2000) is written in Chinese. It deals exclusively with screw compressors and gives a very good coverage of design theory and practice.

Very few journal papers have been published on screw compressors. The bulk of publications are therefore to be found in conference proceedings. The most notable of these are the biennial compressor conference at Purdue University in the USA and the VDI Schraubenkompressoren Tagung held every four years at the university of Dortmund in Germany. International conferences on compressors have also been organised by the IMechE at irregular intervals. However, since 1999, these have been held at this university on a biennial basis.

2.2 ROTOR PROFILES

Modern developments in screw compressors began with *Lysholm's* (1942) work when he was looking to develop a high speed compressor to link to a turbine for a gas turbine power plant. The key problem was to manufacture rotors with a suitable profile so that they would mesh freely without a high rate of leakage through them. Lysholm's original asymmetric profiles were point generated, which led to a huge wear rate in the cutting tool. This effectively made them impossible to manufacture. *Nilsen* (1967) patented the SRM symmetric profile, made up entirely of circular arcs. This was the first of the envelope generated profiles. Unfortunately, the leakage rate through the blowhole was unacceptably high. The announcement by SRM of their "A" profile (1973) was the turning point in screw compressor development. This was a profile that was relatively easy to manufacture, especially with NC machine tools, and reduced the blow hole area by 90%. From then on, the market for screw compressors grew rapidly,

accompanied by a huge number of patents being filed on variations in rotor profile design.

Rinder's (1979) use of a rack as the common basis for profile generation, of both the male and female rotors, had some deficiencies. *Stošić* (1996) improved on this to produce his "N" profile rack generated rotors, which appear to be one of the best available at present since they combine small blow hole area with a large displacement area, short sealing line, low rotor contact forces and almost pure rolling contact between the male and female rotors.

Edström (1989) gave an interesting review paper demonstrating the importance of clearance distribution around the rotors by the specification of quality classes for screw compressors. *Stošić* (1999) gives a complete review of rotor profiling techniques as well as all the additional modern design concepts which must be included in screw compressor design in order to obtain an optimum result.

There are many other papers published on rotor profiling. Some of the more significant of these are by *Sing and Onuschak* (1984), *Xion and Dagang* (1986), *Pang and Xing* (1990), *Singh and Schwartz* (1990) and *Zhang and Hamilton* (1992).

The prerequisite for successful three-dimensional numerical analysis of a screw compressor is the generation of a suitable block structured numerical mesh. The domain surrounding screw compressor rotors therefore should be divided in two, one for the male and another one for the female rotor in order to be mapped in a fully structured manner. To achieve that, the rack generation procedure can be used. A rack is a rotor of infinite radius that always lies between the male and female rotor profiles and has a shorter length then either of them. The modern rack generation method suggested by *Stošić and Hanjalić* (1996) can be used for this purpose. It defines the primary profile as a rack, Figure 2-1. The generation of rotor profiles is then based on the envelope method, which states that two surfaces are meshed if each generates or envelops the other under a specified relative motion. This is presented in details by *Litvin* (1998) and *Stošić* (1996).

If the primary curves are given on the rack, their coordinates x_{0r} and y_{0r}, as well as their first derivatives, $\frac{\partial x_{0r}}{\partial t}$ and $\frac{\partial y_{0r}}{\partial t}$, or $\frac{dy_{0r}}{dx_{0r}}$ are all known. In that case, curves on the male rotor are generated as:

$$\begin{aligned} x_{01} &= x_{0r}\cos\theta - (y_{0r} - r_{1w})\sin\theta \\ y_{01} &= x_{0r}\sin\theta + (y_{0r} - r_{1w})\cos\theta \end{aligned} \tag{2.1}$$

with the meshing condition in the form:

$$\frac{dy_{0r}}{dx_{0r}}(r_{1w}\theta - y_{0r}) - (r_{1w} - x_{0r}) = 0 \tag{2.2}$$

The female rotor coordinates are produced from the same set of equations if the indices and angle are replaced accordingly. The solution of the coordinates as a function of the angle θ is obtained directly in this case without the need for a numerical iterative procedure. The detailed derivation of equations is given in Appendix I where the specification of the primary curves on the 'N' rack profile is also given.

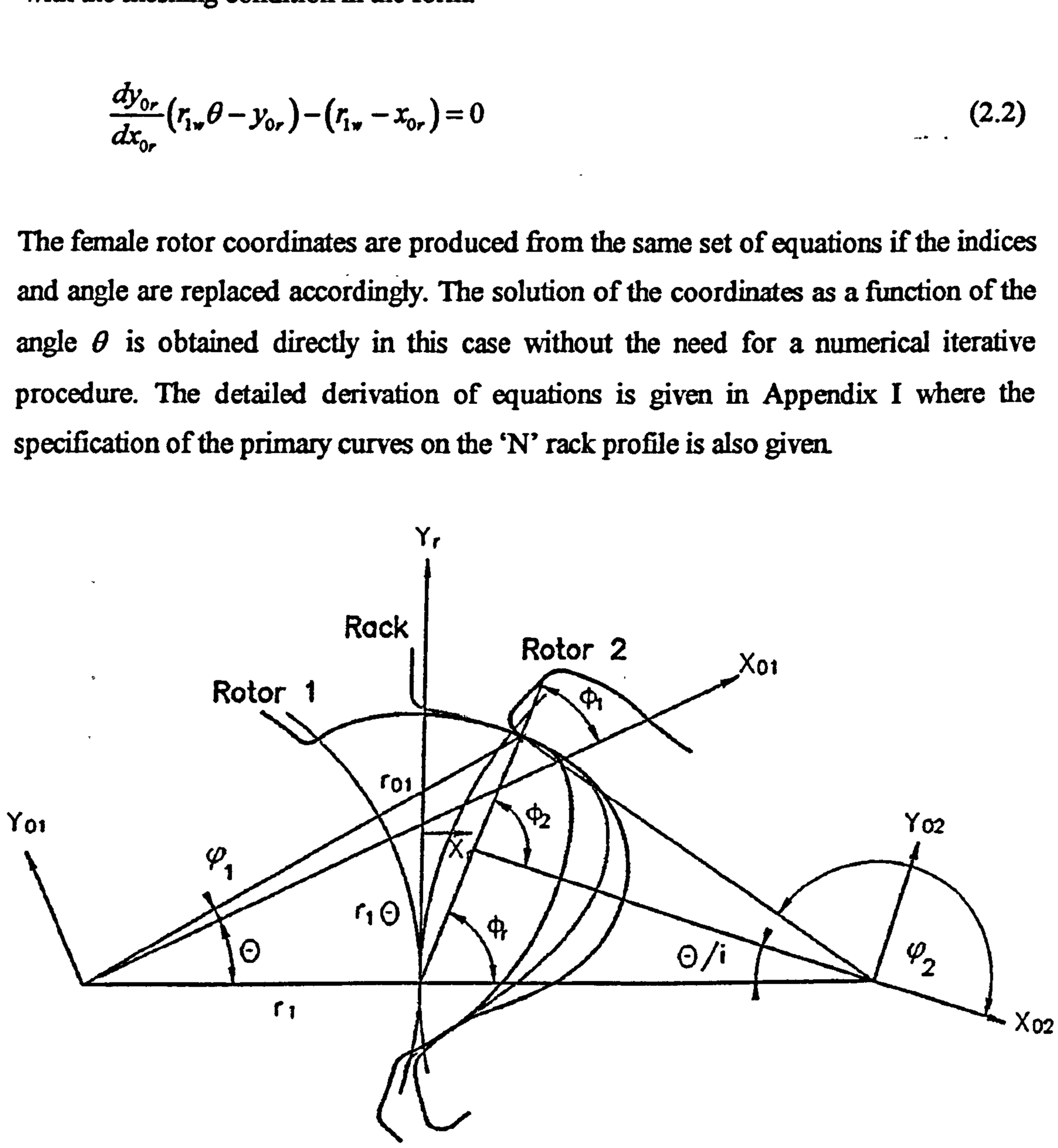

Figure 2-1 Position of the rack and rotors for rack generation procedure

2.3 NUMERICAL ANALYSIS OF SCREW COMPRESSOR PROCESSES

First designs of screw compressors were carried out assuming an ideal gas in a leak proof working chamber going through a compression process which could reasonably be approximated in terms of pressure-volume changes by the choice of a suitable value of exponent "n" in the relationship pV^n = Constant. The advent of digital computing made it possible to model the compression process more accurately.

The first stage was to obtain an algorithm which could be used to estimate the trapped volume between the rotors and the casing and the areas of all leakage passages, at any rotational angle. The latter are formed by clearances between the rotors and between the rotors and the casing. In addition, the area of the inlet or exit passage exposed to bulk flow of fluid into or out of the working chamber had to be obtained where applicable.

The assumption of dimensionless non-steady bulk fluid flow and steady one dimensional leakage flow through the working chamber, together with suitable flow coefficients through the passages and an equation of state for the working fluid, made it possible to develop a set of non-linear differential equations which describe the instantaneous flow of fluid, work and heat transfer through the system. These could be solved numerically to estimate pressure-volume changes through the suction, compression and delivery stages and hence determine the nett torque, power input, fluid flow and isentropic and volumetric efficiencies in a compressor. In addition, assuming that any injected oil passed through the machine lobe in contact with the casing and attributing a mean droplet diameter to the injected oil, enabled account to be taken of oil injection. Such models were then refined by comparing predictions, derived from them, with experimentally derived performance data.

A number of papers have been published describing various aspects of this work, starting with equivalent modelling of reciprocating compressors as, for example, by *Stošić* (1977). This has been followed by many papers by *Stošić et al* (1986), (1988), (1992), (1994) on screw compressors. This work resulted in a suite of computer programs called SCORPATH for profiling, modelling and optimisation of screw compressors. More details of one-dimensional modelling of screw machines by the method stated above are given in Appendix II.

Similar work was also carried out by other authors. *Fleming and Tang* (1992), (1994) and (1998) presented their mathematical model which includes outstanding analysis of leakage flows and optimisation procedures for application to screw compressors used in refrigeration. *Fujiwara and Osada* (1995) presented their prediction model while *Kauder* et al (1994), (1998) published very interesting papers not only on mathematical modelling but also on experimental verification of leakage flows and applications of screw compressors. *Holmes* (1994) and *Sauls* (1994) and (1998) contributed to better understanding of compressor clearances in mathematical modelling and practice.

2.4 COMPUTATIONAL FLUID DYNAMICS

Computational fluid dynamics covers a broad area, which attracted the interest of many investigators at the beginning of the computer era. It is based on the numerical simulation of the conservation laws of mass, momentum and energy, derived for a given quantity of matter or control mass. The work has been widely publicised in books, journals and conference papers.

Many books on fluid dynamics such as *Bird et al* (1962), *Fox and McDonald* (1982) and *White* (1986) contain a detailed derivation of general conservation laws. Three main groups of methods have been developed through the years as described by *Ferziger and Perić* (1995). These are the finite difference, finite element and finite volume methods. It is believed that the first of these was first described by *Euler* in the 18th century but, more recently, *Smith* (1985) gave a comprehensive account of all aspects of it.

The finite element method was initially developed for structural analysis, but later has also been used for the study of fluid flow. It has been described extensively by many authors, such as *Oden* (1972), *Fletcher* (1991) and *Zienkiewicz and Taylor* (1991).

A good summary of the finite volume method is given by *Versteeg and Malalasekera* (1995). Since the finite volume method has already been used to solve problems involving unsteady flow with moving boundaries and strong pressure-velocity-density coupling, it is of particular interest for this thesis. The 'space conservation law' was introduced by *Trulio and Trigger* (1961) and used in conjunction with a finite difference method. The importance of the space conservation law was discussed by *Demirdžić and*

Perić (1988) and introduced to the finite volume method for prediction of fluid flow in complex domains with moving boundaries by the same authors (1990) and also *Demirdžić, Issa and Lilek* (1990). They followed the attempts of many other authors to apply it to solve some special cases. Typically, *Gosman and Watkins* (1977), *Gosman and Johns* (1978) and *Gosman* (1984) reported the calculations of flows in a cylinder with moving boundaries. *Stošić* (1982) applied the method to internal unsteady flows of a compressible fluid. *Thomas and Lombard* (1979) presented solutions of steady and unsteady supersonic flows while *Gosman* (1984) and *Durst et al* (1985) reported that simple transformation of the conservation equations enables easy discretisation when only one of the domain boundaries moves in one direction. *Perić* (1985) introduced a finite volume methodology for prediction of three-dimensional flows in complex ducts where among others he gave an evaluation of various pressure-derivation algorithms for orthogonal and non-orthogonal grids. Additional analysis on pressure-velocity coupling is given by *Perić* (1990) and later discussed and improved by *Demirdžić at al* (1992) and *Demirdžić and Muzaferija* (1995) where they applied the method simultaneously to fluid flow and solid body stress analysis. Turbulence modelling is discussed by many authors, among whom *Hanjalić* (1970) gave an essential introduction to its wider use. *Bradshaw* (1994) and *Hanjalić* (1994) gave good summaries on the subject. *Lumley* (1999) outlined important subjects on turbulence in internal flows of positive displacement machines.

A comprehensive source for the latest information on general CFD subjects can be found in journals such as *Transactions of the ASME (Journal of Fluids Engineering, Journal of Engineering for Gas Turbines and Power and Journal of Heat Transfer), the AIAA Journal, Journal of Fluid Mechanics, Journal of Computational Methods in Sciences and Engineering and Proceedings of the IMechE.*

2.5 GRID GENERATION

Grid generation problems are mainly connected with computational fluid dynamics but, as reviewed by *Thompson* (1996), the applicability of the concepts used in making numerical grids is not in any way limited to this area. Several international conferences have been held on grid generation. Conference Proceedings edited by *Smith* (1992),

Eiseman et al (1994) and *Soni et al* (1996) are typical examples of these and describe a number of applications to CFD and other fields, especially computer graphics.

There are four major textbooks on grid generation. The early monograph by *Thompson, Warsi and Mastin* (1985) is now also published on the Web http://www.erc.msstate.edu/education/gridbook. It covers the entire subject of grid generation developed around structured grids with boundary conforming. A later book by *Knupp and Steinberg* (1993) gives fundamentals of grid generating techniques. *Thompson's* (1999) Handbook of Grid Generation describes the principles of all structured, unstructured and hybrid grids that can be generated either analytically or by solving partial differential equations (PDE). It also gives a very detailed review of most of the major computer codes used for meshing. A book on 'Grid generation Methods' by *Liseikin* (1999) was originally printed in Russian by the Siberian Branch of the Russian Academy of Sciences in Novosibirsk and then translated into English and printed in Germany and the USA. It gives a most detailed mathematical basis of grid generation methods with all necessary theoretical backgrounds. It pays special attention to reviewing the most recent and promising approaches and methods, which have not been sufficiently covered in previous monographs.

A considerable number of general methods for structured grid generation have been reviewed by *Thompson* (1984), *Thompson, Warsi and Mastin* (1985), *Eiseman* (1985), *Liseikin* (1991), *Thompson and Weatherhill* (1993) and *Thompson* (1996). The last one was also published on the Web in year 2000: http://www.erc.msstate.edu/~joe/gridconf. All these consider an algebraic approach to grid generation as well as to the solution of either elliptic, hyperbolic or parabolic partial differential equations. From these, it can be deduced that more control of numerical mesh orthogonality and smoothness is achievable by solving the PDE than by using an analytical approach. However, these methods are generally more computer time consuming then the algebraic ones.

Although, officially, transfinite interpolation for meshing purposes was first introduced at the grid conference in Nashville in 1982 by *Gordon and Thiel,* algebraic grid generation, which uses a transfinite interpolation method, has its roots in the early work by *Gordon* (1969, 1973). Many authors after that referred to their achievements in analytical methods. It started with *Smith's* Algebraic Grid Generation in 1982 when

Hermite interpolation between two opposite boundaries was presented. Then *Vinkour* (1993) introduced one-dimensional stretching functions. Two, four and six boundary interpolation which use one-dimensional stretching functions were well summarised by *Shih et all* (1991) and later applied to complex grids using enhanced control of grid distribution by *Steinhorsson, Shih and Roelke* (1992). Their latest paper proposed the use of multidimensional stretching functions, applied to two opposite boundaries in the four-boundary method. Other simpler methods were also developed and reported such as that of *Saha and Basu* (1991), but they were applicable only to rather simple grids. Orthogonality and clustering control for algebraic grid generation was reported by *Chawner and Anderson* (1991). An algebraic homotopy procedure for 2 and 3-D domains was introduced by *Moitra* (1992). *Zhu, Rodi and Schoenung* (1992) suggested a fast method for smooth grids by algebraic transfinite interpolation. Some of the methods previously reported were revised in the paper given by *Soni* (1992) and applied to internal flow configurations. More recently, *Liou and Yeng* (1995) presented an algebraic method which generates a numerical grid by combining two grids and uses a marching method in calculating the final mesh. Zhou (1998) presented a 'simple' method using functions of the first, second or third order to interpolate between the boundaries. The method, although simple and fast, often produces overlapping and irregularity for complicated domains. The main problem that remained during all these years of development of algebraic methods was that meshes generally have not been orthogonal and smooth and that overlapping appeared as the major problem in complex domains. More recently, *Lehtimaki* (2000) suggested another method in which the first step is to generate a correct mesh without overlapping, not necessarily smooth and orthogonal, and then to apply orthogonalization and smoothing to it by moving internal points. The method appeared to be extremely useful but required additional checking of the mesh regularity. *Field* (2000) in his journal paper presented qualitative measures for initial meshes, which, together with a good description and mathematical background of the grid quality measures by *Liseikin* (1999), reasonably covers the problem.

Differential methods for the structured grids solve elliptic, parabolic or hyperbolic equations were discussed by many authors and were well summarised by *Thompson* (1985, 1996 and 1999) and *Liseikin* (1999).

Surveys on general adaptive methods were presented by *Eiseman* (1987), *Liseikin* (1996 and 1999) and *Thompson* (1999). Practical applications of adaptive methods have been published by *Kim and Thompson* (1990) and *Samareh-Abolashi and Smith* (1992). The latest described a practical approach to the grid adaptation based on two physical properties. The method was used for dynamic grid adaptation in supersonic flow domains.

The methods for unstructured grids were revised by a number of authors among whom are *Thompson* (1985, 1999), *Liseikin* (1999), *Eiseman* (1987) and *Owen* (1998). The latter published his review on unstructured grid methods on the Web (http://www.andrew.cmu.edu/user/sowen/survey/index.html) where a summary on recently developed methods in automatic generation for complicated domains is given. Among these methods, the major ones are conformal mapping by *Barker and Lantz* (1997), control point grid generation by *Eiseman* (1991 and 1992) and quad-mapping by *Owen et al* (1998).

More recently a huge effort has been made to develop grid generation in Cartesian co-ordinates by *Lin and Chen* (1998). Its main advantage lies in the fact that the conservation laws are completely satisfied, without the need for additional terms, but they have a great disadvantage in the need for mesh refinement in the vicinity of the boundaries.

2.6 CFD IN SCREW COMPRESSORS

Despite a significant increase in the number of papers published recently in the area of computational fluid dynamics, only a few deal with the application of computational fluid dynamics to screw compressors. All of them are recent papers which started with *Stošić et al* in 1996. That paper describes the principles of three dimensional numerical modelling applied to positive displacement screw machines. However, it was not successful due to the relatively poor grid generation applied. *Kovačević, Stošić and Smith* published a number of papers between 1999 and 2001. These papers introduced 3-D numerical analysis to the screw compressor world.

Chapter 3

Aims of the Research and Contribution to Knowledge

3.1 AIMS OF THE RESEARCH

The aim of this investigation was to establish a means to simulate flow processes in screw machines that would fully account for three dimensional effects. To achieve this, the following objectives were set:

- To develop an analytical grid generation method which would describe the changing shape of screw compressor flow passages, by means of points, cells and regions of moving finite volume numerical mesh.

- To enable a general CFD solver to be used for the fast calculation of flow parameters within a screw compressor or expander, allowing for either ideal or real fluids, with or without change of phase, and valid for both oil free and oil injected machines.

- To produce a stand alone computer program which would automatically generate a finite volume numerical mesh, prepare user subroutines for a general CFD solver and make a pre-processor script to import geometry definition, initial and boundary conditions and to set the operational parameters of the solver automatically.

- To validate results obtained from three-dimensional numerical calculations, thus derived, by comparison with measurements obtained from a real oil injected air compressor

3.2 CONTRIBUTION TO KNOWLEDGE

As a result of the work described in this thesis being carried out, the following original contributions have been made to the modelling of flow through screw expanders and compressors. These have advanced both the scope and accuracy of the analysis of such machines and, when implemented, should enable them to be designed and developed at less cost and with improved performance:

- A wholly original boundary adaptation procedure has been developed in order to allow for convenient mapping of the internal grid points of a screw compressor. This is sufficiently flexible to fit any arbitrary rotor profile. The procedure includes a practical transformation method which adapts the computationally transformed region to produce a regular boundary distribution on the outer mesh boundary.

- An algebraic grid generation method has been developed which enables the complex three-dimensional domain of a screw machine to be mapped regularly even in regions with a high geometrical aspect ratio.

- The grid thus formed can be transferred directly to a general CFD solver

- Novel boundary conditions are introduced during the calculation procedure to keep the pressures in the inlet and outlet chambers constant at their final desired values rather than letting them vary with the compressor cycle. By this mean, the convergence of the solution is greatly speeded up.

- A fast procedure has been specially developed to estimate the properties of real fluids and how these vary as a result of phase change in two-phase flow. The procedure is based on the gas compressibility factor. By this means the fluid properties in each cell can be estimated with reasonable accuracy in a short time even when the grid is large.

- A means has been developed to simulate two-phase flow within the machine by two different procedures by use of the Euler-Lagrangean approach.

- All these procedures have been combined to create a stand alone computer program called SCORG (Screw Compressor Rotor Geometry Grid generator). This serves as a pre processor which may then be attached to any general CFD solver that permits solutions based on finite volume analysis.

Chapter 4

Three-dimensional Numerical Analysis in Screw Machines

4.1 INTRODUCTION

With the advent of computer technology and the accompanying computational methods, the design and working process analysis of positive displacement machinery by means of 3D computational continuum mechanics (CCM) is slowly but persistently becoming a reality. In general, the modelling process of CCM can be split into four main steps that are identified here and described in more details in the text.

1. The first step is to define the problem in question. The convenience of solution and implementation of results into the design process are greatly based on this critical starting step. There are two possibilities for the working domain to be selected in positive displacement machines of the screw type. The first approach is based on the selection of one interlobe on the main rotor and the corresponding interlobe on the gate rotor to make a computational domain. This is probably the easiest to be implemented but it doesn't take account of some important phenomena such as. interlobe leakage, blow-hole losses, oil injection and oil distribution. Another approach assumes that the whole domain of a screw machine is analysed. This includes the suction chamber and its port, compression or expansion chamber with moving rotor boundaries and the discharge system of the machine. By this means, the leakage paths and eventually additional inlet or outlet ports are included in the

domain that is to be analysed. Realism in representing the machine working process gives a large advantage to this approach. The design procedure and CCM numerical analysis can then be easily connected and interchanged and the calculation of the operational parameters of such machines is thereby facilitated. Unfortunately, such a complex geometry cannot be represented by a small number of computational points. Therefore, methods for increasing the speed of the solution are required. It is also necessary to decide which boundary conditions to use. These should connect the working domain with the surroundings in both, the physical and numerical sense.

2. The second step is the choice of a mathematical model that is capable of describing the problem. There are two types of situation. One, where an adequate mathematical description exists and can be used, e.g. heat conduction, elastic stress analysis, laminar fluid flow, and the other a case for which an adequate mathematical description either does not exist or is impractical to use, e.g. non-linear stress analysis and turbulent fluid flow. In the case of a positive displacement machine there is hardly an analytical solution that can be found. This is because highly compressible flow appears inside the domains with turbulent flow regimes and domains with low Reynolds numbers. There are additional non-linearities introduced by two-phase flow, particle flow, moving and stretching domains and sliding boundaries. Due to all these, the mathematical model implemented here needs to cope with a variety of different requirements. It is based on the general laws of mass, momentum, energy and space conservation. The resulting system of governing equations is not closed because it contains more unknowns than resulting equations. It is closed by constitutive relations which give information about the response of a particular continuum material to external influences. The whole concept of mathematical modelling is based on the phenomenological approach which employs the principle of a continuum as the physical background. It can be applied only when an elementary part of material or the smallest characteristic length of the flow, which has to be analysed, is much bigger then the mean free molecular path. Fortunately, this condition is fulfilled for the majority of fluids and practically for all solid structures. This enables a phenomenological approach to be applied to study processes in positive displacement machines.

3. The mathematical description of problems in continuum mechanics is very rarely amenable to a closed-form analytical solution and an iterative numerical procedure is the only alternative that can be applied to solve models in positive displacement machines. Numerical methods transform differential equations of the mathematical model into a system of algebraic equations. To do that a number of approximations are made: the continuum is replaced by a set of computational points with finite distances between them in space and time, while the continuous functions which represent the exact solution of the mathematical model are approximated by polynomials of a finite order, typically second. Because of the complexity of positive displacement machines, the standard approach to spatial discretisation is not applicable. A special grid generation method has to be developed and applied to positive displacement machines. Equations are discretised by the finite volume method which appears to have a more conservative form of governing laws then any other numerical method. The result of discretisation is a system of algebraic equations the size of which depends on the number of numerical cells.

4. The resulting set of algebraic equations is then solved by approximate iterative methods. Iterations are necessary due to the non-linearity of the mathematical model. Even for linear problems, iterative solution methods are usually more efficient than a direct one. In addition, iterative solution methods are less sensitive to round-off errors due to the finite accuracy of the computer arithmetic. Single or double precision is used, normally with 7 and 15 significant digits respectively.

4.2 MATHEMATICAL MODEL OF CONTINUUM APPLIED TO PROCESSES IN SCREW MACHINES

A mathematical model of transport processes, which exist within the twin screw and other positive displacement machines, is presented here. It includes the mass, momentum and energy conservation equations in integral form, a space conservation law, which has to be satisfied for problems with a moving mesh, constitutive relations required for the problem closure, a model of dispersed flow, models of turbulence in fluid flow and boundary conditions.

All equations are presented in a symbolic coordinate-free notation which directly conveys the physical meaning of particular terms without unnecessary reference to any coordinate system. However, numerical solution of these equations requires a coordinate system and vectors and tensors have to be specified in terms of their components. When necessary, the Cartesian coordinate system will be used, which ensures that the discretised equations contain all the conservation properties of the continuum equations.

4.2.1 Governing Equations

Fluid trapped within a screw compressor can be gas, vapour or a wet mixture of liquid and vapour. Its density varies with both pressure and temperature. The compressor flow is governed by equations based on the basic laws of continuity, momentum and energy conservation. The most general approach is to write these equations in integral form and apply them to an arbitrary part of the fluid or solid continuum of volume V, which is bounded by a moving surface S, Figure 4-1.

The conservation principle of an intensive property of matter written for the control volume occupied by some quantity of mass is often called Reynolds' transport theorem or a control volume equation. It is defined as:

$$\frac{d}{dt}\int_{V_{CM}} \rho\phi dV = \frac{d}{dt}\int_{V_{CV}} \rho\phi dV + \int_{S} \rho\phi(\mathbf{v}-\mathbf{v}_s)ds \qquad (4.1)$$

where, V_{CM} is the volume of the control mass, V_{CV} is the control volume enclosed by the surface S. Vector ds stands for the outward pointing surface vector defined by its unity vector **n** and surface area dS as $d\mathbf{s}=\mathbf{n}\,dS$. In equation (4.1), ϕ represents a conserved property per unit mass. It can be mass, momentum, energy, concentration or other property.

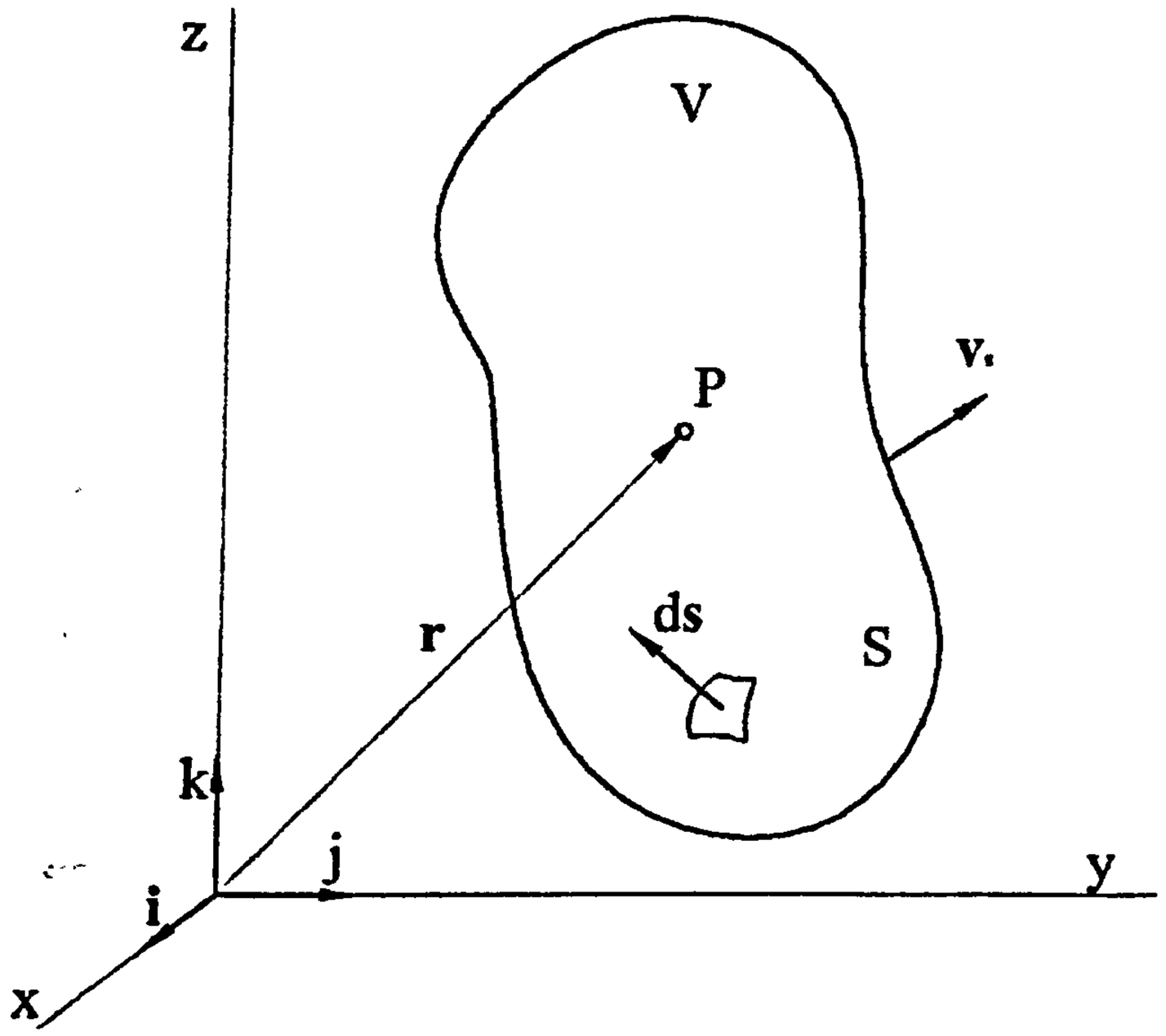

Figure 4-1 Control volume of part of the continuum

Vector $\mathbf{v}_s$ is the velocity with which the surface of the control volume moves. If the control volume is fixed, then its surface velocity $\mathbf{v}_s$=0. Equation (4.1) then makes the rate of change of the amount of property in the control mass equals to the sum of the rate of change of the property within the control volume and the net flux of the property through the control volume boundary due to relative fluid motion. This equation represents the Eulerian approach. The last part of the equation is called the convective term. If the control volume moves with the same velocity as the boundary of the control mass, then the boundary velocity is equal to the velocity of the control mass, $\mathbf{v}=\mathbf{v}_s$. This form of equation, which has a convective term equal to zero, is called the Lagrangian approach. For convenience, the control volume is denoted as V and S is its surface.

If the variable of the conserved property in (4.1) is ϕ =1, then the control volume equation represents the continuity equation:

$$\frac{d}{dt}\int_V \rho dV + \int_S \rho(\mathbf{v}-\mathbf{v}_s)\cdot d\mathbf{s} = 0, \tag{4.2}$$

If the conserved property in equation (4.1) is velocity, i.e. ϕ=**v**, then this equation is the momentum equation:

$$\frac{d}{dt}\int_V \rho \mathbf{v} dV + \int_S \rho \mathbf{v}(\mathbf{v}-\mathbf{v}_s)\cdot d\mathbf{s} = \sum f\,, \tag{4.3}$$

where the right hand side of the equation represents the sum of surface and body forces which act on the matter in the control volume. Since the body forces acting on the whole matter trapped in the control volume are independent of the shape of the boundary surface they represent a vector field and can be integrated over the control volume. However, surface forces such as pressure forces, normal and shear stress forces or surface tension forces, depend on the surface on which they act, and from the molecular point of view, they represent macroscopic momentum fluxes across the surface (*Ferziger and Perić* 1995). In order to close the system of equations, these fluxes must be written in terms of properties whose conservation is governed by the equation in question. In equation (4.3) the conserved property is the velocity **v**. For a screw compressor, as in most engineering problems, working fluids are assumed to be Newtonian. For these fluids, Stokes' law, which gives a relation between stress **T** and rate of deformation **D**, can be applied. Similarly, Hookes' law gives a similar relation for thermo-elastic solids. In both cases, the momentum equation (4.3) becomes:

$$\frac{d}{dt}\int_V \rho \mathbf{v} dV + \int_S \rho \mathbf{v}(\mathbf{v}-\mathbf{v}_s)\cdot d\mathbf{s} = \int_S \mathbf{T}\cdot d\mathbf{s} + \int_V \mathbf{f}_b dV \tag{4.4}$$

where **T** is the stress tensor and $\mathbf{f}_b$ is the resultant body force.

If the conserved property ϕ in equation (4.1) is scalar, e.g. enthalpy or concentration, then the equation can be written in the following form:

$$\frac{d}{dt}\int_V \rho \phi dV + \int_S \rho \phi(\mathbf{v}-\mathbf{v}_s)\cdot d\mathbf{s} = \sum f_\phi\,, \tag{4.5}$$

where the term on the right hand side is the sum of all the modes of transport of property ϕ, other then convection which is already on the left side of this equation, and

any sources or sinks of that property. This sum generally consists of two terms; the diffusive transport and the sink or source of the conserved property. The diffusive transport can be written in universal form as:

$$f_\phi^d = \int_S \Gamma \operatorname{grad}\phi \cdot d\mathbf{s} = \int_S \mathbf{q}_\phi \cdot d\mathbf{s}. \tag{4.6}$$

Γ is the diffusivity of property ϕ. Equation (4.5) in that case becomes a generic conservation equation:

$$\frac{d}{dt}\int_V \rho\phi dV + \int_S \rho\phi(\mathbf{v}-\mathbf{v}_s)\cdot d\mathbf{s} = \int_S \mathbf{q}_\phi \cdot d\mathbf{s} + \int_V S_\phi dV, \tag{4.7}$$

where S_ϕ is the source or sink of property ϕ per unit mass. Equation (4.7) appears to be a generic equation valid for all intensive properties of matter.

From equation (4.7) one can get the energy equation, in the form of enthalpy, directly as:

$$\frac{d}{dt}\int_V \rho h dV + \int_S \rho h(\mathbf{v}-\mathbf{v}_s)\cdot d\mathbf{s} = \int_S \mathbf{q}_h \cdot d\mathbf{s} + \int_V s_h dV + \int_V (\mathbf{v}\cdot\operatorname{grad} p + \mathbf{S}:\operatorname{grad}\mathbf{v})dV - \int_S p\mathbf{v}_s \cdot d\mathbf{s} + \frac{d}{dt}\int_V p dV. \tag{4.8}$$

S is the viscous part of the stress tensor defined as:

$$\mathbf{S} = \mathbf{T} + p\mathbf{I}. \tag{4.9}$$

I is a unit tensor.

If applied to the concentration scalar $c_i = {}^{m_i}/_{m}$, where m_i denotes the mass of the dispersed fluid in the working fluid and m defines the overall mass, equation (4.7) becomes:

$$\frac{d}{dt}\int_V \rho c_i dV + \int_S \rho c_i (\mathbf{v} - \mathbf{v}_s)\cdot d\mathbf{s} = \int_S \mathbf{q}_{c_i}\cdot d\mathbf{s} + \int_V S_{c_i} dV, \tag{4.10}$$

where $\mathbf{q}_{ci}$ is the diffusion flux and S_{ci} is the source or sink of the dispersed phase.

If the conserved property in equation (4.7) is defined as $\phi=1/\rho$ then this equation becomes the space conservation law which must be satisfied if the domain boundaries move:

$$\frac{d}{dt}\int_V dV - \int_S \mathbf{v}_s \cdot d\mathbf{s} = 0. \tag{4.11}$$

This equation links the rate of change of volume V and surface velocity $\mathbf{v}_s$.

Equations (4.2), (4.4), (4.8), (4.10) and (4.11) make a mathematical model which is valid for the majority of fluids and solids in engineering practice. For the numerical modelling of a screw machine, the first three of these equations should be solved for the working gas, which is also called a background fluid. Equation (4.10) should be solved for the disperse phase, which is either oil or some other fluid injected into the working chamber and dispersed into the background fluid, while the equation of space must be satisfied for any case, because the compression or expansion in the positive displacement machine is caused entirely by the movement of the boundary. In two-phase flow, the liquid phase of the working fluid can also be considered as the dispersed phase, e.g. a refrigerant. This approach assumes that the dispersed phase is a passive 'species' in the background fluid. It allows separate calculations for these two phases. The influence of the dispersed phase on the main flow and vice versa is through the source terms in the governing equations. Such a method does not require the additional calculations of mixture properties such as density and viscosity. This is convenient and physically sound in the case of an oil-injected compressor where the two phases are fluids of a different type. Although these two flows are usually calculated from the unique density and viscosity of the vapour-liquid mixture, it is more convenient to take account of the values of the vapour and liquid properties separately with concentration as the blending factor between them. Such an approach is usually called the Euler-Lagrangean method.

4.2.2 Constitutive Relations

The numerical method described in the previous paragraph contains information about material properties that are still not considered in the model. These are used to express the stress tensor **T**, heat flux $\mathbf{q}_h$ and diffusion flux $\mathbf{q}_{ci}$. There are many situations in engineering practice where relatively simple assumptions can be made to define values for these. If a working fluid can be regarded as Newtonian, as in the case of a screw compressor, then Stokes, Fourier's and Fick's laws are used to close the system of the model equations. Since the governing equations defined in the previous paragraph are derived on the assumption that matter is a continuum, they are general and valid for both fluids and solid materials. For Newtonian fluids, the stress tensor, which represents the molecular rate of transport of momentum and closes equation (4.4), can be defined by Stokes law as:

$$\mathbf{T} = 2\mu\dot{\mathbf{D}} - \frac{2}{3}\mu \operatorname{div}\mathbf{v}\mathbf{I} - p\mathbf{I}, \tag{4.12}$$

where the rate of strain is defined as:

$$\dot{\mathbf{D}} = \frac{1}{2}\left[\operatorname{grad}\mathbf{v} + (\operatorname{grad}\mathbf{v})^T\right]. \tag{4.13}$$

Superscript T represents the transposed tensor. Stokes law gives the relation between the stress and the rate of deformation for Newtonian fluids.

On the simplest assumption, solid material can be treated thermo-elastic. For thermo-elastic solids, the constitutive relation that closes equation (4.4) is Hooke's law given here in Duhamel-Neumann's form. It defines the relation between the stress and strain in solids as:

$$\mathbf{T} = 2\eta\mathbf{D} - \lambda \operatorname{div}\mathbf{u}\mathbf{I} + (3\lambda + 2\eta)\alpha_t \Delta T\mathbf{I}, \tag{4.14}$$

where the strain tensor is:

$$\mathbf{D} = \frac{1}{2}\left[\operatorname{grad}\mathbf{u} + (\operatorname{grad}\mathbf{u})^{T}\right]. \tag{4.15}$$

Equations (4.12) and (4.14) have the same form. This allows them to be incorporated into a mathematical model and solved by the same method. By this means, the simultaneous calculation of fluid flow and deformation in solids permits the analysis of fluid solid interaction.

The viscous part of the stress tensor, which appears in equation (4.8), is now fully defined by equations (4.9), (4.12) and (4.13). However, the heat flux through the surface boundary $\mathbf{q}_h$ is not yet specified. Fourier's law defines it as a product of the thermal conductivity κ and the temperature gradient.

$$\mathbf{q}_h = \kappa \operatorname{grad} T. \tag{4.16}$$

It is common practice to model the mass flux of the dispersed phase, relative to the mean flow, defined by equation (4.10), by use of Fick's law:

$$\mathbf{q}_{c_i} = \rho D_i \operatorname{grad} c_i, \tag{4.17}$$

where D_i is the mass diffusivity of the dispersed phase. In the case of only one fluid dispersed in the main flow, which is the most common case in oil injected screw compressors, equation (4.17) fully satisfies the overall mass concentration equation:

$$\mathbf{q}_{c_i} = \rho c_i (\mathbf{v}_{c_i} - \mathbf{v}_m). \tag{4.18}$$

The velocity of the dispersed phase is $\mathbf{v}_{ci}$, while the mass averaged velocity of the mixture is $\mathbf{v}_m = \sum_{i=0}^{N} c_i \mathbf{v}_{c_i}$. Equation (4.18) is completely satisfied if one fluid is dispersed in the background phase. Otherwise, it is valid if each fluid satisfies its own equation. On the other hand, Fick's law would satisfy equation (4.18) only if

$\sum_{i=0}^{N} c_i \mathbf{q}_{c_i} = 0$. This happens only if the diffusion coefficients of all dispersed fluids have the same value. More on this topic can be found in *Ferziger and Perić* (1995)

Even if all the variables, which define the material properties, are known, the system of equations is still not closed because the pressure p exists in both, the energy equation (4.8) and in the stress tensor (4.12) which forms part of the momentum equation (4.10). The equation of state, which balances the mass equation with thermodynamic properties pressure and temperature, closes the system.

$$\rho = \rho(p,T), \quad e = e(p,T) \tag{4.19}$$

Equations of state are directly applicable to all engineering fluids and solids, both ideal and real. Common examples are incompressible fluids and solids where $\rho=const$ and $e=C_vT$, or ideal gases where $\rho=p/RT$, $e=C_vT$. However, real fluids are not rare in screw machinery. In that case, density of the real gas or mixture can be calculated based on the user specified procedure and later introduced to the model. These equations must have the form of equation (4.19).

4.2.3 Multiphase Flow

In an oil-flooded screw compressor, oil is a dispersed phase of the working fluid. The liquid part of two-phase flow in positive displacement machines can also be regarded as a dispersed phase and calculated in the same manner. In both cases, flow through the machine has a multiphase character. That is because more then one fluid or aggregate phase of the same fluid is present and occupies the working domain. There are two different approaches to multiphase flows. One of them is the Eulerian approach where each of two or more phases is contained in its own domain strictly separated in space from other and connected with the domains of the other phase through the boundary interface. An example of this is an oil tank in which the level of oil is above the space occupied by the gas. If the Eulerian approach is assumed, then the sharp interface between oil and water exists and separate numerical meshes can be generated. Both, oil and water have to satisfy the governing equations described in 4.2.1.

This is not applicable to the two-phase flow within a screw machine. More appropriate is the so-called Eulerian-Lagrangian approach in which both phases occupy a common working domain without a strict interface between them. In such a case, the background fluid must satisfy the governing equations of mass, energy and momentum, while the dispersed phase should satisfy the governing equation of concentration. Such an approach assumes that the dispersed phase is either a passive or an active component. The dispersed phase in the form of oil or other injected liquid has an important role in the screw compressor working cycle. It is there to cool the fluid, seal the clearance gaps and lubricate the compressor moving parts. The influence of the dispersed phase on the background fluid and vice versa must be incorporated in the governing equations. This is done through source terms in the mass, momentum and energy equations.

4.2.3.1 The energy Source

The energy balance of a dispersed phase trapped in the control volume can be written in the following form:

$$\frac{d(m_i h_i)}{dt} = m_i \frac{dh_i}{dt} + h_{iL} \frac{dm_i}{dt} = \dot{Q}_{con} + \dot{Q}_{mass}, \tag{4.20}$$

The first term on the right hand side of this equation represents the convective heat flux between the dispersed phase and the background fluid while the second term represents the heat transfer due to mass interchange between the phases. The last one is significant only for two-phase flow of the same fluid in the working chamber. In the case of an oil-flooded compressor, the convection term has a significant role. In equation (4.20) h_i is specific enthalpy per unit of mass while h_{iL} defines the enthalpy of vaporisation. It represents the difference between the enthalpies of the liquid and vapour phases, i.e. the dispersed and continuous phases. If the specific heat of oil at constant pressure is constant, then equation (4.20) becomes:

$$\frac{d(m_l T_l)}{dt} = m_o C_{p_o} \frac{dT_o}{dt} + h_L \frac{dm_L}{dt} = \dot{Q}_{con} + \dot{Q}_{mass}, \tag{4.21}$$

There are two approaches to implement convective heat transport between the dispersed phase and the background fluid.

The first approach assumes that the dispersed phase is completely dissolved in the background fluid. That means that the droplet size of the dispersed phase is very small, ie. $d_o \to 0$. In that case, an ideal process of heat transfer can be assumed where the temperature of the dispersed phase is assumed equal to the temperature of the background fluid $T=T_o$. Heat exchanged between the phases is then calculated from the temperature difference of the continuous phase in two consecutive steps multiplied by the mass and specific heat of the dispersed phase as:

$$\dot{Q}_{con} = m_o C_{p_o} \frac{dT}{dt} \approx m_o C_{p_o} \frac{T^k - T^{k-1}}{\delta t}, \tag{4.22}$$

where T^k is the temperature in the current time step and T^{k-1} is the temperature from the previous time step or iteration. δt is the time step. If the time step is small then this equation has the exact differential form of convective heat transfer. The assumption of an infinitesimally small droplet size is not completely correct but analysis of the influence of oil on screw compressor performance conducted by *Stošić et al* (1992) showed that a change in droplet size from 0 to 100 μm, does not affect the oil and consequently the gas temperature too much. Therefore, it is accurate enough to calculate the heat exchanged between the continuous and dispersed phase by means of equation (4.22).

When necessary, another approach can be used to calculate the convective term in equation (4.21). It should be applied whenever the temperatures of the continuous and dispersed phases cannot be considered to be equal. It is then assumed that the dispersed phase, contained in the control volume, consists of spherical droplets with a Sauter mean diameter defined as:

$$d_o = 0.0092\left(\frac{\rho_o \sigma_o}{|\mathbf{v}|}\right)\left(1+\frac{1}{c_o}\right)^{0.7}, \tag{4.23}$$

where σ_o is the surface tension and $|\mathbf{v}|$ is the absolute velocity of the fluid. The convective heat flux then becomes:

$$Q_{con} = \pi d_o \kappa \mathrm{Nu}(T - T_o), \tag{4.24}$$

where, T and T_o are temperatures of the continuous and dispersed phases respectively and the Nusselt number is given by:

$$\mathrm{Nu} = 2 + 0.6\,\mathrm{Re}^{0.5}\,\mathrm{Pr}^{0.33}. \tag{4.25}$$

In the previous equation the Prandtl number is defined as:

$$\mathrm{Pr} = \frac{\mu C_p}{\kappa}. \tag{4.26}$$

Reynolds number is:

$$\mathrm{Re} = \frac{\rho|\mathbf{v}_o - \mathbf{v}|d_o}{\mu}, \tag{4.27}$$

The velocity of dispersed phase is $|\mathbf{v}_o|$. There are again two possible approaches. The first is to assume the velocity of the dispersed phase to be the same as the velocity of the continuous phase. In this case $\mathbf{v}=\mathbf{v}_o$. This can be assumed if the size of droplet defined by equation (4.23) is small, e.g. less then 20 μm. If this is not the case, a different approach has to be applied and the velocity vector of the dispersed phase has to be calculated by another procedure. Whatever the velocity, the temperature of the dispersed phase is derived from the balance of two equations that define heat transfer namely: (4.22), which represents the amount of heat taken in by the dispersed phase,

and (4.24) which defines amount of heat given out by the continuous phase. This can be written as:

$$m_o C_{p_o} \frac{T_o^k - T_o^{k-1}}{\delta t} = \pi d_o \kappa \mathrm{Nu} (T - T_o^k), \tag{4.28}$$

where T_o^k and T_o^{k-1} are temperatures of the dispersed phase in the two consecutive time steps.

When equation (4.25) is applied, the temperature of the dispersed phase becomes:

$$T_o = T_o^k = \frac{T + k_t T_o^{k-1}}{1 + k_t}, \tag{4.29}$$

where the time constant k_t is defined as:

$$k_t = \frac{m_o C_{p_o}}{\pi d_o \mathrm{Nu} \kappa \delta t}. \tag{4.30}$$

In all the previous equations, the mass of the dispersed phase in the control volume is calculated from the mass concentration c_o defined from equation (4.10) as:

$$m_o = \rho_o V_o = \frac{\rho_o \rho V c_o}{\rho(1 - c_o) + \rho_o c_o}, \tag{4.31}$$

where ρ_o and ρ are the densities of the dispersed and continuous phase respectively. Both densities are calculated from the equation of state (4.19).

The last term in equation (4.21) represents heat transfer due to mass transfer between the phases. It is significant when a real fluid evaporates or condenses in the machine. It can be expressed as:

$$\dot{Q}_{mass} = h_L \frac{dm_L}{dt} \approx h_L \frac{\Delta m_L}{\delta t} = h_L \frac{m_L - m_L^{'}}{\delta t} = h_L \dot{m}_L, \tag{4.32}$$

where Δm_L is the mass exchanged between the liquid dispersed phase and the continuous phase. It is defined as the difference between the mass of the continuous phase in the control volume calculated from the mass balance equation (4.2) and the mass of the continuous phase calculated by the equation of state (4.19) at a pressure obtained from the governing equations and the saturation temperature at the same pressure.

The latent heat of evaporation h_L is the difference between the specific enthalpy of liquid h_l and specific enthalpy of vapour h_v at saturation pressure p which is calculated from the model:

$$h_L = h_v - h_l \tag{4.33}$$

Since these two enthalpies are not known at present they should be calculated together with other properties of the real fluid.

The heat fluxes calculated from equations (4.24) and (4.32) represent the source terms in the energy equation (4.8).

4.2.3.2 The Mass Source

The mass of the dispersed phase changes in two-phase flow because of evaporation or condensation in the control volume. The amount of mass exchanged between the two phases is defined as:

$$\dot{m}_L = \frac{dm_L}{dt} \approx \frac{\Delta m_L}{\delta t} = \frac{m_L - m_L^{'}}{\delta t}. \tag{4.34}$$

In practice, if the control volume is assumed constant during one time step, the pressure and temperature are calculated from the governing equations together with the mass of the continuous phase. The mass concentration of the dispersed phase is calculated from equation (4.10). This procedure defines the mass of the dispersed phase m_o through equation (4.31). If two-phase flow exists in the control volume, the temperature of the mixture is the saturation temperature for the calculated pressure. If the temperature calculated by the model does not satisfy this condition, mass must be exchanged between the dispersed and continuous phases to establish equilibrium. The exchanged mass transfers the heat of evaporation between the phases until equilibrium is established. The heat of evaporation is calculated from the balance equation of the heat exchanged between the phases and the heat required to adjust the temperature of the mixture to the saturation temperature for the pressure calculated in the control volume:

$$\Delta m_L \cdot h_L = m \cdot C_{pm} \cdot (T - T_{sat}) \tag{4.35}$$

This mass becomes a source or sink in the mass equation for the continuous phase. Also, it is subtracted from the concentration of the dispersed phase through the source term in equation (4.10).

4.2.3.3 The Momentum Source

The equation of motion for an individual droplet of the dispersed phase in a positive displacement machine is given in the form of an ordinary differential equation based on Newton's second law:

$$\frac{d(m_o \mathbf{v}_o)}{dt} = \mathbf{f}_{drag} + \mathbf{f}_{pres} + \mathbf{f}_{body} + \mathbf{f}_{am}, \tag{4.36}$$

where the pressure forces $\mathbf{f}_{pres}$, body forces $\mathbf{f}_{body}$ and apparent mass forces $\mathbf{f}_{am}$ often can be neglected. The interphase drag force $\mathbf{f}_{drag}$ is:

$$\mathbf{f}_{drag} = -\frac{1}{2}\rho A_o C_{drag} |\mathbf{v}_o - \mathbf{v}|(\mathbf{v}_o - \mathbf{v}), \tag{4.37}$$

where $A_o = d_o^2 \pi/4$ is the surface of the dispersed phase particle with Sauter mean diameter d_o, $\mathbf{v}_o$ is the velocity of the dispersed phase in the control volume and C_{drag} is the drag coefficient which, in case of a Newtonian fluid, depends only on the Reynolds number defined by equation (4.27). When applicable, equation (4.36) is used to calculate the velocity of the dispersed phase while equation (4.27) gives a source term for the momentum equation. If one assumes ideal heat transfer with a particle of size 0, then the drag force is also 0.

4.2.4 Equation of State of Real Fluids

For ideal fluids $u=f(t)$ and $\rho=f(p,t)$ i.e. $u \neq f(p)$. In the case of air compressors, which are the most common type of screw machine, this is a sufficiently close approximation. However, refrigerating, air conditioning and process compressors operate on fluids which are not ideal. In that case, more complex functions are required to describe fluid property change. Many software packages are available today for the calculation of real fluids. Some examples of these are NIST, a widely used professional software package, the IIIR routines and other software based on alternative equation of state. Often, users develop software for their own requirements which gives good agreement over the required operating conditions.

Most of these packages are highly robust and accurate, but impractical for use in CFD because of the large number of calculations required to obtain the required thermodynamic properties. Two software packages were tested during the development of the 3-D mathematical model of a screw machine. The THERPROP subroutines, developed previously by *Smith et al* (1994), required about 30 minutes for the calculation of thermodynamic properties in each numerical iteration in a screw compressor, defined by 500,000 numerical cells. The NIST routines required 30% more time. This means that one time step could not be calculated in less then 20 hours. Since, flow in a screw compressor is compressible, a change of volume induces a change in pressure. This then becomes the driving force which alters all the other fluid properties

which are functions of pressure. Saturation temperature and other values such as specific volume, latent heat of evaporation or enthalpies, should then be calculated from the known pressure. Unfortunately, all P-ρ-T equations define pressure explicitly, but other values only implicitly. Thus, to calculate the temperature of saturation, for example, an iteration method is required which takes a relatively long time to converge.

In the case of two-phase flow, the following thermodynamic property values are required: saturation temperature, density of the mixture, specific heat of the mixture, latent heat of evaporation and C_ρ, a constant that appears in the mass flux correction in the coupling procedure of the mass equation and equation of state. The use of this constant is explained by many authors, among whom are *Ferziger and Perić* (1995) and previously *Stošić* (1982). It defines the rate of change of density with change in pressure to correct the pressure-velocity coupling procedure. It is expressed as:

$$C_\rho = \left(\frac{\partial \rho}{\partial p}\right)_T, \tag{4.38}$$

for constant temperature in one iteration. In the case of an ideal fluid the value of this constant is derived directly from the equation of state $p/\rho = RT$ as:

$$C_\rho = \left(\frac{\partial \rho}{\partial p}\right)_T = \frac{\rho}{p} = \frac{1}{RT}. \tag{4.39}$$

However, for a real fluid, the equation of state is different. It is then assumed that:

$$\frac{p}{\rho} = zRT = z(p,T)RT, \tag{4.40}$$

where z is the compressibility factor. The compressibility factor is generally a non-linear function of pressure and temperature. There are many approximations derived for this factor with more or less accuracy. For this study, the compressibility factor is assumed to be a linear function of the working pressure given in the form:

$$z = pB_1 + B_2, \tag{4.41}$$

where B_1 and B_2 are constants different for each fluid. For the ideal gas B_1=0 while B_2=1. The compressibility factor is approximated such that coefficients B_1 and B_2 are calculated from measured thermodynamic properties of saturated vapour at pressures of 1 and 20 bar. Screw machines usually operate within this range of working pressures regardless of their application and this approximation does not involve a large error in the estimation of thermodynamic properties. It leads to a maximum error of approximately 2% at 10 bar. This is sufficiently accurate but outside this range different coefficients need to be used.

If the compressibility factor at the working pressure and temperature is known, then the density of the vapour or gas is derived from:

$$\rho_v = \frac{p}{zRT}, \tag{4.42}$$

It can be reasonably assumed that liquids in screw machines used for lubrication and generated as a result of the condensation process, are incompressible at the machine pressures. This means that the density of the liquid is constant:

$$\rho_l = const, \tag{4.43}$$

The density of a liquid-vapour mixture in the saturated domain can be written as:

$$\rho = \frac{1}{\frac{1-c_2}{\rho_v} - \frac{c_2}{\rho_l}} \rho_v = \frac{p}{(1-c_2)zRT + \frac{c_2}{\rho_l}p}, \tag{4.44}$$

To obtain an equation for C_ρ, the temperature is regarded constant within the iteration. The first derivative of equation (4.44) gives:

$$\left(\frac{d\rho}{dp}\right)_T = \frac{1-(1-c_2)\rho RT\frac{dz}{dp}-\frac{c_2}{\rho_l}\rho}{(1-c_2)zRT+\frac{c_2}{\rho_l}p}. \tag{4.45}$$

The derivative in the second term on the right side represents the change of compressibility factor with pressure. It follows from equation (4.41) that this derivative is constant and has the value B_1. Introducing that feature into the previous equation, the coefficient C_ρ can finally be obtained:

$$C_\rho = \left(\frac{d\rho}{dp}\right)_T = \frac{1-(1-c_2)\rho RT\,B_1-\frac{c_2}{\rho_l}\rho}{(1-c_2)zRT+\frac{c_2}{\rho_l}p}. \tag{4.46}$$

If as a consequence of the pressure and temperature in the control volume, the working fluid is liquid, which gives c_2 =1, the coefficient C_ρ reads zero and its value is not a function of pressure. If only vapour or real gas occupy the working chamber, c_2=0 and equation (4.46) becomes:

$$C_\rho = \left(\frac{d\rho}{dp}\right)_T = \frac{1}{zRT}-\frac{\rho_v B_1}{z}. \tag{4.47}$$

If the fluid is ideal, then B_1 becomes zero and z tends to one. In that case equation (4.46) becomes the same as equation (4.39). However, if the fluid is real, B_1 becomes slightly negative and z tends to values less then 1. This means that the second term becomes positive and it contributes to the value of the first term. The value of that term increases with the change of the 'fluid reality', which is expressed through constants B_1 and B_2 in (4.41). This term becomes significant in comparison with the first term if the fluid is real. In the case of ammonia, for example, at pressure of 5 bar the first term has a value of $6.7\cdot10^{-6}$ while the value of the second term is $2.9\cdot10^{-2}$. The coefficient C_ρ derived from equation (4.47) is later used for calculation of a pressure in the pressure-velocity-density coupling procedure.

Other thermodynamic properties are not directly derived from the equation of state but, as a consequence of the fluid behaviour, these are calculated from thermodynamic properties of both the liquid and vapour phases.

The saturation temperature is calculated from a modified version of Antoine's equation, which is in its original form expressed as:

$$\log p = A_1 - \frac{A_2}{t + A_3} \tag{4.48}$$

which is an explicit expression for saturation pressure as a function of temperature. More on that can be found in *Walas* (1984). Constants A_1, A_2 and A_3 vary for different fluids and they are obtained from experimental results. The value of the coefficient A_3 is usually small and in many cases can be neglected. In that case, the equation explicitly gives saturation temperature in terms of pressure as:

$$T_{sat} = \frac{A_2}{A_1 - \log p} - A_3 \tag{4.49}$$

The saturation temperature calculated from the previous equation is used in equation (4.35) to estimate the mass exchanged during evaporation/condensation. That equation gives the mass which transfers the latent heat of evaporation from one phase to the other. The latent heat of evaporation is calculated for the saturation pressure by means of the Clapeyron equation. This is expressed as:

$$h_L = T_{sat}\, v_{lv} \left(\frac{dp}{dT}\right)_{sat}, \tag{4.50}$$

where v_{lv} is the difference between the vapour and liquid specific volumes. Typically, more about equation (4.50) can be found in *Cengel and Boles* (1989).

The specific heat at constant pressure is a fluid property needed to calculate the specific enthalpy of the mixture. The specific heat of the mixture C_{pm} is the weighted sum of the specific heats of vapour C_{pv} and liquid C_{pl} for constant pressure, ie:

$$C_{pm} = (1 - c_2) C_{pv} + c_2 C_{pl} \tag{4.51}$$

The specific heat of vapour can be calculated from the following equation:

$$C_{pv} = D_0 + D_1 T + D_2 T^2 + D_3 T^3 \tag{4.52}$$

where D_0, D_1, D_2 and D_3 are constants which vary for different fluids. Their values can be found in *Sonntag and Borgnakke* (2001). If the specific heat of liquid at constant pressure is assumed constant, which is reasonably accurate over a limited temperature range, then equation (4.51) gives the specific heat of the mixture. Even if the concentration of the liquid phase in the working chamber is equal to zero, this equation can be used to express the specific heat of the working fluid, which in this case is vapour.

By use of the equations derived in this Section, the properties of real fluids, which are liquid, vapour or their mixture, are completely described. The procedure is fast and efficient for calculation in the numerical CFD solver, because all equations are analytical and the variables are derived explicitly from the pressure, the value of which is obtained from the mass-velocity-pressure coupling procedure. The procedure is equally applicable to ideal gases, and incompressible fluids. The coefficient C_ρ calculated from the equation (4.46) is used in the next iteration as a source term.

4.2.5 Turbulent Flow

Most engineering flows can only be regarded as mean flows calculated on an average basis, since small scale fluctuations of all flow quantities with high frequency are always present in both space and time. The flow is in fact in a particular state of continuous instability, which is called turbulence. Such flows are called turbulent flows.

Turbulent flows are well described by the governing differential equations presented in section 4.2. However, their direct numerical simulation requires a mesh with a spacing

smaller than the length scale of the smallest turbulent eddies at which the energy is transformed to heat and time steps smaller than the smallest time scale of the turbulent fluctuations. Some calculations show that the average length scale of the smallest eddies in positive displacement machines is of the order of $10\mu m$ while their time scale is of the order of a couple of milliseconds, *Lumley* (1999). This requires computer resources, which are not available at the present state of computer technology.

Alternatives are either large eddy simulation, in which only the largest unsteady motions are resolved and the rest is modelled, or a solution of the Reynolds averaged Navier-Stokes equations, where all turbulent effects on the mean flow are modelled as functions of mean fluid flow quantities. The first method is also very time and space consuming.

The Reynolds averaged Navier-Stokes equations (RANS) are obtained by using a statistical description of the turbulent motion formulated in terms of averaged flow quantities. Many RANS models of turbulence are developed to date which are suitable for different fluid flow situations. Only two of them are described in some details in Appendix III. These are the Zero-Equation model and the Standard k-ε two-equation model. More details on turbulence phenomenon can be found for example in *Ferziger and Perić* (1995) and *Wilcox* (1993).

4.2.6 Pressure Calculation

In the procedure described above, the pressure in the source term of the fluid momentum equation, has remained unknown, while at the same time no use has been made of the continuity equation. The problem lies in the fact that the pressure does not appear explicitly in the continuity equation, which consequently cannot be considered as 'an equation for pressure', and the continuity equation for incompressible flows acts just as an additional constraint on the velocity field. This constraint can be satisfied only if the pressure field is adjusted. However, pressure is not a conserved property and does not have its governing transport equation. A method of calculation of the pressure and pressure gradient fields consists, in general, of three steps. The first one is to obtain the velocity and density fields from the momentum equation regardless of whether the

continuity equation is satisfied. The second is a predictor stage in which a pressure correction is calculated to satisfy the continuity equation and the third one is a corrector stage in which new values of the velocity, pressure and density fields are calculated. The method is known as a SIMPLE algorithm. It is explained in Appendix V.

4.2.7 Boundary Conditions

A novel treatment of compressor boundaries was introduced in the numerical calculation of the screw compressor. The compressor is positioned between relatively small suction, discharge and eventually oil receivers. Such a system is bounded with walls and, therefore, separated from its surrounding only by these walls. The system communicates with the surroundings through the receivers. The normal practice is to keep the pressure in these receivers constant. To do that, an appropriate amount of mass and energy is injected or subtracted from these receivers. In this Section, only standard wall boundary conditions and the novel treatment of a boundary domain with constant pressure are explained. More information about standard boundary conditions can be found in *Ferziger and Perić* (1995) or in software user manuals for the applied CFD code.

4.2.7.1 Wall Boundaries

There are two types of walls applied to a screw compressor: moving walls, if they bound the domain on the compressor rotors, and stationary walls in all other places. Boundary conditions on these walls are explicitly given for all equations in the numerical model. In the case of turbulent flow, which appears in a screw compressor, dependent variables vary rapidly near the solid boundaries and a method, which can model near wall effects, has to be used. If the flow is laminar, then either Dirichlet boundary conditions, where the dependent variable is known on the boundary, or Neuman boundary conditions, where the flux of the dependent variable is given on the boundary, can be used.

Screw compressor walls are treated as 'no-slip walls', the case when viscous fluid sticks on the boundary wall.

Boundary conditions for the momentum equation are given through the known velocities on the wall, which represent Dirichlet boundary condition. For boundaries on the rotors, the velocities are calculated from the prescribed speed of rotation n of the male rotor as:

$$\omega_1 = \frac{2n\pi}{60}; \qquad \mathbf{v}_{1i} = \mathbf{r}_{1i}\,\omega_1$$
$$\omega_2 = -\omega_1 \frac{z_1}{z_2}; \qquad \mathbf{v}_{2i} = \mathbf{r}_{2i}\,\omega_2 \tag{4.53}$$

Index *1* indicates the male rotor while the value *2* is related to the female rotor. z_1 and z_2 are the number of lobes on the rotors, $\mathbf{r}_{1i}$ and $\mathbf{r}_{2i}$ are radius vectors of the boundary points on the male and female rotors in the absolute coordinate system respectively. ω_1 and ω_2 are the angular velocities on the male and female rotors respectively. For all stationary walls, the wall velocity is equal to zero.

More details on equations, which incorporate wall boundaries to the mathematical model of the screw compressor process, are given in Appendix IV.

4.2.7.2 Constant pressure in the inlet, outlet and oil receivers

Even if the compressor cycle can be considered steady, this is true only if it is averaged in time over a period in which compressor completes a number of cycles. However, within one cycle, the compressor system is always in a state of transition. Such transition is caused by rotation of the rotors, which moves the corresponding part of the numerical mesh. That movement is defined by the angular velocity ω_r. Movement of the computational domain causes change in the cell volume, which further causes pressure change within the control volume. Pressure difference between the cells causes fluid to flow through the machine. Contrary to the rotor domains, other parts of the compressor such the inlet and outlet ports and receivers maintain constant volume. The fluid flow

induced between the rotors inevitably leads to change of the pressure in the parts which keep a constant volume. In the real compressor, such a situation causes additional fluid to flow in or out of the chambers keeping the pressure constant. This process is simulated in the numerical procedure.

The first possibility is to apply standard inlet and outlet boundaries. However, in that case, either inlet velocity or mass flux should be prescribed in advance, which is extremely difficult. Compressor flow depends on the rotor speed and varies considerably during the cycle. Additionally, reverse flow can exist at the outlet boundary if it is not far enough from the discharge port. That situation is not allowed with the standard boundary conditions. Therefore, these boundary conditions are not adequate for a screw compressor.

The other possibility is to apply pressure boundaries at the inlet and outlet. In the standard pressure boundary condition a prescribed pressure on the boundary is combined with the Neuman boundary condition:

$$\left(\frac{\partial \mathbf{v}}{\partial n}\right)_B = 0 \tag{4.54}$$

to obtain boundary velocities $\mathbf{v}_B(\mathbf{r}_b,t)$. Different treatments are necessary in the case of supersonic and subsonic flows. If the outlet flow is supersonic, for example, then both pressure and velocity should be obtained by extrapolating from the upstream region. It is obvious that the pressure boundary conditions are similar to the inlet or outlet boundaries, firstly because they couple pressure and velocity directly and secondly because for all equations, apart from the momentum equation, the boundary properties are calculated from the velocity. This procedure easily causes instability in the compressor cycle especially when the flow changes its direction at the boundary.

In opposition to both the types of boundary condition mentioned above, application of the boundary domain, in which an amount of mass is injected or subtracted to maintain constant pressure, is natural and gives a stable and relatively fast solution.

Starting from the equation of state of a real fluid (4.40) for constant instant temperature and density of fluid in a receiver of volume V, or in an individual numerical cell of volume V_i, the following equation can be derived:

$$\dot{V}_{add} = \frac{\partial V_i}{\delta t} = \frac{V_i}{p_i}\frac{\partial p_i}{\delta t} \tag{4.55}$$

It gives the relation between the volume change and pressure change. The value of $\dot{V}_i$ is the volume flow that corresponds to the change in pressure ∂p_i during time ∂t. As the density is assumed constant, then the mass flux, which corresponds to the pressure change, is:

$$\dot{m}_{add} = \rho_i \frac{V_i}{p_i}\frac{\partial p_i}{\partial t} \tag{4.56}$$

This is the amount of mass, which must be added or subtracted to the receiver of constant volume V or to an individual numerical cell placed in the considered receiver to maintain the pressure constant.

The amount of mass calculated from (4.56) represents a mass source in the pressure correction procedure explained in Section 4.2.6. It will maintain constant pressure in the considered cell and the momentum equation correction would result new velocity in the cell.

The energy equation must also be corrected in order to keep the system in balance. It is done through the volume source in the governing equation of energy:

$$\dot{q}_{add} = m_i C_{pi}\frac{\partial T_i}{\partial t} = m_i C_{pi}\frac{T_i - T_r}{\partial t}. \tag{4.57}$$

In the last term T_i is temperature calculated in the cell, T_r is specified temperature which has to be maintained and ∂t is time step.

When an amount of mass of dispersed phase is added to the selected set of cells, the equation for species also has to be updated. The concentration of the dispersed phase can be known, or prescribed, in some domains while in others it has to be estimated. For example, the concentration of oil in the oil injection port has always a value which is close to 1. Similarly, the concentration of liquid in the inlet port of a two-phase expander is defined by the pressure and quality of the mixture. However, there are some compressor domains where the value of concentration is not known but the pressure has to be maintained constant. In that case, the value of concentration must be extrapolated from the neighbouring domain.

When the concentration is known, then its value should be kept as close as possible to the prescribed value. The mass of the dispersed phase carried by the continuous phase is calculated by equation (4.31) in which the concentration c_o is substituted by the prescribed value c_p. The last term in the transport equation for the concentration of the dispersed phase (4.10), is the volume source term which is expressed as:

$$\int_V S_{c_i} dV = S_{c_i} V_i = \rho \frac{\partial c_i}{\partial t} V_i = \dot{m}_i . \tag{4.58}$$

This volume source, when integrated over the cell volume, is the amount of mass of the dispersed phase added to or subtracted from the mass of the numerical cell.

If the concentration of the dispersed phase has to be maintained constant, a correction to the equation of species has to be added through the volume source. The source term in equation (4.10) is the mass flux of the dispersed phase. Its calculation is based on the desired concentration of the dispersed phase. Equation (4.31) is used for that and c_o is replaced by the desired concentration in the cell. In such a situation, the volume source in the oil concentration equation becomes:

$$S_{c_o} = \int_V S_{c_o} dV = m_{o_{add}} = \frac{\rho_o \rho_m V c_{o_{cons}}}{\rho_m (1 - c_{o_{cons}}) + \rho_o c_{o_{cons}}} \tag{4.59}$$

In the case of two-phase flow with evaporation or condensation, the equation for the concentration of liquid phase of the working fluid has to be updated through its volume source term. This term is calculated from the equation (4.34) as:

$$S_{\alpha_1} = \int_V S_{\alpha_1} dV = -\dot{m}_L \approx -\frac{\Delta m_L}{\delta t} \tag{4.60}$$

Other equations, like the equations for the turbulence model, do not need to be updated for this case.

4.3 FINITE VOLUME DISCRETISATION

4.3.1 Introduction

This part of Chapter 4 presents an overview of the numerical method employed to solve the fluid flow equations described in detail in the previous sections of this Chapter. The adopted numerical method can also be applied to solid body stress analysis, both independently and when coupled with fluid flow.

The finite volume discretisation of time, space and the equations is described here. This is fully implicit and can accommodate both structured and unstructured moving grids with cells of arbitrary topology. The numerical implementation of the initial and the wall boundary conditions is also explained. Although this procedure is described here only for fluid flow in screw compressors, it is a general one and can be used for the solution of any physical problem which is described by the given set of governing equations.

The segregated approach is used to solve the resulting set of coupled non-linear algebraic equation systems. This leads to a decoupled set of linear algebraic equations for each dependent variable. These equations are solved by an iterative conjugate gradient solver which retains the sparsity of the coefficient matrix, thus achieving the efficient use of computer resources.

If an appropriate constitutive relation is applied to each conservation law, namely mass, momentum and energy balance, a closed set of M equations is obtained for each numerical cell in a particular time step. The number of equations M depends on the problem that has to be solved. Usually, in the case of screw compressor two-phase flow with oil injection model, 7 equations are required for each numerical cell. It is important to note that all the conservation equations, except the continuity equation, can be conveniently written in the form of the following generic transport equation

$$\frac{d}{dt}\int_V \rho\phi dV + \int_S \rho\phi(\mathbf{v}-\mathbf{v}_s)\cdot d\mathbf{s} = \int_S \Gamma_\phi \operatorname{grad}\phi \cdot d\mathbf{s} + \int_S \mathbf{q}_{\phi S}\cdot ds + \int_V q_{\phi V}\cdot dV \qquad (4.61)$$

The continuity equation is combined with the momentum equation to obtain an equation for pressure or pressure correction. The meaning of symbols used in this equation is given in the nomenclature. The diffusive flux and sources are given in Table 4-1 for each transported property ϕ.

Table 4-1 Terms in the generic transport equation (4.61)

Equation	ϕ	Γ_ϕ	$\mathbf{q}_{\phi S}$	$q_{\phi V}$
Momentum	v_i	μ_{eff}	$\left[\mu_{eff}\left(\operatorname{grad}\mathbf{v}\right)^{\mathrm{T}} - \left(\frac{2}{3}\mu_{eff}\operatorname{div}\mathbf{v} + p\right)\mathbf{I}\right]\cdot\mathbf{i}_i$	$f_{b,i}$
Energy	e	$\frac{k}{\partial e/\partial T} + \frac{\mu_t}{\sigma_T}$	$-\frac{k}{\partial e/\partial T}\frac{\partial e}{\partial p}\cdot\operatorname{grad} p$	T: grad $\mathbf{v} + h$
Concentration	c_i	$\rho D_{i,\mathrm{eff}}$	0	S_{ci}
Space	$\frac{1}{\rho}$	0	0	0
Turbulent kinetic energy	k	$\mu + \frac{\mu_t}{\sigma_k}$	0	$P - \rho\varepsilon$
Dissipation	ε	$\mu + \frac{\mu_t}{\sigma_\varepsilon}$	0	$C_1 P\frac{\varepsilon}{k} - C_2\rho\frac{\varepsilon^2}{k} - C_3\rho\varepsilon\operatorname{div}\mathbf{v}$

The possibility of expressing all transport equations in the form of a single prototype equation (4.61) conveniently facilitates the discretisation procedure. This, together with the appropriate initial and boundary conditions, forms the mathematical model of the continuum mechanics problems.

All dependent variables are stored in the centre of a cell in a collocated variable arrangement. It requires only one set of control volumes to be generated. This facilitates implementation of the boundary conditions and eventually the multigrid method and local grid refinement.

The Finite Volume Method (FVM) is used to solve the governing equations. It includes the discretisation of space, time and the equations that describe the problem. A representation of vector and tensor components in absolute Cartesian coordinate system is applied, which gives a strong conservation form for all the equations.

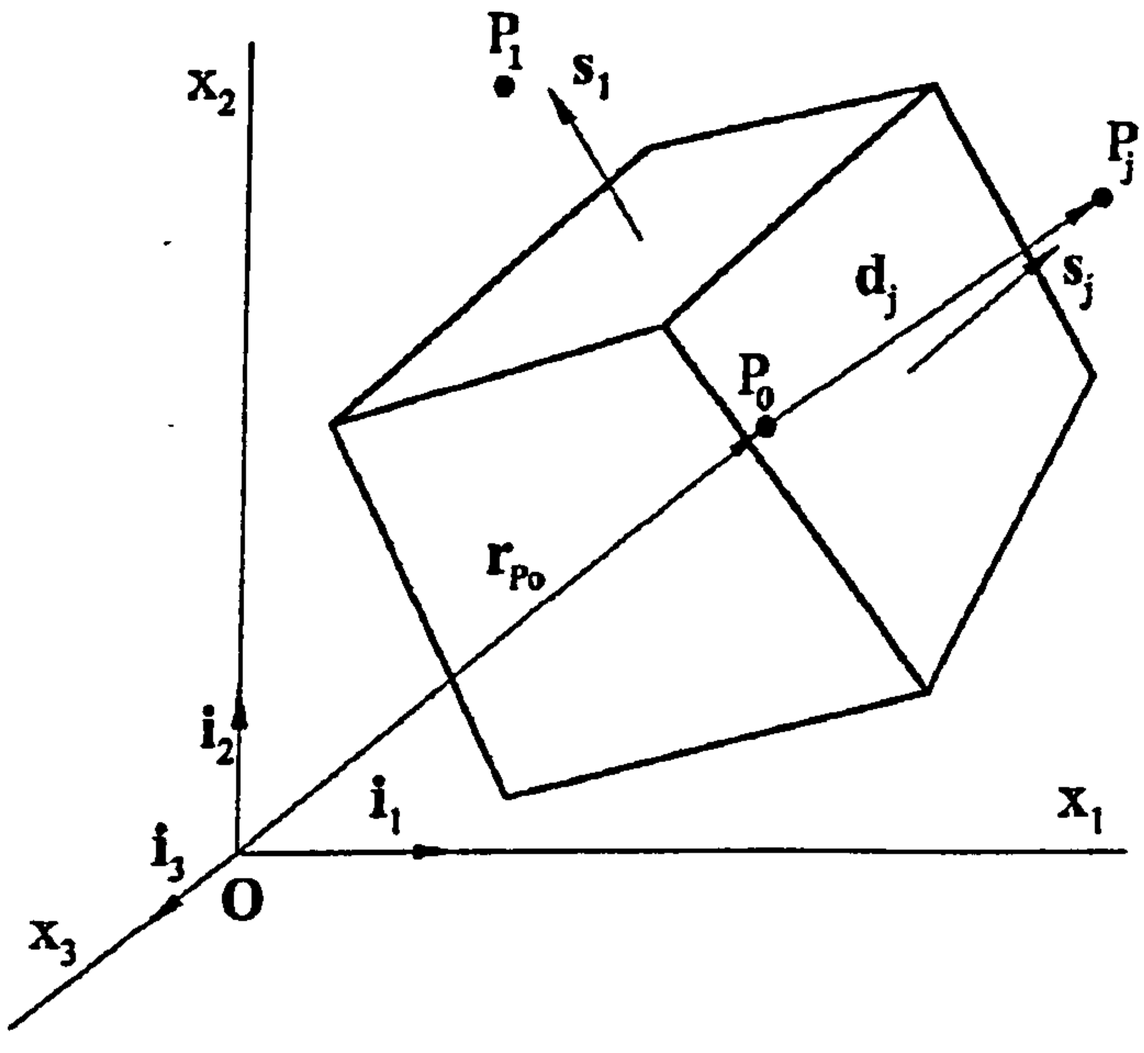

Figure 4-2 Notation applied to a hexahedral control volume

Equation (4.61) can bee written for the control volume in Cartesian coordinate frame as presented in Figure 4-2. This equation is still general and exact:

$$\frac{d}{dt}\int_V \rho\phi dV + \sum_{j=1}^{n_f}\int_{S_j} \rho\phi(\mathbf{v}-\mathbf{v}_s)\cdot d\mathbf{s} = \sum_{j=1}^{n_f}\int_{S_j} \Gamma_\phi \operatorname{grad}\phi\cdot d\mathbf{s} + \left(\sum_{j=1}^{n_f}\int_{S_j} \mathbf{q}_{\phi S}\cdot ds + \int_V q_{\phi V}\cdot dV\right) \qquad (4.62)$$

It consists of four terms: the rate of change in time, the convection term, the diffusion and the source terms respectively. Equations for all quantities are then written in the form of equation (4.62) and the system of $n*m$ partial differential equations is made. The number of numerical cells (control volumes) is n while the number of unknowns for each cell is marked with m. System (4.62) must be transferred to the system of $n*m$ algebraic equations in order to be numerically solved. Due to that, the surface and volume integrals have to be replaced by quadrature approximations, the spatial derivatives have to be replaced by some interpolation function, the time integration scheme have to be selected and the surface velocities $\mathbf{v}_s$ have to be determined.

4.3.2 Space Discretisation

Space can be discretised by an unstructured mesh with polyhedral control volumes (CVs) with an arbitrary number of faces. However, for accuracy reasons, hexahedra are preferred and therefore used wherever possible. This also facilitates the local grid refinement, which may be essential for accuracy reasons in some cases. Chapter 5 is completely dedicated to the spatial discretisation of a screw compressor working domain and, therefore will not be explained here further.

4.3.3 Time Discretisation

The time interval of interest should be subdivided into an arbitrary number of subinterval time steps, which are not necessarily of the same duration. However, the procedure used for mesh movement, given later in Chapter 5, requires the time steps in the simulation procedure of the screw compressor working cycle to be constant. It is designed to form a working cycle where all variables at the start and end of a calculation cycle are equal. The calculation cycle can be represented by rotation of the male rotor either for a full revolution or only for one tooth rotation. The constant time step, however, is not given arbitrarily. It depends on the chosen number of rotational steps within the tooth angle on the male rotor and the speed of rotation n. The angular speed of the male rotor is:

$$\omega_1 = 2\pi \frac{n}{60} \quad [rad/s]. \tag{4.63}$$

Unity angle is the angle for which the male rotor is rotated in one time step. If the compressor speed is considered constant then the unity angle can be calculated as:

$$\delta\varphi = \frac{\varphi}{n_{ang}} \tag{4.64}$$

where φ is the interlobe angle of the male rotor and n_{ang} is number of divisions of that angle for the rotation of one full interlobe. The time step is then defined as

$$\delta t = \frac{\partial\varphi}{\omega_1} \tag{4.65}$$

Although the time step in the majority of calculations of screw compressor performance is constant, if a transient state has to be calculated, the time step changes during marching in time. This is especially the case for compressor start up and shut down procedures. In these cases, the time step within two consequent rotations of the compressor rotors depends on the first time derivative of the compressor speed. Again, it is necessary to calculate the angular velocity for each time step and consequently to update the time step.

4.3.4 Discretisation of Equations

4.3.4.1 Discretisation principles

The equations which define the problem and which are written in the form of general equation (4.62) are discretised prior to solving. The result of discretisation is expressed in the form of a system of algebraic equations which then can be solved efficiently. Surface and volume integrals are replaced by quadrature approximations, spatial derivatives are replaced by some interpolation function and either two-times-level or

three-times-level integration scheme in time is selected. These procedures are explained in more details in Appendix V.

4.3.4.2 Boundary and Initial Conditions

The boundary conditions on the cell faces, coinciding with the boundary of the solution domain, have to be applied prior to solution of the system of algebraic equations. All boundaries of the screw compressor fluid flow which connect with the compressor solid parts are no-slip walls with either, a known temperature or a temperature approximated through the earlier explained procedure. Due to that, a cell face flux ϕ_j^* becomes a boundary flux ϕ_B in all equations where boundary cell faces are considered. In such a case, the mass flux in the momentum equation at the boundary is zero, the heat flux through the boundary for the energy equation is calculated from the wall temperature and the thermal conductivity in the near wall region, while the concentration flux reads zero. Diffusive fluxes are also replaced with their boundary values.

Screw compressor flow simulation is always transient, which requires initial conditions to be prescribed for the dependent variables in each control volume of the computational domain. The proper estimation of these plays a significant role in the computational time required to obtain consistent results.

The initial values of the velocities in the momentum equation are set to zero in all cells within the working chamber. The initial pressures prescribed for the cells in the inlet and outlet receiver are the inlet and outlet pressure. For all other cells the initial values are calculated by linear interpolation between these values in respect to the relative distance in z direction as:

$$p_i^0 = p_{inl}^0 + \frac{z_i}{L}\left(p_{out}^0 - p_{inl}^0\right). \tag{4.66}$$

z_i is a cell centre distance starting from the coordinate origin, while L is the overall compressor length. This simple method to prescribe initial values often gives a consistent final solution within 4 to 5 compressor cycles. The initial temperature is calculated in the same manner as the pressure by linear interpolation between prescribed

inlet and outlet temperatures. The density is then calculated according to equation (4.44) Concentration is also interpolated between the prescribed values at the inlet ρ^0_{inl} and outlet ρ^0_{out} of the compressor similarly to the other variables. The initial values of kinetic energy and its dissipation rate are set as zero throughout the domain.

If the Euler implicit time integration is employed, these prescribed values at time t_0 are sufficient for the calculation. If, however, the three time level implicit scheme is used, values at the time $t_{-1} = t_0 - \delta t_0$ should be given. They are set at the same value as those at time t_0.

4.3.4.3 Derived System of Algebraic Equations

If the discretisation methods and boundary conditions are implemented in the prototype equation (4.62) for all control volumes then the derived algebraic equation has the same form for all variables:

$$a_{\phi 0}\phi_{P_0} - \sum_{j=1}^{n_i} a_{\phi j}\phi_{P_j} = b_\phi, \tag{4.67}$$

where index 0 determines the control volume in which the variable is calculated and index j defines the neighbouring cells. The number n_i represents the internal cell faces between the calculating cell and its neighbouring cells. The right hand side contains all terms for which the variables are known from either the previous iteration or the time step. All the coefficients, central $a_{\phi 0}$, neighbouring $a_{\phi j}$ and right hand side b_ϕ, are treated explicitly using the deferred correction approach to increase computational efficiency.

$$a_{\phi j} = \Gamma_{\phi j} \frac{\mathbf{s}_j \cdot \mathbf{s}_j}{\mathbf{d}_j \cdot \mathbf{s}_j} - \min(\dot{m}_j, 0),$$

$$a_{\phi 0} = \sum_{j=1}^{n_f} a_{\phi j} + \frac{(\rho V)_{P_0}^{m-1}}{\delta t_m},$$

$$b_\phi = \sum_{j=1}^{n_f} \Gamma_{\phi j} \left((\text{grad}\,\phi)_j \cdot \mathbf{s}_j - \overline{\text{grad}\,\phi} \cdot \mathbf{d}_j \frac{\mathbf{s}_j \cdot \mathbf{s}_j}{\mathbf{d}_j \cdot \mathbf{s}_j} \right) - \tag{4.68}$$

$$\sum_{j=1}^{n_f} \frac{\gamma_\phi}{2} \dot{m}_j \left((\mathbf{r}_j - \mathbf{r}_{P_0}) \cdot (\text{grad}\,\phi)_{P_0} + (\mathbf{r}_j - \mathbf{r}_{P_0}) \cdot (\text{grad}\,\phi)_{P_j} + (\phi_{P_j} - \phi_{P_0}) \frac{\dot{m}_j}{\text{abs}(\dot{m}_j)} \right) +$$

$$Q_{\phi S} + Q_{\phi V} + \sum_{B=1}^{n_B} a_{\phi B}\, \phi_B + \frac{(\rho V \phi)_{P_0}^{m-1}}{\delta t_m}.$$

$\mathbf{d}_j$ is a distance vector. It is effective if the mesh is non-orthogonal and then it is used to correct the cell face value. It is defined as the normal distance between the line connecting two neighbouring cell points and the cell face centre. n_B is the number of boundary faces surrounding the cell P_0. The coefficient $a_{\phi B}$ for the centre point at the boundary cell face is calculated similarly to the neighbouring coefficient $a_{\phi j}$ assuming a distance between the boundary point and the centre of the cell.

4.4 SOLUTION PROCEDURE FOR A COUPLED SYSTEM OF NONLINEAR ALGEBRAIC EQUATIONS

Equations in the form of (4.67) are obtained for each dependent variable like velocity, pressure, temperature, concentration etc., at all numerical points of the computational domain. As a consequence of convective transport and because of other flow characteristics, the equations are non-linear and coupled together. In order to be solved in an efficient way, they must be linearized and decoupled. The segregate iterative algorithm is adopted which consists of the following steps:

1. Equations (4.67) are linearized and temporarily decoupled by assuming that coefficients $a_{\phi j}$ and source terms b_ϕ are known in advance from the previous iteration or time step. As a result, a sub-set of linear algebraic equations is obtained for each dependent variable. This can be written in the matrix notation:

$$A_\phi \phi = \mathbf{b}_\phi \tag{4.69}$$

Here A_ϕ is $N \times N$ matrix, vector ϕ contains values of the dependent variables ϕ at N nodal points in the CV centres and $\mathbf{b}_\phi$ is the source vector. The resulting matrix A_ϕ obtained by the discretisation method has the following features:

- It is sparse, with the number of non-zero elements in each row equal to the number of nearest neighbours plus one, $n_i + 1$.
- The matrix is symmetric only for the momentum equation of elastic solid body and pressure correction for incompressible fluids.
- The matrix is diagonally dominant $A_{\phi_i} \geq \sum_{j=1}^{n_i} a_{\phi_j}$, which allows a solution of the equation system (4.69) by a number of iterative methods resulting in very small computer memory requirements. The conjugate gradient method (CG) is used when the matrix is symmetric and the CGSTAB method is used when the matrix is asymmetric.

2. Equation (4.69) is solved in sequence for each dependent variable. There is no need to solve equation (4.69) to a tight tolerance since its coefficients and sources are only approximate based on the values of the dependent variables from the previous iteration or time step. A reduction of the sum of absolute residuals by one order of magnitude normally suffices. These iterations are called inner iterations.

3. The sequence of step 2 is repeated in the outer iterations by updating the coefficient matrix and the source terms until the solution converges.

$$\mathbf{r}_\phi = A_\phi \phi - \mathbf{b}_\phi \tag{4.70}$$

The convergence criterion is usually achieved when residuals (4.70) are reduced for three to four orders of magnitude. This means that the variable values do not change on three to four most significant digits.

More information can be found in *Golub and van Loan* (1990), *Sonneveld* (1989), *Van den Vorst and Sonneveld* (1990), *Demirdžić* (1997) and *Kaludjerčić* (1998).

4.5 SCREW COMPRESSOR INTEGRAL PARAMETERS

Once a solution is obtained in the form of the velocity and pressure fields within the compressor, integral parameters, which quantify the screw compressor working cycle, can be calculated.

Integral parameters are used to evaluate and compare the processes in screw machines and to serve as input parameters for the design of these machines. They are divided into two groups; those based on the compressor delivery, which is the volume flow calculated at the suction conditions, and those based on the compressor power input. Other integral parameters are calculated from the previous two. These are specific power, volumetric and adiabatic efficiencies, load on the compressor rotors and bearings, torque on the male and female rotors and oil flow. Apart from these, the indicator diagram can be calculated from the pressure distribution within the compressor working cycle.

The volume flow is calculated at the inlet and at the outlet of the screw compressor. There are two possibilities to calculate and check the flow at the compressor inlet and outlet. These are:

i) the use of the Gauss divergence theorem to calculate flow from the velocity in each particular cell in the cross section and then to integrate them over the complete cross section

ii) integration of the mass sources along the inlet and outlet receivers to calculate the volume flow

The Gauss divergence theorem is expressed as:

$$\int_S \mathbf{v} \cdot d\mathbf{s} = \int_V div\mathbf{v} dV \,. \tag{4.71}$$

When integrated over a layer of cells in the cross section of the inlet or outlet port this equation becomes:

$$\dot{V}_2 - \dot{V}_1 = \sum_{i=1}^{I} (v_f S_{fi})_2 - \sum_{i=1}^{I} (v_f S_{fi})_1 = 0 \;\rightarrow\; \dot{V}_f^{(i)} = \sum_{i=1}^{I} v_f S_{fi} \quad (i = 1,2,\ldots,I), \qquad (4.72)$$

where index f represents the direction of flow. In the case of the inlet port it is usually along the y axis, and for the outlet port it is the z axis. S and v are the cell surface area and the velocity component in the direction of fluid flow. Equation (4.72) is calculated for each time step in the compressor working cycle. When integrated over the compressor cycle it gives a total volume fluid flow at local fluid parameters:

$$\dot{V} = 60 \cdot \sum_{t=t_{start}}^{t_{end}} \dot{V}^{(t)} \qquad \left[m^3/\min\right]. \qquad (4.73)$$

The volume flow obtained by this equation can be compared with the volume flow calculated from the mass added or subtracted to the inlet and outlet receivers. These two should be the same for each time step as well as for the complete compressor cycle.

Together with the volume flow, the mean density values are calculated for each time step:

$$\overline{\rho}^{(t)} = \sum_{i=1}^{I} \rho_i \,. \qquad (4.74)$$

If the average density is multiplied by the corresponding volume flow it gives the mass flow in the integral form as:

$$\dot{m} = \sum_{t=t_{start}}^{t_{end}} \dot{V}^{(t)} \cdot \overline{\rho}^{(t)} \qquad (4.75)$$

Once calculated, compressor inlet and outlet mass flows must be the same for the stationary working condition of a screw compressor.

Another group of variables is based on the value of pressure in the working chamber.

A cell on the rotor boundary is shown in Figure 4-3. Pressure in the cell generates the force on the boundary surface. That force is calculated as the product of the pressure in the rotor boundary cell and the boundary cell surface area. This force can be also divided in three components acting in x, y and z directions of the absolute coordinate system. When calculated, these three components are:

$$F_x = p_b A_{xb}; \qquad F_y = p_b A_{yb}; \qquad F_z = p_b A_{zb}, \tag{4.76}$$

where p_b is the pressure in the boundary cell and A_{xb}, A_{yb} and A_{zb} are projections of the boundary cell surface in the main directions of the absolute coordinate system.

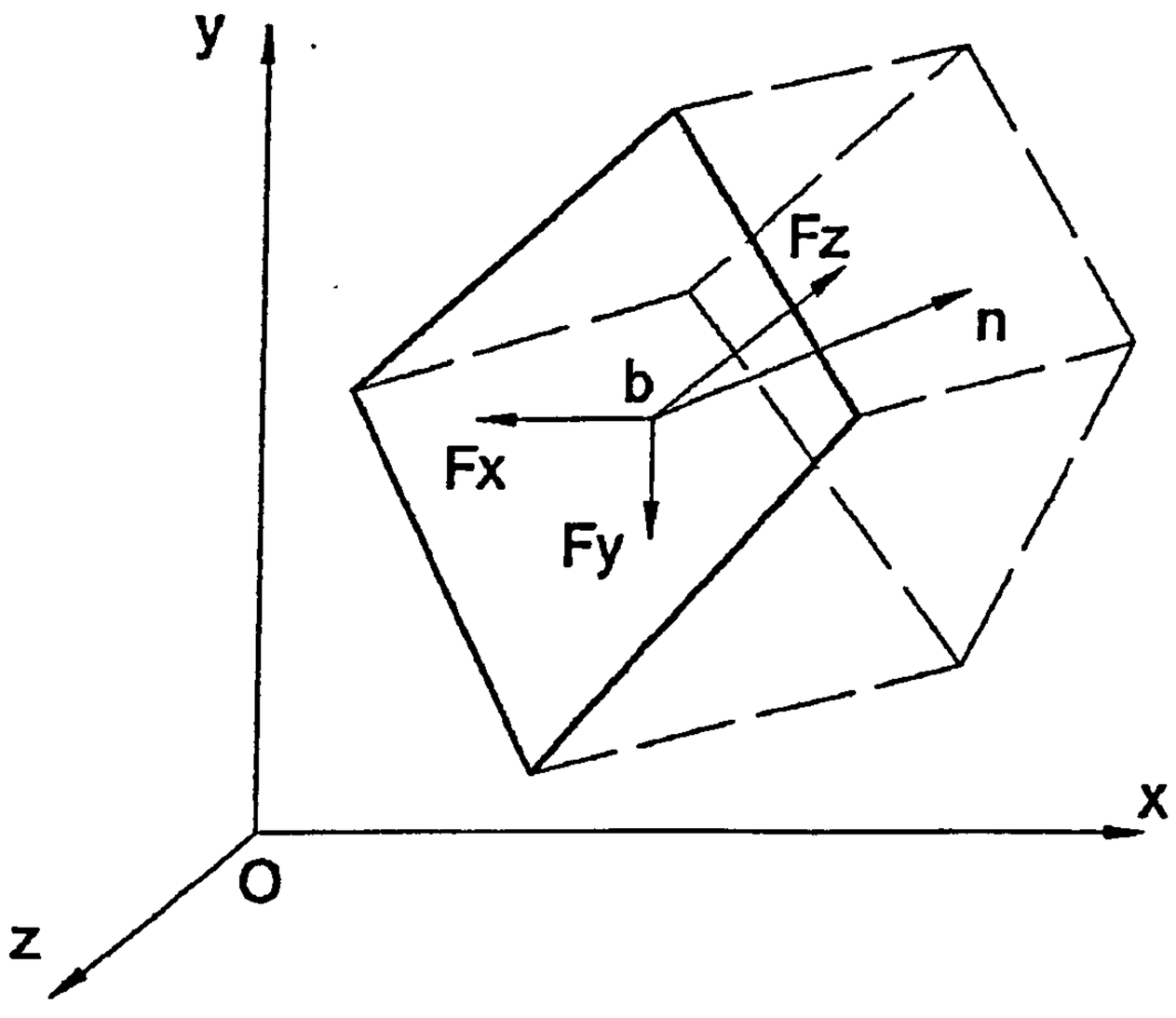

Figure 4-3 Pressure forces on the boundary surface

Pressure forces at the cell boundary and restraint forces are shown in Figure 4-4. In order to calculate restraint forces and torques, the force balance must be satisfied.

The force balance for this system is expressed by:

$$
\begin{aligned}
\Sigma F_x{=}0: &\quad F_{xD}(i)+F_{xS}(i)-F_x(i)=0\\
\Sigma F_y{=}0: &\quad F_{yD}(i)+F_{yS}(i)-F_y(i)=0\\
\Sigma F_z{=}0: &\quad F_a(i)-F_z(i)=0\\
\Sigma M_x{=}0: &\quad -F_{yD}(i)\,l+F_y(i)\,z(i)-F_z(i)\,y(i)=0\\
\Sigma M_y{=}0: &\quad F_{xD}(i)\,l-F_x(i)\,z(i)+F_z(i)\left[x(i)-a\right]=0\\
\Sigma M_z{=}0: &\quad T+F_x(i)\,y(i)-F_y(i)\left[x(i)-a\right]=0
\end{aligned}
\tag{4.77}
$$

In these equations l is the rotor length and a is the rotor axis distance. The equations are valid for both rotors. The distance between the male rotor axis and origin $a=0$, while for the female rotor a has the value of the axis distance. Indices 1 or 2 stand for the male and female rotors respectively.

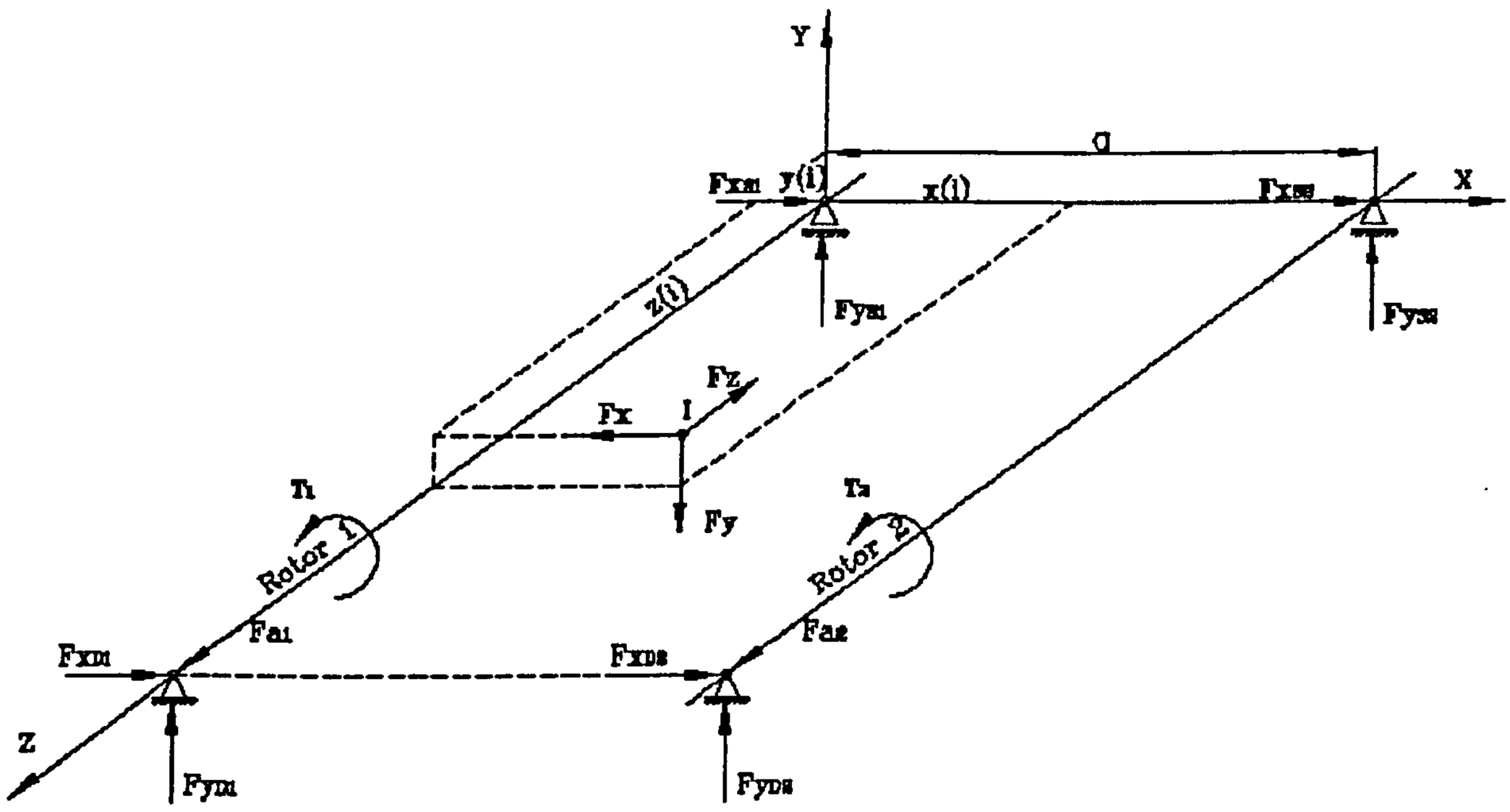

Figure 4-4 Restraint forces and torques on rotors

The torque and restraint forces on the suction and discharge bearings are calculated from these equations as:

$$F_{xS}(i)=\frac{F_y(i)\,z(i)-F_z(i)\,y(i)}{l} \qquad F_{xD}(i)=F_x(i)-F_{xS}(i)$$

$$F_{yS}(i)=\frac{F_x(i)\,z(i)-F_z(i)\left[x(i)-a\right]}{l} \qquad F_{yD}(i)=F_x(i)-F_{xS}(i) \qquad (4.78)$$

$$F_{rS}(i)=\sqrt{F_{xS}^2(i)+F_{yS}^2(i)} \qquad F_{rD}(i)=\sqrt{F_{xD}^2(i)+F_{yD}^2(i)}$$

$$T(i)=F_z(i)\,y(i)-F_y(i)\left[x(i)-a\right] \qquad F_a(i)=F_z(i)$$

All forces in equation (4.78) are reacting forces on the supports caused only by the pressure force in one boundary cell *i*. To obtain the integral radial and axial forces and torque they must be integrated over the whole boundary and for both rotors:

$$F_{rS}=\sum_{i=1}^{I}F_{rS}(i),[N] \qquad F_{rD}=\sum_{i=1}^{I}F_{rD}(i),\,[N]$$

$$F_a=\sum_{i=1}^{I}F_a(i),[N] \qquad T=\sum_{i=1}^{I}T(i),\,[Nm] \qquad (4.79)$$

Once calculated, the torque is used for calculation of the power transmitted to the rotor shaft:

$$P=2\cdot\pi\cdot n\cdot(T_M+T_F)\ ,[W] \qquad (4.80)$$

where n is speed of the male rotor while T_M and T_F are torque on the male and female rotor respectively. Specific power is defined as:

$$Pspec={}^{P}\!/_{\dot{V}}\cdot 1000 \quad ,\left[{}^{kW}\!/_{m^3\,\min}\right] \qquad (4.81)$$

And finally, values η_v and η_i are volumetric and adiabatic efficiency respectively:

$$\eta_v={}^{\dot{V}}\!/_{V_d} \qquad \eta_i={}^{P_{ad}}\!/_{P} \qquad (4.82)$$

where V_d is the theoretical displacement and P_{ad} is the adiabatic power input.

Since the pressure in the working chamber does not vary too much in one interlobe within one time step, it was sufficiently accurate to average the pressure values arithmetically in each working chamber in order to plot the pressure versus shaft angle, (p-α) diagram.

4.6 CLOSURE

The method of simulating the three-dimensional fluid flow within a screw machine has been derived in this Chapter from the five governing equations of momentum, energy, mass, concentration and space conservation. In order to be solved, the equations are accompanied by constitutive relations for a Newtonian fluid in the form of Stokes, Fourier's and Fick's laws. Although this model is generally applicable, there are at least three features derived in this chapter without which the solution of the flow pattern within a screw machine would not be possible. Firstly, there is the application of Euler-Lagrange method for the solution of multiphase flow of both the injected fluid and the liquid phase of the main fluid. These equations define mass, energy and concentration source terms for the main equations. The introduction of a 'boundary domain' in which the pressure is kept constant by injection or by subtraction of mass, is the next innovation in this thesis and it allows simulation of the real operational mode of a screw compressor. Finally, a rather simple method is used here for calculation of the properties of real fluids. This permits a fast but still reasonably accurate procedure even for the calculation of processes like evaporation or condensation within the working chamber.

The equations of the mathematical model are discretised in space and time by means of a finite volume method which gives a strong conservative form to the resulting system of coupled algebraic equations. They are produced in a convenient form to be solved using the fast and accurate conjugate gradient method.

The method of calculating compressor integral parameters from the derived fields of pressure and velocity is also described in this Chapter. It gives an opportunity for verification of the method by comparison of the derived results with one-dimensional models or experimental data.

Spatial discretisation plays a significant role in the speed and accuracy aspects of the equation discretisation methods derived in this chapter. The use of a hexahedral numerical mesh is preferable for this purpose. Analytical transfinite interpolation is employed in this thesis for the generation of a suitable numerical mesh for screw machines with a boundary adaptation method, smoothing and orthogonalization.

Chapter 5

Grid generation of Screw Machine Geometry

5.1 INTRODUCTION

The finite volume method, described in Chapter 4, is a powerful technique which allows fast and accurate solution of the governing equations for fluid flow within complex geometries. The resulting system of algebraic equations is more conservative then those generated by other discretisation methods like finite difference or finite element methods. To use this method a spatial domain must be replaced by a finite number of discrete volumes constructed between grid points. The number of control volumes used to discretise a computational domain depends on the geometry and physics of the problem and on the required accuracy. The number of grid points used to construct numerical cells depends on the dimensionality of the problem and on the type of numerical cell selected for calculation. For two-dimensional cases, numerical cells can be constructed from three or more numerical points, but triangular and rectangular cells are those mostly used in practice. If the problem is three-dimensional, the most frequently used cells are tetrahedral and hexahedral volumes constructed around four and eight numerical points respectively. However, volumes may be constructed from an arbitrary number of faces for which a corresponding number of points can be calculated. The use of hexahedral cells gives the most conservative interpolation of values in neighbouring cell centres and is therefore the preferred grid type. This is especially important when geometrical and physical parameters vary substantially across a domain, which is the case in a screw machine.

The process of replacing a spatial domain by a system of grid points is called grid generation. The grid generation process, referred to as space discretisation, is essential for accuracy, efficiency and ease of numerical solution. Ability to generate an 'acceptable' grid system is a factor which determines whether a three-dimensional numerical method, such as the finite volume, can be used. Inability to generate an adequate numerical mesh for screw machine was the main reason why screw machines have not been previously analysed by use of three-dimensional numerical methods.

The grid generation process is performed in the selected coordinate system with constraints given for a specific problem. Therefore, a coordinate system must be introduced and the required constraints have to be set. The absolute Cartesian coordinate system is used in the grid generation process because it gives the best results for the finite volume method.

5.1.1 Types of Grid Systems

Eiseman et all (1994) classified the grid systems which can possibly be used by numerical methods as structured, unstructured or mixed, depending on how the grid points are connected to each other. These types are presented in Figure 5-1. Unstructured numerical grids are the most versatile and usually are the easiest to generate of all the types mentioned above. However, obtaining solution with them is more difficult then from structured grids. Finite difference methods are still been developed to make unstructured grids more suitable for calculation.

Structured grid systems are further classified as either single or composite grids. A single grid is based on the single boundary fitted coordinate system, as shown in Figure 5-2. A composite grid consists of two or more single grids, each in its own coordinate system, patched together. Depending on how the individual single grids are assembled together, a composite grid system can further be classified as completely discontinuous, partially discontinuous, partially continuous and completely continuous as shown in Figure 5-2.

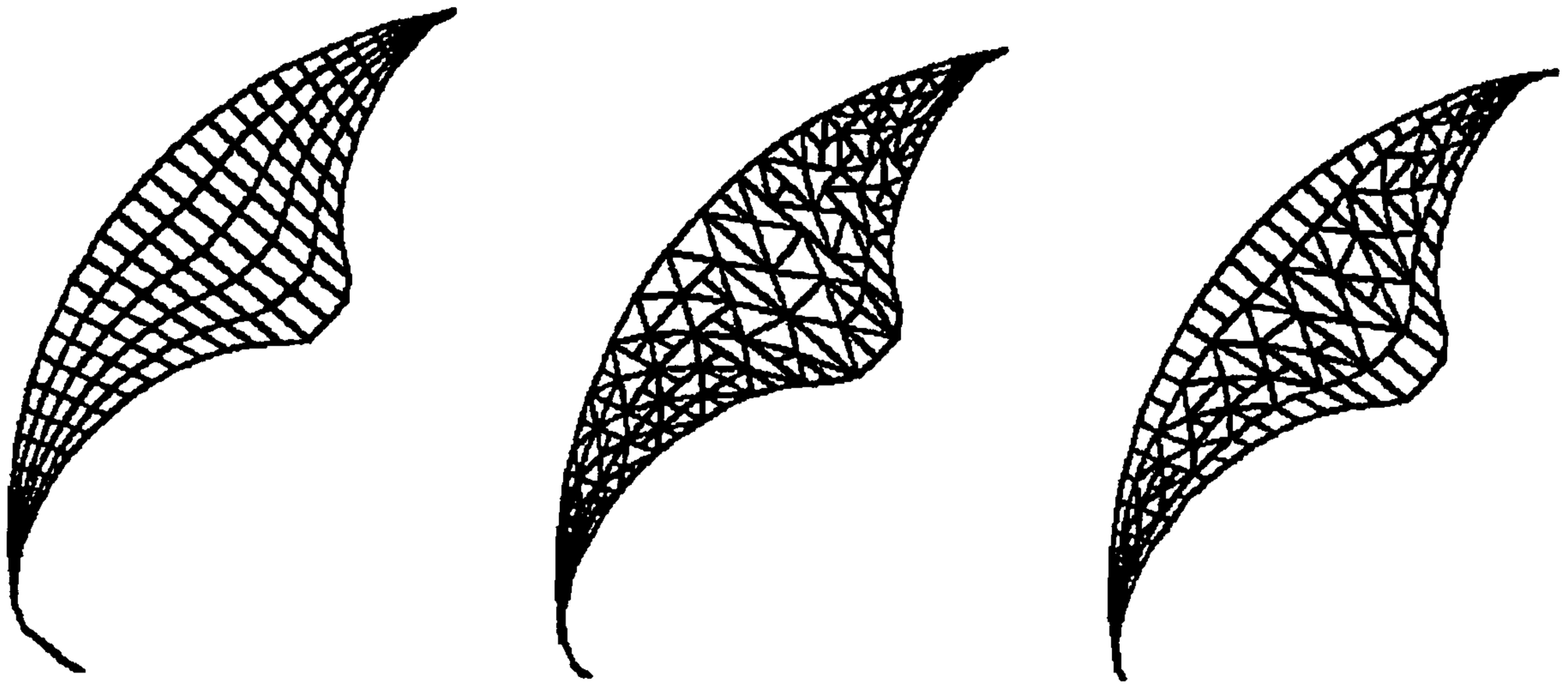

a) structured *b)unstructured* *c)mixed*

Figure 5-1Types of a grid system

Figure 5-2a shows an overlapping or Chimera grid. This grid is usually easier to construct and implement for complex geometries. However, its conservation is not always conveniently enforced on block boundaries. The patching process in this case requires only the generation of a single grid over each compressor rotor without considering the interface between them. The only constraint in this case is the amount of overlapping between the grids on the rotors. This type of grid has other advantages. One of them is that it allows a separate computation on each grid, which saves the computer resources. Fortunately, this advantage can be achieved by other types of composite grids. However, the biggest disadvantage of the overlapping grid is difficulty in obtaining solutions, which is greater than for other types of composite grids. Difficulties appear because the interpolation schemes to transfer information from one single grid to another are employed in parallel with maintaining conservation and monotonicity in the overlapping regions. More about Chimera grids can be found in Liseikin 1999 or Thompson et al (1999).

Partially discontinuous composite grids are usually called block-structured grids with non-matching interface. Grids of this type are generated in following manner. Firstly, the domain of interest is partitioned into a number of non-overlapping continuous blocks. Then a structured numerical mesh is generated within each of the blocks. After that the blocks are patched together through the non-overlapping interface. This type of grid is flexible and retains some characteristics similar to the overlapping grid; it allows

generation of the grid with the desired resolution and topology in each particular block and each of these, if necessary, can be later refined in a blockwise manner. However, these grids are more difficult to generate then overlapping grids. On the other hand, developed methods for conservative treatment of a non-matching interface already exist and these are well implemented in standard CFD software, as given by *Muzaferija and Demirdžić* (1995). Block structured grids are used for spatial discretisation of screw machine rotors.

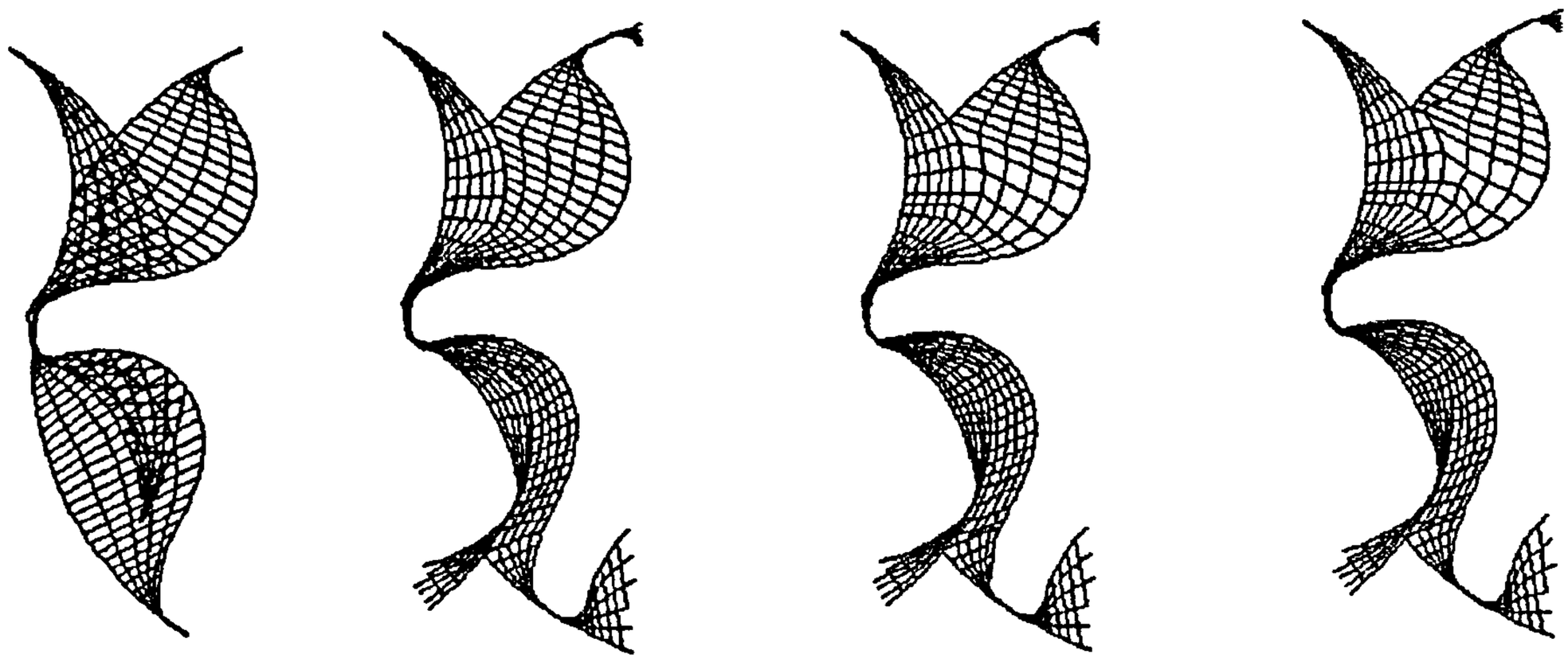

a) completely discontinuous | *b) partially discontinuous* | *c) partially continuous* | *d) completely continuous*

Figure 5-2 Types of composite structured grids

The other two, namely partially and completely continuous composite grids, are more difficult to generate. Their points at the matching interface coincide with each other. In the case of complex three-dimensional domain, this can be extremely difficult. When generated properly, these grids can be numerically treated as a single grid because there is no real interface between them. In that case, conservation of properties is completely satisfied as for the single grid. These types of grid are applied in this thesis for generation of the suction and discharge chambers and in all other sub domains of a screw machine other then the rotors. More on this can be found in *Eiseman et al* (1994)

When a structured grid system, either single or composite, is used for finite volume discretisation, the final numerical mesh must satisfy a number of conditions (*Shih at al* 1991):

1. The total number of grid points should be kept to the minimum needed for the numerical method to yield a solution of the desired accuracy. This is an important condition for both, efficiency and accuracy of the numerical method, and can be achieved by clustering points in some domains and scattering them elsewhere. To do this, an appropriate adaptation method has been developed and applied to the screw compressor boundaries, as described in 5.3.1.
2. The numerical points which form the boundary grid lines should always coincide with the boundary of the spatial domain regardless of the complexity or motion of the boundary. The ease of implementation of boundary conditions relies on this mesh property.
3. If possible, one set of grid lines should align with the flow direction. This condition is not always easy to fulfil in the case of complicated three-dimensional domains, but it can help in obtaining an accurate numerical solution.
4. The set of grid lines that intersects the boundaries should be perpendicular to the boundary. This allows easier implementation and calculation of derivatives at the boundaries of the domain. In the interior, the intersecting lines need be only nearly orthogonal.
5. The spacing between the grid points should change slowly from a region with concentrated points to a region with sparsely distributed nodes, especially if the gradients of the flow values are large in these regions.

The next section gives a brief outline of the methods available to produce a block structured numerical mesh of the required type with the desired properties.

5.1.2 Grid Generation Methods for Structured Grids

The most efficient structured grids are the so called boundary-fitted or boundary-confirming grids. These grids are formed in such a manner that one set of points is fitted to the boundary of a domain so that the boundary conditions are directly applied to the

boundary region without the need for interpolation. In that case, the boundary conditions are considered as input data to the algorithm.

It is a common practice to generate and distribute numerical points on physical boundaries and then extend them successively from the boundary to the interior of the domain. Based on this, three basic groups of grid generation methods have been developed; see *Liseikin* (1999):

1. Algebraic methods, which use interpolation or some special functions,
2. Differential methods based on the solution of partial differential equations in the transformed spatial region, and
3. Variational methods, based on optimisation of the grid quality properties.

Algebraic methods calculate interior points of the grid through formulas of transfinite interpolation. Transfinite interpolation (TFI) is defined as a multivariate interpolation procedure or a Boolean sum of univariate interpolations in each of the computational coordinates, *Thompson* (1999). These are relatively simple and they enable the grid to be generated rapidly. The spacing and slope of the coordinate lines are controlled by the coefficients in the transfinite interpolation formulas. However, in regions with a complicated shape, cell faces generated by algebraic methods can severely degenerate so that cells overlap or cross the boundary. These methods are therefore commonly used to generate grids in domains with smooth boundaries which are not highly deformed, or as an initial approximation for iterative processes in an elliptic grid solver. It is shown in this thesis that algebraic methods can generate a screw compressor numerical grid of the desired quality if used in conjunction with boundary adaptation and procedures to obtain orthogonal grids.

Differential methods are based on an iterative procedure to solve elliptic, parabolic or hyperbolic equations of spatial point distribution. The interior coordinate lines derived through these methods are always smooth with the important feature that discontinuities on the boundary surface do not extend into the interior of the domain. In practice, hyperbolic systems are simpler then elliptic or parabolic ones but these are not always mathematically correct and are not applicable to regions in which a complete boundary surface is strictly defined. All these methods are more time and space consuming

compared with algebraic methods, and therefore are not used here for the generation of the screw compressor numerical mesh.

Variational methods can be used to generate grids which should satisfy more then one generating condition, such as non-degeneracy, smoothness, uniformity, non-orthogonality or adaptivity, which cannot be satisfied simultaneously either by algebraic or differential methods. However, these are not widely used in practical grid generation, mainly because of their formulation, which does not always lead to a well posed mathematical problem.

5.1.3 Desired Properties of a Computational Grid

A numerical grid should discretise a physical domain in such a manner that the computation of the physical quantities can be carried out as efficiently as possible. The accuracy, which is one of the efficiency components of computation, is influenced by a number of factors such as: grid size, cell size, expansion factor etc.

The grid size is indicated by the number of grid points, while the cell size implies the maximum value of the length of the cell edges. A grid generation procedure should be able to produce a mesh for an arbitrary number of cell nodes or for an arbitrary cell size in such a way that the cell size is reduced if the desired number of nodes increases. This property is important for obtaining an accurate solution which might require refined cells to be generated in specific domains of interest. The ability to increase the number of grid points and to reduce the size of a cell enables the convergence rate to be studied and the accuracy of different grid sizes to be compared. The next important factor in the size of grid cells is so called expansion factor f_e. It is the ratio of characteristic dimensions for two neighbouring cells. This factor defines the rate of change of cell size and is preferably close to unity. To suggest a maximum value for this factor is difficult. It depends on a local grid topology and the oscillation of dependent variables in the considered region.

Grid orthogonalisation and smoothness are properties achieved by algebraic grid generation procedure to facilitate the solution of a numerical solver. The finite volume

method is not as sensitive to a grid non-orthogonality as other numerical methods, but a certain level of orthogonality and smoothness is recommended. The most important is the grid orthogonality at boundaries. It allows easier implementation of boundary conditions and greatly increases the stability of the calculation. It is especially important at the interface between grid blocks where a special interpolation method is required.

Cell and/or grid deformation can be formulated as a measure of departure of the cell from a standard and non-deformed cell. Cell deformation is defined through at least three characteristic values: the aspect ratio, angle of non-orthogonality and a warp angle, as shown in Figure 5-3. Both the numerical accuracy and stability are greatly dependent on these three factors which define the degree of the grid distortion. The aspect ratio f_a is defined as the ratio between the longest and the shortest edge of the numerical cell. Preferably, it should be close to unity. The angle of non-orthogonality θ_{no} is, by definition, the angle between the surface vector and the distance vector which connects the centres of two neighbouring cells which share that surface. Its value should preferably be close to zero. The warp angle θ_w is the measure of non-coplanarity of the cell face. For coplanar cell faces, these two vectors are parallel and the warp angle becomes zero. Otherwise, the angle between the surface normal of two triangular subsurfaces differs from zero. In the ideal case this should not happen. More on qualitative measures of numerical mesh can be found in *Field* (2000).

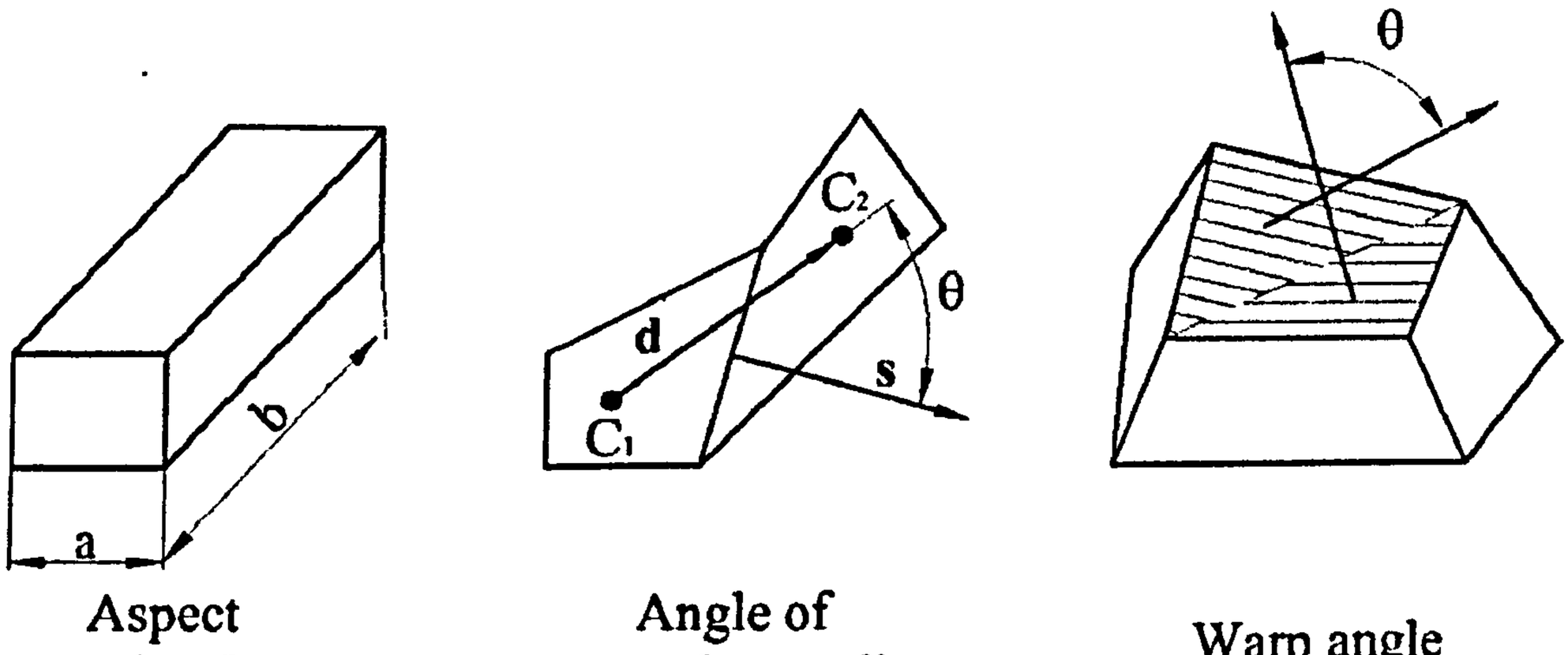

Figure 5-3 Measures of grid quality

Although the limiting values for mesh quality measures are different for each particular problem, following value limits are recommended:

Expansion factor	$fe < 2$
Aspect ratio	$f_a < 10$
Angle of non-orthogonality	$\theta_{no} < 50°$
Wrap angle	$\theta_w < 50°$

Consistency with geometry is a property of the numerical mesh that is difficult to measure but that significantly influences the result. It has two important aspects. The first criterion is that the numerical mesh must have a sufficient number of points in the interior of the computational domain which describe the physical domain accurately. When the number of points increases to infinity, their distance should reduce to zero. This is an important requirement for the numerical mesh of a screw machine where the domain size changes by several orders of magnitude between the clearance and the main domain while the number of points is kept constant. The other requirement is that a sufficient number of points must be specified on the boundary to represent it accurately. It can be achieved by increasing the number of points or by adaptation of the boundary according to its geometry. If both requirements are fulfilled, then the numerical mesh is called boundary fitting or boundary confirming mesh.

Consistency of solution constrains a grid generation method with the physics of the flow. This means that the numerical grid should generally be finer in the regions of high flow gradients, while in the rest of the domain it can be sparser. This condition is difficult to fulfil at the very beginning of the grid generation process or prior to obtaining a solution. Due to that, based on the available data, a grid generation method should be able to adjust the numerical mesh to the geometry, the flow regime and the experience of the user. Generally, if the direction of numerical points follows the direction of flow and if the distance between the points is smaller in the regions near the walls, this condition may be fulfilled. The grid is sometimes dynamically adapted during the calculation of physical values, but to couple a grid generation and flow calculation requires additional effort. A numerical grid for a screw machine is generated here based on the algebraic system where the coupling with the flow simulation becomes more difficult. Due to this, the grid generated by this method is adapted to the

geometrical conditions of a screw machine to obtain the required consistency with the physical solution elements before getting a solution, i.e. in a generation process independent of the flow simulation.

Compatibility with the numerical method is a convenient means of obtaining a solution with a specific type of a numerical mesh. Finite volume methods, in this current state, are generally capable of producing a solution with both, structured and unstructured grids. However, conservation principles are easier to obtain on structured meshes with hexahedral cells. Therefore, hexahedrae should be generated wherever possible. This gives the possibility of connecting the generated numerical mesh to a wider range of numerical solvers. These need not be specifically developed for the calculation of unstructured grids.

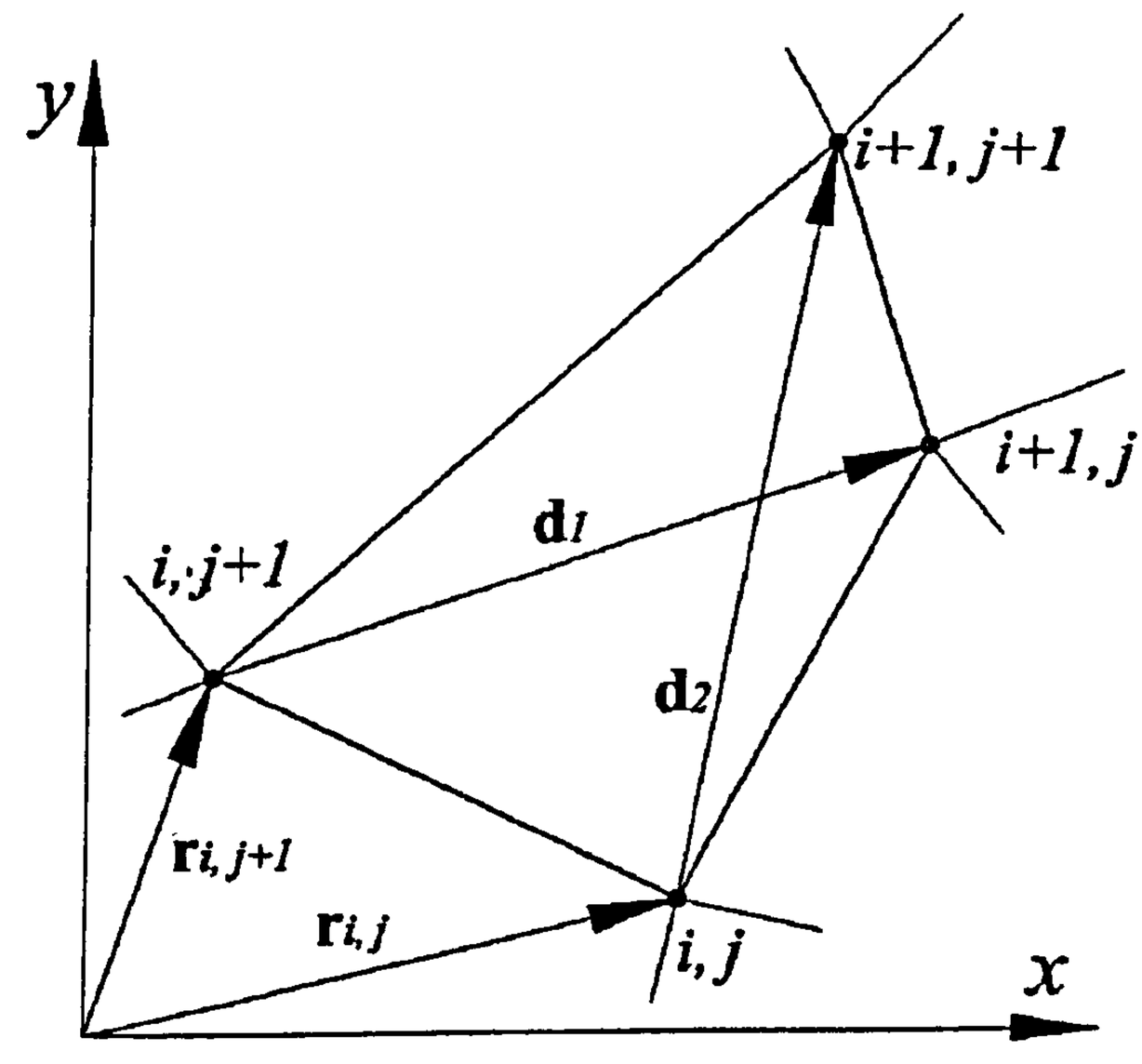

Figure 5-4 Vector definition of a two-dimensional cell

Quality measures should be quantified to confirm and compare the quality of different meshes. Some of these can be grouped in only one criterion defined as skewness value and calculated to give a measure of the quality for each particular cell and for the mesh as a whole. If a two-dimensional cell is considered, the skewness value σ_s can be defined as the cell area divided by two quantities represented by maximum lengths of cell edges in two curvilinear coordinate directions as shown in Figure 5-4:

$$\sigma_s = \frac{A}{e_1 e_2}, \tag{5.1}$$

where

$$e_1 = \max\left\{\left|\mathbf{r}_{i+1,j} - \mathbf{r}_{i,j}\right|, \left|\mathbf{r}_{i+1,j+1} - \mathbf{r}_{i,j+1}\right|\right\}; \quad e_2 = \max\left\{\left|\mathbf{r}_{i,j+1} - \mathbf{r}_{i,j}\right|, \left|\mathbf{r}_{i+1,j+1} - \mathbf{r}_{i+1,j}\right|\right\},$$

and the cell area is calculated as half the vector product of the diagonals:

$$A = \frac{1}{2}\mathbf{d}_1 \times \mathbf{d}_2.$$

The sign of the skewness factor indicates whether a numerical cell is regular or not. Only positive values are obtained for regular cells, while negative values of skewness factor indicate that the cell is inverted or twisted. At the same time, this factor indicates whether the cell is orthogonal or not. For an orthogonal cell the skewness value σ_s=1. Otherwise, the value of the skewness factor tends to zero with increased non-orthogonality. The skewness factor is calculated here for a two-dimensional cell because a numerical mesh for a screw machine is generated from two-dimensional calculations in cross sections which are later conveniently connected in the third dimension. For three-dimensional cells the skewness can be calculated as a ratio of cell volume and three quantities of maximum lengths of edges in three curvilinear coordinate directions. Calculation of the cell volume, being a problem in its own right, is calculated by the method proposed by *Kordulla and Vinkour (1983)*.

Because of their properties, the grid quality measures are calculated for every cell in a computational domain to check the quality of each particular cell and the mesh can be accepted as regular only if all cells have a skewness value greater then zero.

5.1.4 Grid Topology

Block structured grids allow convenient grid generation for complex geometries. However, although the grid generation process is simplified when the whole domain is

subdivided into a number of simpler blocks, it is not always easy to select a suitable grid topology within a block. Also, although simpler than the whole domain, a sub-domain is not necessarily simple enough for efficient grid generation. The aim of algebraic grid generation is to find a transformation function $x(\xi)$ which transforms a computational domain Ξ^n to the physical domain X^n or vice versa, as shown in Figure 5-5. Four basic topology types are commonly used to specify a numerical grid within the block. These are polyhedral, H, O and C grids. Only polyhedral and O grids will be used in screw machine grid generation process and their explanation is given in the text.

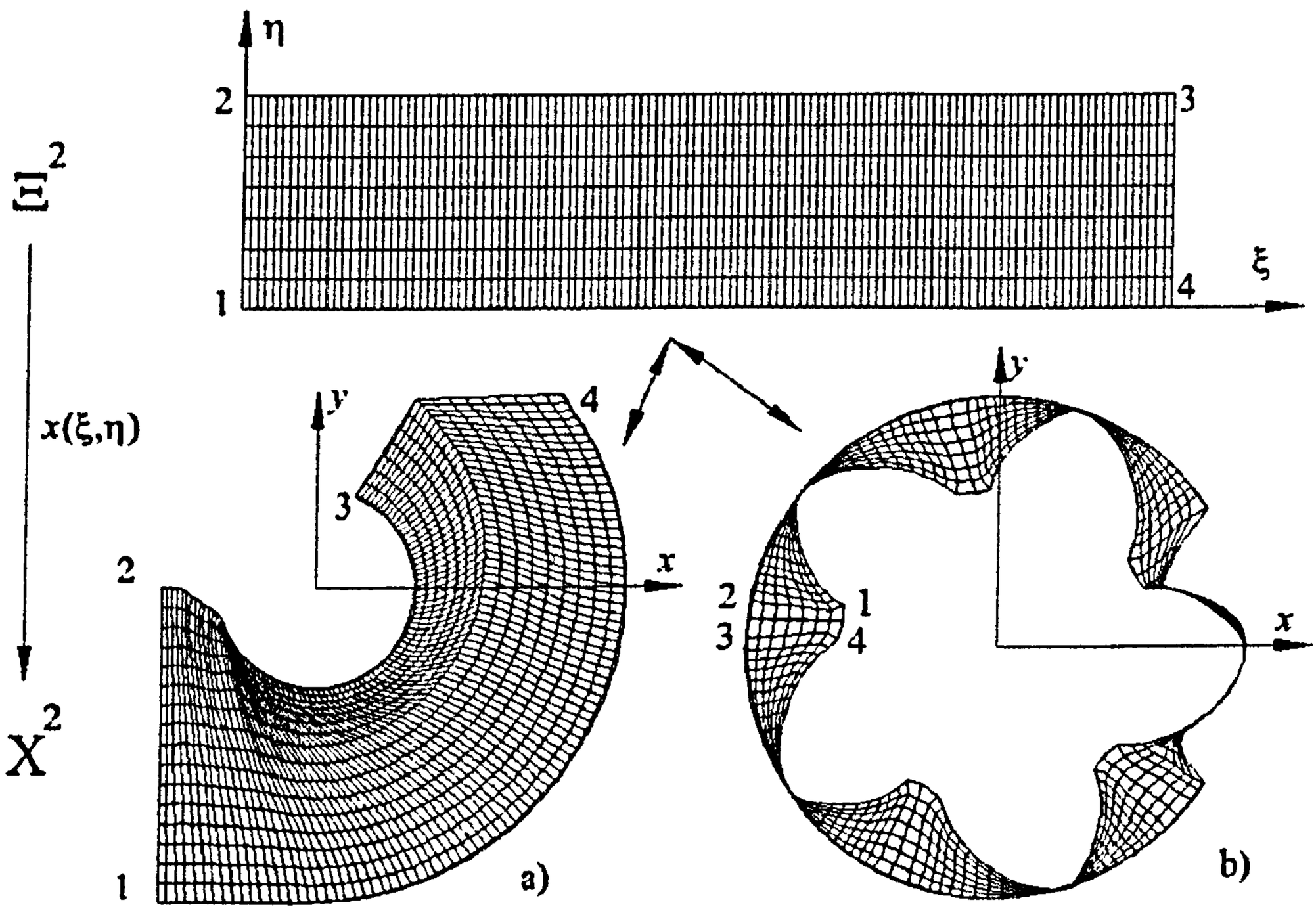

Figure 5-5 Patterns of grid topology in a screw machine

a) Block type grid, b) O-type grid

a) A block grid is represented as a polyhedron which retains the schematic form of a block domain. This type is mainly used for single-block grids. A numerical grid has all the properties of the computational block and fulfils all requirements of a physical domain through boundary fitting to the computational domain. In the generation of a screw machine geometry, it is used to produce grids of the

inlet and outlet ports as well as of other regions which retain polyhedral block shape. Both physical and numerical domains retain their block shape as shown in Figure 5-5a. The numerical domain is transformed in a hexahedral block while the physical domain remains fitted within the specified boundaries.

b) A numerical grid of O type is generated as a solid cube or rectangle in the computational domain and transformed from the physical domain as presented in Figure 5-5b. This type of numerical grid has only two boundary faces in a two-dimensional domain and four boundaries in a 3D domain. The remaining two boundary faces are connected implicitly point to point.

H and C grid types are constructed by a similar procedure to a block grid, with the required shape formed by explicit connectivity between required points.

5.2 DECOMPOSITION OF A SCREW MACHINE WORKING DOMAIN

In order to apply a CFD procedure, the spatial domain of a screw machine has to be replaced by a grid with discrete finite volumes. The number of these volumes depend on the problem dimensionality and accuracy required. A composite grid, made of several structured grid blocks patched together and based on a single boundary fitted co-ordinate system is used to transform the geometry of a screw machine into discrete volumes as shown in Figure 5-6. The numerical mesh consists of several sub-domains, two of which are critical and difficult to generate. These represent the fluid domains around the male and female compressor rotors. Not only is a main working domain contained in them but also all the clearances and leakage paths, such as the radial, axial and interlobe leakage gaps and the blow-hole area. The suction and discharge ports, suction and discharge receivers and other openings, such the oil injection port, are each presented by an additional block. The grid blocks are then connected over the defined regions on their boundaries which coincide with the other parts of the entire numerical mesh.

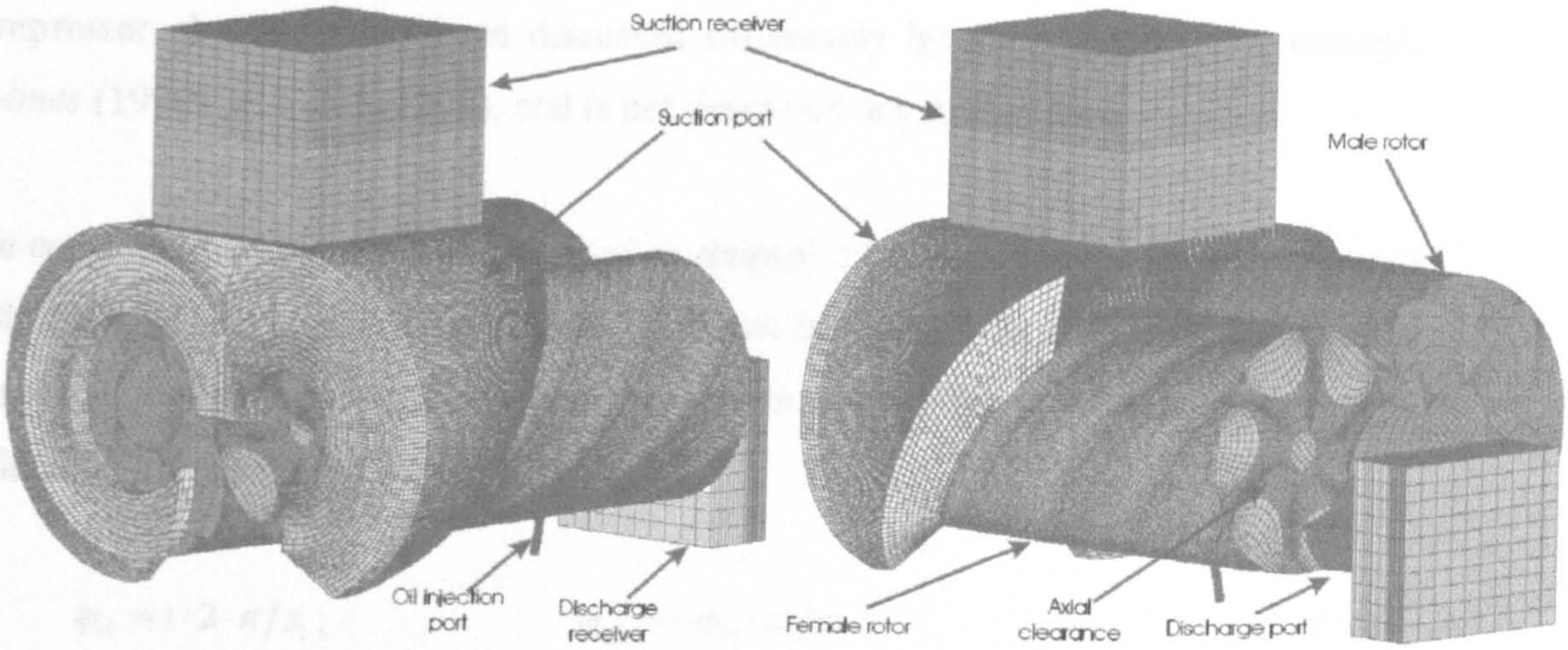

Figure 5-6 Numerical mesh of a screw compressor

a) Suction side *b) Discharge side*

The rotors of a screw machine are helical type elements generated by the simultaneous revolving of the rotor profile around the rotor axis and translation along the axis. That allows generation of the entire screw machine geometry within a two-dimensional definition of the rotors by the calculation of points in cross sections and connecting them with appropriate vertices in other cross sections. Screw compressor rotors are generated from 'slices' each of which is calculated separately following the procedure described further. These are the main machine parts between which the whole compression process takes place. Therefore, these are studied in more details while the grid generation of other parts of the numerical mesh is explained only briefly.

Grid generation of screw machine rotors starts from the definition of their spatial domains determined by the rotor profile coordinates and their derivatives. These are obtained by means of a rack generation procedure described in Chapter 2 and discussed in more details by *Stošić* (1998). A distribution of characteristic curves is specified on the rack, which is a rotor of infinite radius that has the shortest possible lobe length. Interlobe clearances are accounted for by the geometry and added to the rack at this point. The interlobe clearances depend on the application of the screw machine and their distribution is specified in advance. Clearances can be distributed uniformly, which closely applies to the situation of dry machines when the rotors are not in direct contact. However, for other applications where one rotor directly drives another one, the clearance distribution differs from the uniform. The application and distribution of

compressor clearances has been discussed extensively by many authors, for example *Holmes* (1990) or *Stošić* (1998), and is not described any further here.

The envelope meshing method described in chapter 2.2 is then applied for generation of both the male and female rotor profiles as shown in Figure 5-7a. The rotor definition is completed by multiplying a copy of the profile around the rotor axis for an angle defined by the number of lobes:

$$\varphi_{r1} = i \cdot 2 \cdot \pi / z_1; \qquad \varphi_{r2} = -\varphi_{r1} \cdot z_1 / z_2, \tag{5.2}$$

where z_1 and z_2 are number of lobes on the male and female rotors respectively. By this means, a parametric definition of screw machine rotors is obtained for each cross section orthogonal to the rotor axis in the entire domain. By means of this procedure, the inner boundary of the future "O" mesh is obtained on the rotors. The discretisation of that boundary is explained later in 5.3.3.

The next step is to obtain an outer boundary of the "O" mesh. To do that, the rack already generated is connected to the outer circle to form a closed line as shown in Figure 5-7b. The circle, to which the rack is connected, represents a rotor housing. It is formed by adding a radial clearance to the outer rotor circle r_o:

$$r_{1_o} = r_{1_o} + \delta_{r_1}; \qquad r_{2_o} = r_{2_o} + \delta_{r_2}. \tag{5.3}$$

Figure 5-7c shows both parts of the mesh together. Grid generation continues with the discretisation of these two boundaries. The easiest way to distribute the points on the boundary is to put constant distances between the points along the profile. However, in such a case, some details of a particular rotor can be lost and the simulation process can lead to an inaccurate result. Therefore, other procedure has to be performed. Preferably, the boundaries are discretised according to the rotor geometry and flow characteristics. This is done by adaptation of the point distribution on the boundaries. The adaptation is applied to the inner boundary in parametric form by the rotor coordinates. The point distribution on the other boundary is modified, based on rotor discretisation in order to form a boundary definition which later enables a regular generation of grid inner points. That procedure is described in 5.3.4.

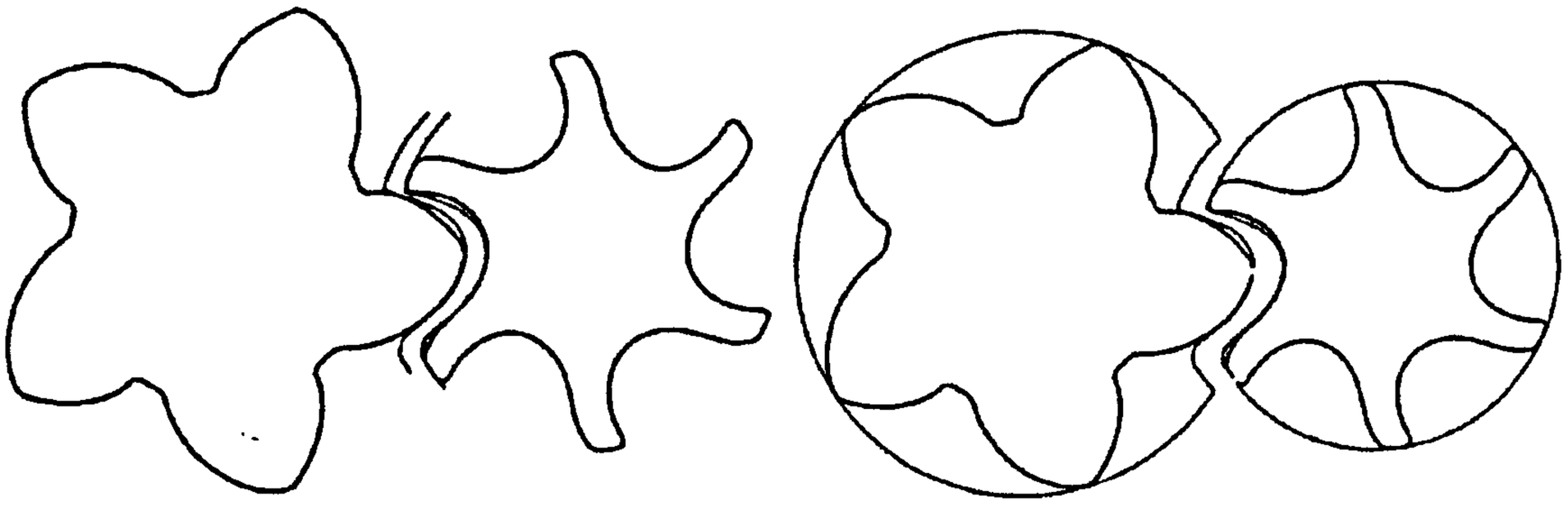

a) Generation of rotor profiles *b) Outer circle*

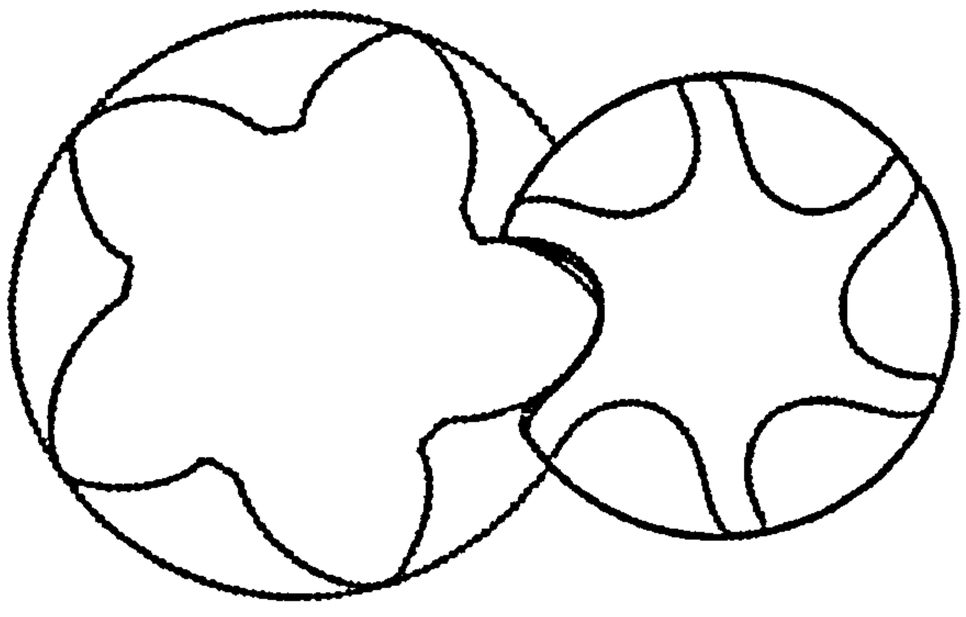

c) Boundary discretisation

Figure 5-7 Phases in the generation of screw compressor rotor boundaries

When both boundaries are mapped by an equal number of boundary nodes, an analytical transfinite interpolation is applied to generate the internal points of the numerical mesh, as will be explained later. The screw machine rotors are described by the boundary and internal points in a sequence of rotor cross sections. The 3-D numerical mesh is formed by connecting these points in consecutive cross sections. Preferably, the entire numerical mesh is formed of hexahedral control volumes with a right-hand definition in which eight grid points form a right-handed coordinate system as in Figure 5-8. However, if a hexahedral definition is not possible, the numerical cells may degenerate to form some of the three proposed cell shapes: the prism, pyramid or tetrahedron, as shown in Figure 5-9. It should be mentioned that in the case of the degenerated cells, when the edges collapse, the coinciding points should not be modified to have the same index, i.e. all vertices should remain to define a cell.

After cells of the entire numerical mesh are defined, it is necessary to form boundary regions through which the different domains are connected or on which the boundary conditions are applied.

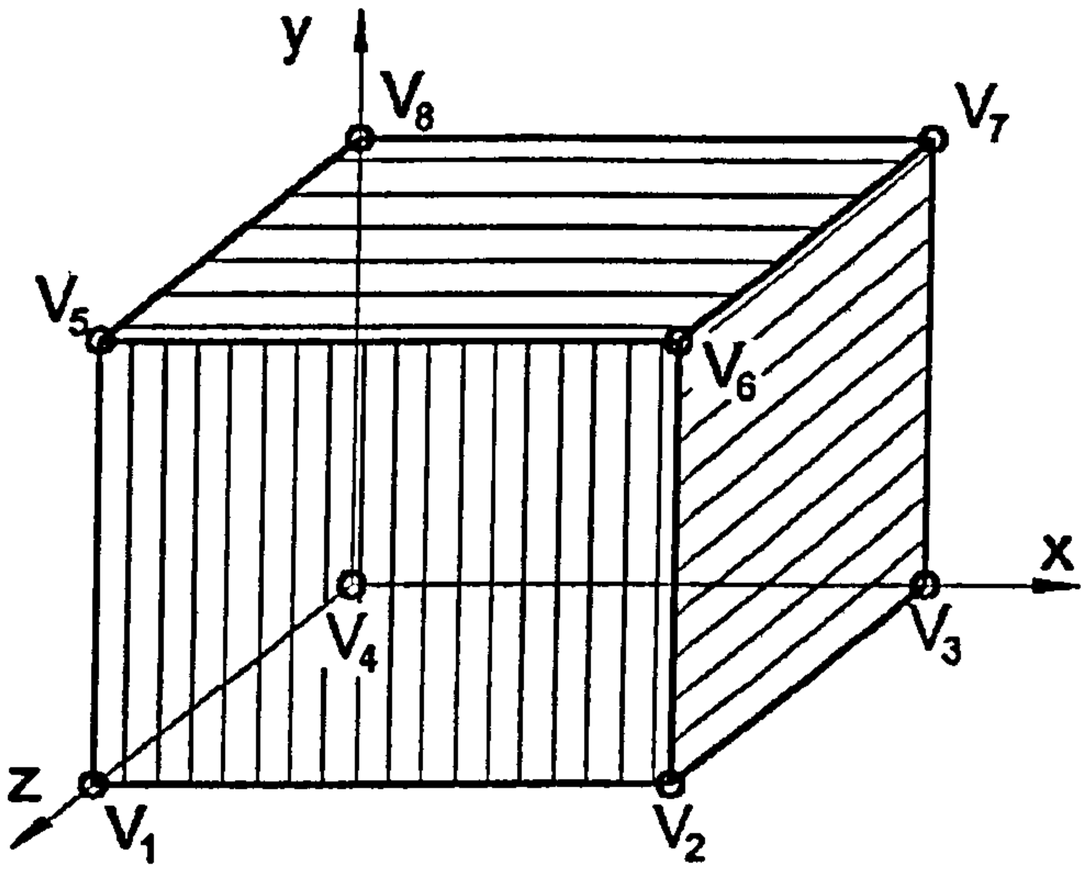

Figure 5-8 Hexahedral numerical cell

Region elements are formed of either a quadrilateral or triangular shape depending on to the shape of boundary cell face, by the same vertices by which the boundary cell face is defined. Therefore, the entire numerical mesh is defined by the vertex, cell and region specifications. This general form of data structure allows a convenient connection to a general numerical solver of a finite volume type.

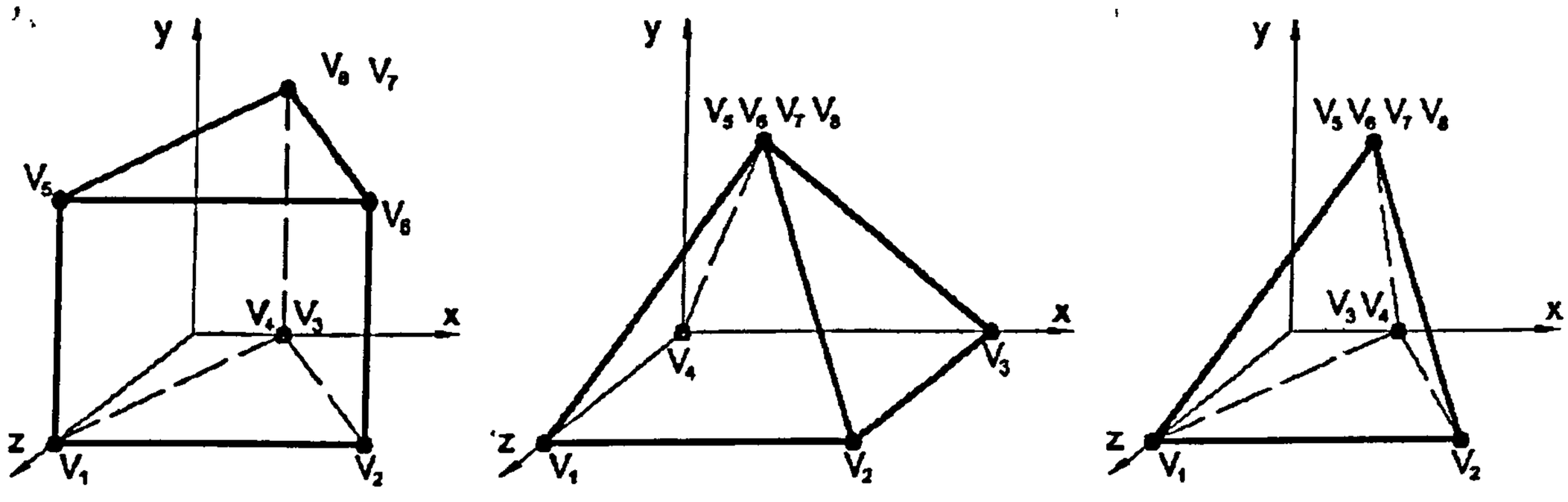

Figure 5-9 Degenerated cell shapes: prism, pyramid and tetrahedron

5.3 GENERATION AND ADAPTATION OF DOMAIN BOUNDARIES

Methods for grid adaptation were extensively discussed by many authors like *Liseikin* (1998) or *Thompson et al* (1998). Generally, they can be classified as differential or algebraic methods. Differential methods are based on a solution of the Euler-Lagrange

differential equations, usually solved simultaneously with other equations of fluid flow when the mesh is adapted, together with the development of a solution for fluid flow. Algebraic methods are based on a direct equidistribution technique which does not require solution of the differential equations. Consequently, they require less computational effort.

Numerical grid adaptation can be performed both dynamically and statically. Dynamic adaptation is mainly used for simulation of fluid flows with excessive local gradients of the dependent variables. It is then applied, together with calculations of the flow properties. On the other hand, static grid adaptation is usually used to improve a numerical grid in advance, before obtaining a solution. Adaptation is based on the existing boundary geometry and on the flow characteristics expected in the domain.

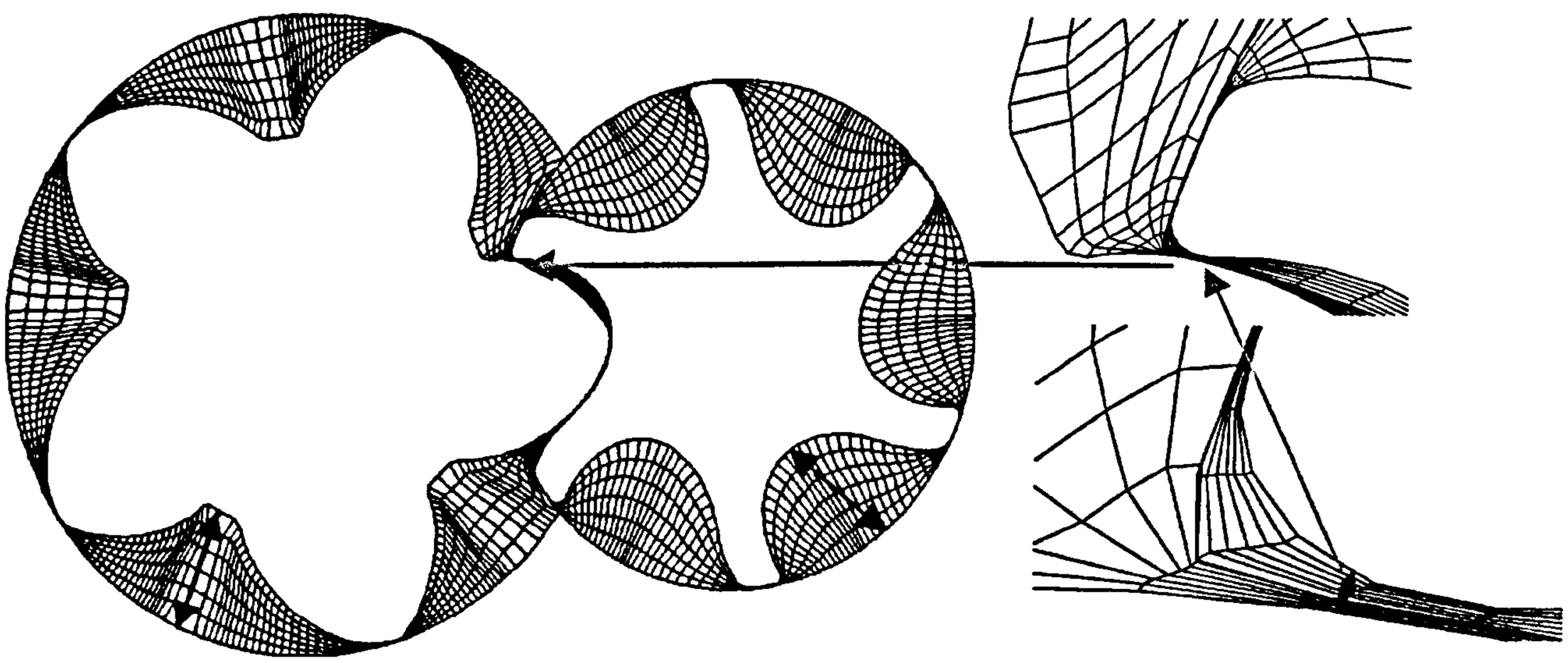

Figure 5-10 Comparison of cell sizes in the working chamber and clearances

In this thesis, a static analytical adaptation is applied to rotor boundaries of the screw machine. There are two reasons for this; i) the cell irregularity and ii) accurate representation of the boundaries. Firstly, excessively deformed cells appear in the clearance regions as a consequence of the reduction of the cell face in the radial direction, as shown in Figure 5-10. Since the number of cells in the radial direction is the same for the clearances and the working cavity, a large aspect ratio appears which can be as high as 1000. Therefore, the cell shapes easily become unacceptable or the

cell becomes too deformed for accurate calculation. Secondly, if a low number of boundary points is applied to a very curved boundary, for example on the top of the female rotor, some of the geometry features which greatly affect flow, could be lost. This situation can be overcome by introducing more cells along the boundary or alternatively by local mesh refinement. Both approaches lead to an increase in the number of control volumes, which adversely affects both the efficiency and speed of calculation.

The approach accepted here therefore distributes more numerical points where required as, for example, in the clearances, and less at other places. The numerical mesh in Figure 5-10 is generated from the adapted 2-D rotor boundaries where the ratio of the working chamber to clearance size was 400.

5.3.1 Adaptation function

The analytical equidistribution technique is based on minimization of the distribution error by redistributing points along the curve to keep the product of the 'weight function' and the grid spacing constant, i.e.

$$X_\xi \cdot W = const. \tag{5.4}$$

where X_ξ represents the grid spacing and W is the weight function.

This equation can be treated as the Euler-Lagrange equation which, when integrated with a respect to a computational coordinate ξ, becomes:

$$X(\xi) = \int_0^\xi \frac{d\xi}{w(\xi)} \Big/ \int_0^1 \frac{d\xi}{w(\xi)} . \tag{5.5}$$

In equation (5.5), both the grid spacing and the weight function depend on the computational coordinate ξ. This means that the equation is implicit and must be solved iteratively.

However, if equation (5.4) is integrated with respect to the physical coordinate x, it then gives the explicit form which can be solved directly. Its explicit form in function of the physical coordinate is according to *Samareh-Abolhassani and Smith* (1992):

$$\xi(x) = \int_{x_{min}}^{x} W(x)dx \Big/ \int_{x_{min}}^{x_{max}} W(x)dx . \tag{5.6}$$

Finally, if the starting equation is integrated with a respect to the natural coordinate or the arc-length, which follows the curve, it gives:

$$\xi(s) = \int_{0}^{s} W(s)ds \Big/ \int_{0}^{S\max} W(s)ds . \tag{5.7}$$

The latest form of the equation appears to be the most appropriate for adaptation of complex curves which represent the boundaries of screw machines. Its one-dimensional nature allows adaptation along one single grid line only, or along the set of grid lines which all follow a single natural direction. Multidimensional adaptation can be achieved by successive repetition of this procedure along all the sets of grid lines.

The way a grid line is adapted depends only on the selection of the weight function. *Samareh et al.* (1992) suggested use of a weight function in the form of:

$$W(s) = 1 + \sum_{i=1}^{I} b^i f^i(s), \tag{5.8}$$

where i is a number of variables which influence the adaptation, b^i are constants and $f^i(s)$ are adaptation functions or their first derivatives. Value 1, added to equation (5.8), is there to ensure uniformity of distribution. The adaptation function, which appears in the same equation, is integrated along the length of the grid

$$F^i(s) = \int_{0}^{s} f^i(s)ds . \tag{5.9}$$

Equations (5.7), (5.8) and (5.9) together give:

$$\xi(s)=\frac{s+\sum_{i=1}^{I} b^i F^i(s)}{S_{\max}+\sum_{i=1}^{I} b^i F^i(S_{\max})}. \tag{5.10}$$

Equation (5.10) can be used to move the grid points along a fixed curve. Parameters b^i and F^i have positive values to ensure monotonicity of $\xi(s)$. However, if the line, which is adapted, changes in time, or if the adaptation has to be applied to a group of grid lines in a two or three dimensional grid, b^i has to be updated to keep the same emphasis of the point concentration. In this more general case it is useful to define a grid point ratio R^j assigned to each particular function f^j as:

$$R^j = b^j F^j(S_{\max}) \Big/ \left\{ S_{\max}+\sum_{i=1}^{I} b^i F^i(S_{\max}) \right\}, \quad j=1,2,...,I \tag{5.11}$$

Now, if the grid point ratio (5.11) is calculated, continuous updating of b^i is avoided and the emphasis of the point concentration is kept constant. After implementing (5.11) in equation (5.10), the final form of the adaptation function becomes:

$$\xi(s)=\frac{s}{S_{\max}}\left\{1-\sum_{i=1}^{I} R^i\right\}+\sum_{i=1}^{I}\left\{R^i \frac{F^i(s)}{F^i(S_{\max})}\right\} \tag{5.12}$$

5.3.2 Adaptation variables

In order to map boundaries of a computational domain using the previous equation, adaptation variables, which form a weight function, must be selected. The boundary adaptation should be conducted in conjunction with geometrical characteristics of the boundary and flow characteristics in the nearby region. In this thesis, the simultaneous use of any combination of two variables is presented. Although the adaptation variable

can be any significant factor, six adaptation variables with different effects are presented here:

The tangent angle on the curve at the calculation point $$\alpha_P = \arctan\left(\frac{\partial x_P}{\partial y_P}\right),$$

The radius of curvature in the vicinity of the calculation point $$r_P = \frac{1+y_P'^2}{y_P''}\cdot\frac{3}{2},$$

The distance of the calculation point from the rotor centre $$d_P = \sqrt{x_P^2 + y_P^2}, \qquad (5.13)$$

The curve flatness around the calculation point $$E_P = \frac{\sqrt{\left(x_P - x_{P_o}\right)^2 + \left(y_P - y_{P_o}\right)^2}}{d_P - d_{P_o}},$$

Sinusoidal distribution of points $$C_{\sin} = \sin(\pi \cdot k_P / K),$$

Cosinusoidal distribution of points $$C_{\cos} = \left|\cos(\pi \cdot k_P / K)\right|.$$

All the variables selected above are geometrical characteristics of the boundary which, when represented through their gradients along the boundary curve, give various distributions in the characteristic region. For example, if a radius of curvature changes rapidly with the natural coordinate, then the application of r_P as the adaptation variable will give more points in this region than in other places. A similar situation happens if other adaptation variables are applied.

Although the computational method introduced in this thesis allows adaptation by two selected adaptation variablesit is still general, which means that any number of adaptation variables can be introduced for adaptation if necessary.

5.3.3 Adaptation based on two adaptation variables

As mentioned previously, any geometrical or flow characteristic can be used as a boundary adaptation. For illustration of the method, the gradients of a tangent angle and radius of curvature have been used as weight functions f_k^1 and f_k^2 respectively in the first and second adaptation criterion:

$$f_k^1 = \left|\frac{\partial \alpha_P}{\partial s}\right|_k = \left|\frac{\alpha_{Pk+1} - \alpha_{Pk-1}}{s_{k+1} - s_{k-1}}\right|, \qquad f_k^2 = \left|\frac{\partial r_P}{\partial s}\right|_k = \left|\frac{r_{Pk+1} - r_{Pk-1}}{s_{k+1} - s_{k-1}}\right| \tag{5.14}$$

In the previous equation, index k counts the numerical points along the curve which is adapted. Here, weight functions are given both differentially and in the form of finite differences. Derivatives with respect to the arc-length, i.e. the physical coordinate, are the most convenient for the static adaptation. However, in the case of a general dynamic adaptation, the derivatives with respect to the computational coordinate ξ can be more suitable. There are many ways to represent them. The most usual is a central differencing on the computational mesh with equidistant distribution of the points, which gives:

$$f_k^1 = \left|\frac{\partial \alpha_P}{\partial \xi}\right|_k = \left|\frac{\alpha_{Pk+1} - \alpha_{Pk-1}}{2}\right|, \qquad f_k^2 = \left|\frac{\partial r_P}{\partial \xi}\right|_k = \left|\frac{r_{Pk+1} - r_{Pk-1}}{2}\right|. \tag{5.15}$$

The second step to modify the boundaries is to evaluate the integral adaptation variable (5.9) which will later be used to calculate the point distribution from equation (5.10). Here a trapezoidal rule for non-uniform spacing of the physical coordinate s_k is used for calculation of the integrated adaptation variable in each numerical point. The discretised formula has a standard form for all applied weight functions:

$$F^i(S_1) = 0, \qquad F^i(s_k) = F^i(s_{k-1}) + \frac{\left[f_k^i + f_{k-1}^i\right] \cdot \left[s_k - s_{k-1}\right]}{2}, \tag{5.16}$$

where $k=2,3,\ldots,K$ is the number of points along the curve, while $i=1,2,\ldots, I$ is the number of variables used for adaptation.

The third step is the calculation of a new computational coordinate along the curve as a function of the previous physical coordinate. This step is performed through equation (5.12) which requires the grid ratio from equation (5.11) to be known. As a result, a new coordinate distribution is given as function of the previous distribution as:

$$\xi(k) = \xi(S_k). \tag{5.17}$$

In a more convenient form, this equation, which gives a new distribution of points, can be written as:

$$\xi(k)=\frac{S_k}{S_K}\cdot\left(1-\sum_i R^i\right)+\sum_i \frac{F^i(S_k)}{F^i(S_K)}\cdot R^i, \tag{5.18}$$

where R^i is the weight coefficient for each adaptation variable when applying a new distribution. The sum of factors R for all adaptation variables i should be less then or equal to 1.

Finally, the fourth step is to find the inverse function of (5.17) which gives a new physical coordinate $\bar{S}_k$ in the new coordinate system $\bar{\xi}_k$. This can be done by an interpolation procedure which aims to find a new arc-length in the form of

$$\bar{S}_k(\bar{\xi}_k)=\sum_{m=1}^{K} L_m(\bar{\xi}_k)\cdot S_k(\xi_k), \tag{5.19}$$

where the bar values represent new values of the physical and computational coordinates and the others are previous values of the same coordinates. A new transformed coordinate and both, the starting and ending value n_{min} and n_{max} of the Lagrangian product of transformed coordinates:

$$\begin{aligned}&\bar{\xi}_k=(k-1)/(K-1)\\&L_m(\bar{\xi})=\prod_{\substack{n=n_{min}\\ n\neq m}}^{n=n_{max}}\left(\bar{\xi}-\xi_m\right)\Big/\left(\xi_n-\xi_m\right)\end{aligned} \tag{5.20}$$

must satisfy the conditions:

$$\xi_{n_{min}-1}\le\bar{\xi}_k\le\xi_{n_{min}};\qquad 1\le n_{\min}\ and\ n_{\max}\le K. \tag{5.21}$$

An example of the use of a geometrical weight function to adapt the rotor boundary of a screw machine is shown in Figure 5-11. On the left hand side figure, a uniform

distribution is shown along the pair of rotors with 4/6 lobes on the male/female rotors. The male rotors diameter is 142.25 mm with and the axis distance is 108.4 mm. The number of cells generated by such a distribution of boundary points on the both rotors is the same.

The boundary distribution on rotors on the right hand side is modified with the equal value of 0.2 of two weighting functions, namely the tangent angle and the radius of curvature. As a result, a much better arrangement of both the boundary points and entire mesh is obtained. This is particularly visible in the gaps and rotor inter-connections. However, in parts of the numerical mesh where the cells are not so deformed and where the pattern of flow variables is expected to be nearly uniform, the cell size is not modified at all.

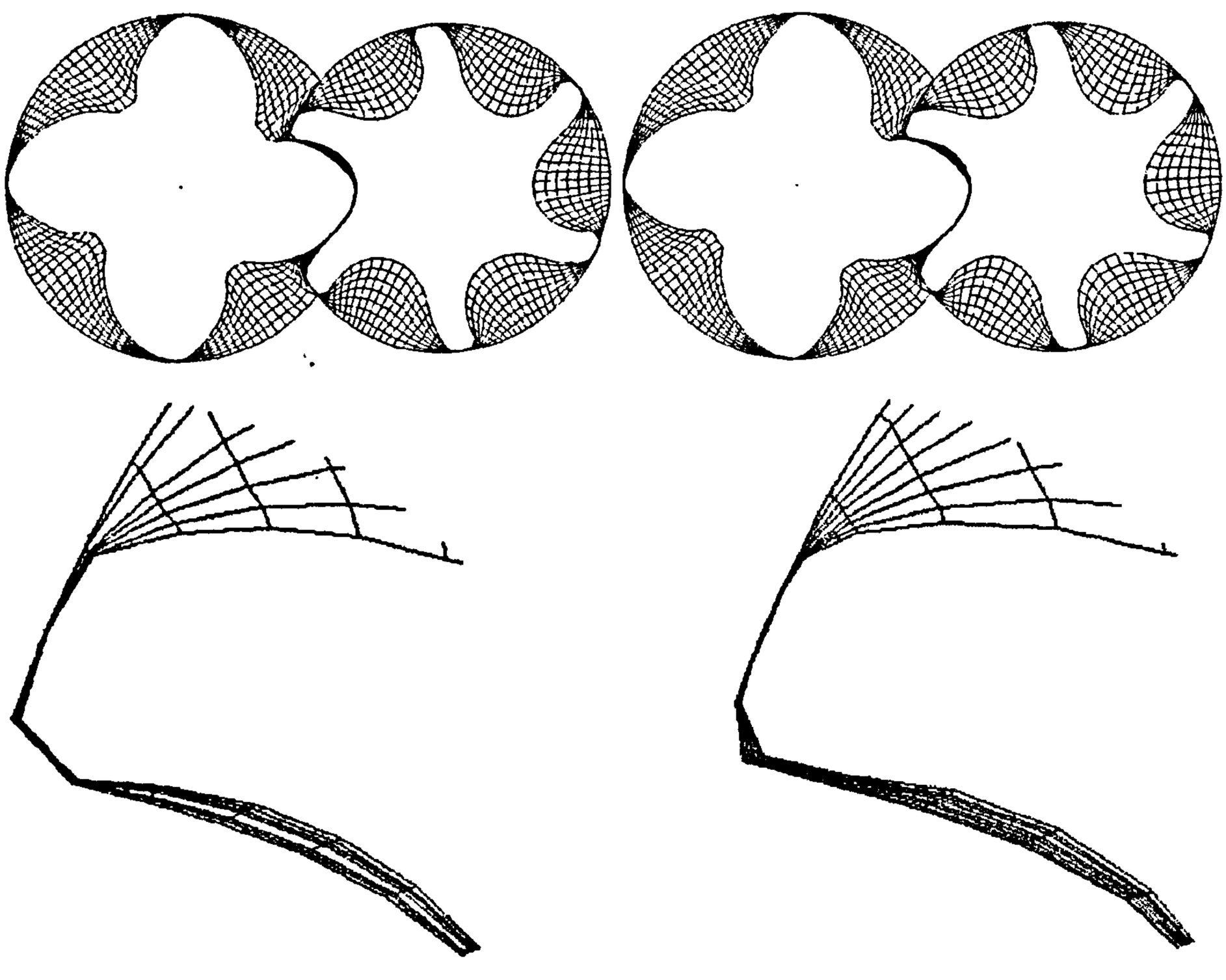

Figure 5-11 Comparison between the original (left) and adapted rotors (right)

The distribution of boundary points plays a significant role in the grid generation process. A more appropriate boundary distribution allows easier generation of inner mesh nodes.

5.3.4 Mapping of the outer boundary

As explained in 5.3.3, the desired distribution on the rotor inner boundary of a 2-D "O" mesh is obtained by adapted mapping. In Figure 5-12, points are given in index notation with respect to the physical coordinate system:

$$\mathbf{r}_{i,j=0} = \mathbf{r}_{i,j=0}(x,y) \tag{5.22}$$

The outer boundary needs to be mapped with the same number of points as the inner boundary. This usually means that the cells in the structured grid generated from nodes on the boundaries are regular. The easiest way to obtain the same number of points on both boundaries is to apply the same arc-length distribution of points to the outer boundary as to the inner one. This successfully distributes the boundary nodes for generation of the inner points only if the mesh is simple and its aspect ratio does not change rapidly. However, for complex meshes and high aspect ratios, this method usually does not produce a distribution which results in a regular mesh. Therefore, a new arc-length on the outer boundary has to be specified before the generation of the inner points can be performed. The procedure starts with the transformation of the outer boundary to a straight line, then its adaptation to a new coordinate system and subsequently continues with reverse transformation to the physical boundary in parametric form. To apply the procedure, the outer circle is first mapped with the same number of points and the same arc-length distribution as the rotor itself:

$$\mathbf{r}_{i,j'=1} = \mathbf{r}_{i,j'=1}(x,y) = \mathbf{r}_{i,j'=1}\left(\frac{s_i}{s_I}\right) \tag{5.23}$$

where s_i is a natural coordinate of the rotor i.e. this is a distance from the starting point to the point i along the rotor curve, while s_I is the length of the rotor boundary.

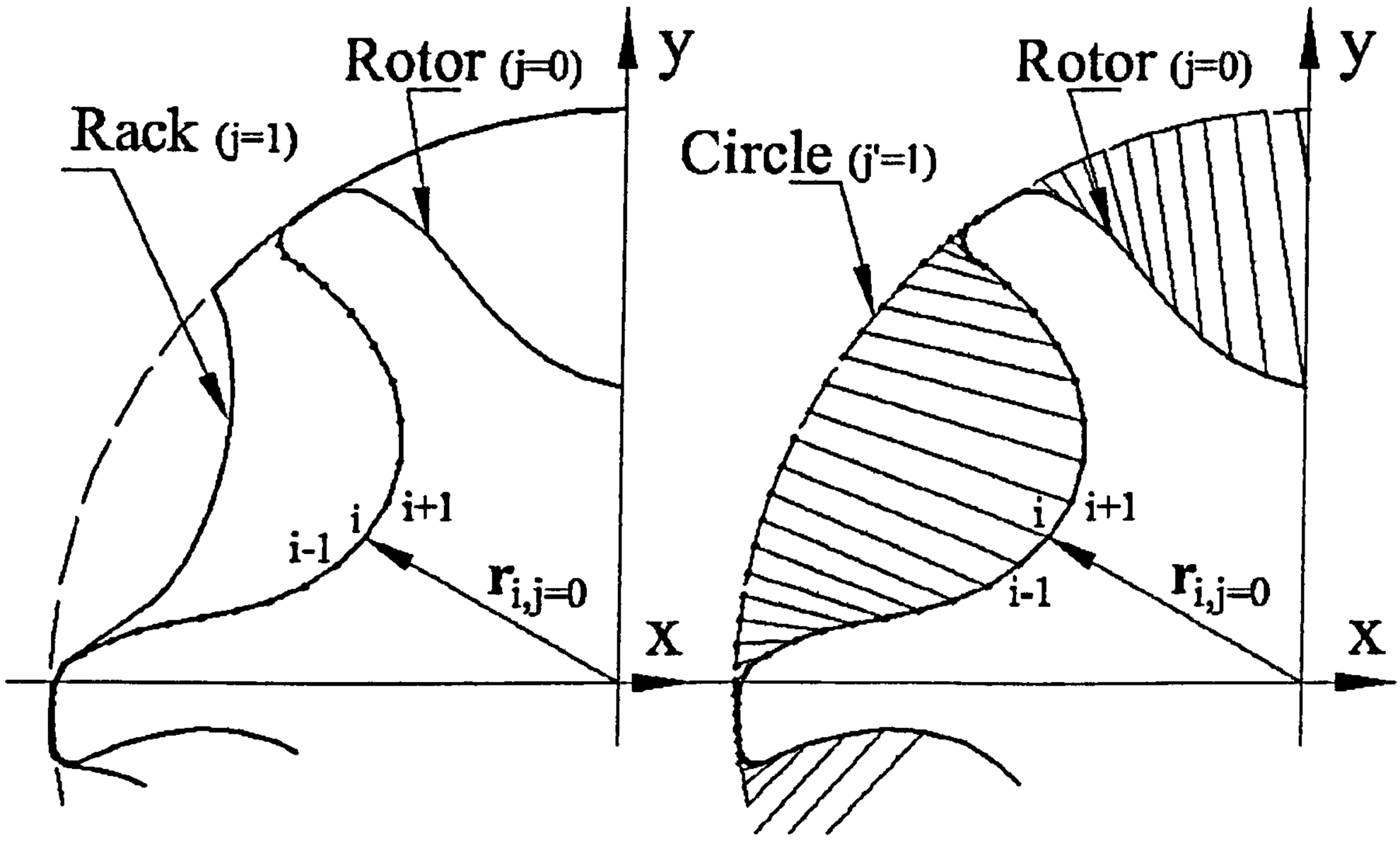

Figure 5-12 Point distribution for rotor and circle with equal arc-length

Figure 5-12 shows how the initial distribution of the points on the outer circle is achieved by the same arc-length as on the screw compressor female rotor. The distribution of points obtained by this means is not always satisfactory especially if the points are extrapolated to the rack.

Lengths *a*, *b* and *c* are shown for an arbitrary point *i* in the physical domain as shown on the left side of Figure 5-13. These are calculated as:

$$a=\sqrt{\left(x_i-x_{i-1}\right)_{j=0}^2+\left(y_i-y_{i-1}\right)_{j=0}^2},$$

$$b=\sqrt{\left(x_{i-1,j=0}-x_{i-1,j'=1}\right)^2+\left(y_{i-1,j=0}-y_{i-1,j'=1}\right)^2}. \tag{5.24}$$

$$c=\sqrt{\left(x_{i,j=0}-x_{i-1,j'=1}\right)^2+\left(y_{i,j=0}-y_{i-1,j'=1}\right)^2}$$

The angle between *a* and *c* is determined by the cosine theorem:

$$\cos\alpha_{oc}=\frac{a^2+b^2-c^2}{2ab} \tag{5.25}$$

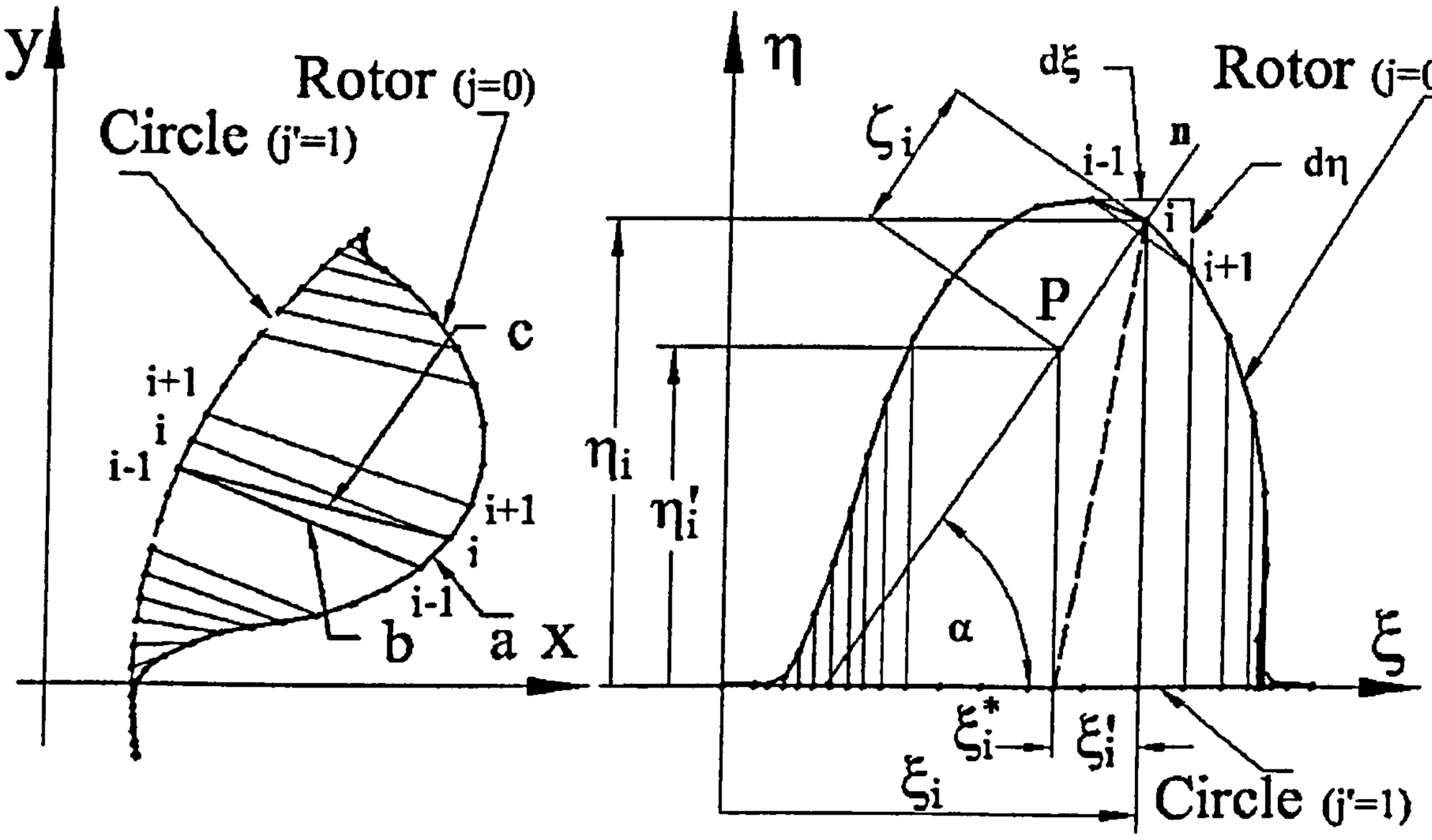

Figure 5-13 Transformation from physical (left) to computational domain (right)

The computational coordinate system ξ-η with transformed coordinates of the rotor and circle is shown in the right diagram of Figure 5-13. The outer circle in the physical domain is transformed to the straight line along the ξ axis in the computational domain. The rotor profile is transformed from the physical to the computational domain so that each computational point on the rotor has the same value on the ξ coordinate as its corresponding point on the circle.

The point coordinates in the computational domain are given by the following expressions:

$$\begin{aligned} \xi_{i,j=0} &= \xi_{i-1,j=0} + c\cos\alpha_{ac}, & \xi_{i,j'=1} &= \xi_{i,j=0} \\ \eta_{i,j=0} &= c\sin\alpha_{ac}, & \eta_{i,j'=1} &= 0 \end{aligned} \tag{5.26}$$

The computational cells are formed between the points in the computational domain, as shown in Figure 5-13. As a consequence of the transformation, both the right and left cell boundaries are produced as vertical lines. Unfortunately, some of the cells generated by this procedure are either inverted or twisted. However, these can become

regular if the points on the straight edge in the computational domain can be rearranged to form a monotonically increasing or decreasing sequence. In that case, the reverse transformation from the computational domain would also give a regular point distribution on boundaries in the physical domain.

Consider point *i* in the computational domain on the rotor boundary as shown in the right diagram of Figure 5-13. The line normal to the rotor profile in that point is defined by the angle between that line and ξ axis as:

$$\tan\alpha = \frac{d\xi}{d\eta} \tag{5.27}$$

Assume that point P lies on that normal line and its projection to ξ axis gives the desired point distribution on the horizontal boundary, as shown in the diagram by the dashed line. The position of point P is defined by its vertical coordinate η'_i. The distance between points P and i is given by ζ_i, which is a function of the vertical coordinate of point P_i. In that case, the horizontal projection of the point P_i can be calculated as:

$$\xi_i^* = \xi_i - \xi'_i, \tag{5.28}$$

The vertical projection is specified as:

$$\eta'_i = \eta_i - \zeta_i \cdot \sin\alpha . \tag{5.29}$$

The ratio between the distance ζ_i and the vertical coordinate of point P_i is given by:

$$k_i = \frac{\eta'_i}{\zeta_i}, \tag{5.30}$$

where the coefficient k_i can be any number greater then or equal to zero. If k_i is equal to zero then the point P_i is positioned on the ξ axis. However, if $k \to \infty$ then ζ_i becomes zero and point P_i corresponds to point *i* on the rotor. In that case, the distribution of the

points is unchanged. By inserting (5.30) into equations (5.28) and (5.29), the new point projection on the ξ axis becomes:

$$\xi_i^* = \xi_i - \eta_i \cdot \frac{\cos\alpha}{k_i + \sin\alpha}. \qquad (5.31)$$

If the coefficient k in equation (5.31) has a constant value $k=1$, the new point distribution in the computational domain is always regular, as shown in the left part of Figure 5-14.

It then remains to make the inverse transformation from the line in the computational domain to the circle in the physical domain with respect to the new arc-length:

$$\mathbf{r}^*_{i,j'=1} = \mathbf{r}^*_{i,j'=1}(x,y) = \mathbf{r}_{I,j'=1}\left(\frac{\xi_i^*}{\xi_I^*}\right). \qquad (5.32)$$

The result of that procedure is shown on the right diagram in Figure 5-14. Linear interpolation or extrapolation between corresponding points on the circle $j'=1$ and rotor $j=0$ gives the point on the rack, as shown in the right drawing of Figure 5-14.

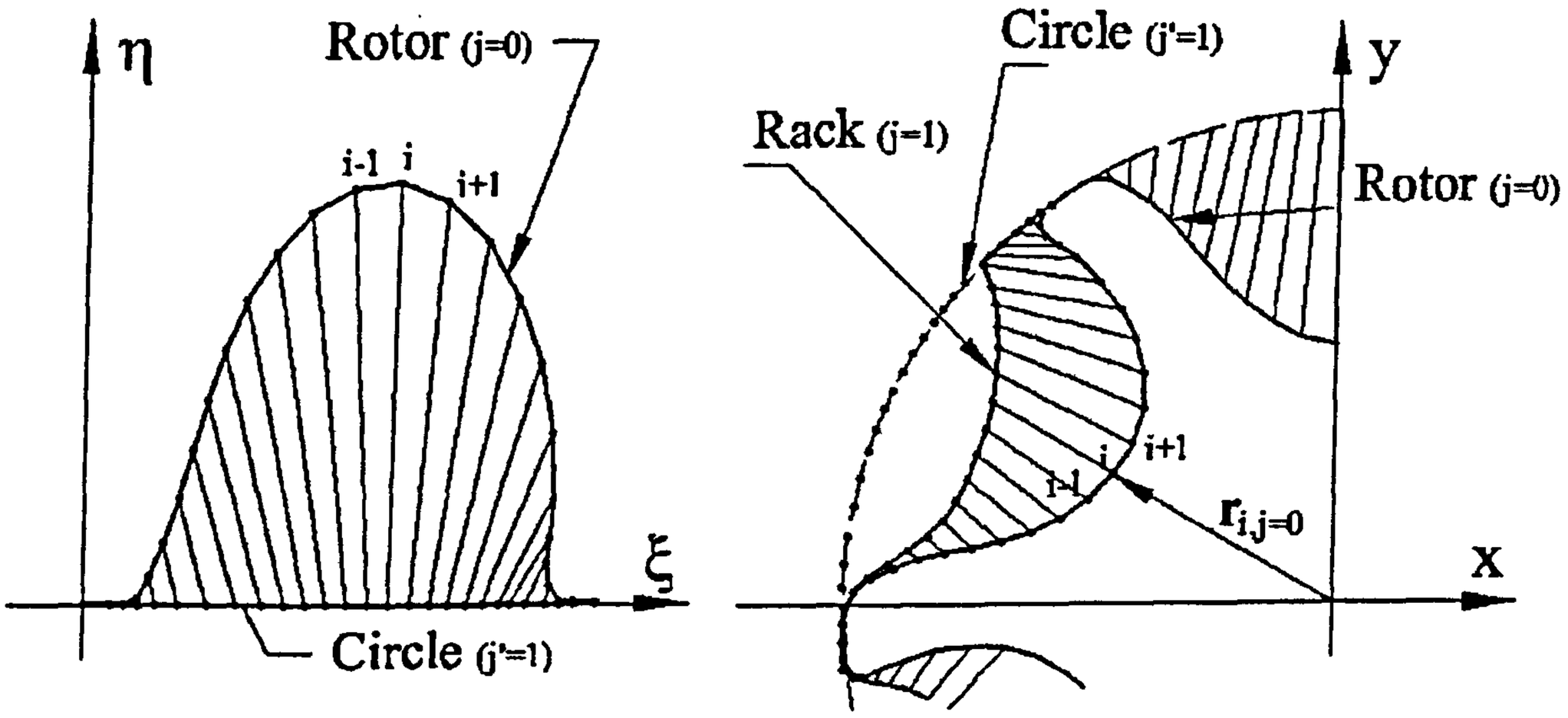

Figure 5-14 Final point distribution in computational (left) and physical (right) domain

The method presented in this chapter ensures the satisfactory distribution of boundary points in the 2D cross section of the screw machine rotor domains. This was not achievable by any other method found in the open literature. The level of redistribution can be controlled by the factor k_i, which may be constant for all points through the domain or can be changed for each point by use of some characteristic parameter. For the screw machine rotors, it appears that a constant value $k=1$ always gives a regular distribution of points on the boundaries, which is an essential prerequisite for successful generation of the internal points.

5.4 ALGEBRAIC GRID GENERATION FOR COMPLEX BOUNDARIES

Algebraic grid generation methods are often based on a transfinite interpolation (TFI). It is defined as a multivariate interpolation procedure or a Boolean sum of univariate interpolations along each computational coordinate (*Thompson* 1999). The method is commonly used for grid generation in domains with smooth boundaries that are not highly deformed, or as an initial approximation for the iterative process of an elliptic grid solver. In this thesis, a transfinite interpolation is used in conjunction with the boundary adaptation and orthogonalization procedure which appeared to be a successful method for screw machine numerical grid generation. A good summary on TFI is given by *Smith* (1982).

After the boundaries of a physical domain have been calculated and the boundary points adapted to the geometry conditions, they have to be mapped to a computational domain in which the calculation of the inner nodes of a computational mesh will be performed. The coordinates of the 2D physical domain are given in an x-y coordinate system while the computational coordinates are ξ-η as shown in Figure 5-15. The transfinite interpolation method is used for calculation of the inner point coordinates. Both, the block grid (left) and the "O" grid (right) are mapped to a similar computational grid. These domains are highlighted in the figure.

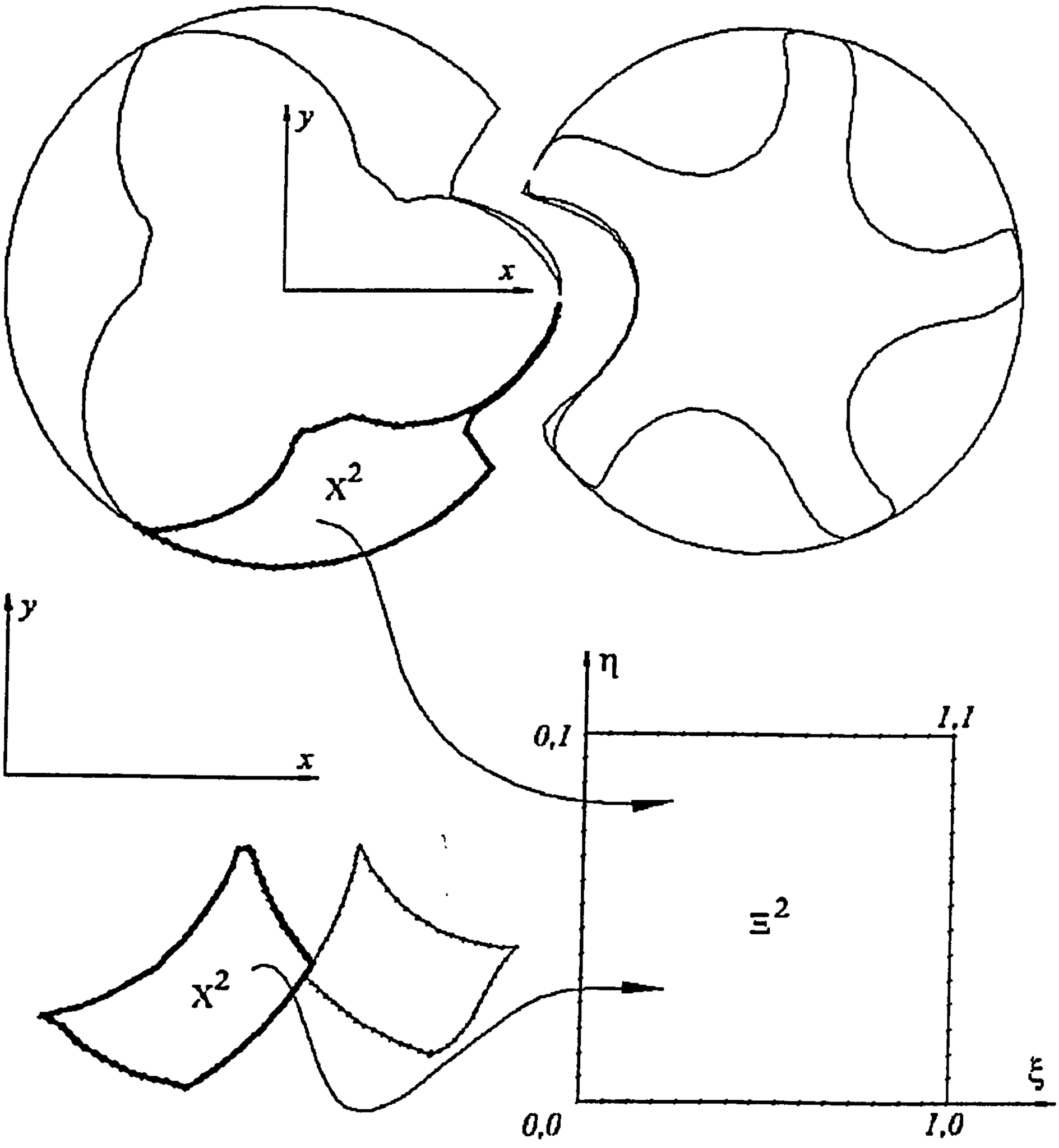

Figure 5-15 Conformal mapping of a physical domain X^2 to computational domain Ξ^2

5.4.1 Standard Transfinite Interpolation

The coordinates of four boundary faces generated with the help of adaptation methods in two dimensions can be written in vector form as:

$$\begin{aligned} \mathbf{a}_l(\eta) &= \mathbf{r}(\xi_l, \eta), \qquad l = 1,2 \\ \mathbf{b}_l(\xi) &= \mathbf{r}(\xi, \eta_l), \qquad l = 1,2, \end{aligned} \tag{5.33}$$

where the coordinates of the transformed computational coordinate system, ξ and η, are:

$$\xi = \frac{(i-1)}{(I-1)} \quad \text{and} \quad \eta = \frac{(j-1)}{(J-1)}.$$

i and j denote point numbers on the physical coordinate while I and J are the overall number of points on these coordinates. The coordinates of the interior points are by definition of the transfinite mapping method given as:

$$\begin{aligned} \mathbf{r}_1(\xi,\eta) &= \sum_{l=1}^{2} \alpha_l(\xi)\mathbf{a}_l(\eta) \\ \mathbf{r}(\xi,\eta) &= \mathbf{r}_1(\xi,\eta) + \sum_{l=1}^{2} \beta_l(\eta)[\mathbf{b}_l(\xi) - \mathbf{r}_1(\xi,\eta_l)], \end{aligned} \tag{5.34}$$

Blending functions $\alpha_1(\xi)$ and $\beta_1(\eta)$ are arbitrary functions of the computational coordinates that satisfy the cardinality conditions given by (5.35) to ensure that the edges of the domain are reproduced as a part of the solution.

$$\begin{aligned} \alpha_l(\xi_k) &= \delta_{kl}, \qquad k=1,2 \;\; l=1,2 \\ \beta_l(\eta_k) &= \delta_{kl}, \qquad k=1,2 \;\; l=1,2 \end{aligned} \tag{5.35}$$

where δ is the Kronecker's delta, *Chawner and Anderson* (1991).

By use of equation (5.33), the equation (5.34) for a 2-D domain can be written in the following general form of the transfinite interpolation method, which gives a connection between the coordinates in the physical and numerical domains:

$$\begin{aligned} x(\xi,\eta) &= X_1(\xi,\eta)\alpha_1(\xi) + X_2(\xi,\eta)\alpha_2(\xi) \\ y(\xi,\eta) &= Y_1(\xi,\eta)\beta_1(\eta) + Y_2(\xi,\eta)\beta_2(\eta) \end{aligned} \tag{5.36}$$

The ability of the analytical transfinite interpolation method (5.36) to produce a regular distribution of internal points is highly dependent upon the selection of blending

functions $\alpha_1(\xi)$ and $\beta_1(\eta)$. These functions define the curvature and orthogonality of the internal grid lines.

5.4.1.1 LaGrange blending functions

The simplest method of obtaining blending functions is by the LaGrange interpolation:

$$\begin{aligned} \alpha_1(\xi) &= 1-\xi \qquad \alpha_2(\xi) = \xi \\ \beta_1(\eta) &= 1-\eta \qquad \beta_2(\eta) = \eta \end{aligned} \tag{5.37}$$

Applying (5.37) to equation (5.36) gives the inner mesh points as:

$$\begin{aligned} x(\xi,\eta) &= (1-\xi)X_1(\xi,\eta)+\xi X_2(\xi,\eta) \\ y(\xi,\eta) &= (1-\eta)Y_1(\xi,\eta)+\eta Y_2(\xi,\eta) \end{aligned} \tag{5.38}$$

where X_1 and Y_1 are points on one boundary while X_2 and Y_2 define the other boundary of a physical domain. The connections between the two opposite boundaries are produced here as straight lines, generally non-orthogonal to boundaries. This method gives a satisfactory mesh only for simple geometries and is not usually applicable to the rotor domains of screw machines except as the initial grid for further orthogonalisation and smoothing. On the other side, physical domains of a less complex shape can be successfully mapped, but orthogonality of the boundaries is generally not achieved. A numerical mesh generated by the transfinite interpolation method with LaGrange blending functions is presented in Figure 5-16. On the left side of the figure, the discharge port of a compressor is mapped (a), while on the right side a working chamber of 3/5 rotors is presented (b). The detail in the top left corner shows how the transition between the main domain and the clearances is mapped.

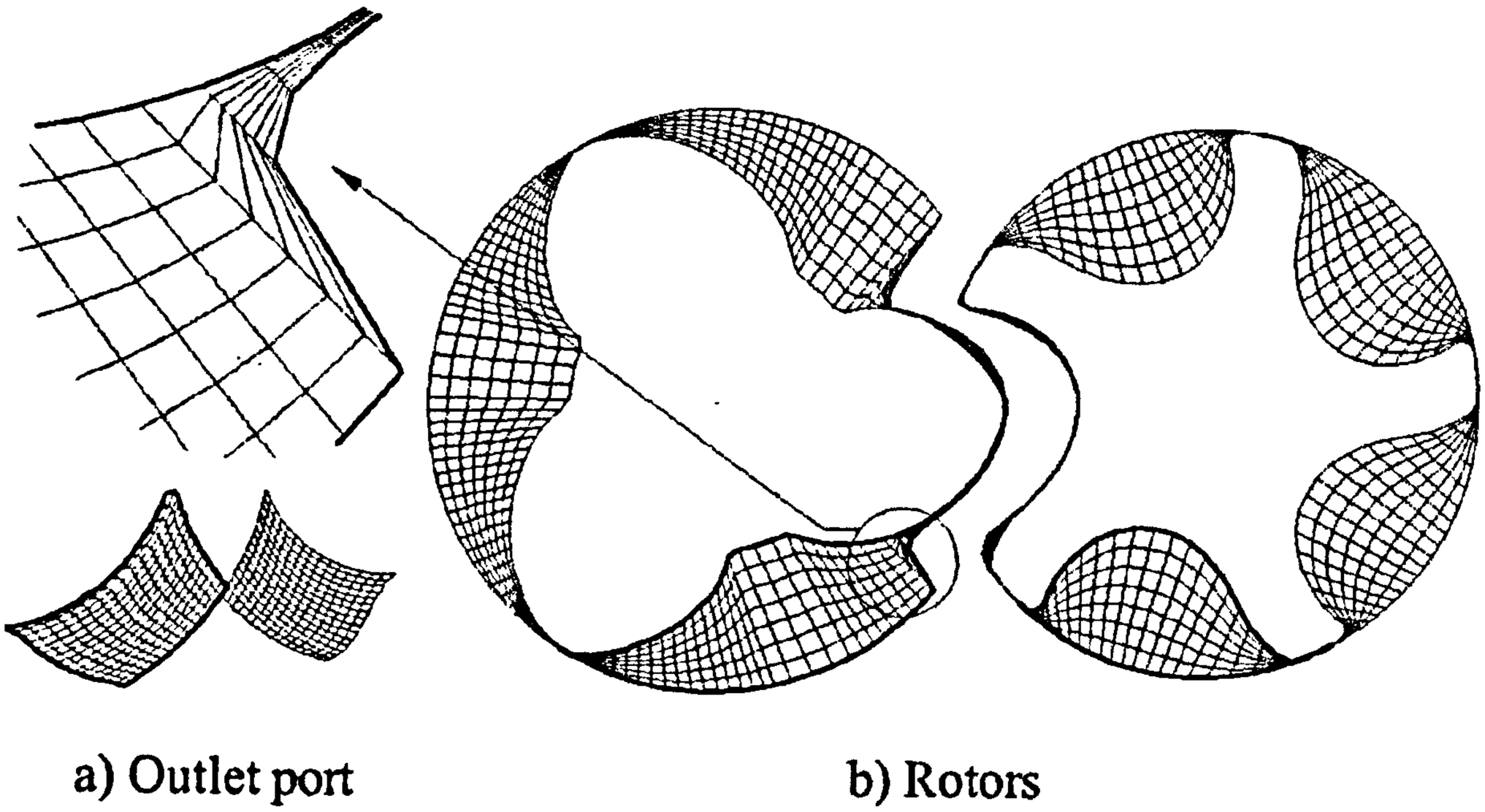

a) Outlet port b) Rotors

Figure 5-16 Numerical mesh generated by TFI using LaGrange blending function

5.4.2 Ortho transfinite interpolation

A better and more accurate solution can be obtained by applying a modified transfinite interpolation formula with Hermite blending functions. More details on this method can be found in *Smith* (1982), *Shih et al* (1991), and *Thomson et al* (1995). Equation (5.34) can be written in a more general form as:

$$\mathbf{r}_1(\xi,\eta)=\sum_{l=1}^{2}\sum_{n=0}^{1}\alpha_l^{n}(\xi)\mathbf{a}_l^{n}(\eta)$$

$$\mathbf{r}\,(\xi,\eta)=\mathbf{r}_1(\xi,\eta)+\sum_{l=1}^{2}\sum_{n=0}^{1}\beta_l^{n}(\eta)[\mathbf{b}_l^{n}(\xi)-\frac{\partial^n}{\partial\eta^n}\mathbf{r}_1(\xi,\eta_l)]\,, \tag{5.39}$$

Chawner and Anderson (1991) referred the previous equation as an Ortho transfinite interpolation formula. The representation of boundary points in this formula is given similarly to (5.33) but it includes the derivatives on the boundaries:

$$\mathbf{a}_l^{n}(\eta)=\frac{\partial^n}{\partial\xi^n}\mathbf{r}(\xi_l,\eta), \qquad l=1,2 \quad n=0,1$$
$$\mathbf{b}_l^{n}(\xi)=\frac{\partial^n}{\partial\eta^n}\mathbf{r}(\xi,\eta_l), \qquad l=1,2 \quad n=0,1 \tag{5.40}$$

The equation of the simple TFI (5.34) contains eight terms, four of which refer to edges and four to corners. On the other hand, the Ortho TFI (5.39) contains not only terms of coordinate data on four edges and four corners, but also their derivatives on four edges, two tangent vectors in each corner and a mixed derivative in each corner. This forms a combination of 24 terms. This means that a standard TFI formula (5.34) is a subset of the ortho TFI.

Cardinality conditions are consequently more complex for ortho methods because the conditions are imposed on the slope of the blending function as:

$$\frac{\partial^n}{\partial\xi^n}\alpha_l^{n}(\xi_k)=\delta_{kl}\delta_{nm}, \qquad k=1,2 \;\; l=1,2 \;\; n=0,1 \;\; m=0,1$$
$$\frac{\partial^n}{\partial\eta^n}\beta_l^{n}(\eta_k)=\delta_{kl}\delta_{nm}, \qquad k=1,2 \;\; l=1,2 \;\; n=0,1 \;\; m=0,1 \tag{5.41}$$

Indices l and k in equations (5.39) to (5.41) correspond to the boundary faces of the 2-D domain while the indices m and n indicate the domain corners.

Equation (5.39) applies to a two-dimensional domain. However, it can easily be applied to three dimensions if the coordinate z is added perpendicularly to the x-y plane and accounted for in the equation. Physical domains, which have to be mapped, can be classified either as a two-, four- or six- boundary mapping problem. In which group the problem is categorised depends not only on the dimensionality of the domain, but also on the characteristics of the boundaries. Examples are shown in Figure 5-17. Case a) is a two-boundary mapping problem where only two opposite boundaries in the y direction need to be mapped. In case b), all four boundaries must be mapped in order to preserve the regular boundary fitting. Case c) is a three-dimensional problem in which all six boundaries must be mapped, *Yang and Shish* (1986), *Shih et all* (1991). The geometry of the rotor domains in a screw machine can be regarded as 2½ dimensional. It is

because the rotors of a screw machine are generated from a profile which is revolved around its axis and moved along the same axis. In that case, the four boundary mapping method has to be applied at each of the 2-D cross sections, which are later connected to obtain a three dimensional mesh.

Figure 5-17 Classification of physical domains with respect to mapping requirements

5.4.2.1 Hermite blending functions

Contrary to the LaGrange blending functions used in the previous section, Hermite blending functions will be applied here to involve derivatives at the end curve points to enforce orthogonality at the boundaries. The blending functions are applied in a cubic form as:

$$\begin{aligned} \alpha_1^0 &= h_1(\eta) = 2\eta^3 - 3\eta^2 + 1, \qquad \alpha_1^1 = h_2(\eta) = -2\eta^3 + 3\eta^2 \\ \alpha_2^0 &= h_3(\eta) = \eta^3 - 2\eta^2 + \eta, \qquad \alpha_2^1 = h_4(\eta) = \eta^3 - \eta^2 \end{aligned}, \tag{5.42}$$

which satisfy cardinality conditions (5.41). The Hermite blending functions h_1 to h_4, defined by the previous equation, are now functions only of the computational coordinate η. Applying these functions to equation (5.39) for a two dimensional problem, one can easily get:

$$\begin{aligned} x'(\xi,\eta) &= X_1(\xi)h_1(\eta) + X_2(\xi)h_2(\eta) + \frac{\partial x(\xi,\eta_0)}{\partial \eta}h_3(\eta) + \frac{\partial x(\xi,\eta_1)}{\partial \eta}h_4(\eta) \\ y'(\xi,\eta) &= Y_1(\xi)h_1(\eta) + Y_2(\xi)h_2(\eta) + \frac{\partial y(\xi,\eta_0)}{\partial \eta}h_3(\eta) + \frac{\partial y(\xi,\eta_1)}{\partial \eta}h_4(\eta) \end{aligned}. \tag{5.43}$$

The values for computational coordinates at the start and end points in the previous equation are η_0=0 and η_1=1. The boundary points in the same equation are

$$\begin{aligned} X_1 &= x(\xi,\eta_0) = X_1(\xi) \qquad Y_1 = y(\xi,\eta_0) = Y_1(\xi) \\ X_2 &= x(\xi,\eta_1) = X_2(\xi) \qquad Y_2 = y(\xi,\eta_1) = Y_2(\xi) \end{aligned}. \tag{5.44}$$

Equations (5.43) represent a two-boundary method of transfinite interpolation procedure with Hermite blending functions for two-dimensional domains. The partial derivatives at the boundaries ensure orthogonality. These are:

$$\begin{aligned} \frac{\partial x(\xi,\eta_0)}{\partial \eta} &= K_1(\xi)(-\frac{\partial Y_1}{\partial \xi}) \qquad \frac{\partial x(\xi,\eta_1)}{\partial \eta} = K_2(\xi)(-\frac{\partial Y_2}{\partial \xi}) \\ \frac{\partial y(\xi,\eta_0)}{\partial \eta} &= -K_1(\xi)(-\frac{\partial X_1}{\partial \xi}) \qquad \frac{\partial y(\xi,\eta_1)}{\partial \eta} = -K_2(\xi)(-\frac{\partial X_2}{\partial \xi}) \end{aligned} \tag{5.45}$$

The coefficients K_1 and K_2 are positive numbers smaller than 1. They are usually chosen by a trial and error to avoid overlapping of connecting curves inside the domain.

The four-boundary method, which assumes interpolation between all four boundaries of the 2-D domain can be written in the following form:

$$\begin{aligned} x(\xi,\eta) &= x'(\xi,\eta) + \Delta x(\xi,\eta) \\ y(\xi,\eta) &= y'(\xi,\eta) + \Delta y(\xi,\eta) \end{aligned} \tag{5.46}$$

For this boundary method, two additional opposite boundaries must be mapped. These are:

$$\begin{aligned} X_3 &= x(\xi_0,\eta) = X_3(\eta),\ Y_3 = y(\xi_0,\eta) = Y_3(\eta) \\ X_4 &= x(\xi_1,\eta) = X_4(\eta),\ Y_4 = y(\xi_1,\eta) = Y_4(\eta) \end{aligned} \tag{5.47}$$

The first term in (5.46) is calculated in equation (5.43) while the second term defines a mapping between the other two boundaries as:

$$\begin{aligned} \Delta x(\xi,\eta) = (X_3 - X'_3)h_5(\xi) + (X_4 - X'_4)h_6(\xi) &+ \left(\frac{\partial x(\xi_0,\eta)}{\partial \xi} - \frac{\partial x'(\xi_0,\eta)}{\partial \xi}\right)h_7(\xi) \\ &+ \left(\frac{\partial x(\xi_1,\eta)}{\partial \xi} - \frac{\partial x'(\xi_1,\eta)}{\partial \xi}\right)h_8(\xi) \\ \Delta y(\xi,\eta) = (Y_3 - Y'_3)h_5(\xi) + (Y_4 - Y'_4)h_6(\xi) &+ \left(\frac{\partial y(\xi_0,\eta)}{\partial \xi} - \frac{\partial y'(\xi_0,\eta)}{\partial \xi}\right)h_7(\xi) \\ &+ \left(\frac{\partial y(\xi_1,\eta)}{\partial \xi} - \frac{\partial y'(\xi_1,\eta)}{\partial \xi}\right)h_8(\xi) \end{aligned} \tag{5.48}$$

The partial derivatives at the boundary points in equation (5.48) ensure that appropriate derivatives in the corners of the domain are accounted as part of the solution:

$$\frac{\partial x'(\xi_0,\eta)}{\partial \xi} = h_1(\eta)\frac{\partial x(\xi_0,\eta_0)}{\partial \xi} + h_2(\eta)\frac{\partial x(\xi_0,\eta_1)}{\partial \xi}$$
$$\frac{\partial x'(\xi_1,\eta)}{\partial \xi} = h_1(\eta)\frac{\partial x(\xi_1,\eta_0)}{\partial \xi} + h_2(\eta)\frac{\partial x(\xi_1,\eta_1)}{\partial \xi}$$
$$\frac{\partial y'(\xi_0,\eta)}{\partial \xi} = h_1(\eta)\frac{\partial y(\xi_0,\eta_0)}{\partial \xi} + h_2(\eta)\frac{\partial y(\xi_0,\eta_1)}{\partial \xi}, \qquad (5.49)$$
$$\frac{\partial y'(\xi_1,\eta)}{\partial \xi} = h_1(\eta)\frac{\partial x(\xi_1,\eta_0)}{\partial \xi} + h_2(\eta)\frac{\partial x(\xi_1,\eta_1)}{\partial \xi}$$

while the remaining partial derivatives in the same equation account for derivatives on two additional edges as:

$$\frac{\partial x(\xi_0,\eta)}{\partial \xi} = -K_3(\eta)(-\frac{\partial Y_3}{\partial \eta}) \qquad \frac{\partial x(\xi_1,\eta)}{\partial \xi} = -K_4(\eta)(-\frac{\partial Y_4}{\partial \eta})$$
$$\frac{\partial y(\xi_0,\eta)}{\partial \xi} = K_3(\eta)(-\frac{\partial X_3}{\partial \eta}) \qquad \frac{\partial y(\xi_1,\eta)}{\partial \xi} = K_4(\eta)(-\frac{\partial X_4}{\partial \eta}) \qquad (5.50)$$

The remaining Hermite factors are:

$$h_5 = 2\xi^3 - 3\xi^2 + 1, \qquad h_6 = -2\xi^3 + 3\xi^2$$
$$h_7 = \xi^3 - 2\xi^2 + \xi, \qquad h_8 = \xi^3 - \xi^2 \qquad (5.51)$$

The four-boundary Hermite interpolation method gives reasonably good distribution of internal points with the freedom to maintain the orthogonality and curvature on and near the boundaries. This method usually gives sufficiently good outcome for domains of the screw machine inlet and outlet ports. However, for the rotor domains of a screw machine, where the geometry changes rapidly, it sometimes causes the internal domain lines to overlap or even to exceed the boundaries. The intensity of that depends on the values selected for the coefficients K_1 to K_4. Figure 5-18 shows some domains as in Figure 5-16 but this time the four-boundary method for Ortho transfinite interpolation is used in combination with Hermite blending functions to generate the grid. On rotors, in the part where radial distance between the opposite sides changes rapidly, this method gives overlapping and even exceeding grid lines over the boundary lines. In other parts of the mesh, the result is sufficiently good and the internal lines are orthogonal to the boundaries. On the other hand, at the outlet port, which is significantly easier to map,

the resulting numerical mesh is regular, boundary fitted and boundary orthogonal. The numerical mesh for the rotor domains presented in this figure is generated with very low values of coefficients K_1 to K_4.

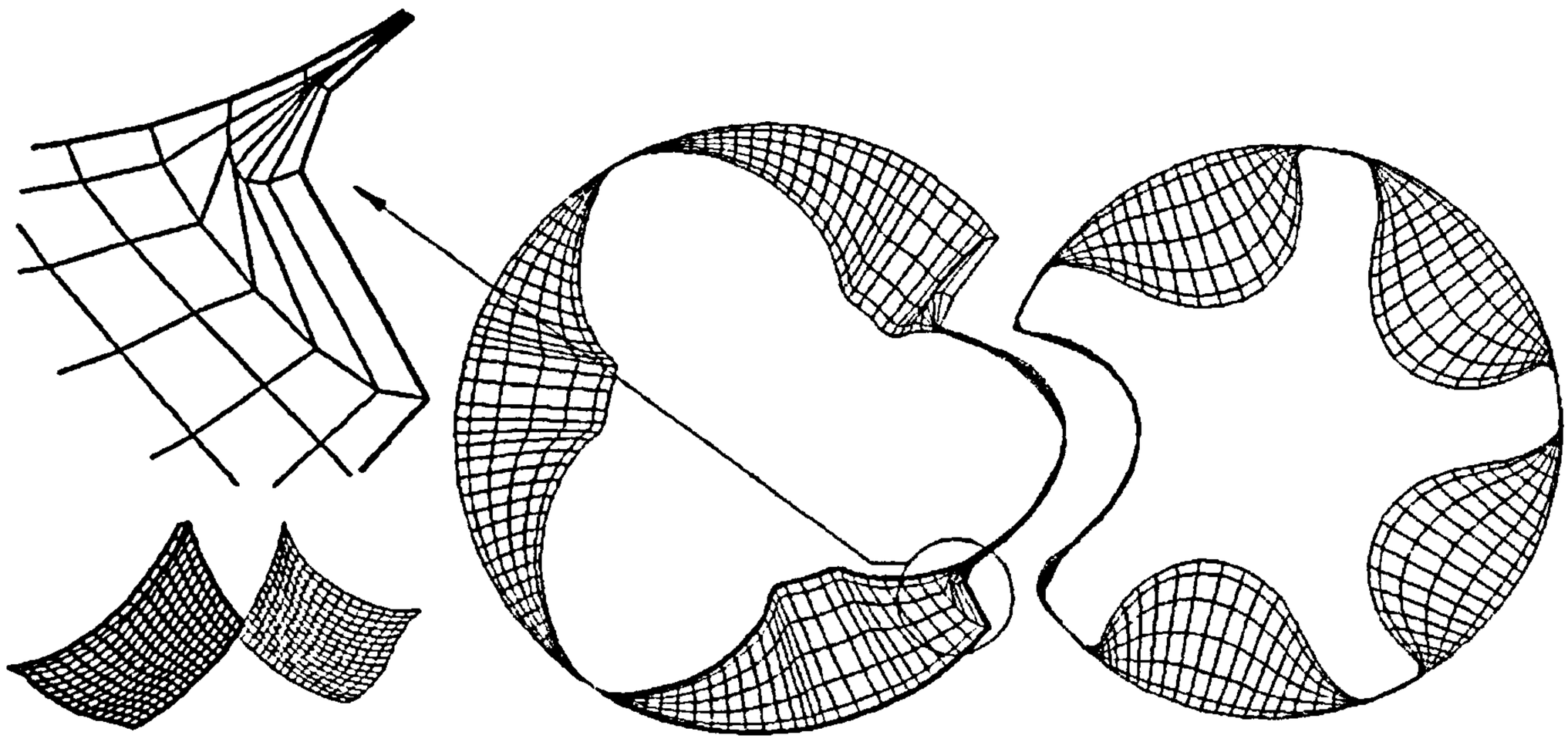

a) Outlet port b) Rotors

Figure 5-18 Numerical mesh generated by TFI using Hermite blending function

5.4.2.2 Multidimensional stretching functions

Algebraic methods presented in previous sections employ either LaGrange or Hermite blending functions to control the distribution of grid points in the physical domain. These functions are generated from one-dimensional stretching functions ξ and η with equal values for all grid lines through out the domain. This is a great limitation for application of TFI, *Thompson* (1985), *Shih et all* (1991). Therefore, for complex geometries an additional method is introduced based on the construction of multidimensional stretching functions as proposed by *Steinthorrsson et al (1992)*. A two-dimensional grid system with x and y coordinates in the physical domain and with coordinates ξ and η in the computational domain is analysed. In the transformed computational domain, coordinates ξ and η vary between zero and one as shown in Figure 5-15. Considering the coordinate ξ it is obvious that all points on boundaries ξ_o and ξ_1 affect the distribution of the inner points in that direction. The same situation

appears for the η coordinates. Therefore, two one-dimensional stretching functions in ξ direction can be identified for two opposite boundaries: $\hat{\xi}_0(\xi)$, $\hat{\xi}_1(\xi)$ for the points on $\eta=0$ and $\eta=1$ respectively. The edges of the computational domain are one-dimensional lines on which one-dimensional stretching functions can be easily obtained either by LaGrange (5.37) or by Hermite interpolation (5.51). In this study, the point distribution on the edges is known and therefore the stretching functions at the boundaries are known in advance.

Multidimensional stretching functions can be determined once the one-dimensional functions are selected. By application of the linear LaGrange interpolation, the following multidimensional function can be constructed:

$$\hat{\xi}(\xi,\eta)=\hat{\xi}_0(\xi)\cdot(1-\eta)+\hat{\xi}_1(\xi)\cdot\eta\,. \tag{5.52}$$

To improve the situation, cubic polynomials similar to Hermite interpolation factors can be used in order to produce multidimensional stretching functions of the following form:

$$\hat{\xi}(\xi,\eta)=\hat{\xi}_0(\xi)\cdot h_1(\eta)+\hat{\xi}_1(\xi)\cdot h_2(\eta)\,, \tag{5.53}$$

where coefficients h_1 and h_2 are obtained from equation (5.42). These coefficients can be functions not only of the computational coordinate η, but also they can be specified as a function of the arc-length of the newly calculated inner grid line, i.e. its natural coordinate, as:

$$h_1(s)=2s^3-3s^2+1,\quad h_2(s)=-2s^3+3s^2\,, \tag{5.54}$$

If the boundaries of the physical domain have to be mapped together with the inner points, then analytical stretching functions have to be calculated each time a boundary is mapped and then updated throughout the entire domain. However, if the boundary points are distributed on the edges in advance, the procedure looks significantly simpler because the natural coordinate s through its arc-length defines a stretching function directly. Based on that, the equivalent stretching functions can be defined as:

$$\hat{\xi}_0(\xi_i)=0 \qquad for \quad i=1$$
$$\hat{\xi}_0(\xi_i)=\frac{d_i}{d_L} \qquad for \quad i=2,3,...L \tag{5.55}$$

where

$$d_i=\sum_{n=2}^{i}\sqrt{(x_n-x_{n-1})^2+(y_n-y_{n-1})^2}\ , \tag{5.56}$$

and used to construct multidimensional stretching functions in (5.52) or (5.53).

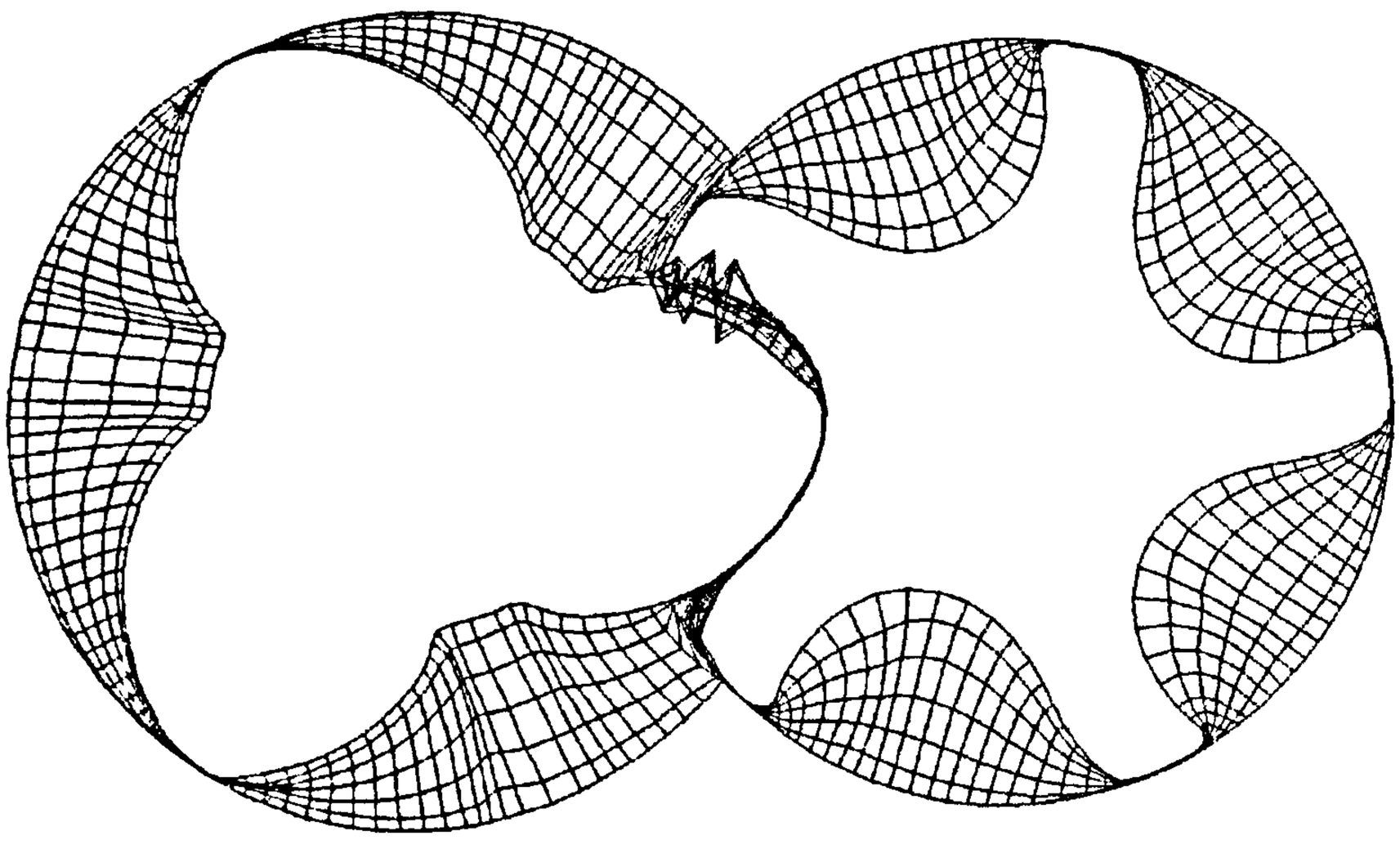

Figure 5-19 Numerical mesh generated with multidimensional stretching functions

(Error is magnified 100 times)

Similarly to ortho TFI, the method described above can be applied on all, one-, two- or three-boundary methods simply by replacing the one-dimensional stretching functions with the multidimensional stretching functions (5.53). This method often gives a satisfactory grid quality for complex systems and it is not too difficult to apply. However, in certain points of the mesh, where gradients of the cell size are extremely high, this method can produce instabilities and severe irregularities of the mesh, which is a consequence of attempts to keep the mesh orthogonal. The numerical mesh generated by this method is shown in Figure 5-19. Error is magnified 100 times to

become visible. The other parts of the mesh are mapped regularly with satisfactory control on orthogonality and smoothness. To use this method further, one must try to prevent unwanted oscillations. One of possibilities for that is described in the next section.

5.4.2.3 Blending functions based on a tension spline interpolation

Hermite transfinite interpolation based on cubic polynomials makes possible extensive skewness or overlap of the grid lines. This is the result of the use of *K*-factors in the equations for TFI. The reason is that *K* factors control the magnitude of the first-derivatives, which in turn control the curvature of the lines. The curvature of these lines is also affected by normal vectors on the edge. It is possible to correct these factors by implementing normalised boundary vectors as described in *Steinthorrsson et al* (1992). Although this approach is simple for a two-boundary method, it requires special attention in the case of a four-boundary method, because of the constraint on orthogonality in the interior and boundary points.

Similar control of the curvature of lines can be achieved if blending functions based on the tension spline interpolation are used instead of Hermite blending functions. The tension spline interpolation changes its nature with change in tension parameter σ which was first introduced by *Thompson et all* (1985).

To use blending functions based on tension spline interpolation, as proposed by *Steinthorrsson et al (1992),* the Hermite blending factors in equation (5.46) should be substituted by:

$$h_1(s)=c_1(1-s)+c_2 s+c_2\left[\frac{\sinh[(1-s)\sigma]-\sinh(s\sigma)}{\sinh(\sigma)}\right]$$

$$h_2(s)=c_1 s+c_2(1-s)-c_2\left[\frac{\sinh[(1-s)\sigma]-\sinh(s\sigma)}{\sinh(\sigma)}\right]$$

$$h_3(s)=c_3\left[(1-s)-\frac{\sinh[(1-s)\sigma]}{\sinh(\sigma)}\right]+c_4\left[s-\frac{\sinh(s\sigma)}{\sinh(\sigma)}\right] \quad , \qquad (5.57)$$

$$h_4(s)=-c_3\left[s-\frac{\sinh(s\sigma)}{\sinh(\sigma)}\right]-c_4\left[(1-s)-\frac{\sinh[(1-s)\sigma]}{\sinh(\sigma)}\right]$$

where the coefficients are defined as:

$$c_1=1-c_2, \qquad c_2=\frac{\sinh(\sigma)}{2\sinh(\sigma)-\sigma\ \cosh(\sigma)-\sigma}$$

$$c_3=\frac{-\alpha}{(\beta^2-\alpha^2)}\sinh(\sigma), \qquad c_4=\frac{\beta}{(\beta^2-\alpha^2)}\sinh(\sigma) \quad . \qquad (5.58)$$

$$\alpha=\sigma\cosh(\sigma)-\sinh(\sigma), \qquad \beta=\sinh(\sigma)-\sigma$$

The curvature of grid lines is now controlled by a tension parameter σ. If the tension parameter increases to infinity ($\sigma\to\infty$), blending functions based on the tension spline interpolation become linear i.e. $h_1(s)\to(1-s)$, $h_2(s)\to s$, $h_3(s)\to 0$ and $h_4(s)\to 0$. However, decrease in this factor to infinity ($\sigma\to 0$) causes the blending functions to become cubic polynomials. This feature gives a significant flexibility to the method. Therefore, equation (5.57) can be used to interpolate any function in the interval [0,1] of the computational coordinate if the function values and first derivatives are known at the end points of the interval. The flexibility of this method ensured is significant role in the grid generation of screw machines.

5.4.3 Simple unidirectional interpolation

There are many cases where the complex, time and space consuming approach presented in the previous section is not essential for achieving satisfactory meshes. This is especially true for regions of less-complex boundary shapes, when boundary orthogonalisation is required or for initial meshes for more complex domains. This is

the case of the outlet port or oil injection port, for example. The idea is to use a simple unidirectional interpolation instead of a TFI, as proposed by *Zhou* (1998). Interpolation is applied between two opposite, non-contacting boundaries of the two-dimensional domain. The method, although simple, can be easily compared with the two-boundary transfinite interpolation method (5.4.2.1) because its nature is originally two-dimensional. However, the same method can be applied to all four boundaries of the domain if the unidirectional interpolation is applied in turn on both pairs of boundaries.

Consider the case in Figure 5-15 in which a physical domain in the x-y coordinate system has to be mapped by use of a computational domain in the ξ-η coordinate system. Both the ξ and η coordinates of the computational domain vary between 0 and 1. An unidirectional interpolation in the following mathematical expression is applied to obtain the grid points of the physical domain:

$$\begin{aligned} x(\xi,\eta) &= x(\xi_0,\eta) + \beta_\xi\left[x(\xi_1,\eta) - x(\xi_0,\eta)\right] \\ y(\xi,\eta) &= y(\xi,\eta_0) + \beta_\eta\left[y(\xi,\eta_1) - y(\xi,\eta_0)\right] \end{aligned} \qquad (5.59)$$

The stretching functions β_ξ and β_η are defined by LaGrange interpolation as:

$$\begin{aligned} \beta_\xi &= (1-w_\eta)\alpha_1(\xi) + w_\eta\alpha_0(\xi) \\ \beta_\eta &= (1-w_\xi)\alpha_1(\eta) + w_\xi\alpha_0(\eta) \end{aligned} \qquad (5.60)$$

where w_ξ and w_η are weight functions of the appropriate coordinates and of the constant m. The aim of this constant is to control the effect of boundary stretching functions α_1 and α_0. The weight functions are:

$$w_\xi = \frac{(1-\xi)^m}{\xi^m + (1-\xi)^m}; \qquad w_\eta = \frac{(1-\eta)^m}{\eta^m + (1-\eta)^m}. \qquad (5.61)$$

The constant m in the above equations takes the values of 1, 2 or 3 which correspond to linear, quadratic and cubic transformation between the opposite boundaries respectively. Stretching functions on the boundaries, which are implemented in equation (5.60), are

calculated as a projection of the appropriate computational boundary on the x or y axis Which axis is used for the projection depends on difference obtained between the two end points on that boundary. If the difference between the end points on the original physical coordinate differs from zero, then that coordinate is used. The specification is given with:

$$\alpha_K(\xi)=\begin{cases}\dfrac{x(\xi,K)-x(0,K)}{x(1,K)-x(0,K)} & \text{if } \left[x(1,K)-x(0,K)\right]\neq 0\\ \dfrac{y(\xi,K)-y(0,K)}{y(1,K)-y(0,K)} & \text{if } \left[x(1,K)-x(0,K)\right]=0\end{cases} \qquad K=0,1 \qquad (5.62)$$

and

$$\alpha_K(\eta)=\begin{cases}\dfrac{y(K,\eta)-y(K,0)}{y(K,1)-y(K,0)} & \text{if } \left[y(K,1)-y(K,0)\right]\neq 0\\ \dfrac{x(K,\eta)-x(K,0)}{x(K,1)-x(K,0)} & \text{if } \left[y(K,1)-y(K,0)\right]=0\end{cases} \qquad K=0,1 \qquad (5.63)$$

Examples of use of the simple unidirectional interpolation are given in Figure 5-20.

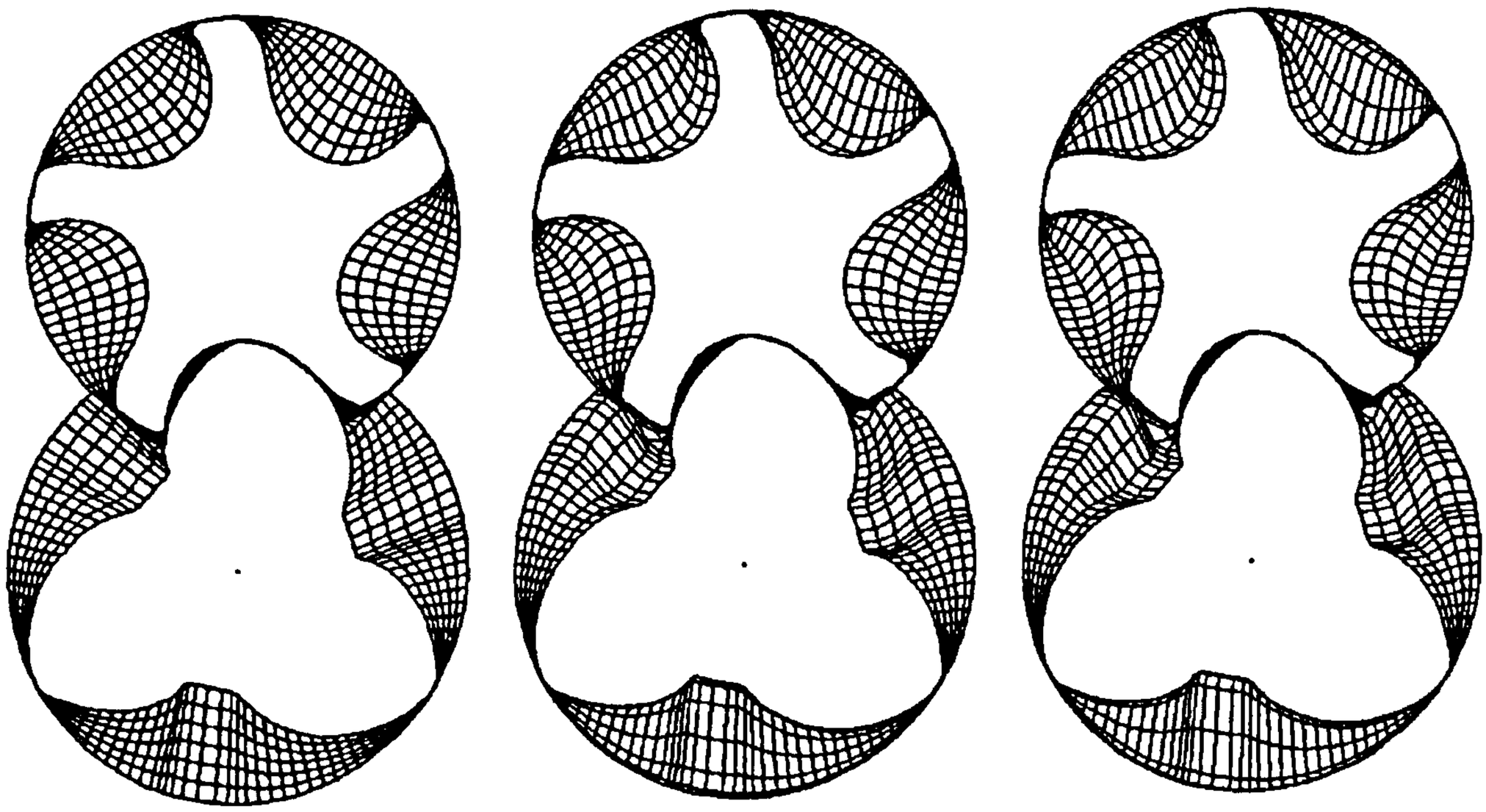

Figure 5-20 Numerical meshes generated by simple unidirectional interpolation

a) linear *b) quadratic* *c) cubic*

The use of the linear weight function is presented in Figure 5-20a. The final mesh is very similar to the one generated by a LaGrange TFI and even the effort required to obtain the result is almost the same. A quadratic weight function (Figure 5-20b) gives a better result for simple numerical meshes. However, for complex meshes it usually gives overlapping grid lines in regions where the mesh changes rapidly. More importantly, the generation of derivatives on boundaries depends on absolute position of the boundary in the physical domain. This cause unwanted and unphysical curvature of the inner grid lines. Therefore, it appears to be almost unacceptable for the generation of complicated screw compressor grids. A similar situation occurs with a cubic weight function (Figure 5-20c), which produces even higher uncertainties about the mesh.

5.4.4 Grid orthogonalization

By combination of the analytical grid generation methods mentioned above, one should generally be able to produce a satisfactory grid for the CFD analysis of screw machine flows. If this is not the case, as for rotors with a very small radius on the lobe tips, the orthogonalization and smoothing, together with the boundary adaptation already explained, must be applied. The approach to orthogonalization of a screw compressor grid is similar to one suggested by *Lehtimaki* (2000).

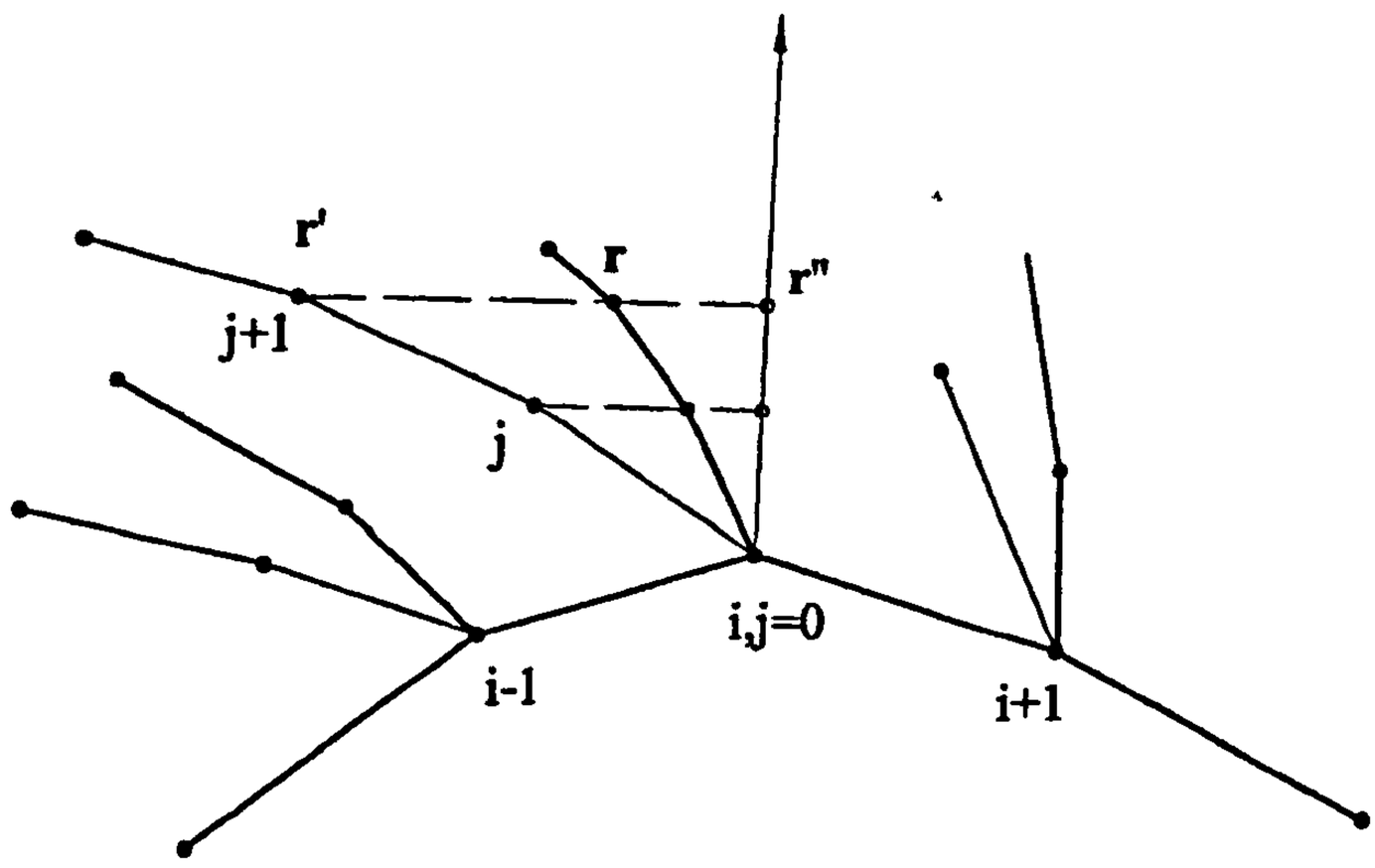

Figure 5-21 Orthogonalization to the boundary line j=0

Ortho TFI with Hermite blending factors provides inherent orthogonality properties. However, this is controlled by *K*-factors on boundaries which in certain cases lead to overlapping of the grid lines. The orthogonalization proposed here is, however, independent of the grid generation process and, therefore, can be performed on any grid generated in advance. This can lead to significant savings in the computational effort otherwise wasted in generation of an orthogonal grid. The method is based on the moving of computational point towards its orthogonal projection to the normal of the boundary (Figure 5-21).

The position of a numerical point in the physical domain, calculated by some algebraic grid generating method, which has to be orthogonalized, is given by vector $\mathbf{r}'_{i,j}$ while the perpendicular projection of that point to the normal of the boundary is $\mathbf{r}''_{i,j}$. A weighing factor between the original point $\mathbf{r}'_{i,j}$ and the projected point is applied to avoid overspecification caused by discrepancy between the two boundaries. The new point is therefore defined by its radius vector:

$$\mathbf{r}_{i,j} = (1 - w_{i,j})\mathbf{r}'_{i,j} + w_{i,j}\mathbf{r}''_{i,j} \tag{5.64}$$

The weighing factor has an exponential form:

$$w_{i,j} = \exp\left\{-C_1\left[\left(1 - \frac{\tilde{\eta}_{i,j}}{\tilde{\eta}_{i,j_{max}}}\right) - 1\right]\right\} \cdot \left[4\xi_{i,0}(1-\xi_{i,0})\right]^{C_2} \tag{5.65}$$

where $\tilde{\eta}_{i,j} = \sqrt{(\xi_{i,j} - \xi_{i,0})^2 + (\eta_{i,j} - \eta_{i,0})^2}$ are the arc-length values. The first term in the equation is used for the damping of the interior of the grid while the second affects the damping to the boundary line. Coefficients are provided to control the amount of damping. Both coefficients in equation (5.65) should have positive values. Higher values of C_1 make damping of the orthogonalization to the interior of the domain higher, while a higher C_2 reduces the region which is orthogonalized to the central part of the boundary. The intensity of orthogonalization is always damped to a certain level defined by the coefficients C_1 and C_2. It implies that the orthogonalization procedure

can be applied many times in succession. Each repetition though leads to further orthogonalization of the mesh.

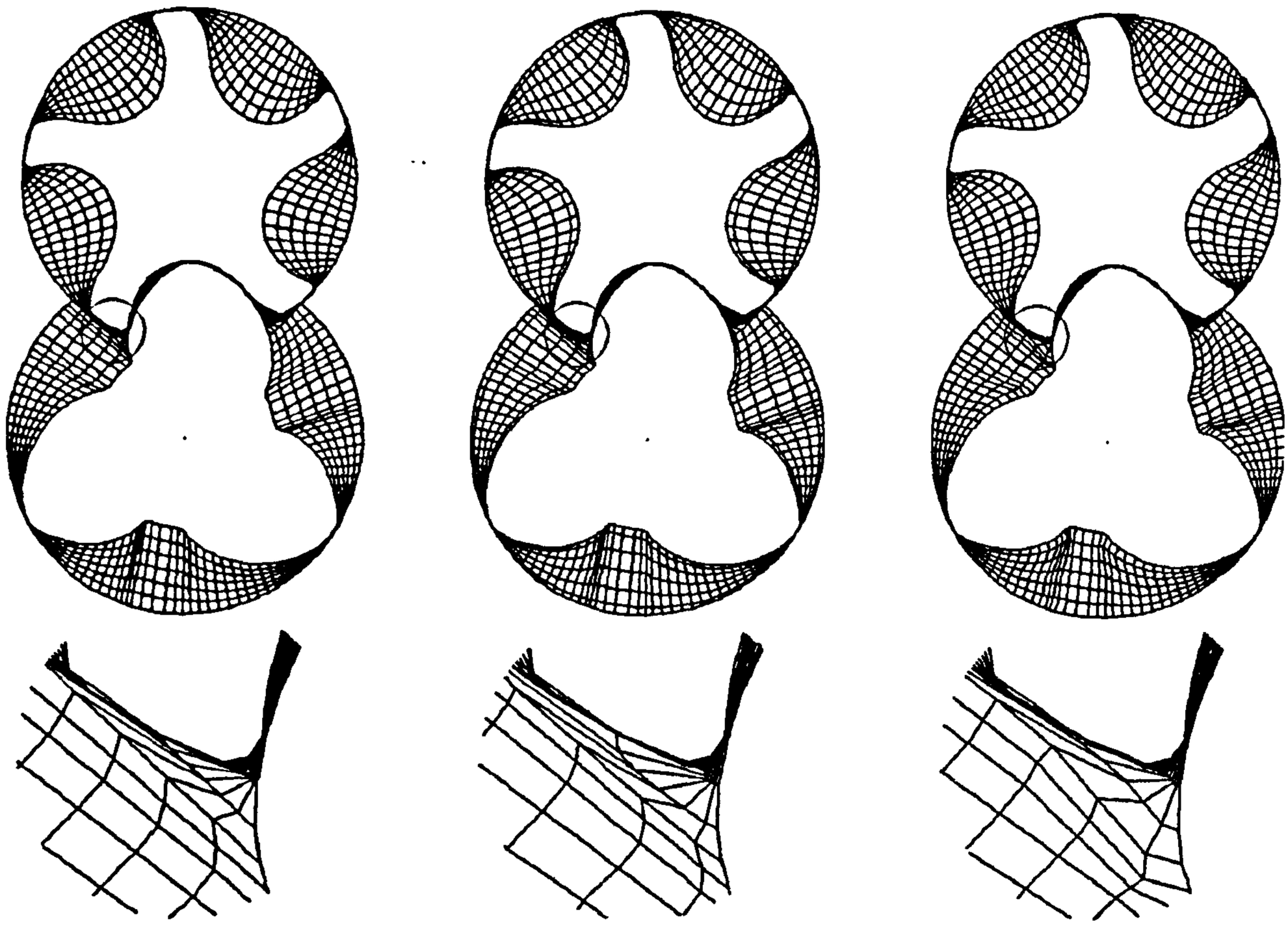

Figure 5-22 Comparison of different grid generation methods

a) LaGrange Standard TFI b) Hermite Ortho TFI c) Orthogonalization

Three numerical meshes are compared in Figure 5-22. Case a) is a standard TFI with LaGrange blending functions which gives a regular but non-orthogonal mesh. This mesh is later used as the basis for the orthogonalization process. The middle case b) is Ortho TFI with Hermite blending functions. The K factors are set to 0.2 to avoid overlapping of grid lines. Therefore, the lines in the main domain tend to be linear, while in the clearance gaps these become more curved but often not properly controlled. In the third case c), the mesh generated by standard TFI (case a) is additionally orthogonalized. The result achieved by orthogonalization in c) is better than both the previous cases. Although the damping of orthogonalization of grid lines is set to be high, the mesh is orthogonal in both the main domains and the gaps. The mesh is more consistent, and regular with lower values of aspect and expansion ratios (5.1.3) than in both the previous cases.

Because of it's obvious advantages, this method is applied whenever possible for the generation of the final mesh used for the finite volume calculation of fluid flow in screw machinery. It can be even further improved by smoothing the numerical mesh which is described in the next section.

5.4.5 Grid smoothing

Discontinuities which appear at the mesh boundary, despite the mesh being orthogonalised, propagate in the interior of the domain causing cells along these lines to remain non orthogonal. The problem can be conveniently solved by introducing a smoothing procedure. The following formula is among easiest to apply:

$$\begin{aligned} x_{i,j}^{n+1} &= x_{i,j}^{n} + C\left(x_{i+1,j}^{n} - 2x_{i,j}^{n} + x_{i-1,j}^{n}\right) \\ y_{i,j}^{n+1} &= y_{i,j}^{n} + C\left(y_{i+1,j}^{n} - 2y_{i,j}^{n} + y_{i-1,j}^{n}\right) \end{aligned} \tag{5.66}$$

where C is constant and n=0,1,2, …,N is the number of repetitions. This constant must satisfy condition $C \leq 0.5$ to preserve the stability of the method. Equation (5.66) can be repeatedly applied as many times as required to obtain a smooth grid. However, its use can affect orthogonality on the boundaries and, therefore, it must be used with care. The difference between a mesh for which the smoothing is not applied (left) and a smooth grid is shown in Figure 5-23.

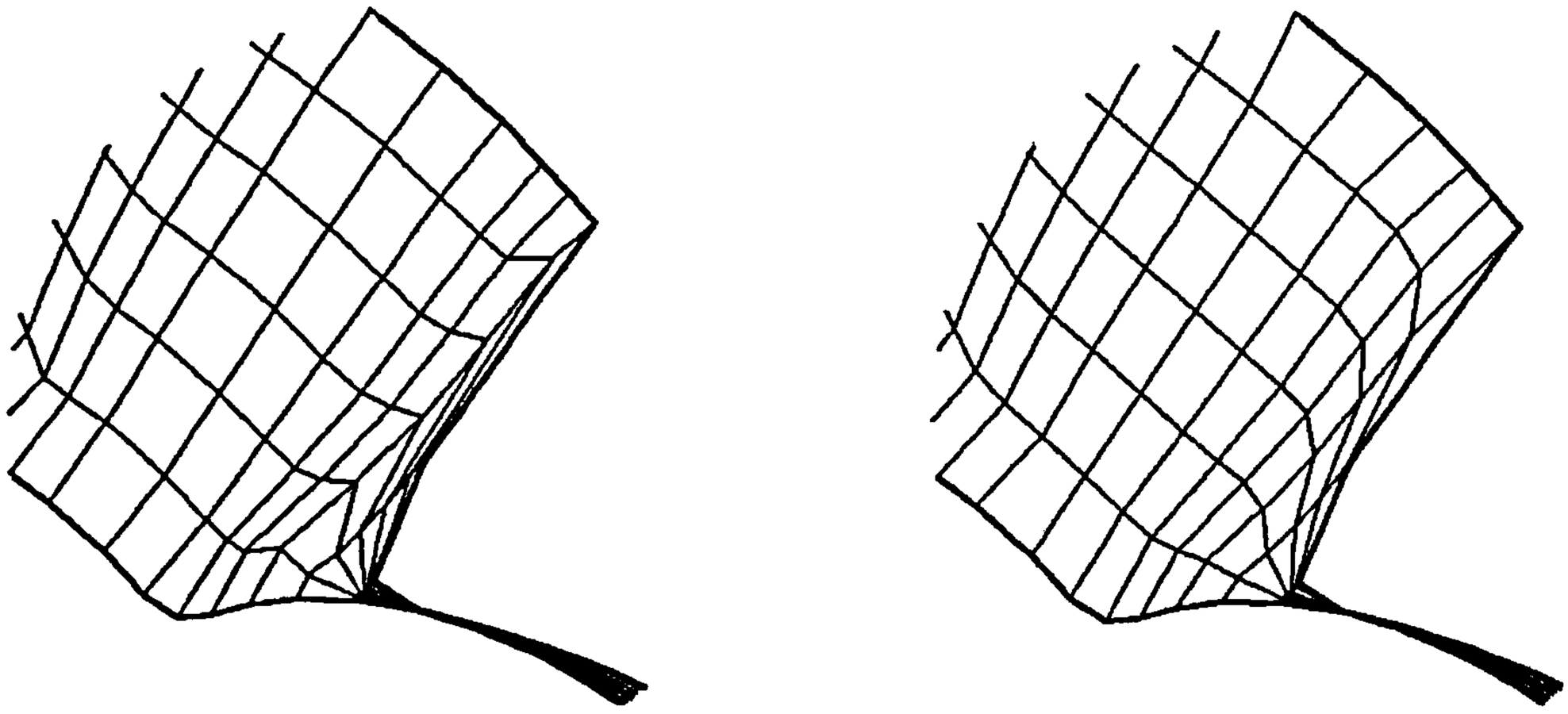

Figure 5-23 Application of smoothing function

left – orthogonal non smooth mesh; right – smooth mesh

5.4.6 Moving Grid

A numerical mesh generated by methods presented previously consists of vertex, cell and region definitions. Each vertex is uniquely defined by its coordinate in the absolute coordinate system:

$$\mathbf{r}_i = \mathbf{r}_i(x, y, z, \tau), \tag{5.67}$$

and the vertex number V_i. Control volumes, i.e. computational cells are generally hexahedrae defined by eight vertices. These can also be deformed by merging vertices, Figure 5-9.

Rotor movement in a screw machine is a rotation around the rotor axis. Male and female rotors rotate in opposite directions to each other at angular speeds proportional to the number of lobes z_1/z_2.

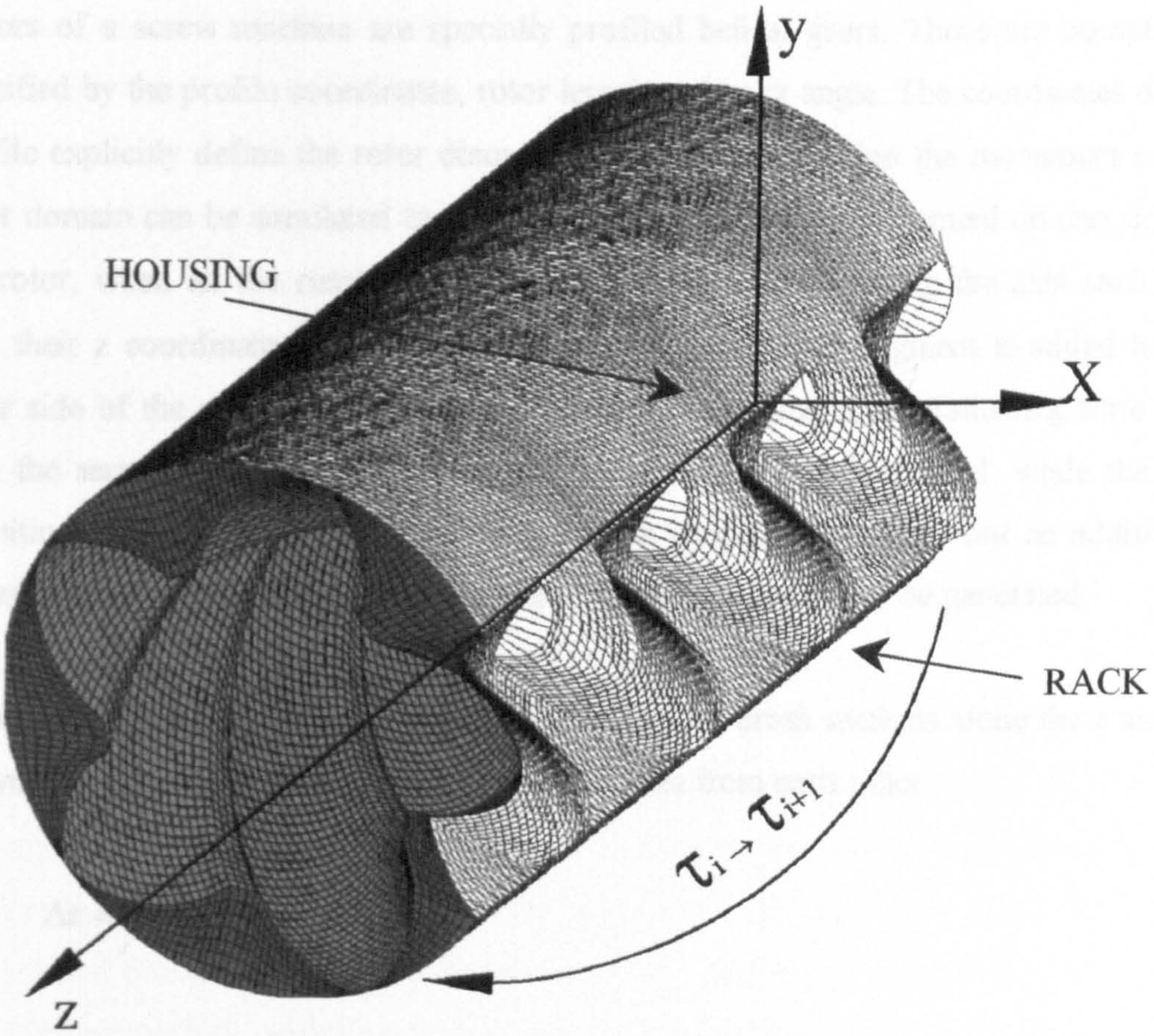

Figure 5-24 Moving strategy for screw machine numerical mesh

To simulate rotation of the rotors by movement of the numerical mesh, one has only to define a new vertex position before the calculation for each time step start. By this means, the cells are moved and deformed without any redefinition other than specifying new vertices positions. Although the inner boundary of the mesh, which belongs to a rotor, rotates around the axis, the other one, represented by the rack and housing does not rotate. The imaginary rack plane used to divide the working chamber of the screw machine rotors in two parts is visible on the main rotor domain in Figure 5-24. It is connected to the housing bore of the machine along a straight line where the bores of the male and female rotors connect. The rack plane moves translatory with speed of the male rotor tip. However, the other part of the same boundary, which represents the machine housing, rotates at the same angular speed as the rotor. Therefore, a complex combination of rotation and translation of the outer boundary has to be performed. It seems almost impossible to do that without disturbing the consistency of the mesh. Therefore, another approach is used.

Rotors of a screw machine are specially profiled helical gears. These are completely specified by the profile coordinates, rotor length and helix angle. The coordinates of the profile explicitly define the rotor diameter. One can imagine that the movement of the rotor domain can be simulated by removing a last cross section segment on one side of the rotor, when all the remaining vertices are moved axially along the axis such that only their z coordinate is changed and finally an appropriate segment is added to the other side of the rotor. By this means, the rotor is mapped in the following time step with the same number of vertices whose positions are only redefined, while the cell definitions remain unchanged. This procedure is simple and reliable but an additional file with vertices with an extended number of cross sections has to be generated.

In Figure 5-24 a mesh which consists of a number of cross sections along the z axis is shown. Cross sections are defined at equal distances from each other

$$\Delta z = L / z_1 n_{lobe},$$

where L is rotor length, z_1 is number of teeth on the male rotor and n_{lobe} is a number of cross sections for one interlobe distance on z axis. By this means, a cell length in the axial direction is specified as constant for all the cells in the domain. This has great advantages for the grid movement, but its weak point is that the time step and machine rotational speed are directly coupled. To show that, a unit angle is defined as

$$\delta\alpha = \frac{\phi_h}{z_1 n_{lobe}}, \tag{5.68}$$

which defines rotation between the two time steps, while the time step is

$$\delta t = \frac{60\,\delta\alpha}{2\pi n}, \tag{5.69}$$

where n is speed of rotation, (rpm). Therefore, the time step is inversely proportional to the speed of rotation. That in turn means that one has to change the numerical mesh in order to keep the ratio of time and spatial step constant. It's not always essential to keep

the ratio constant but it is certainly limited by Courant stability conditions which give a maximum allowed ratio of time and spatial discretisation as:

$$\frac{|u \pm c|\Delta t}{\Delta x} < \alpha_c \tag{5.70}$$

where c is the sound speed and α_c is a parameter which depends on the particular time advanced method used , *Ferziger and Perić* (1995).

5.5 COMPUTER PROGRAM

The procedures described in this chapter have been employed to form a stand alone CAD-CFD interface to generate a 3-D mesh of a screw machine working domain. The interface program is written in Fortran and is named SCORG, which stands for Screw COmpressor Rotor Geometry grid generator. The program calculates a numerical mesh for a screw machine based on given rack or rotor curves, by means of boundary adaptation and transfinite interpolation for all domains within the screw machine. These are: the working chamber, which surrounds the rotors and is divided into two parts of which one belongs to each male and female rotor, the inlet and outlet ports and other openings which may be pre-specified, like an oil injection port, or specified by an user program.

Transfer files to a numerical solver are given in ASCII format. Separate files are produced for a node, cell and region definitions for each domain of screw machine geometry. The transfer files also contain user subroutines for a numerical solver. These specify the initial and boundary conditions, the grid movement, the control parameters and the post-processing functions. The interface files are imported into a commercial CFD package through its pre-processor.

Full details of the structure of SCORG are given in Appendix VI

5.6 CLOSURE

The grid generation procedure for a screw machine working domain is derived in this Chapter. The procedure uses pre-specified rack coordinates and a few other parameters to generate a fully structured hexahedral, block oriented numerical mesh, which includes working chambers around rotors, suction and discharge ports and other openings that may be attached to the machine domain. The prerequisite for successful grid generation is the regular initial distribution of points along the boundaries. This is achieved by a two-parameter static adaptation method derived specially for screw machine rotors from an idea obtained from algebraic dynamical grid adaptation. No record of a similar procedure previously used for any application in grid generation has been found in the open literature available to the author. The second boundary of a screw machine domain is mapped from the first one by transformation methodology, which is also specially derived for the generation of a screw machine and has not yet been found published. It allows a regular distribution of boundary nodes in complex domains. This has not been achieved by any other method to which the author had access. These, together with the successful novel application of the combined transfinite interpolation, orthogonalization and smoothing methods are, in authors opinion, the main contributions of the thesis.

The computer program is developed based on the proposed methodology, written in FORTRAN and available for all windows and unix oriented machines. It automatically generates files which contain the node, cell and region specifications as well as user subroutines for a general CFD solver of a finite volume type. The method and program have been tested on the commercial CFD solver COMET, with which good simulations of positive displacement screw machines were obtained.

Chapter 6

Applications

6.1 INTRODUCTION

This chapter demonstrates the scope of the method developed for three-dimensional analysis of screw compressor. Based on that method, the stand alone program SCORG is made to produce and transfer data of numerical mesh and working parameters to a general CFD numerical solver. The CFD package used in this case was COMET developed by ICCM gmbh from Hamburg. The analysis of the flow and performance characteristics of a number of types of screw machines is performed to demonstrate a variety of parameters used for grid generation and calculation.

The first example is concerned with dry air screw compressor. A common compressor casing is used with two alternative pairs of rotors. The rotors have identical overall geometric properties but different lobe profiles. The application of adaptation technique enables convenient grid generation for geometrically different rotors. The results obtained by three dimensional modelling are compared with those derived from a one-dimensional model, previously verified by comparison with experimental data. The relative advantages of each rotor profile are demonstrated.

The second example shows the application of three dimensional flow analysis to the simulation of an oil injected air compressor. The results, thus obtained, are compared with test results obtained by the author from a compressor and test rig, designed and built at City University. They are presented in the form of both integral parameters and a p-α indicator diagram. Calculations based on the assumptions of the laminar flow are compared to those of turbulent flow. The effect of grid size on the results is also considered and shown here.

The third example gives the analysis of an oil injected compressor in an ammonia refrigeration plant. This utilises the real fluid property subroutines in the process calculations and demonstrates the blow hole area and the leakage flow through the compressor clearances.

6.2 EXAMPLE 1; FLOW IN A DRY AIR SCREW COMPRESSOR

Dry compressors are commonly used to produce pressurised air, free of any oil. A typical example of such a machine, similar in configuration to the compressor modelled, is shown in Figure 6-1. This is a single stage machine with 4 male and 6 female rotor lobes. The male and female rotor outer diameters are 142.380 mm and 135.820 mm respectively, while their centre lines are 108.4 mm apart. The rotor length to main diameter ratio l/d=1.77. Thus, the rotor length is 252.0 mm. The male rotor with wrap angle α_w=248.4^0 is driven at a speed of 6000 rpm by an electric motor through a gearbox. The male and female rotors are synchronised through timing gears with the same ratio as that of the compressor rotor lobes i.e. 1.5. The female rotor speed is therefore 4000 rpm. The male rotor tip speed is then 44.7m/s, which is a moderate value for a dry air compressor. The working chamber is sealed from its bearings by a combination of lip and labyrinth seals.

Each rotor is supported by one radial and one axial bearing, on the discharge end, and one radial bearing on the suction end of the compressor. The bearings are loaded by a high frequency force, which varies due to the pressure change within the working

high frequency force, which varies due to the pressure change within the working chamber. Both radial and axial forces, as well as the torque, on both compressors change with a frequency of 4 times the rotational speed. This corresponds to 400Hz and coincides with the number of working cycles that occur within the compressor per unit time.

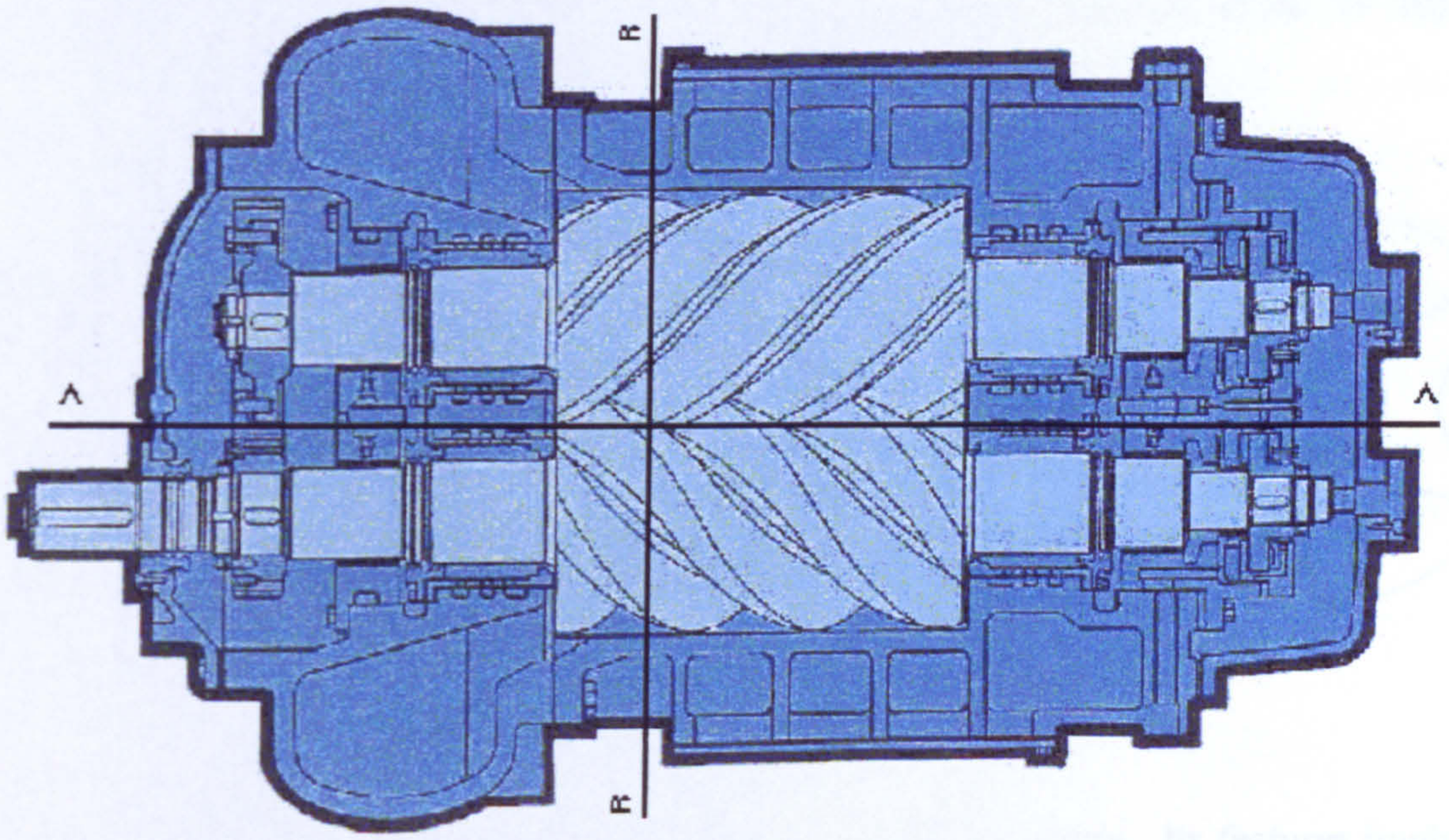

Figure 6-1 Cross section of a dry screw compressor

The compressor takes in air from the atmosphere and discharges it to a receiver at a constant output pressure of 3 bar. Although the pressure rise is moderate, leakage through radial gaps of 150 μm are substantial. In many studies and modelling procedures, volumetric losses are assumed to be a linear function of the cross sectional area and the pressure difference, assuming that the interlobe clearance is kept more or less constant by the synchronising gears. The leakage through the clearances is then proportional to the clearance gap and the length of the leakage line. However, a large clearance gap is needed to prevent contact with the housing caused by rotor deformation due to the pressure and temperature changes within the working chamber. Hence, the only way to reduce leakage is to minimise the length of the sealing line. This can be achieved by careful design of the screw rotor profile. Although minimising leakage is an important means of improving a screw compressor efficiency, it is not the only one. Another is to increase the flow area between the lobes and thereby increase the compressor flow capacity, thereby reducing the relative effect of leakage. Modern

optimisation procedures which lead to enlargement of the male rotor interlobes and reduction in the female rotor lobes. The female rotor lobes are thereby strengthened and their deformation thus reduced.

To demonstrate the improvements possible from rotor profile optimisation, a three dimensional flow analysis has been carried out for two different rotor profiles within the same compressor casing, as shown in Figure 6-2. Both rotors are of the "N" type and rack generated.

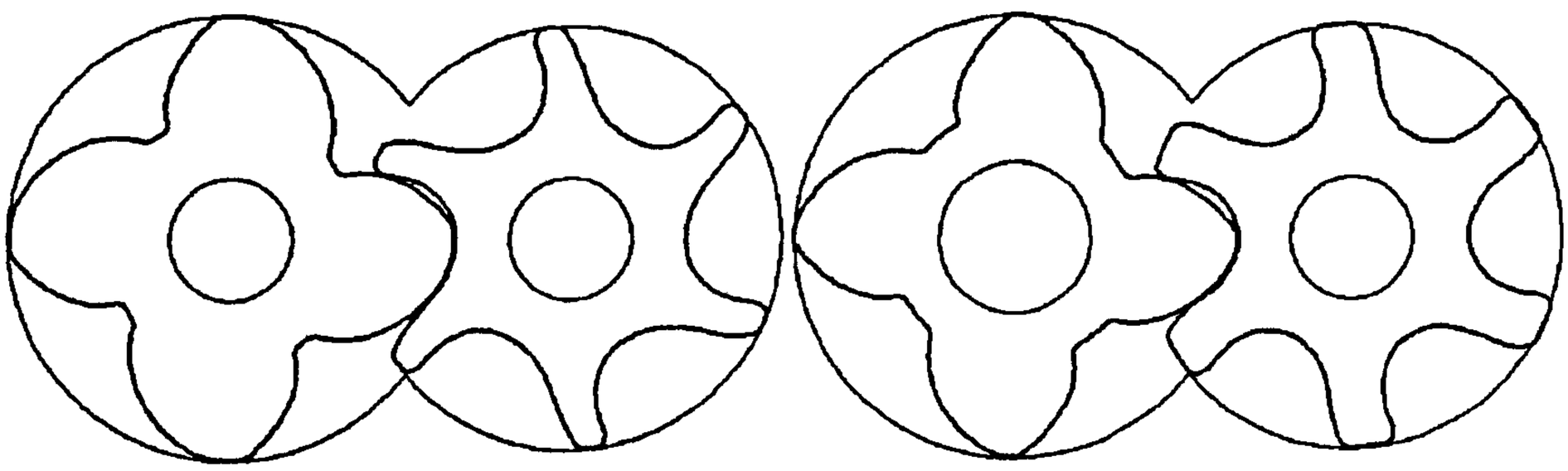

Figure 6-2 'N' Rotors, Case-1 left, Case-2 right

Case 1 is an older design, similar in shape to SRM "D" rotors. Its features imply that there is a large torque on the female rotor, the sealing line is relatively long and the female lobes are relatively weak.

Case 2, shown on the right of Figure 6-2, has rotors optimised for operating on dry air. The female rotor is stronger and the male rotor is weaker. This results in higher delivery, a shorter sealing line and less torque on the female rotor. All these features help to improve screw compressor performance.

The results of these two analyses are presented in the form of velocity distributions in the planes defined by cross-sections A-A and B-B, shown in Figure 6-1.

In the case of this study, the effect of rotor profile changes on compressor integral performance parameters can be predicted fairly accurately with one-dimensional models, even if some of the detailed assumptions made in such analytical models are

inaccurate. Hence the integral results obtained from the three-dimensional analysis are compared with those from a one-dimensional model.

6.2.1 Grid generation

In Case-1, the rotors are mapped with 52 numerical cells along the interlobe on the male rotor and 36 cells along each interlobe on the female rotor in the circumferential direction. This gives 208 and 216 numerical cells respectively in the circumferential direction for the male and female rotors. A total of 6 cells in the radial direction and 97 cells in the axial direction is specified for both rotors. This arrangement results in a numerical mesh with 327090 cells for the entire machine. The cross section for the Case-1 rotors is shown in Figure 6-3. The female rotor is relatively thin and has a large radius on the lobe tip. Therefore, it is more easily mapped then Case-2 which has a smaller tip radius, as shown in Figure 6-4.

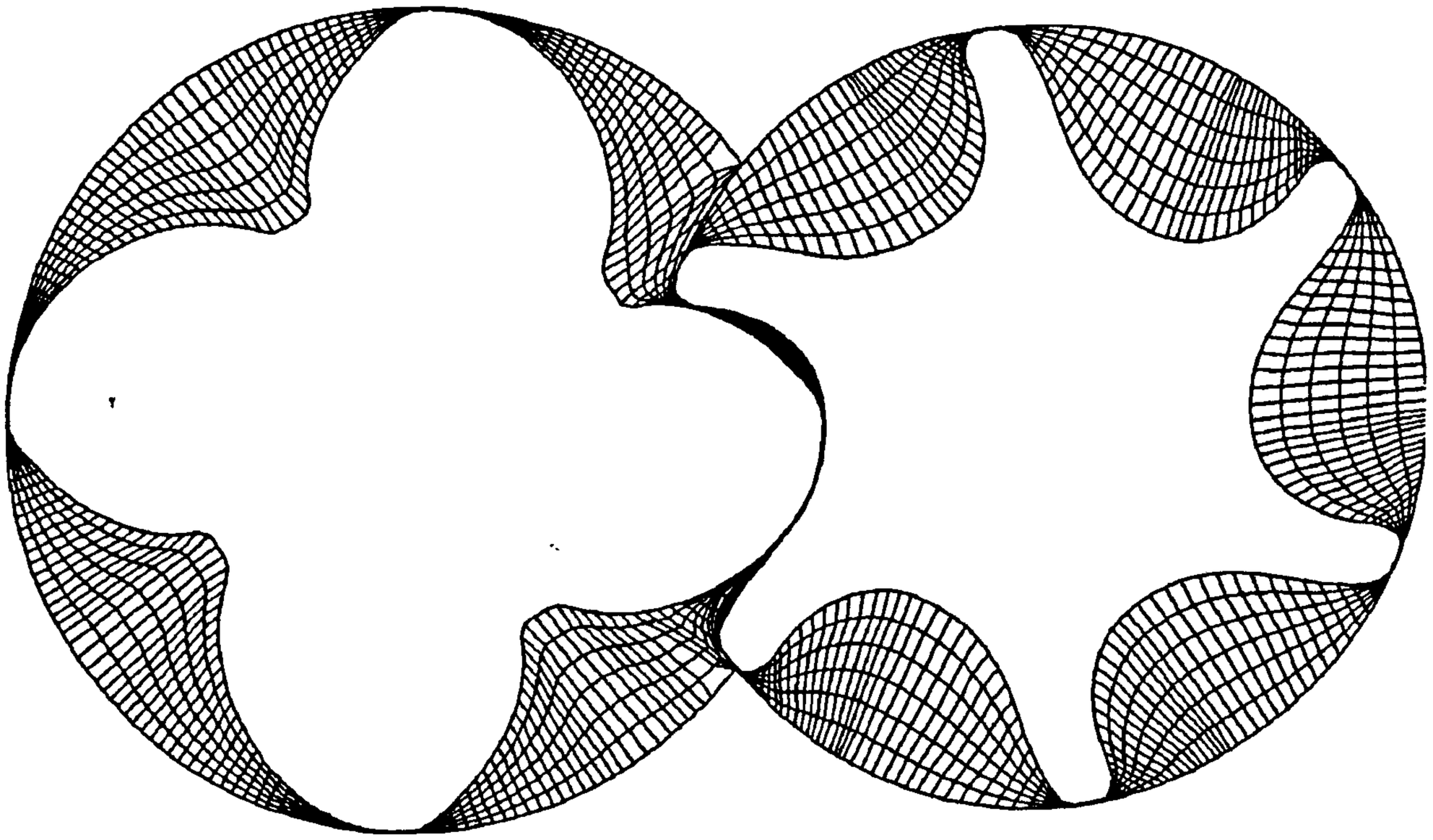

Figure 6-3 Cross section through the numerical mesh for Case-1 rotors

The rotors in Case 2 are mapped with 60 cells along the male rotor lobe and 40 cells along the female lobe, which gives 240 cells along both rotors in the circumferential direction. In the radial direction, the rotors are mapped with 6 cells while 111 cells are

selected for mapping along the rotor axis. Thus, entire working chamber for this compressor has 406570 cells. In this case, different mesh sizes are applied and different criteria are chosen for the boundary adaptation of these rotors. The main adaptation criterion selected for the rotors is the local radius curvature with a grid point ratio of 0.3 to obtain the desired quality of distribution along the rotor boundaries. By this means, the more curved rotors are mapped with only a slight increase in the grid size to obtain a reasonable value of the grid aspect ratio. To obtain a similar grid aspect ratio without adaptation, 85 cells would have been required instead of 60 along one interlobe on the female rotor. This would give 510 cells in the circumferential direction on each of rotors. If the number of cells in the radial direction is also increased to be 8 instead of 6 but the number of cells along axis is kept constant, the entire grid would contain more then a million cells which would, in turn, result in a significantly longer calculation time and increased requirements of computer memory.

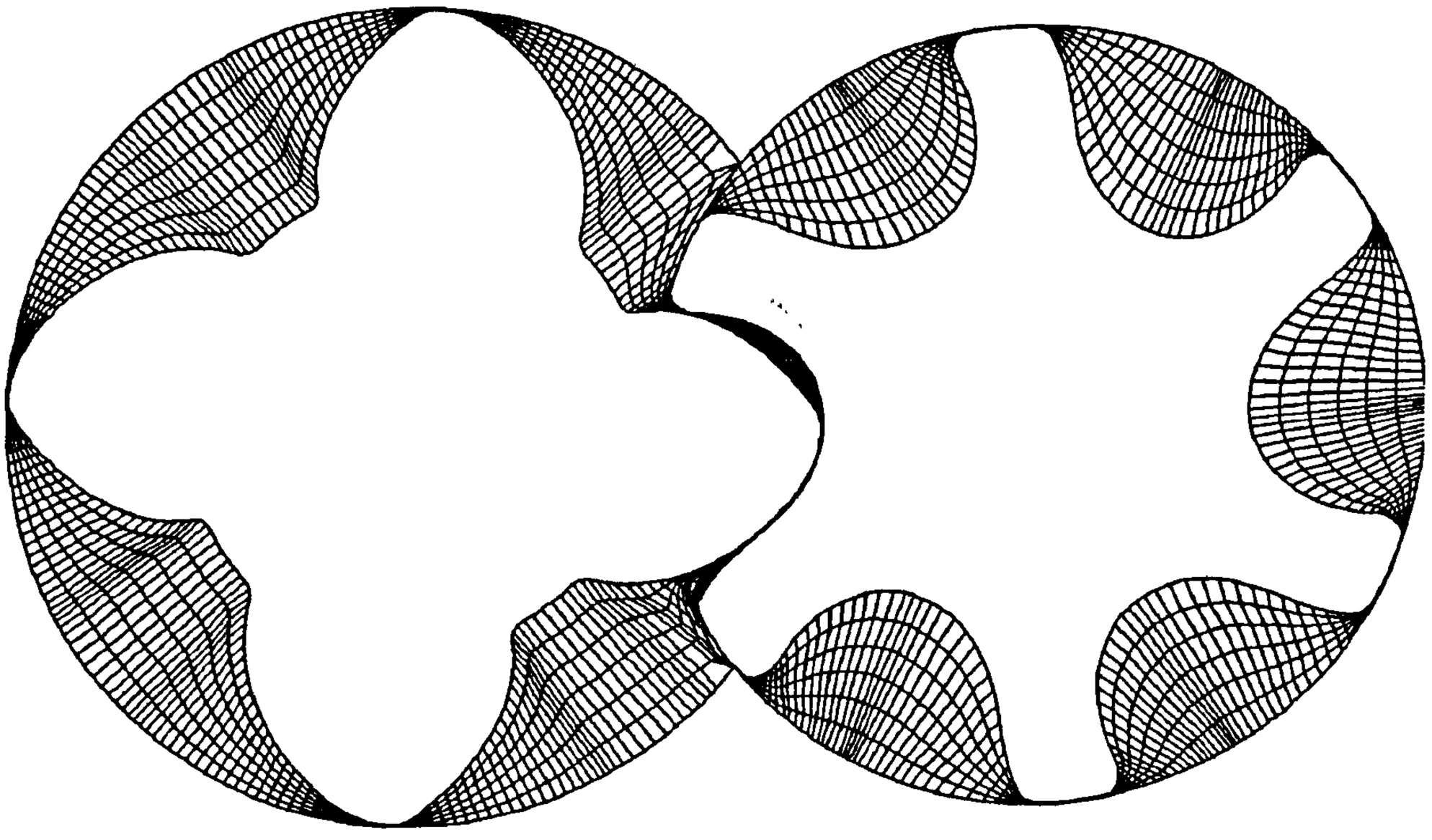

Figure 6-4 Cross section through the numerical mesh for Case-2 rotors

6.2.2 Mathematical model

The mathematical model used is based on the momentum, energy and mass conservation equations as given in Chapter 4. The equation for space law conservation

is calculated in the model in order to obtain cell face velocities caused by the mesh movement. The system of equations is closed by Stoke's, Fourier's and Fick's laws and the equation of state for an ideal gas. This define all the properties needed for solution of the governing equations.

6.2.3 Comparison of the fluid flow calculations for two different rotor profiles

Results are obtained for both, Case 1 and Case 2 compressors and presented here. To establish a full range of working conditions and to obtain an increase of pressure from 1 to 3 bars between the compressor suction and discharge, 15 time steps were required. A further 25 time steps were then needed to complete the full compressor cycle. Each time step needed about 30 minutes running time on an 800 MHz AMD Athlon processor. The computer memory required was about 400 MB.

In Figure 6-5 the velocity vectors in the cross and axial sections are compared. The top diagram is given for Case-1 rotors and the bottom one for Case-2. As may be seen, the Case 2 rotors caused a smoother velocity distribution than the Case 1 rotors. This may have some advantage and could have increased the compressor adiabatic efficiency by reduction in flow drag losses. In both cases, recirculation within the entrapped working chamber occurs as consequence of the drag forces in the air as shown in the figure. On the other hand, in the suction port different fluid flow patterns can be observed. The velocities within all, the working chambers, the suction and discharge ports are kept relatively low while the flow through the clearances changes rapidly and easily reaches sonic velocity.

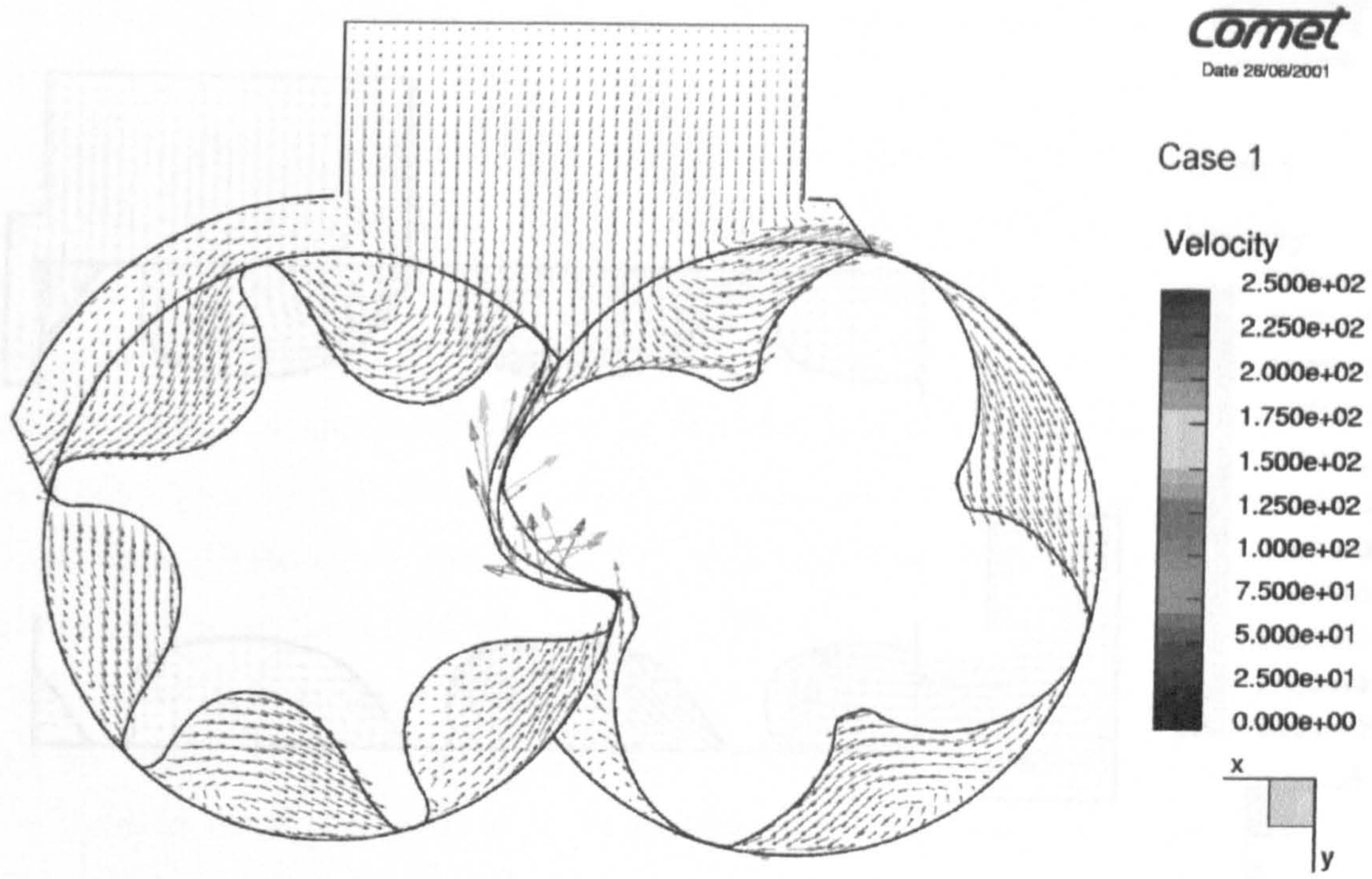

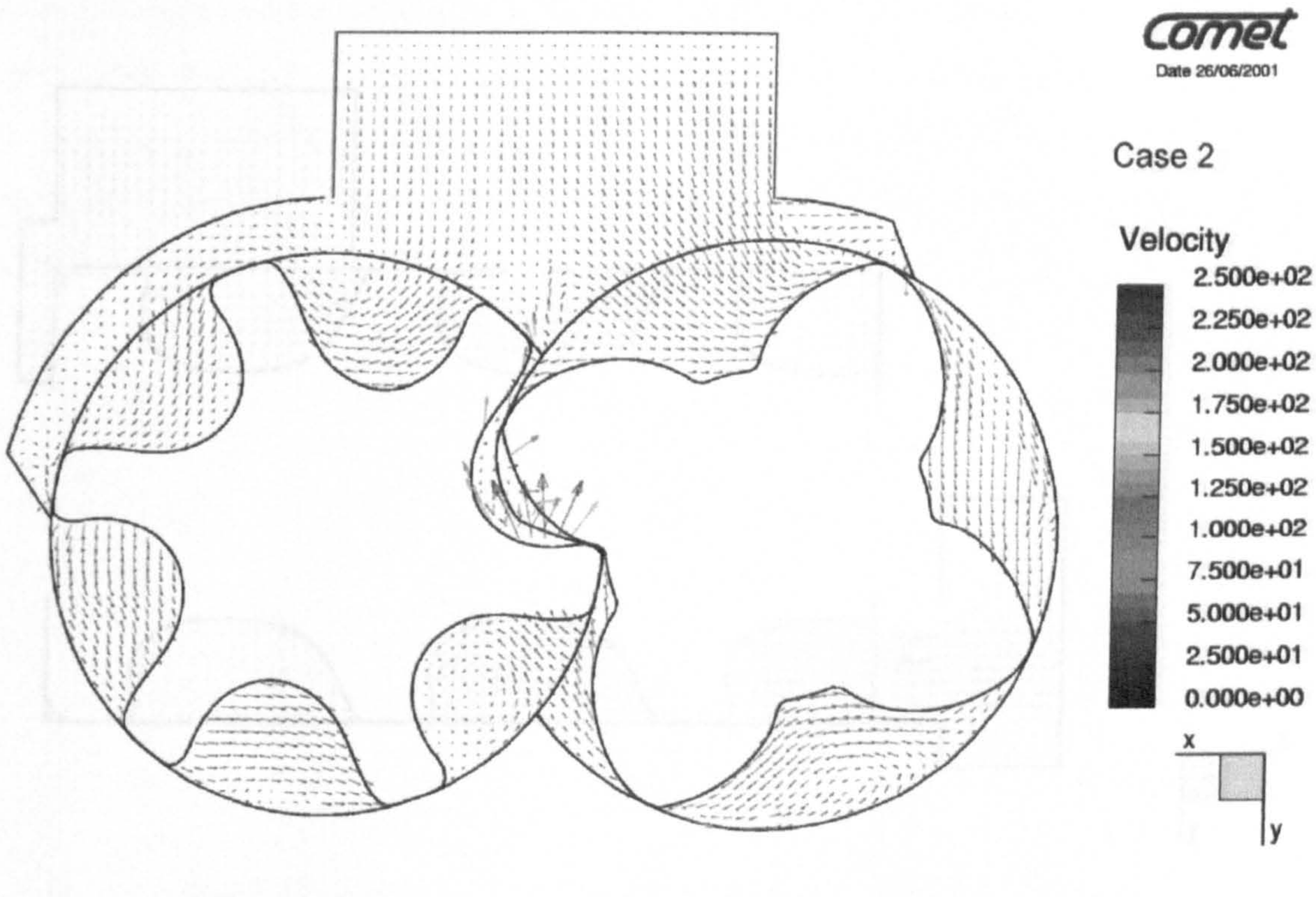

Figure 6-5 Velocity field in the compressor cross section for Case1 and Case2 rotors

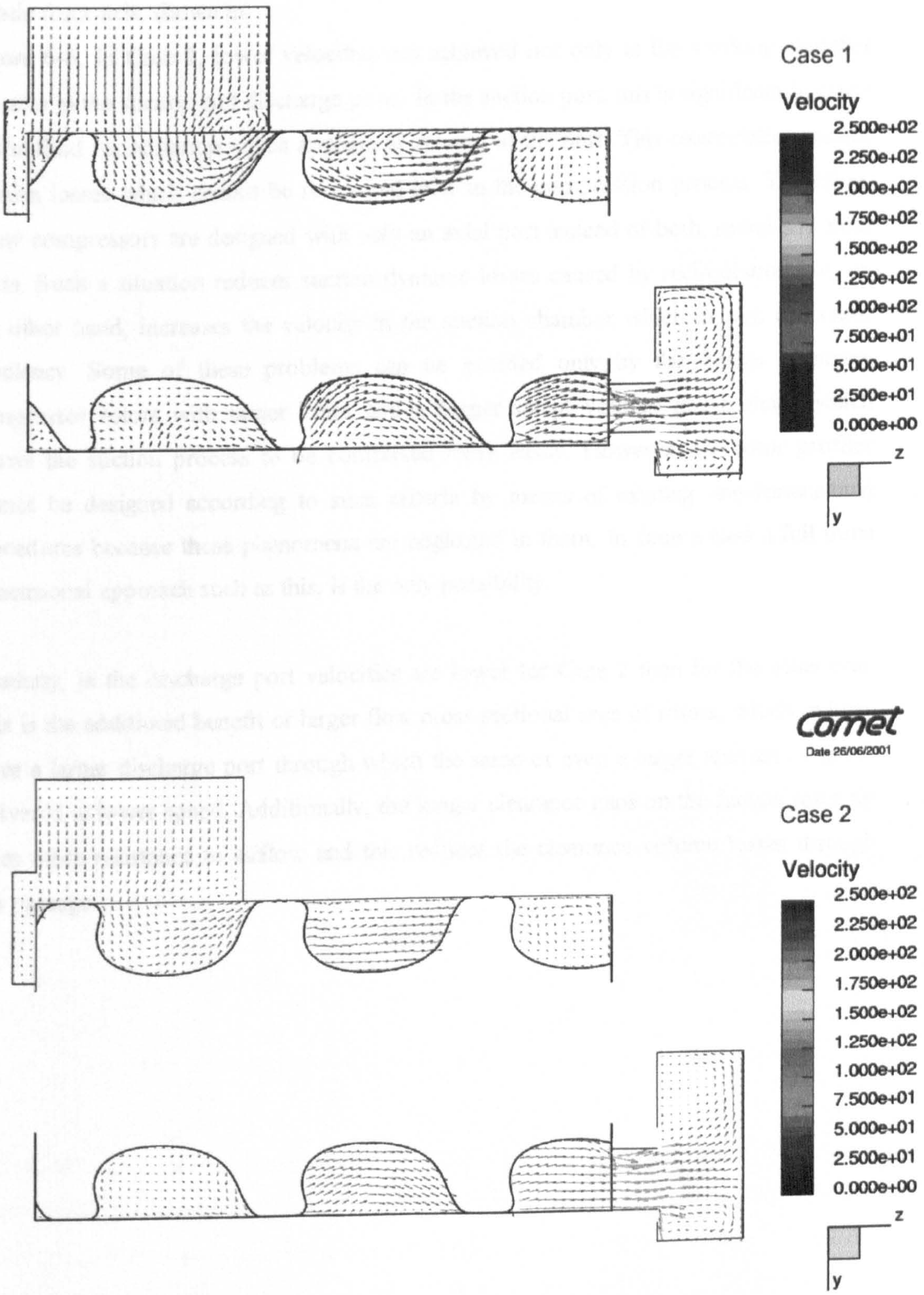

Figure 6-6 Velocity field in the compressor axial section for Case1 and Case2 rotors

These differences are confirmed in the view of the vertical compressor section through female rotor axis, shown in

Figure 6-6. In Case 2, lower velocities are achieved not only in the working chamber but also in the suction and discharge ports. In the suction port, this is significant because of the fluid recirculation which appears at the end of the port. This recirculation causes suction losses which cannot be recovered later in the compression process. Therefore, many compressors are designed with only an axial port instead of both, radial and axial ports. Such a situation reduces suction dynamic losses caused by recirculation but, on the other hand, increases the velocity in the suction chamber which in turn decreases efficiency. Some of these problems can be avoided only by the design of screw compressor rotors with larger lobes and a bigger swept volume and a shape which allows the suction process to be completed more easily. However, the rotor profiles cannot be designed according to such criteria by means of existing one-dimensional procedures because these phenomena are neglected in them. In such a case a full three dimensional approach such as this, is the only possibility.

Similarly, in the discharge port velocities are lower for Case 2 then for the other one. This is the additional benefit of larger flow cross sectional area of rotors, which in turn, gives a larger discharge port through which the same or even a larger amount of gas is delivered at lower speed. Additionally, the longer clearance gaps on the female rotor tip gives more resistance to airflow and this reduces the clearance volume losses through this passage.

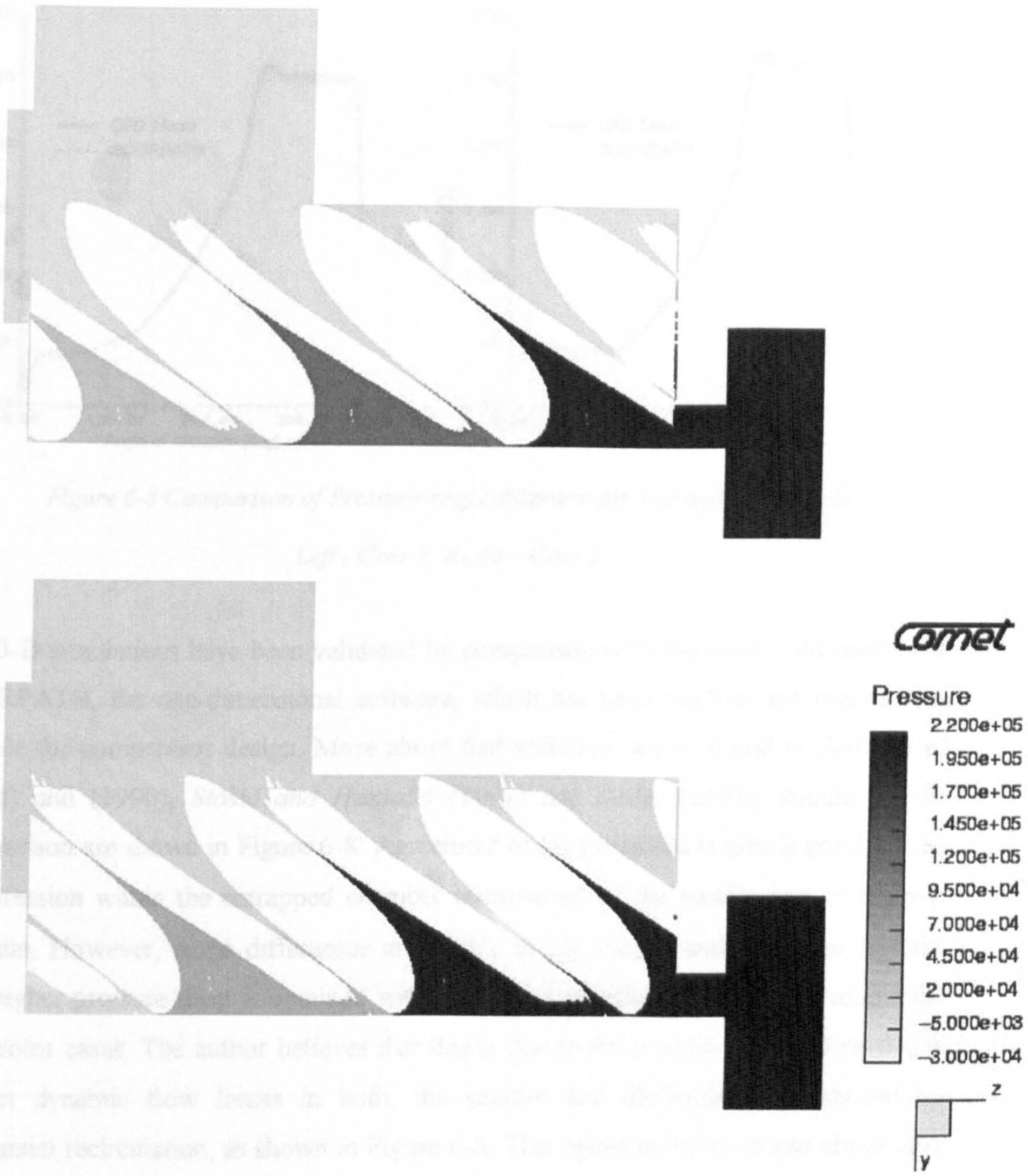

Figure 6-7 Pressure field in the cross section, Case 1 – Top; Case 2 – Bottom

The rise in pressure is similar across the compressor working domains in both cases as presented in Figure 6-7. However, leakages in the second case are smaller due to the shorter sealing line and consequently the pressure rise is slightly steeper. That affects the consumed power, which is lower in Case 2 than in Case 1, despite the higher compressor delivery. These benefits are also visible in Figure 6-9, in which the diagrams of pressure against angle of rotation are presented and compared with each other.

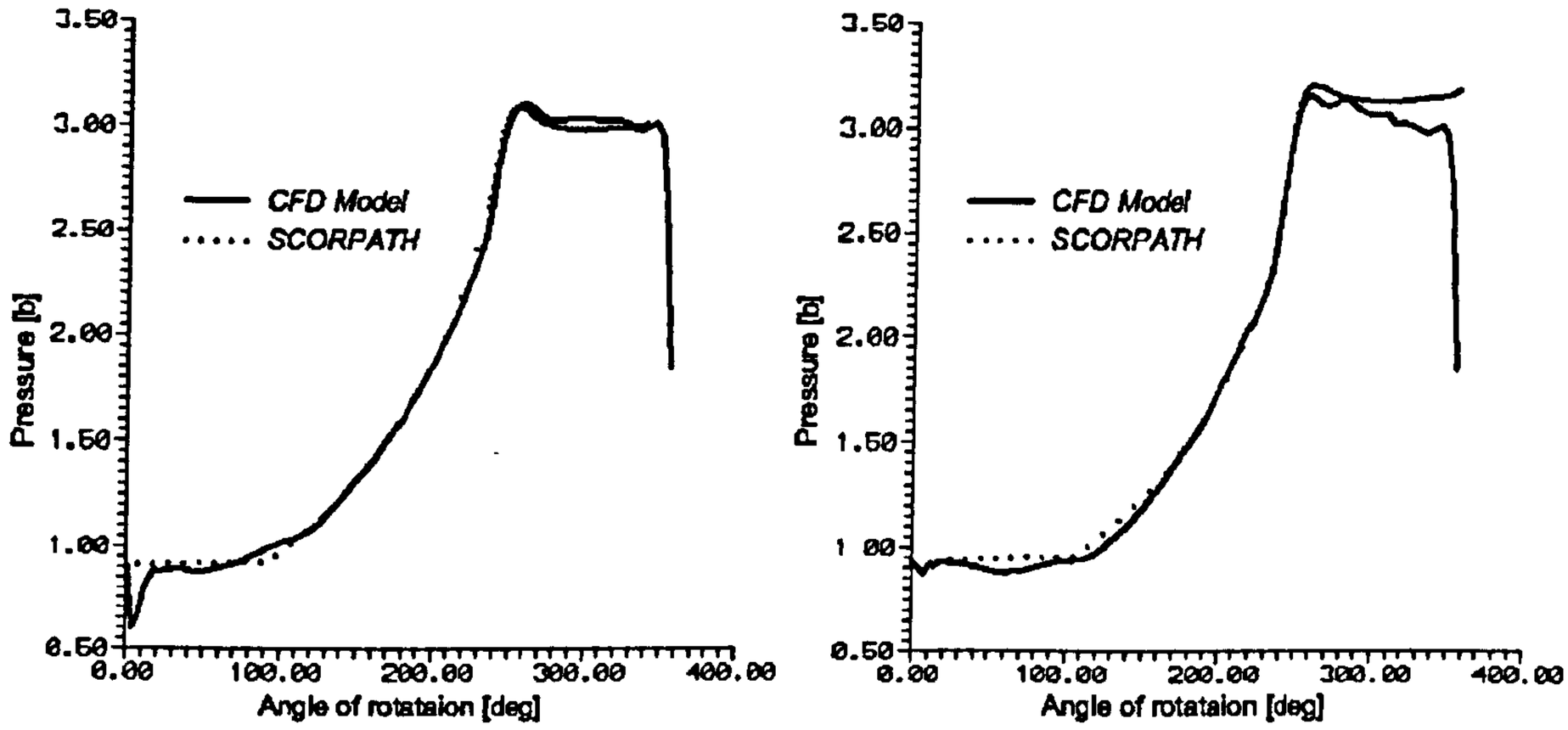

Figure 6-8 Comparison of Pressure-angle diagrams for 1-D and 3-D models

Left - Case 1; Right – Case 2

The 3-D simulations have been validated by comparison with the results obtained from SCORPATH, the one-dimensional software, which has been verified and regarded as reliable for compressor design. More about that software can be found in *Stošić et al* (1988) and (1990), *Stošić and Hanjalić* (1997) and *Stošić* (2001). Results of the comparison are shown in Figure 6-8. Agreement of the presented results is good for the compression within the entrapped chamber represented by the middle part of the p-α diagram. However, some differences are visible in the suction and discharge regions. The higher pressure drop is obtained with the 3-D model then with the 1-D model for both rotor cases. The author believes that this is due to the inability of a 1-D model to predict dynamic flow losses in both, the suction and discharge ports caused by substantial recirculation, as shown in Figure 6-6. This opens many questions about how the shape and position of the inlet and outlet ports can be altered in order to improve screw compressor design. Thus, the mathematical model established in this thesis and the grid generating tool developed for that purpose can be used to explore this furter.

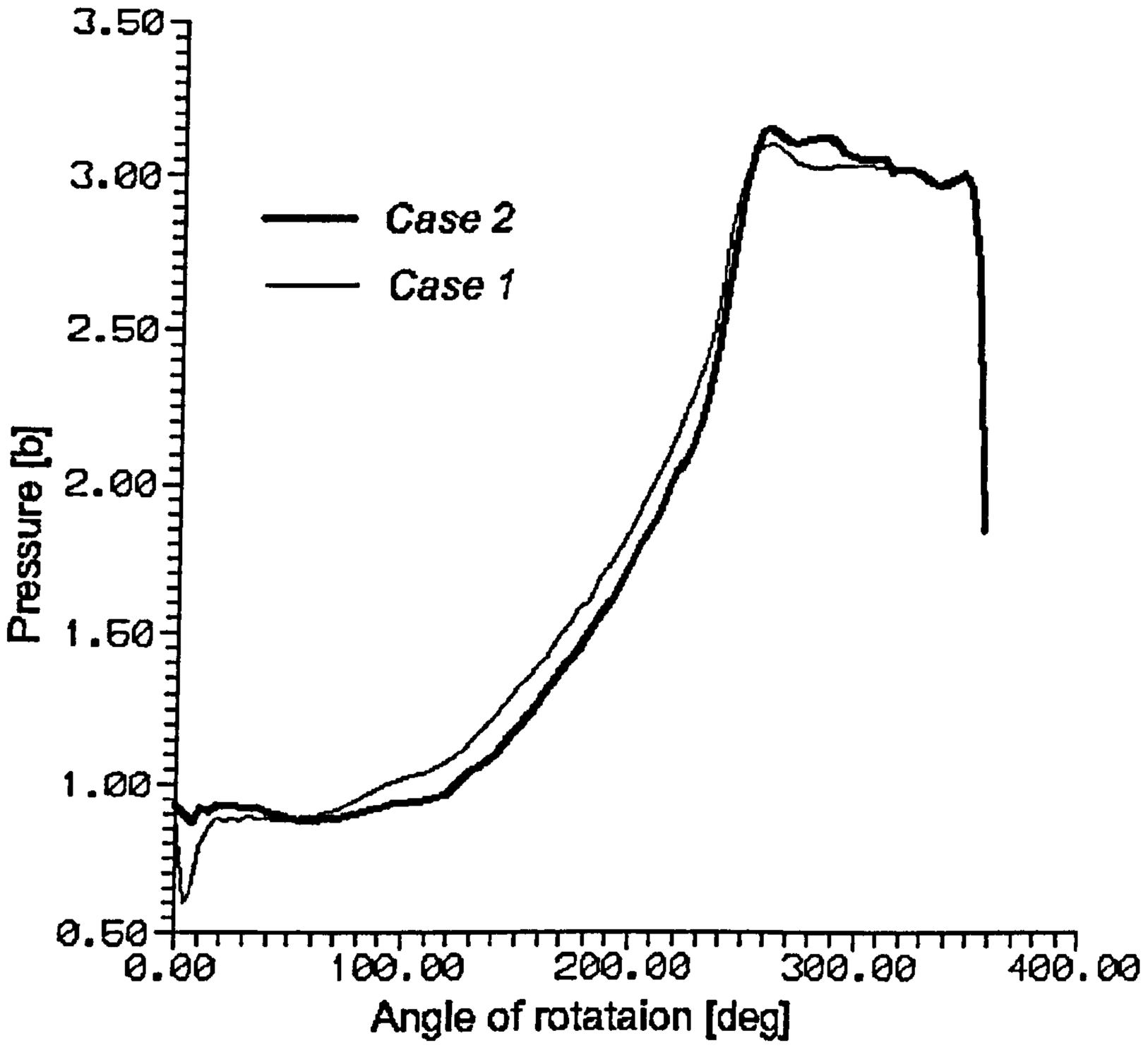

Figure 6-9 Comparison of Pressure-angle diagrams for both cases

Forces on the bearings are a consequence of the pressure differences within the screw compressor working domain. Radial bearing forces on both, the suction and discharge sides are presented in Figure 6-10. The average values are practically the same in both cases. However, the distribution of forces upon the suction and discharge sides differ for the two cases analysed. The forces on both, the male and the female radial bearings are lower for Case 2 then in Case 1, while the bearings on the discharge side are loaded with almost equal force in both cases. Although the radial forces are similar, the torque is significantly different for the two cases. The torque is a function of the compressor suction and discharge pressure, which is according to Figure 6-9 almost the same. However, the profile shape is significantly different for these two cases and consequently the distribution of torque on the male and female rotors is not the same. In Case 2 the torque on the male rotor is higher then in the Case 1 but the torque transmitted to the female rotor is significantly lower, Figure 6-11. The right hand diagram of that figure shows that the torque on the female rotor is reduced from 10 [Nm] in the Case 1 to practically zero in the Case 2, while at the same time the female rotor is thicker. This gives the Case 2 rotors many advantages. Among others, important

features are: lower female rotor deformation caused by pressure, greater flow cross sectional area and shorter sealing line.

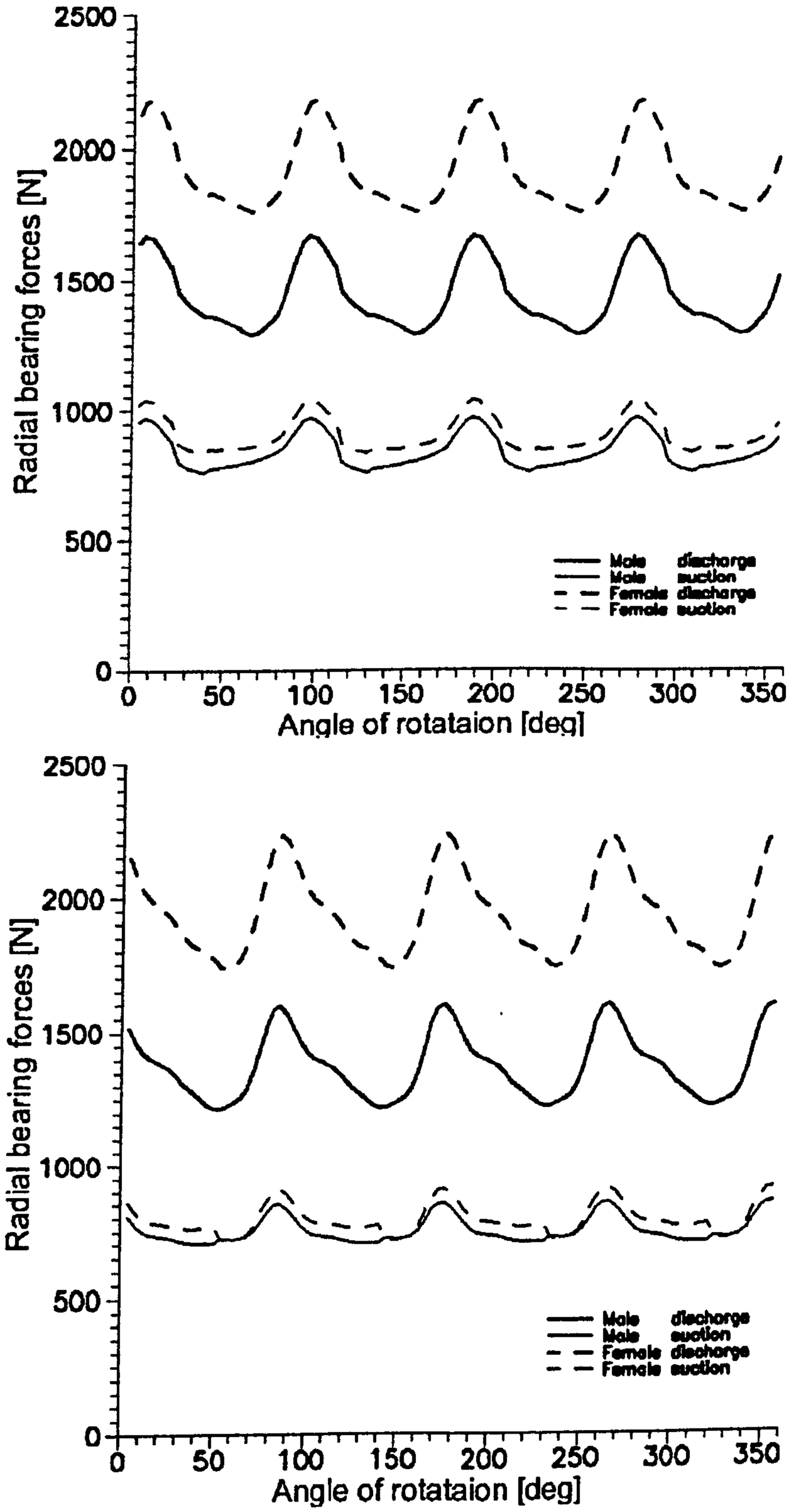

Figure 6-10 Radial bearing forces, Case 1 -top, Case 2 -bottom

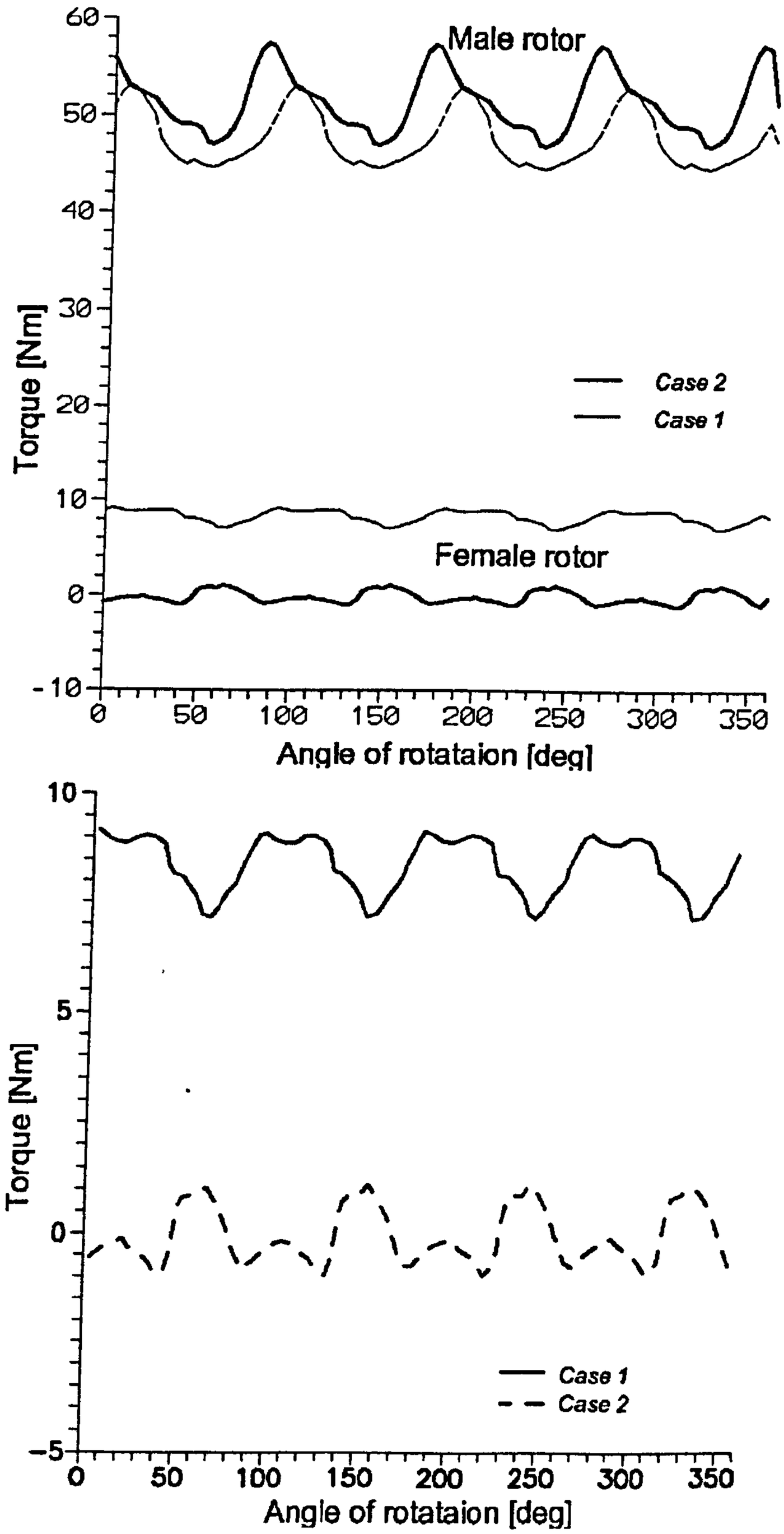

Figure 6-11 Comparison of the compressor torque in Case 1 and Case 2

Top – Both rotors; Bottom – Female rotors

All the features listed above, confirmed by the diagrams, obtained from the 3-D CFD calculations, show that the modern rotors in Case 2 have significant advantages over the more traditional rotors of Case 1. This is also confirmed by comparison of the integral parameters given in Table 6-1. Here it can be seen that the specific power of the compressor with Case 2 rotors is 12% lower then in the other case. This indicates that both, the consumed power is lower and the delivered flow rate is greater. This is confirmed by a 12% higher volumetric efficiency η_v and a 10% higher thermal efficiency η_i for the compressor with the Case 2 rotor profile.

Table 6-1 Comparison of the integral parameters for the two cases

	$\dot{V}$ [m^3/min]	P [kW]	P_{spec} [kW/m^3min]	ηv [%]	ηi [%]
Case 1	**17.285**	**56.757**	**3.283**	**74.371**	**60.960**
Case 2	**19.674**	**55.920**	**2.842**	**83.940**	**67.450**

6.3 EXAMPLE 2; FLOW IN AN OIL INJECTED SCREW COMPRESSOR

Figure 6-12 shows an oil-injected screw compressor, designed and built at City University. A cross section in Figure 6-13 shows how the two rotors are supported by six bearings. Two of these are thrust bearings on the discharge side on the far right of the figure, while the others are cylindrical roller bearings. The oil is supplied to the rotors through an oil injection port in order to seal, cool and lubricate. The same oil is supplied to the bearings, in order to lubricate them. Therefore, no seals are required within the compressor and the only seal is positioned around the driving shaft to seal the compressor from the surroundings, as presented on the far left of this figure. Three cross sections planes are indicated in this figure. Two of them are normal to the rotor axes indicated by A-A and B-B. The first one crosses the suction port, rotors and the oil injection port while the other is nearer to the discharge port. The remaining section is parallel to the rotor axes lying between the rotors. All results in this example are presented in these three cross sections.

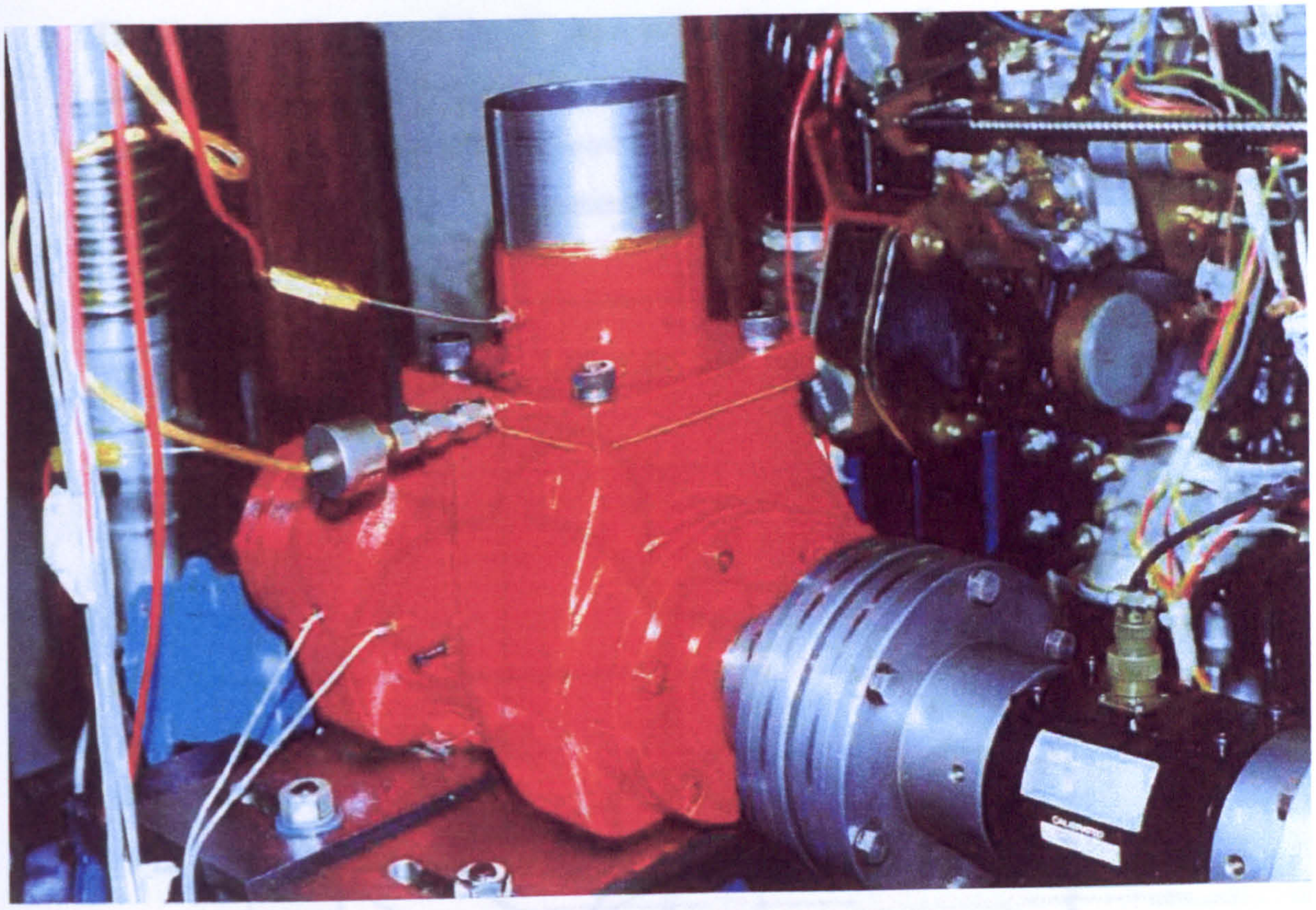

Figure 6-12 Oil injected screw compressor with 'N' rotors.

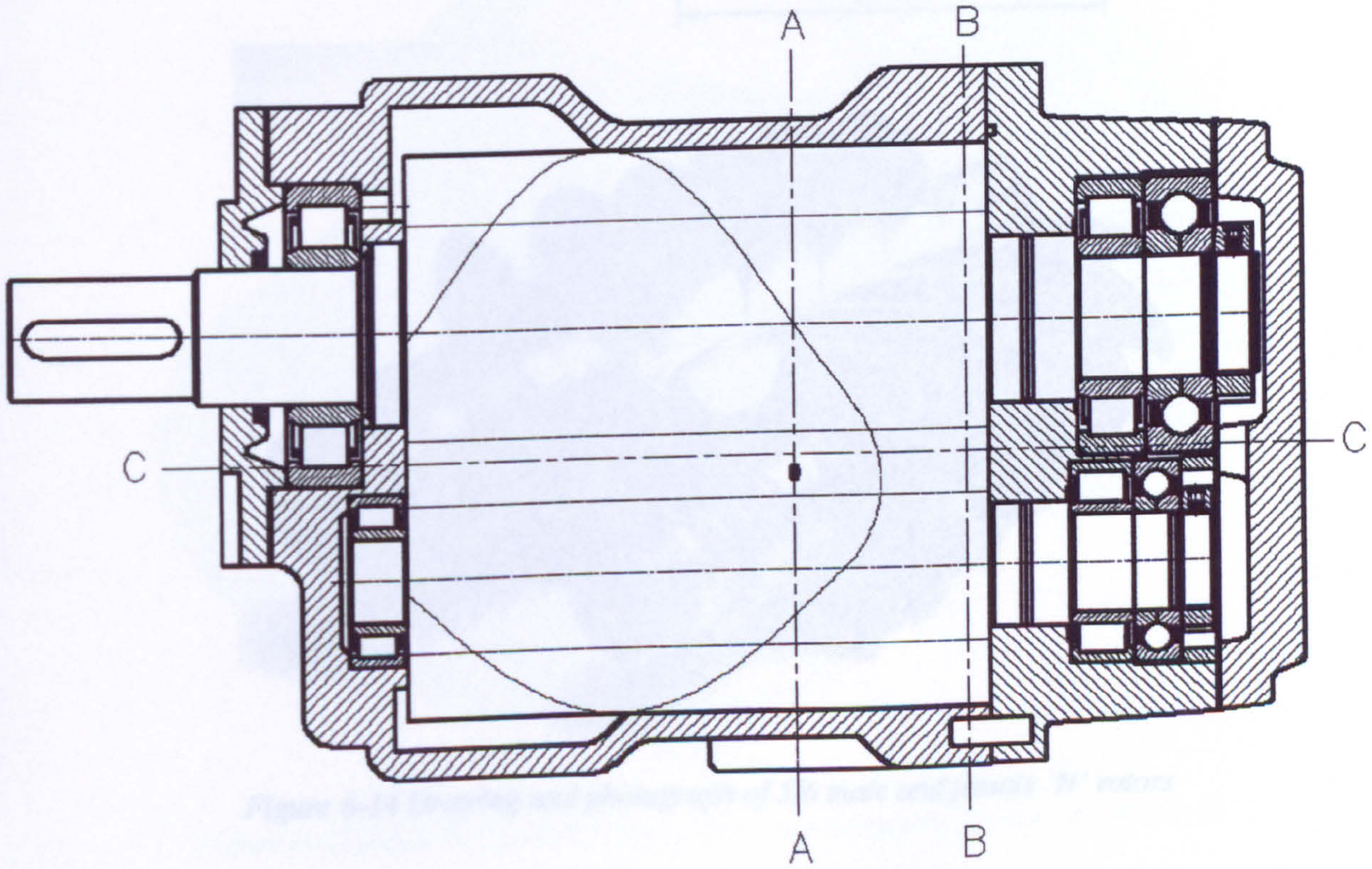

Figure 6-13 Cross section of the analysed oil injected compressor

The Rotor profiles are of the 'N' type with a 5/6 lobe configuration. The rotor outer diameters are 128 and 101 mm for the male and female rotors respectively, and their centre lines are 90 mm apart. The rotor length to diameter ratio is 1.66. Both, a drawing and photograph of the rotors are presented in Figure 6-14.

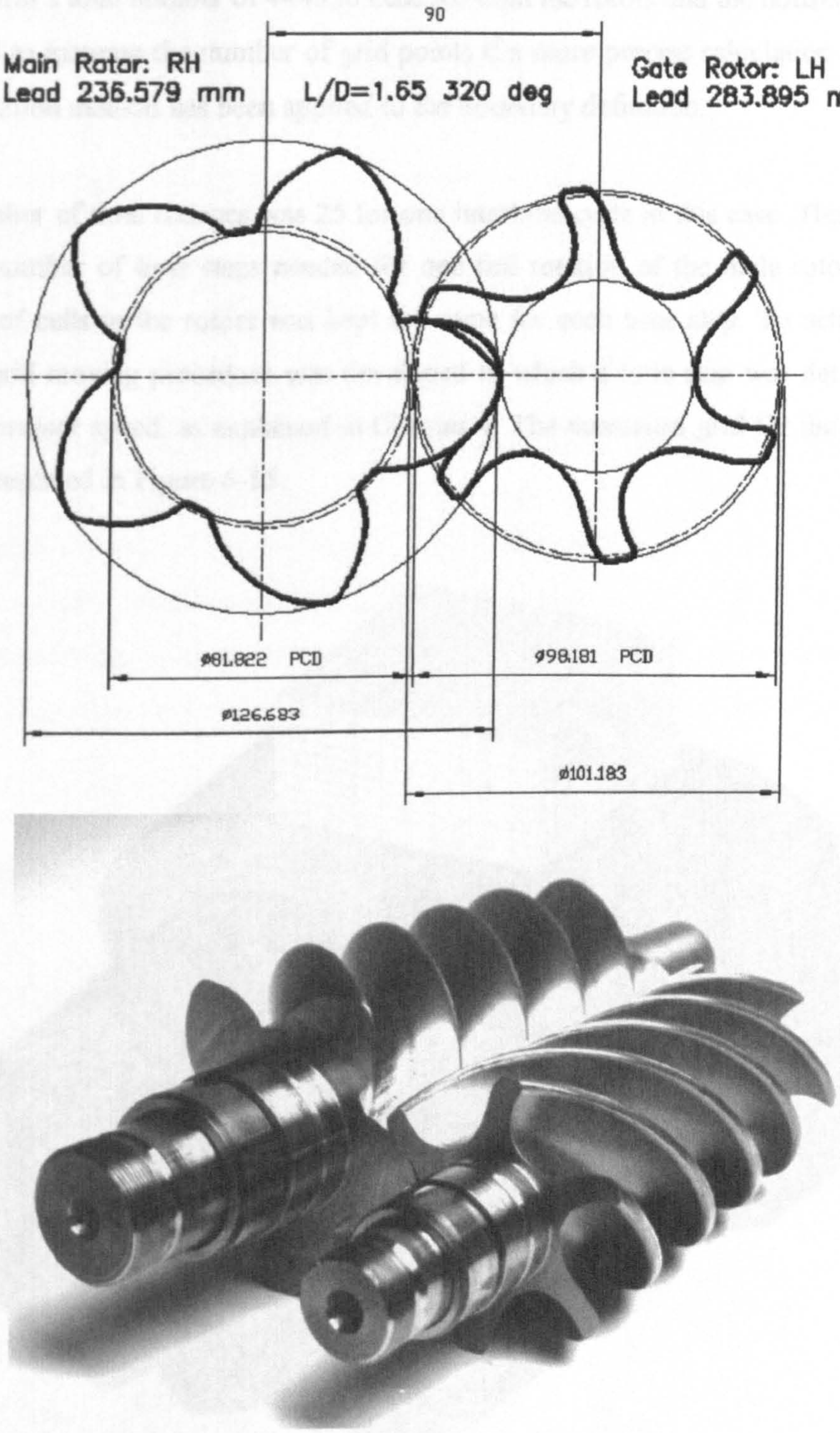

Figure 6-14 Drawing and photograph of 5/6 male and female 'N' rotors

6.3.1 Grid generation

The male and female rotors have 40 numerical cells along each interlobe in the circumferential direction, 6 cells in the radial direction and 112 in the axial direction. These form a total number of 444830 cells for both the rotors and the housing. To avoid the need to increase the number of grid points if a more precise calculation is required, an adaptation method has been applied to the boundary definition.

The number of time changes was 25 for one interlobe cycle in this case. This makes the overall number of time steps needed for one full rotation of the male rotor 125. The number of cells in the rotors was kept the same for each time step. To achieve this, a special grid moving procedure was developed in which a time step was determined by the compressor speed, as explained in Chapter 4. The numerical grid for the initial time step is presented in Figure 6-15.

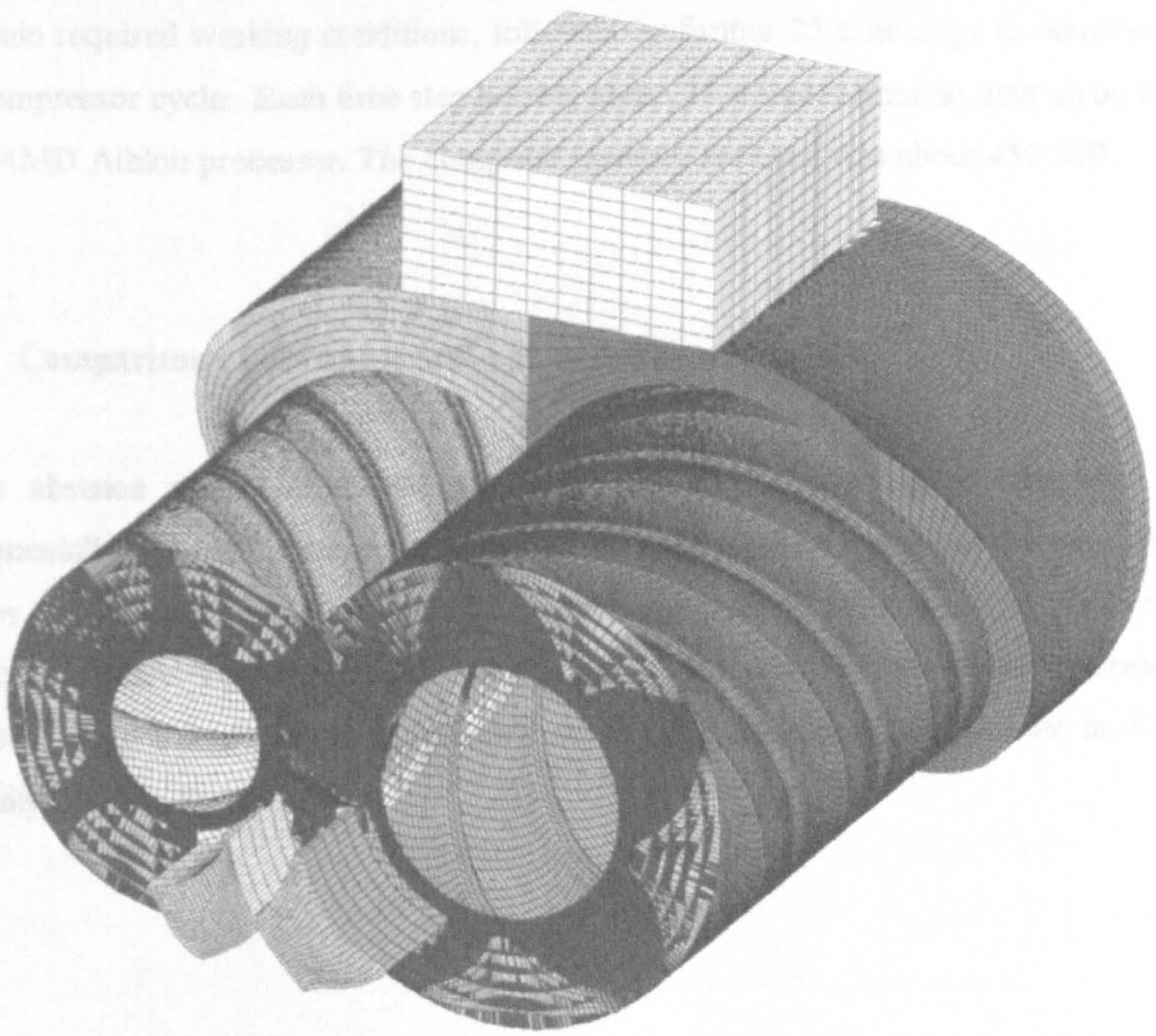

Figure 6-15 Numerical grid for oil injected screw compressor with 444830 cells

6.3.2 Mathematical model

The mathematical model consists of the momentum, energy, mass and space equations, as described in section 4.2, but an additional equation for the scalar property of oil concentration was added to enable the influence of oil on the entire compressor performance to be calculated. The constitutive relations are the same as in the previous example. The oil is treated in the model as a 'passive' species, which does not mix with the background fluid - air. Its influence on the air is accounted for through the energy and mass sources which are added to or subtracted from the appropriate equation of the main flow model. In this case, the momentum equation is affected by drag forces as described in 4.2.3.3.

To establish the full range of working conditions and starting from a suction pressure of 1 bar to obtain an increase in pressure of 6, 7, 8 and 9 bars at discharge, a numerical mesh of nearly 450000 cells was used. For each case only 25 time steps were required to obtain required working conditions, followed by further 25 time steps to complete a full compressor cycle. Each time step needed about 30 minutes running time on an 800 MHz AMD Athlon processor. The computer memory required was about 450 MB.

6.3.3 Comparison of the numerical and experimental results

In the absence of velocity field measurements in the compressor chamber, an experimentally obtained pressure history within the compressor cycle and the measured air flow and compressor power served as a valuable basis to validate the results of the CFD calculation. To obtain these values, the 5/6 oil flooded compressor, already described, was tested on a rig installed in the thermodynamics laboratory at City University London, Figure 6-16.

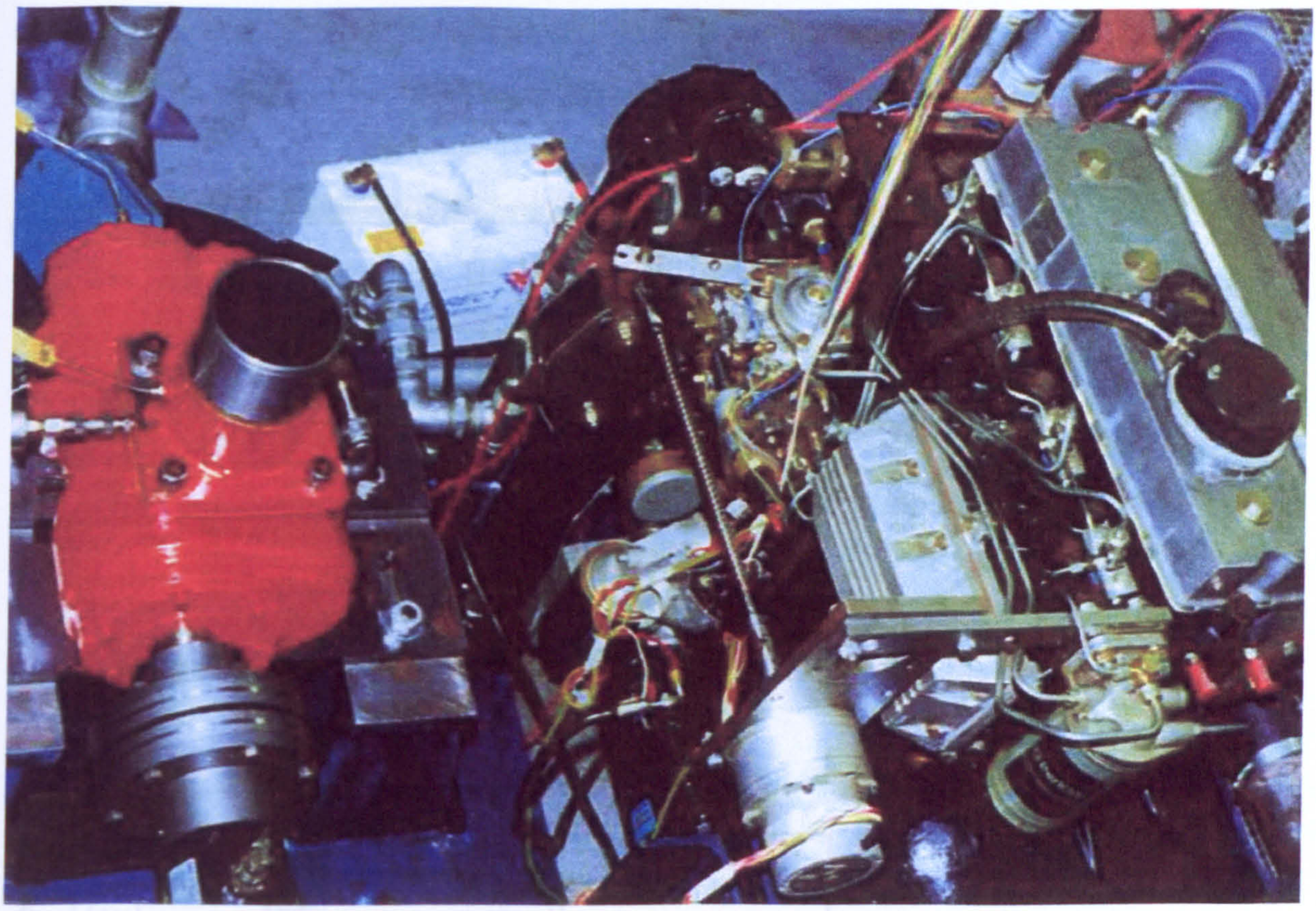

Figure 6-16 Oil-Injected air screw compressor 5/6-128mm (a=90mm) in the test bed

The test rig meets all Pneurop/Cagi requirements for screw compressor acceptance tests. The compressor was tested according to ISO 1706 and its delivery flow was measured following BS 5600. High accuracy test equipment was used for the measurement of all relevant parameters.

The pressures were measured with high quality pressure transducers, with readings taken at the inlet to the compressor, discharge from the compressor and in the separator.

The temperatures were measured by FeCu thermocouples at the inlet to and discharge from the compressor and after the oil separator. Measurements of temperature were also taken of both, the oil and the cooling water at the inlet and of the oil cooler. The oil flow rate was calculated from the cooler and compressor energy and mass balance.

Torque was measured by a laboratory type torque meter transducer IML TRP-500 connected between the engine and the compressor driving shaft. The compressor was driven by a diesel engine prime mover of 100 kW maximum output, which could operate

at variable speed. The compressor speed was measured by a frequency meter and the signal was transferred to a data logger after converting to current.

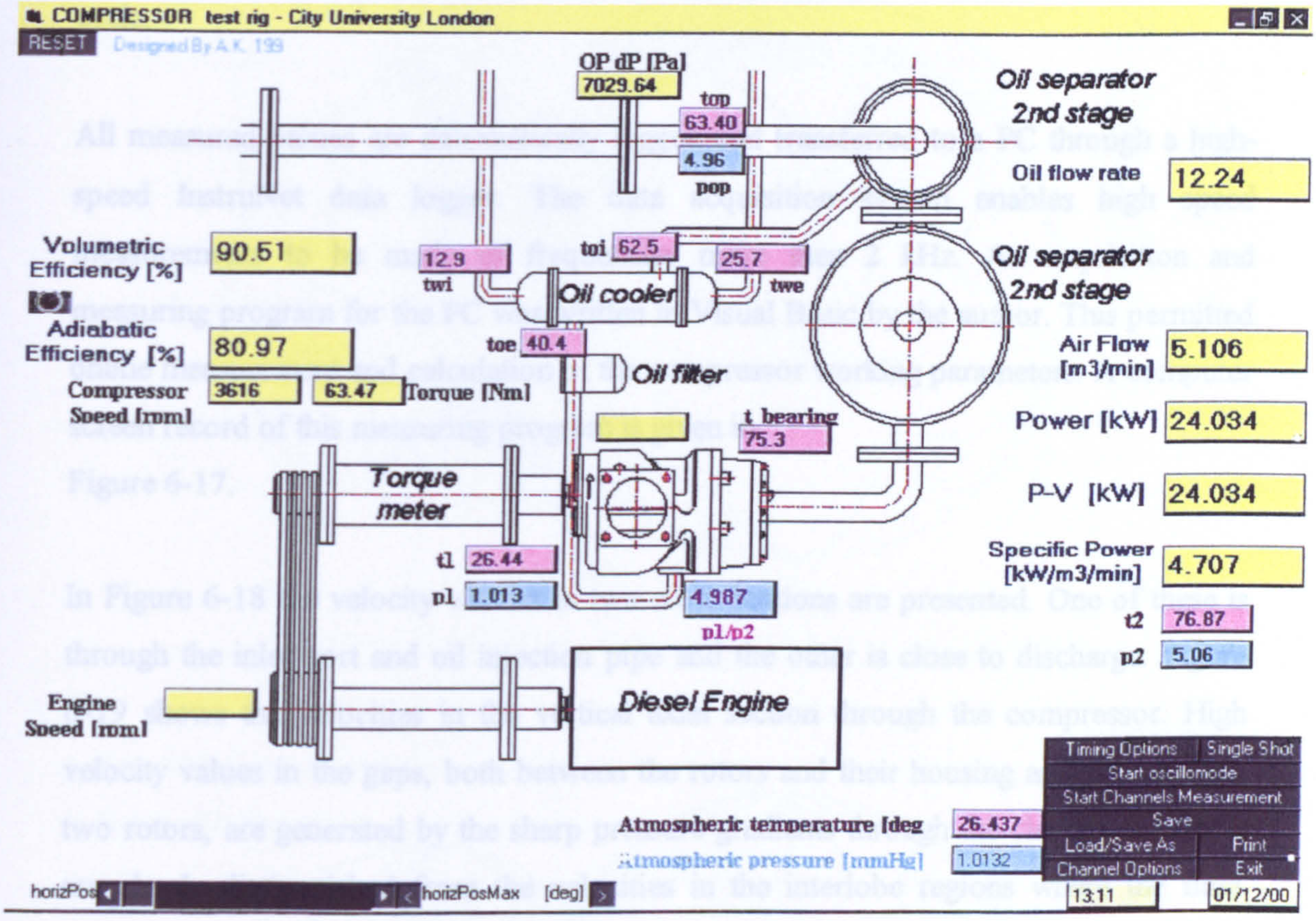

Figure 6-17 Computer screen of compressor test rig measuring program

The compressor flow is measured by the orifice plate according to BS 5600 with the differential pressure measured by a pressure transducer PDCR 120/35WL over an operating range of 0-200 kPa.

The measured values of all relevant pulsating quantities were used to obtain details of the thermodynamic cycle. Of these, the pressure in the trapped volume was the most significant since it was required to plot the machine p-V diagram. Accordingly, a method was developed to construct an entire p-V diagram from the recording of the pressure changes at only 4 discrete points in the machine casing.

The Endevco piezoresistive transducers E8180B were used to measure the instantaneous values of the absolute pressure in the compressor. Each transducer records pressure in

one interlobe space. Starting from the suction end, 4 transducers are positioned in the compressor casing to measure pressure values in the consecutive interlobe spaces. When plotted in sequence they give pressure-time diagram for the whole compressor working cycle.

All measured values are automatically logged and transferred to a PC through a high-speed InstruNet data logger. The data acquisition system enables high speed measurements to be made of frequencies more then 2 kHz. An acquisition and measuring program for the PC was written in Visual Basic by the author. This permitted online measurement and calculation of the compressor working parameters. A computer screen record of this measuring program is given in
Figure 6-17.

In Figure 6-18 the velocity vectors in two cross sections are presented. One of these is through the inlet port and oil injection pipe and the other is close to discharge. Figure 6-19 shows the velocities in the vertical axial section through the compressor. High velocity values in the gaps, both between the rotors and their housing and between the two rotors, are generated by the sharp pressure gradients through the clearances. These are clearly distinguished from the velocities in the interlobe regions where the fluid flows relatively slower. The fluid flow is caused there only by movement of the numerical mesh, which is generated in a manner to follow the movement of the rotors in time. The top diagram shows the cross section in which both the suction port and oil injection opening are crossed. Recirculation in the suction port is substantial and seems to be high because of the position of the oil injection hole. If the oil injection had been positioned further downstream, the recirculation would have been lower. The bottom diagram, which shows a cross section close to the discharge port, indicates that more recirculation is present in the lobes with lower pressures as it is visible in the top of the diagram. The velocities in the high pressure regions are smoothened to relatively low values, to some extent similar to the wall velocities.

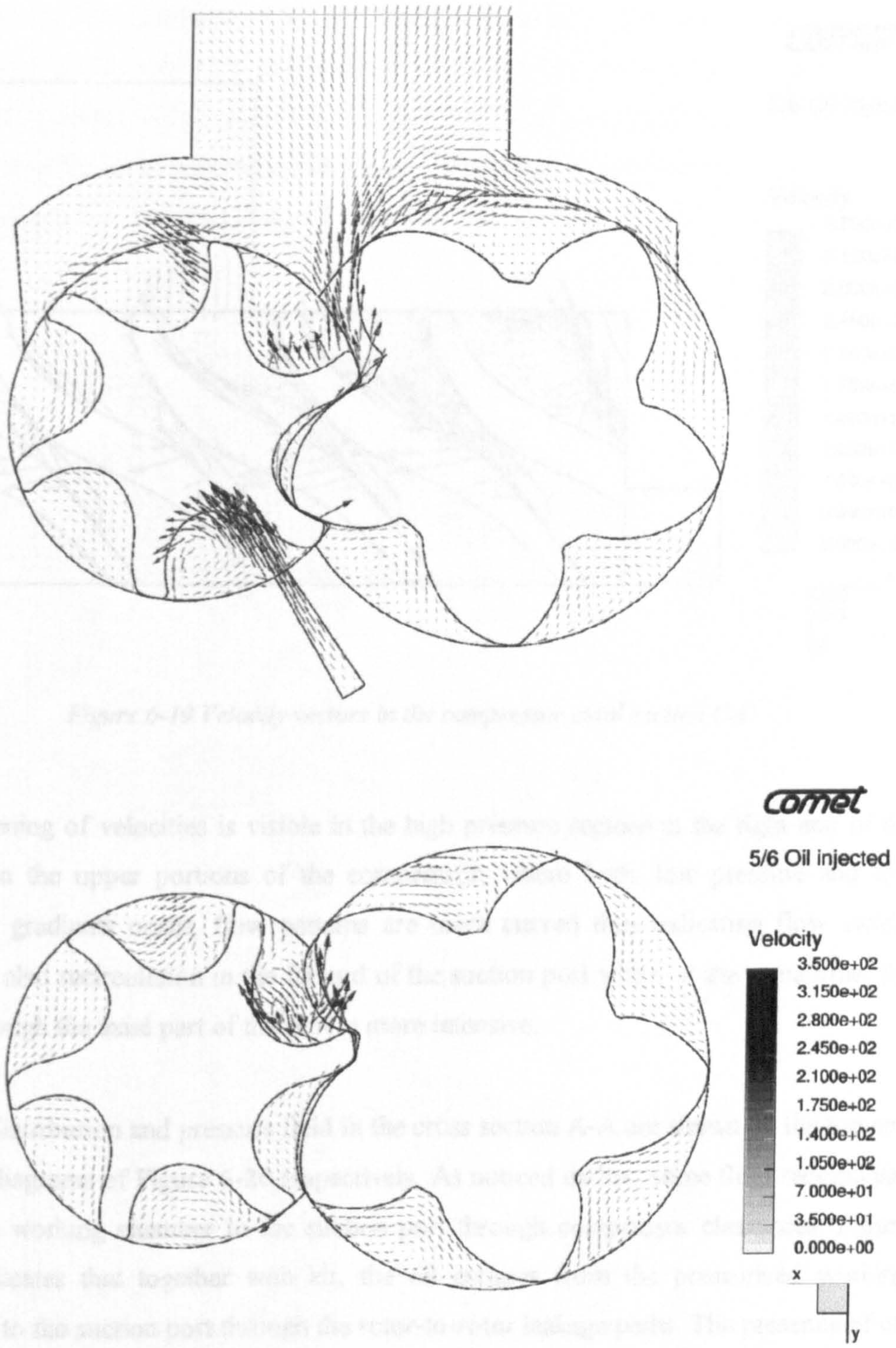

Figure 6-18 Velocity vectors in the two compressor cross sections

Top – cross section A-A through the suction port, Bottom – cross section B-B

The velocity field in the axial section C-C, which crosses both rotors along the rotor bore cusp, is shown in Figure 6-19.

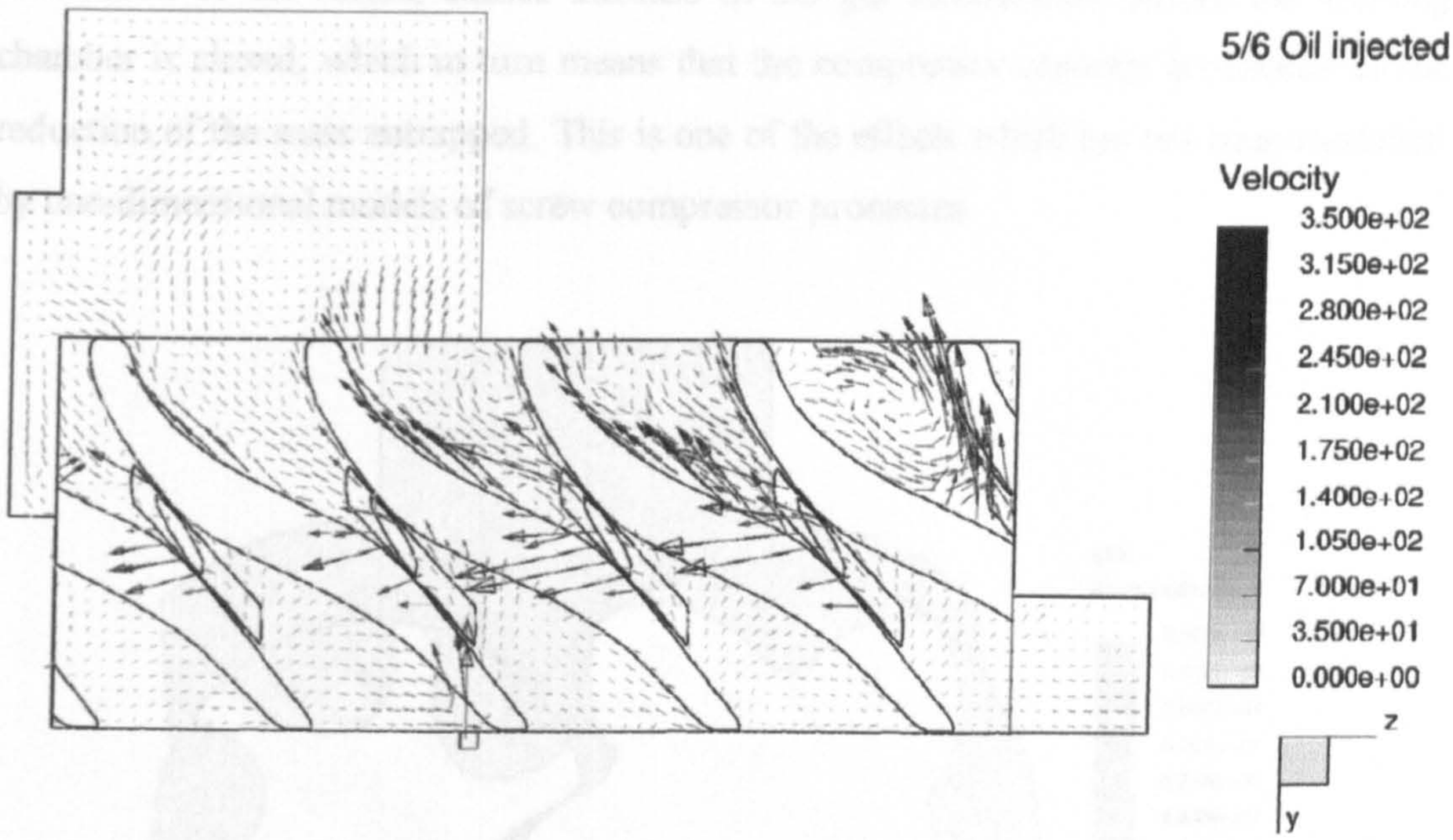

Figure 6-19 Velocity vectors in the compressor axial section C-C

Smoothening of velocities is visible in the high pressure regions at the right end of the figure. In the upper portions of the compressor, where both, low pressure and low pressure gradients occur, flow patterns are more curved thus indicating flow swirls. There is also recirculation in the far end of the suction port while, at the same time, the flow through the axial part of the port is more intensive.

The oil distribution and pressure field in the cross section A-A are shown on the top and bottom diagrams of Figure 6-20 respectively. As noticed earlier, some fluid recirculates from the working chamber to the suction port through compressor clearances. Figure 6-20 indicates that together with air, the oil escapes from the pressurised working chamber to the suction port through the rotor-to-rotor leakage paths. The presence of oil in the suction port was also observed visually by the author during experiments on this compressor. However, no measurements have been done to record that. Some limited results of the experimental investigation on the oil distribution within the screw compressor are published by *Xing et al* (2001). In that case, a compressor was made out of transparent material in order to visualise the oil flow. Although the author has not a complete record of their results, it appears from what they published that the oil flow patterns obtained from the 3-D calculations are similar to those obtained in their

experiments. The presence of hot oil in the suction port, although beneficial for the lubrication of the rotors, causes increase in the gas temperature before the working chamber is closed, which in turn means that the compressor capacity is reduced by the reduction of the mass entrapped. This is one of the effects which has not been modelled by one-dimensional models of screw compressor processes.

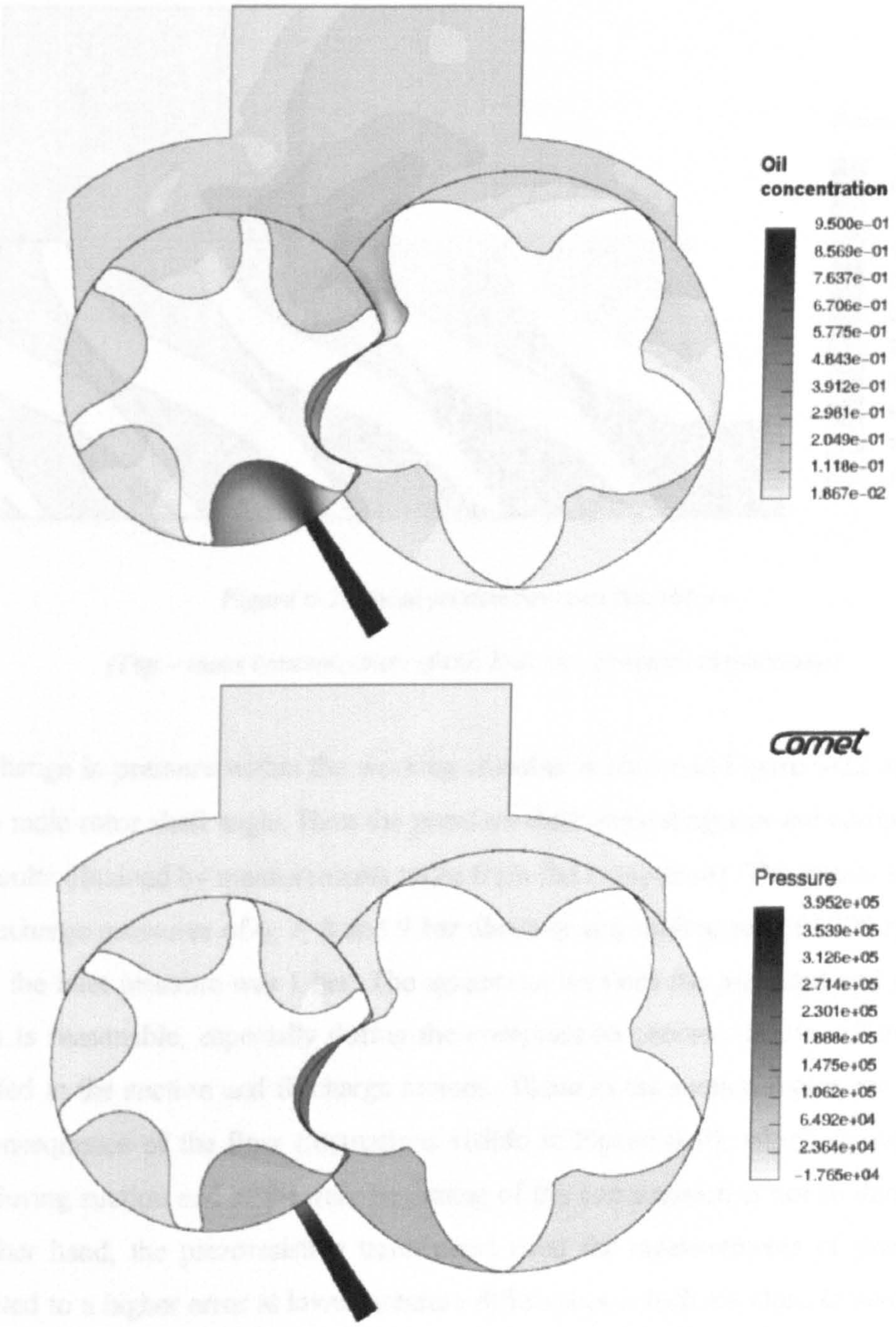

Figure 6-20 Cross section through the inlet port and oil injection port A-A

Top – mass concentration of oil, Bottom - Pressure distribution

Figure 6-21 shows the pressure distribution within the compressor with male rotor speed of 5000 rpm. This figure indicates that the pressure within the each working chamber is almost uniform and that it can be regarded as such for almost all calculations and comparisons. Due to that, the results obtained by the 3-D calculations may be compared with those obtained by measurements.

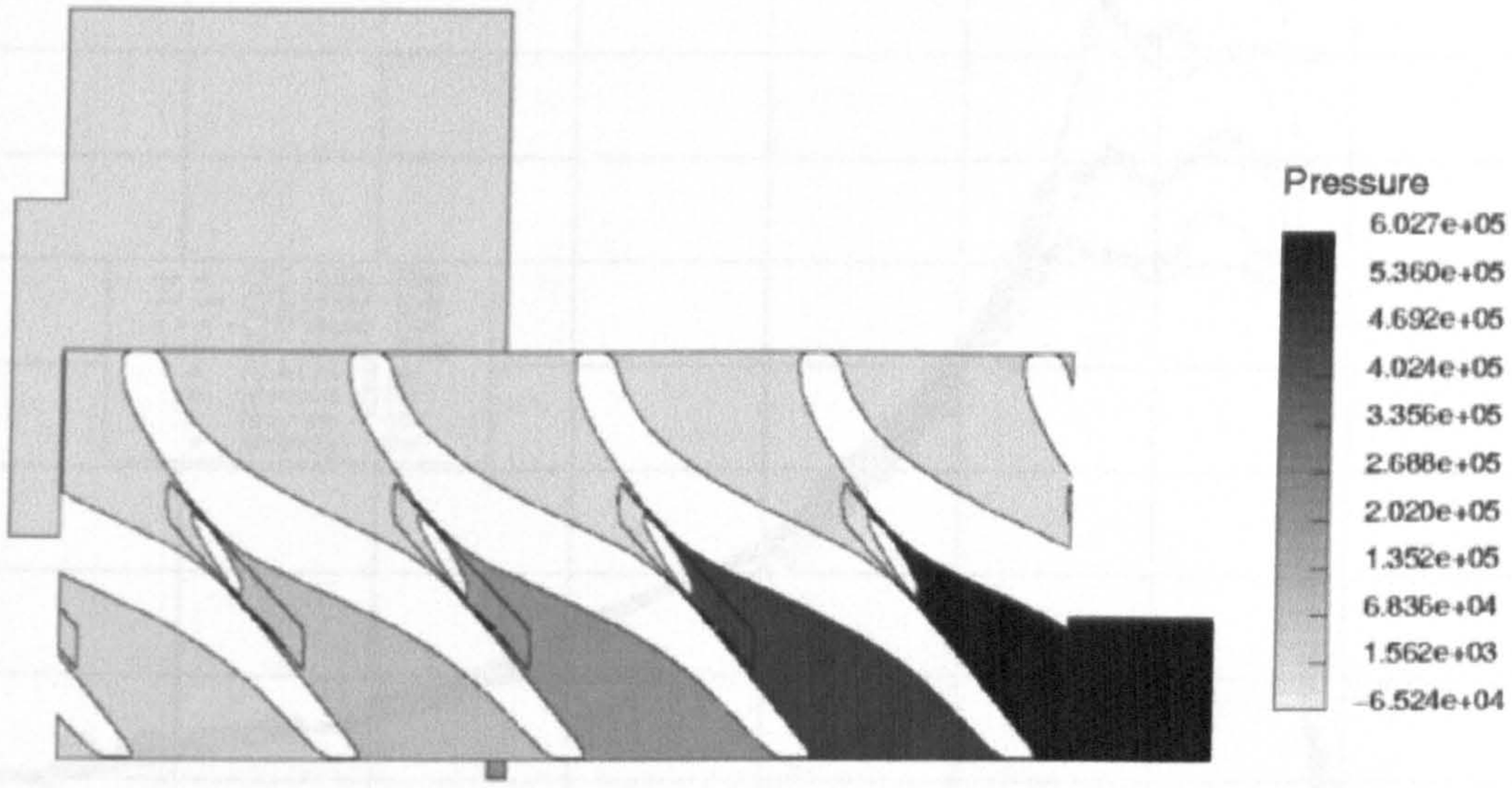

Figure 6-21 Axial section between two rotors

(Top – mass concentration of oil, Bottom - Pressure distribution)

The change in pressure within the working chamber is shown in Figure 6-22 as function of the male rotor shaft angle. Here the pressure-shaft angle diagrams are compared with the results obtained by measurements taken from the compressor. The results shown are for discharge pressures of 6, 7, 8 and 9 bar absolute at a shaft speed of 5000 rpm. In all cases, the inlet pressure was 1 bar. The agreement between the predicted and measured values is reasonable, especially during the compression process. Some differences are recorded in the suction and discharge regions. Those in the suction region are probably the consequence of the flow fluctuations visible in Figure 6-19, which shows that the flow during suction and at the very beginning of the compression is not so damped. On the other hand, the piezoresistive transducers used for measurements of pressure are subjected to a higher error at lower pressure differences, which are close to zero in these areas. The differences recorded at the high pressure end, during the discharge process, are probably generated because of the inability to capture real geometry accurately. The calculated discharge port was simplified from the real one. It was also mapped with

relatively low number of cells. The influence of the mesh size to the calculation accuracy is analysed in more details in section 6.3.5.

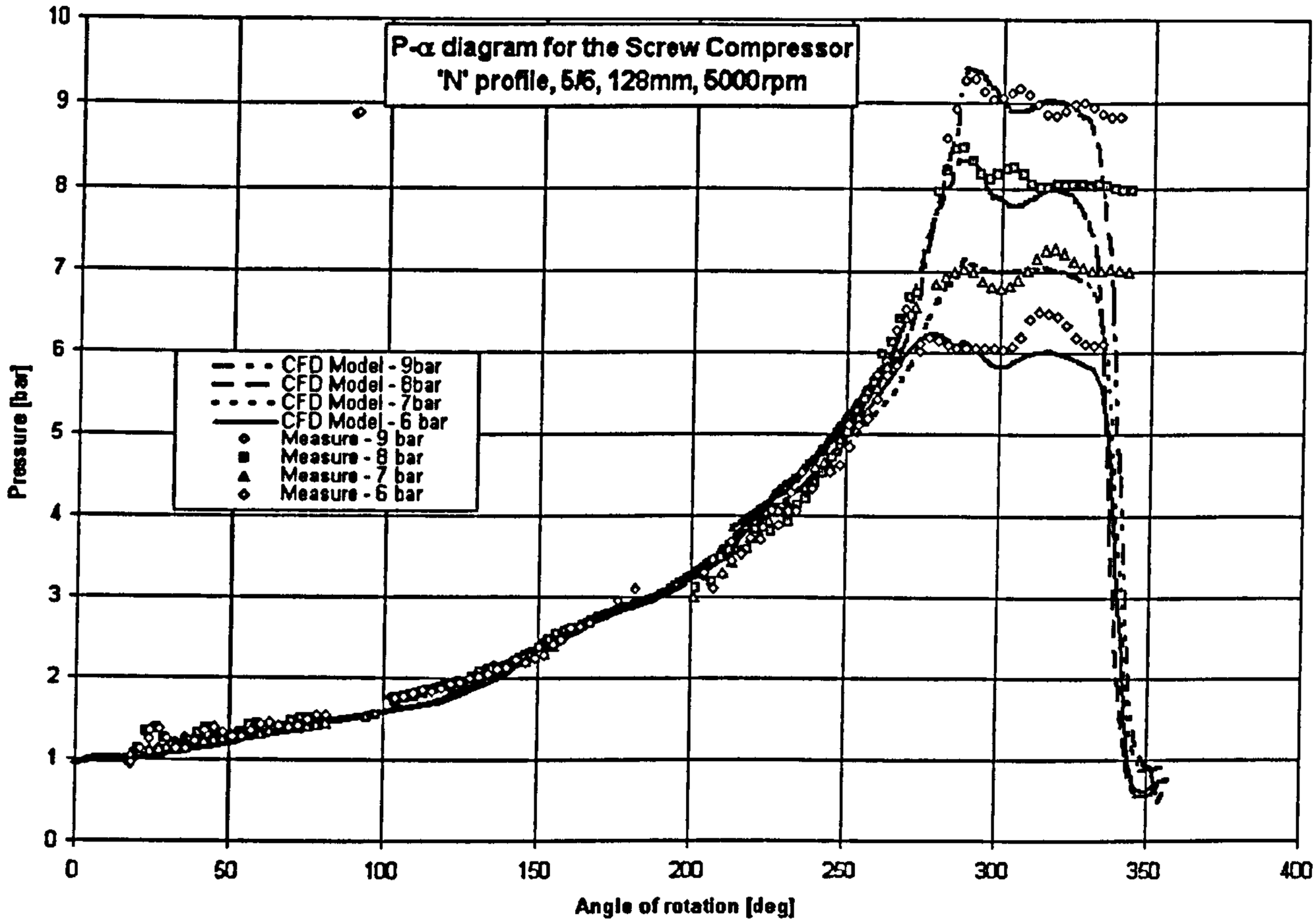

Figure 6-22 Pressure-shaft angle diagram; comparison of CFD calculations and measurements

The compressor radial bearing forces are presented in Figure 6-23. There, the force on the female rotor radial discharge bearing and the force on the male rotor radial suction bearing are given. The reason why these two radial bearings were selected for the diagram is that each of them is loaded with a higher force then its counterpart on the other rotor. It can be seen that both the mean value and amplitude of the forces rise with discharge pressure. More frequent dynamic load with higher amplitude puts a greater demand on the bearings. These have to be selected carefully in compressor design to withstand such loads.

Diagrams of the torque on the male and female rotors are in Figure 6-24 given in respect to the shaft angle. Changes in torque have the same frequency as these in the radial force or in any other parameter of screw compressor process. This corresponds to the product of the shaft speed and the number of lobes on the compressor male rotor. It is

very important for a compressor, which works in the oil flooded operational mode, to have as low as possible torque on the female rotor which is usually driven by the male rotor by direct contact. The rotor profile of this compressor is such that the female rotor operates with very small positive torque.

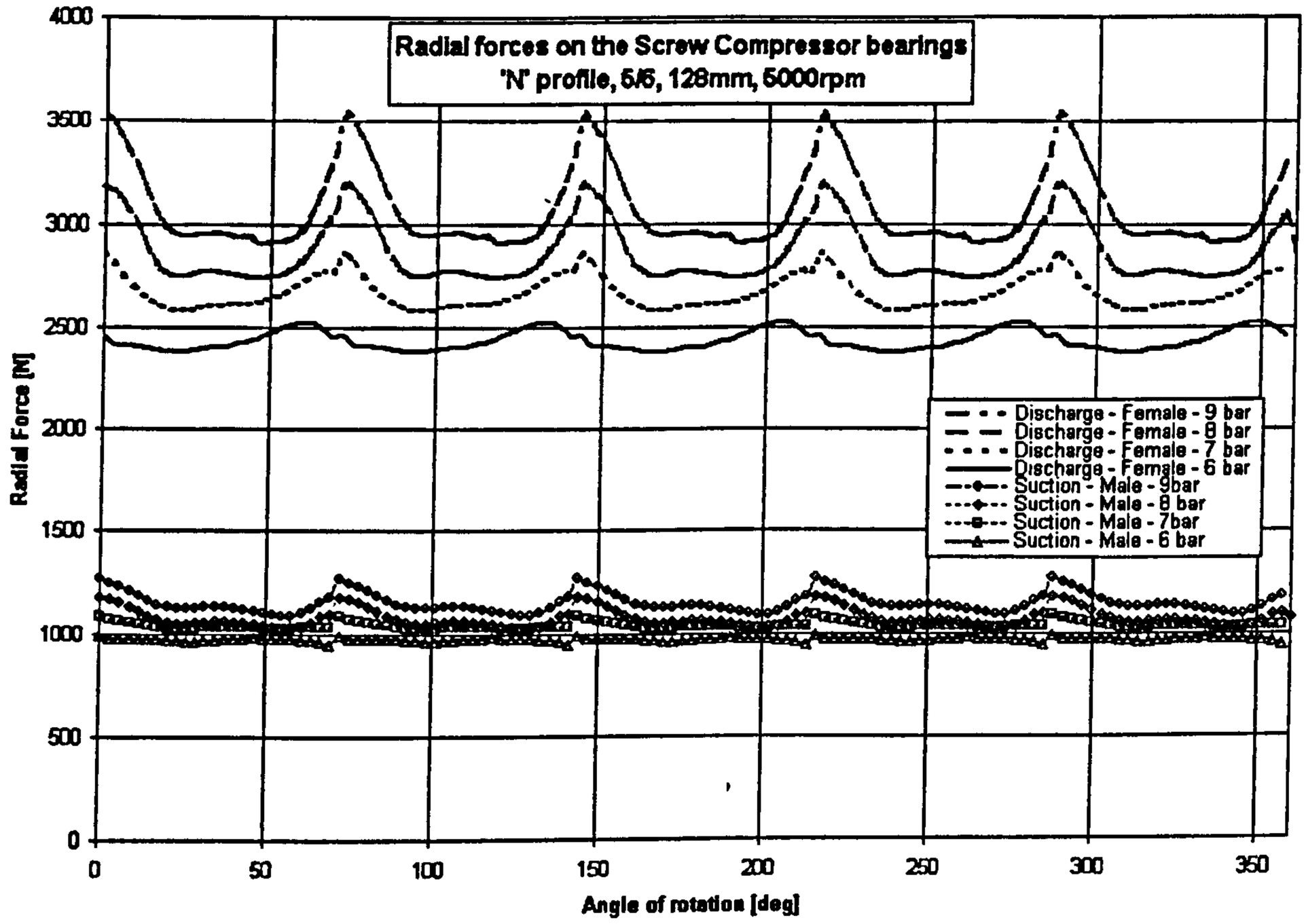

Figure 6-23 Radial bearing forces acting on supporting bearings

The results obtained from the CFD simulation model are later used to calculate such compressor integral parameters as delivered flow rate and consumed power input. From them, the specific power and efficiencies are conveniently obtained by a procedure explained in section 4.5. The estimated and measured values of the compressor delivery and input power are presented and compared in Figure 6-25 for all selected discharge pressures.

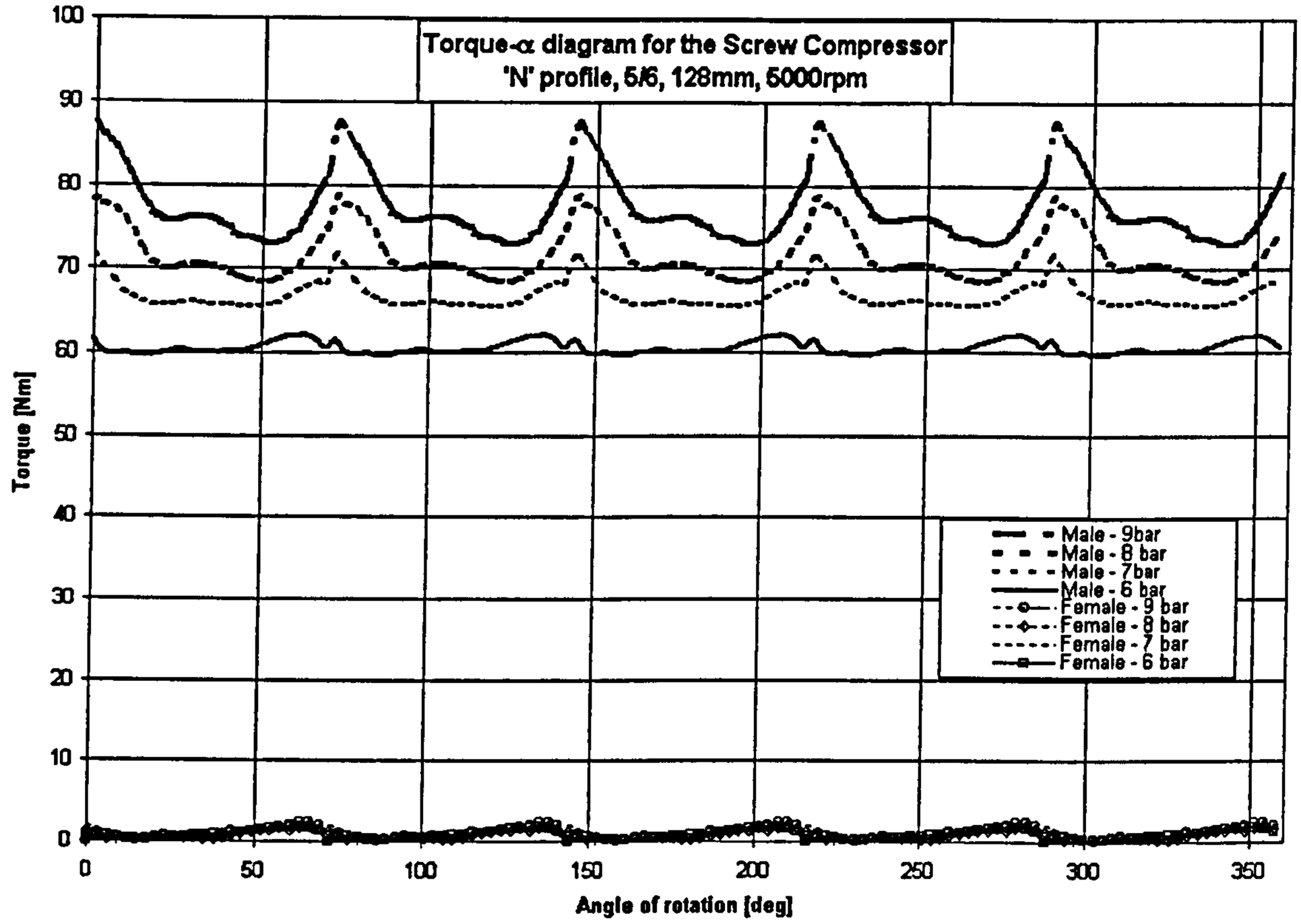

Figure 6-24 Torque on the male and female rotors

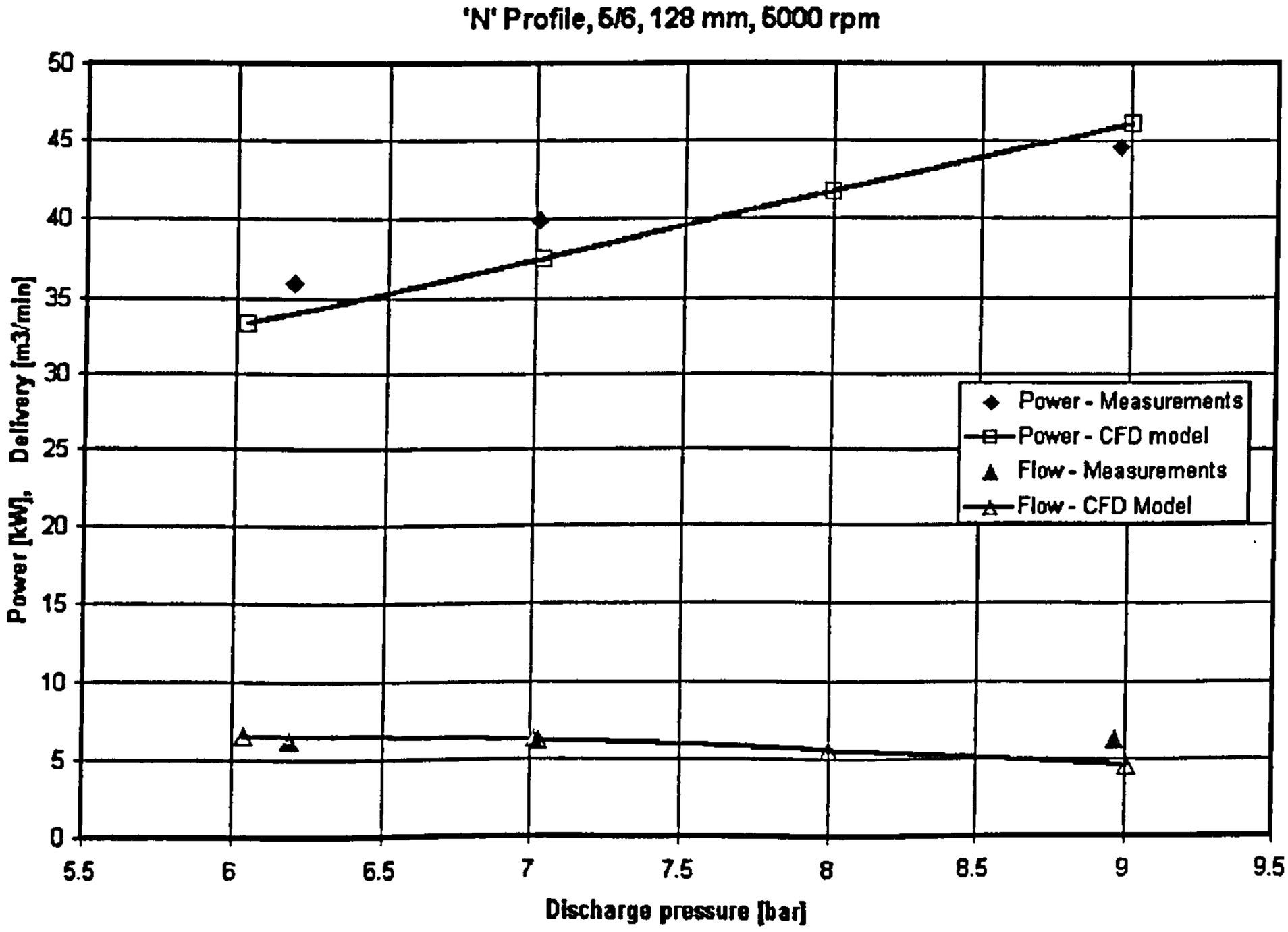

Figure 6-25 Comparison of the integral parameters at 5000 rpm shaft speed

The maximum difference between the estimated and measured power input is 8%, while the value of the compressor flow differ by up to 10%. The difference is larger for low discharge pressures where the calculations gave lower flow rate and higher power consumption then was measured. It implies that certain effects of the compressor flow are not estimated well enough. The results presented for this compressor were obtained by calculation assuming the laminar flow. In the following section, a k-ε model of turbulence is incorporated in the flow calculation and the results are compared with the laminar flow calculations.

6.3.4 Influence of turbulence upon the screw compressor flow

A standard k-ε model of turbulence is applied here and the results of the laminar and turbulent flow calculations obtained by these models within the same screw compressor are compared. The turbulence is implemented through the two additional governing equations of kinetic energy of turbulence and its dissipation as explained in Chapter 3. These two equations are solved separately and their solution, k and ε values, are used to balance the momentum and pressure equations through turbulence viscosity in the next iteration step. The next step approach is applied for two reasons. Firstly, profiles of turbulent kinetic energy and its dissipation contain more peaks than the main velocity profile, which are difficult to capture, and secondly, non-physical negative values of k and ε can possibly appear in some cases which leads to numerical instability. An additional problem in the implementation of the turbulence model to screw compressor calculations is the very high geometry ratio of the main compressor chamber dimensions to the clearances, which can easily reach 1000. In order to maintain the block structured configuration of the numerical mesh, the number of cells in the main domain and in the clearances must be the same. This means that the numerical cells within a compressor change in size by about the same ratio. The kinetic energy of turbulence and especially its dissipation are both 'stiff' in such situations, which easily leads to calculation instability and excessive raise in dissipation rate. To explore such a situation, simple approximate calculations are applied to estimate the dissipation level and the scale of turbulence, which are similar to calculations performed by *Lumley* (1999).

Turbulence is a phenomenon in which a part of mechanical energy of the main fluid flow is transformed to internal energy. It consists of three phases, which can be classified as production, transport and dissipation. In the production phase the kinetic energy of the main flow is transferred to the largest eddies that possibly can appear in the flow. Then the energy is passed on to the next smaller eddies and on to the eddies of progressively smaller scale until the smallest scale of eddies is reached. This constitutes the transport phase of turbulence. The energy passed to the smallest eddies is transformed to heat through the dissipation phase. The amount of energy of turbulence dissipated per unit mass is called the dissipation ε. It is proportional to the energy of the turbulence and the natural time scale of the most energetic eddies. It can be expressed as:

$$\varepsilon = u^2 \frac{u}{l} = \frac{u^3}{l} \sim \frac{k^{\frac{3}{2}}}{l}, \tag{6.1}$$

where u is the velocity, l is the length scale of the most energetic eddies and k is the kinetic energy of turbulence. The smallest scale at which the energy is transferred to heat is called the Kolmogorov microscale,

$$\eta = \sqrt[4]{\frac{\nu^3}{\varepsilon}} \tag{6.2}$$

where ν is the kinematic viscosity. According to *Lumley* (1999), it is the experimental fact that the most energetic eddies, responsible for most of the turbulent transport, are about 1/6 size of the largest eddy. For the screw compressor this will be 1/6 of an interlobe or 1/6 of the clearance in the gaps. Bearing all these facts in mind, the following estimate is valid for the compressor under consideration here.

In the interlobe: The size of an interlobe is obtained as the difference between the outer and inner rotor radii, $\Delta = 24.1\ mm$. This can be regarded as the size of the largest eddy which can fit in the interlobe. The size of the most energetic eddy will thus be $l \approx 4mm$. The fluid velocity in that area is of the same order of magnitude as the rotor velocity. The male rotor rotates at 5000 rpm which gives *33.2 m/s* tip speed and *20 m/s* root

speed. Assume that the turbulent velocity is twice the mean value of these two velocities, i.e. $u \approx 50\ m/s$. The kinematic viscosity of air at 20°C suction temperature is $\nu = 1.51 \times 10^{-5}\ m^2/s$. This gives a dissipation rate of $\varepsilon \approx 3 \times 10^7\ W/kg = 30 MW/kg$, and the length scale of the smallest eddy $\eta \approx 2 \times 10^{-6}\ m = 2\ \mu m$. The value of 30 *MW/kg* is enormous but the mass of air in the interlobe is only about 2 *g* and it remains there for very short time, in this case only about 2 *ms*. The temperature rise within the compressor during that time is not more than 150 *°C*.

In the clearance: Assume the mean clearance size in this compressor is $\delta = 100\ \mu m$. The size of the most energetic eddy in this case is $l \approx 15\ \mu m$. The velocity in the clearances rises to the speed of sound, which for a suction temperature of 20°C has the value of *341 m/s*. For a discharge temperature of 150°C, the speed of sound is *422 m/s*. If the density at discharge has increased six times from the suction value, the kinematic viscosity becomes $\nu \approx 5 \times 10^{-6}\ m^2/s$. In that case, the dissipation rate increases to the enormous value of $\varepsilon \approx 4 \times 10^{12}\ W/kg$ while the Kolmogorov microscale drops to a fraction of a micrometer, say *0.1 μm*. One should bear in mind that the leakage flow is less then 10% of the main flow which means that the mass in the clearances is of the one order of magnitude lower than that of the main flow. In addition, the time for which the fluid remains in the clearance gaps is only a fraction of the compressor cycle. Due to that, the energy wasted by turbulence in clearances is not large.

The Reynolds numbers of turbulence in the main domain and in the clearances can be calculated from the above values using:

$$\frac{\eta}{l} = \left(\frac{\nu^3}{\varepsilon l^4}\right)^{1/4} = \left(\frac{\nu^3}{u^3 l^3}\right)^{1/4} = R_l^{-\frac{3}{4}}. \tag{6.3}$$

In the main domain, the Reynolds number of turbulence is $R_l \approx 2.5 \times 10^4$ and in clearances $R_l \approx 8 \times 10^2$. Assuming the similarity of molecular and turbulent transport of momentum for gases, one can state that the effective viscosity is proportional to the velocity scale and the length scale of the process responsible for transport. Therefore,

the measure of molecular transport is ν and the measure of a turbulent transport is $\nu_T \approx ul$. Then,

$$\frac{\nu_T}{\nu} = \frac{ul}{\nu} = R_t. \tag{6.4}$$

Using the previous equation, values for turbulent or eddy viscosity are obtained in the main domain and in the clearances. These are $\nu_T = 3.8\times10^{-1}\, m^2/s$ in the main domain and $\nu_T = 1.2\times10^{-2}\, m^2/s$ in the clearances. These are far larger than the molecular viscosity.

One more measure can be introduced here. This is the relative distance for which the turbulence will carry a property, which can be momentum or the fluid itself, for example. The relative distance can be estimated from:

$$L \approx \sqrt{\frac{2}{3}\nu_T \tau}, \tag{6.5}$$

where τ is the time for which the turbulence remains in a place. Therefore, in the interlobe, a turbulence will carry a property for $\frac{L}{\Delta} \approx \sqrt{\frac{2}{3}u\frac{l}{\Delta^2}\tau_\Delta} \approx 0.68$, while in the clearances $\frac{L}{\delta} \approx \sqrt{\frac{2}{3}u\frac{l}{\delta^2}\tau_\delta} \approx 0.63$. From these two values, the conclusion may be derived that turbulence plays a role in screw compressor processes. It is more important in the suction domain and interlobes exposed to the suction where turbulent viscosity can be four orders of magnitude higher than its molecular equivalent and where a property is transported by turbulence for about two thirds of the available interlobe space. Turbulence dies out in the compression chambers with the increase of pressure and decrease of velocity and has no significant influence in the discharge domain. In the clearances, turbulent transport exists, but it lasts for an extremely short time and produces no excessive heat. However, the fluid is transported by turbulence for approximately two thirds of the available space in clearances.

The values calculated above give an insight into problems of turbulence. The turbulence effects are in this thesis estimated by turbulence model based on Reynolds averaged Navier-Stokes equations. Both, the kinetic energy of turbulence and its dissipation rate are high in certain regions of the compressor and remain there for an extremely short time. The exact calculation requires a numerical mesh with a large number of numerical cells and a very short time step. As it was not possible, the standard k-ε model is used here to show the ability of the model and to give values of the local and integral parameters of the flow calculated with a model of turbulence. These are compared with the results of laminar flow calculation. Other models of turbulence have not been investigated since that was outside the scope of this thesis. The development of a turbulence model for positive displacement machines is recommended for the future.

In order to compare the significance of turbulent and laminar flow assumptions on the compressor performance predictions without including secondary influences, a further analysis on the earlier used compressor was made, in which the presence of oil was excluded. The numerical mesh taken for this purpose contains 236780 numerical cells. The discharge pressure is kept at 3 bar. A low pressure discharge is preferred because of the larger difference in flow parameters noticed the between laminar flow calculations and measurements under these conditions. It seems that turbulence has more significant influence to this case. The compressor speed was 5000 rpm.

The pressure distribution and velocity field for both the laminar and turbulent flow cases are compared in Figure 6-26. The laminar results on the top diagram and the turbulent ones on the bottom diagram are not significantly different. Higher velocities in the interlobes at low pressure are recorded with laminar flow calculations while the pressure fields seem to be very similar.

The pressure rise in the compressor is compared in more detail in the pressure-angle diagram, Figure 6-27. Only a small difference is recorded between the two flows where a slightly higher pressure was obtained with the turbulent flow model. This gives the impression that turbulence has some influence on the calculation in the leakage path area. Turbulence reduces the leakage flow, which results in more delivery and raises pressure in the working chamber. However, the difference in power obtained by this means was very small, being only 0.5%, as shown in Table 6-2.

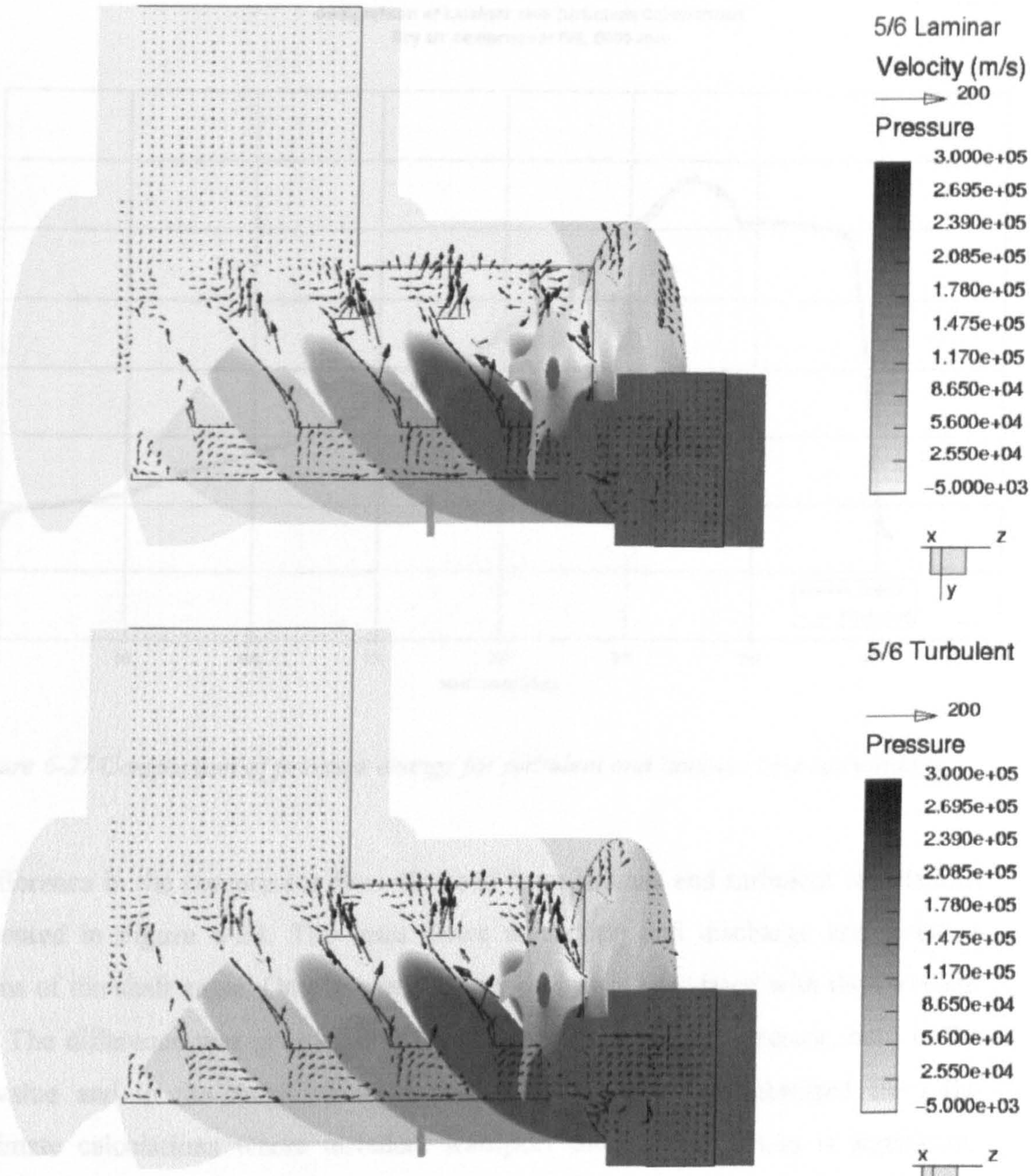

Figure 6-26 Comparison of pressure field and velocity vectors across the screw compressor

Top – laminar model; Bottom – turbulent model

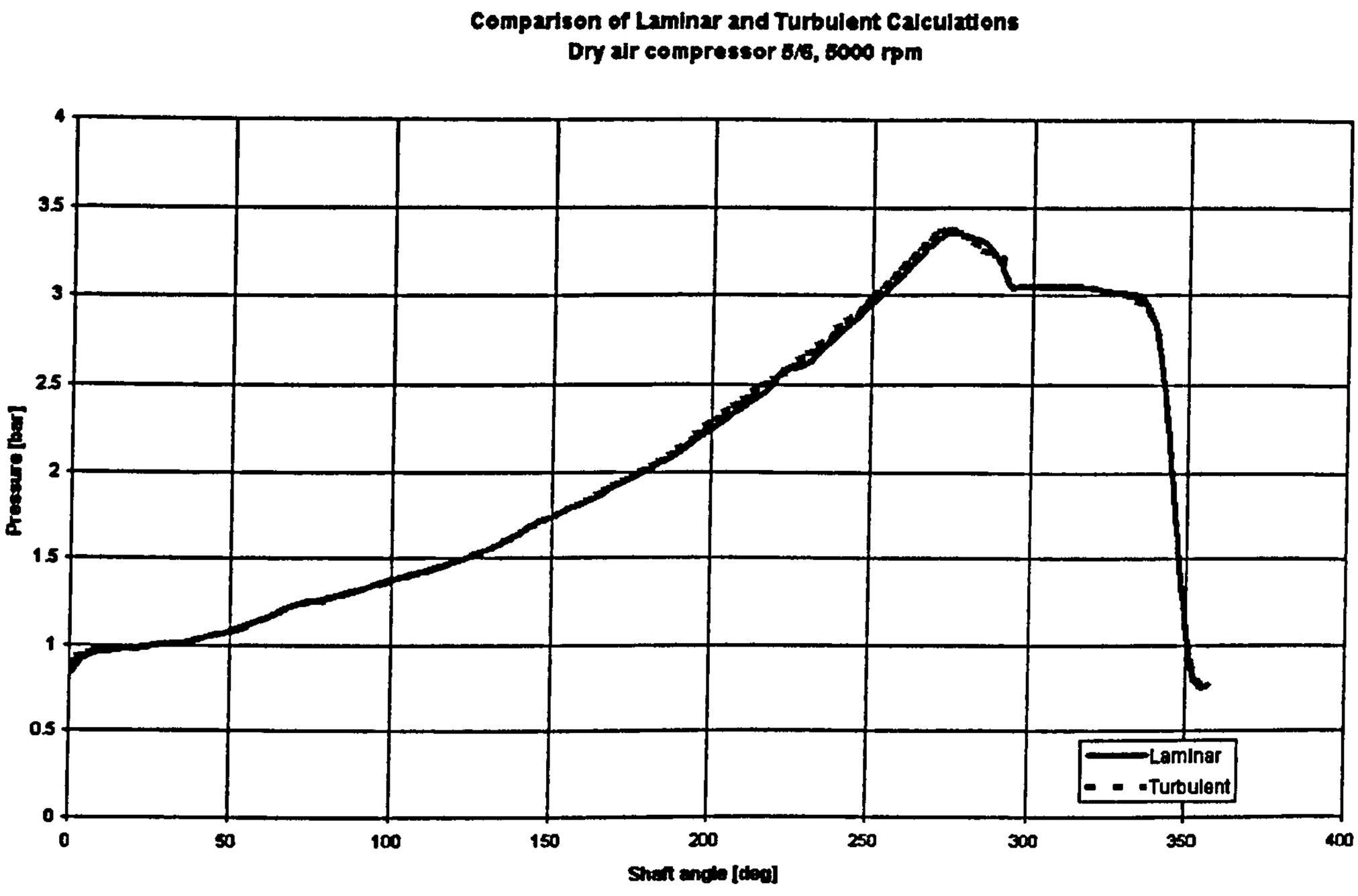

Figure 6-27 Comparison of pressure change for turbulent and laminar flow calculations

The difference in the compressor flow obtained from laminar and turbulent calculations is presented in Figure 6-28. The mass flows at suction and discharge are given as functions of the shaft angle. On average, 4% higher flow is calculated with the turbulent model. The difference was greater at the discharge end of the compressor, both in the mean value and in the amplitude. This agrees with the results obtained from the approximate calculations where turbulent transport through clearances is significant. The difference in flow obtained at the suction end is, on average, below 3% less. This shows that a compressor with large suction opening has no significant dynamical losses, although turbulence exists in the compressor low pressure domains. It is expected that the difference between the laminar and turbulent flow calculations will be smaller for higher discharge pressures and lower compressor speeds.

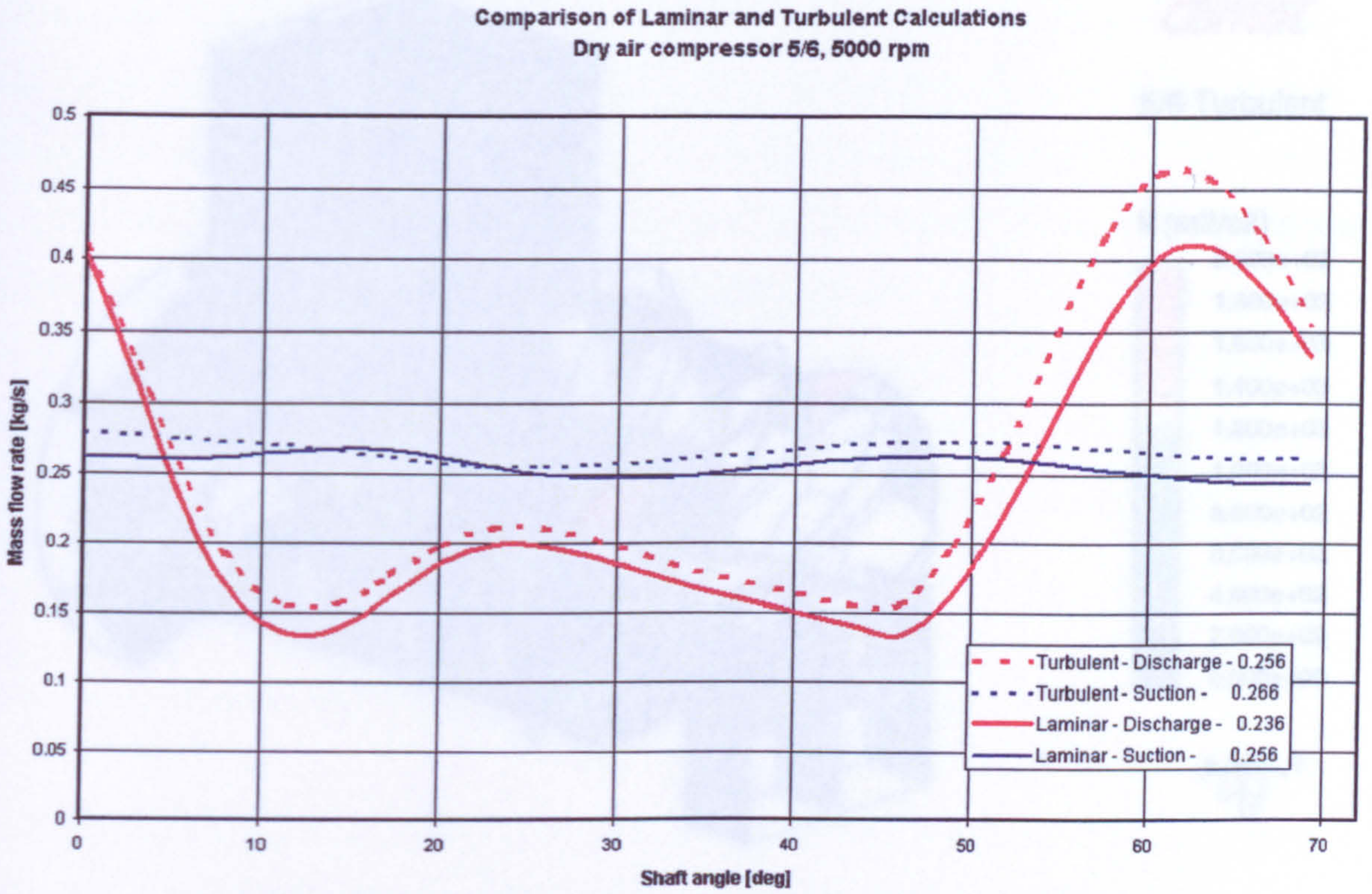

Figure 6-28 Comparison of fluid flow at inlet and exit of screw compressor

The integral parameters obtained from both, the laminar and turbulent numerical models are presented in Table 6-2. According to these results, it can be concluded that turbulence has some influence on the screw compressor. Its effect is greater at lower pressure ratios and low compressor speeds.

Table 6-2 Integral parameters calculated with laminar and turbulent model

	Flow rate [m3/mim]	Power [kW]	Specific power [kW/m3/min]	Outlet temperature [K]
Laminar	2.739	15.569	5.684	402.341
Turbulent	2.861	15.659	5.473	402.476

More detailed insight in the results obtained from the k-ε model of turbulence can be found in the following four figures; Figure 6-29 shows the kinetic energy of turbulence. The dissipation rate is presented in Figure 6-30, the turbulent viscosity in Figure 6-31 and the dimensionless distance from wall y+ is given in Figure 6-32.

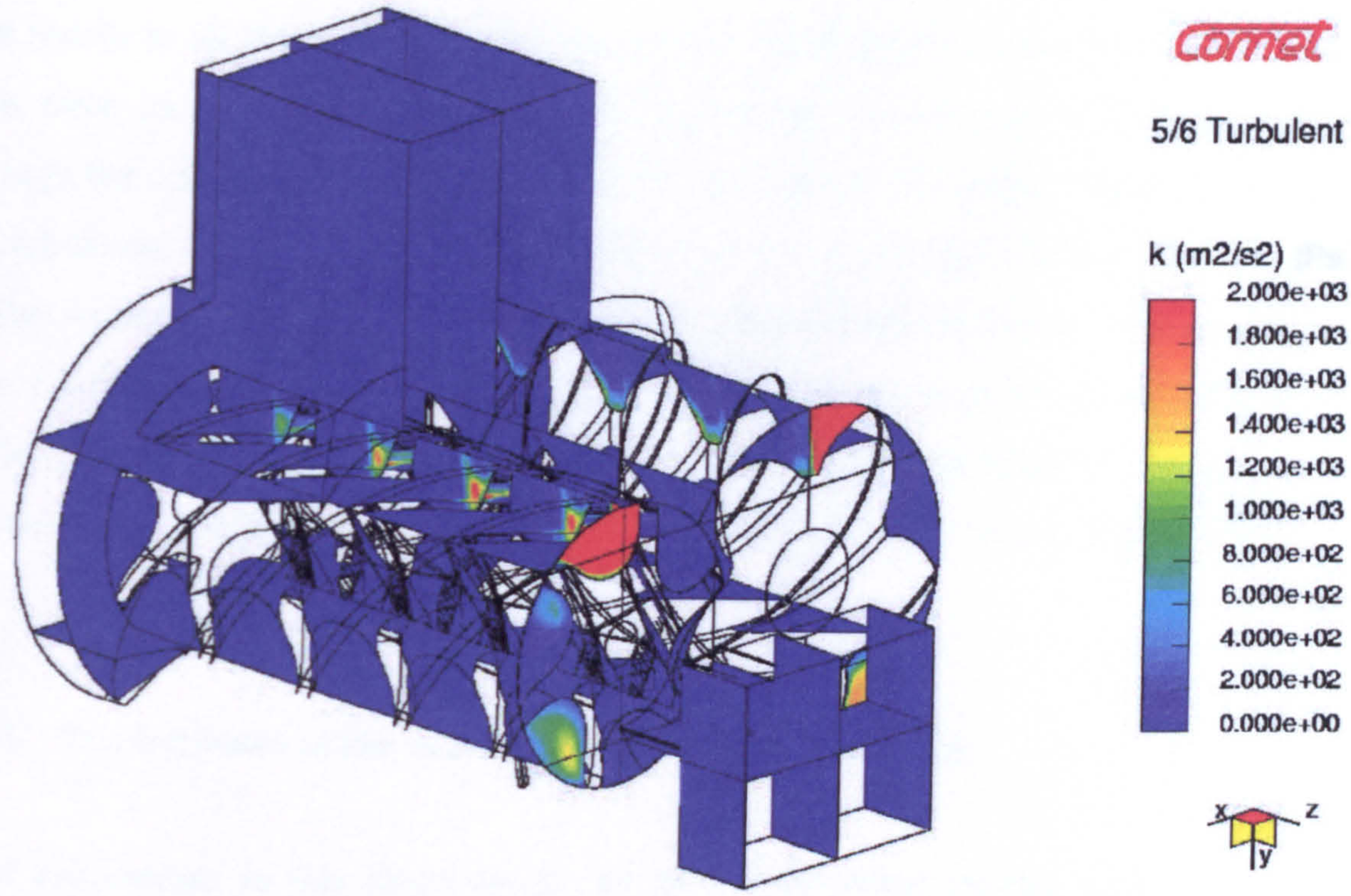

Figure 6-29 Kinetic energy of turbulence within the screw compressor

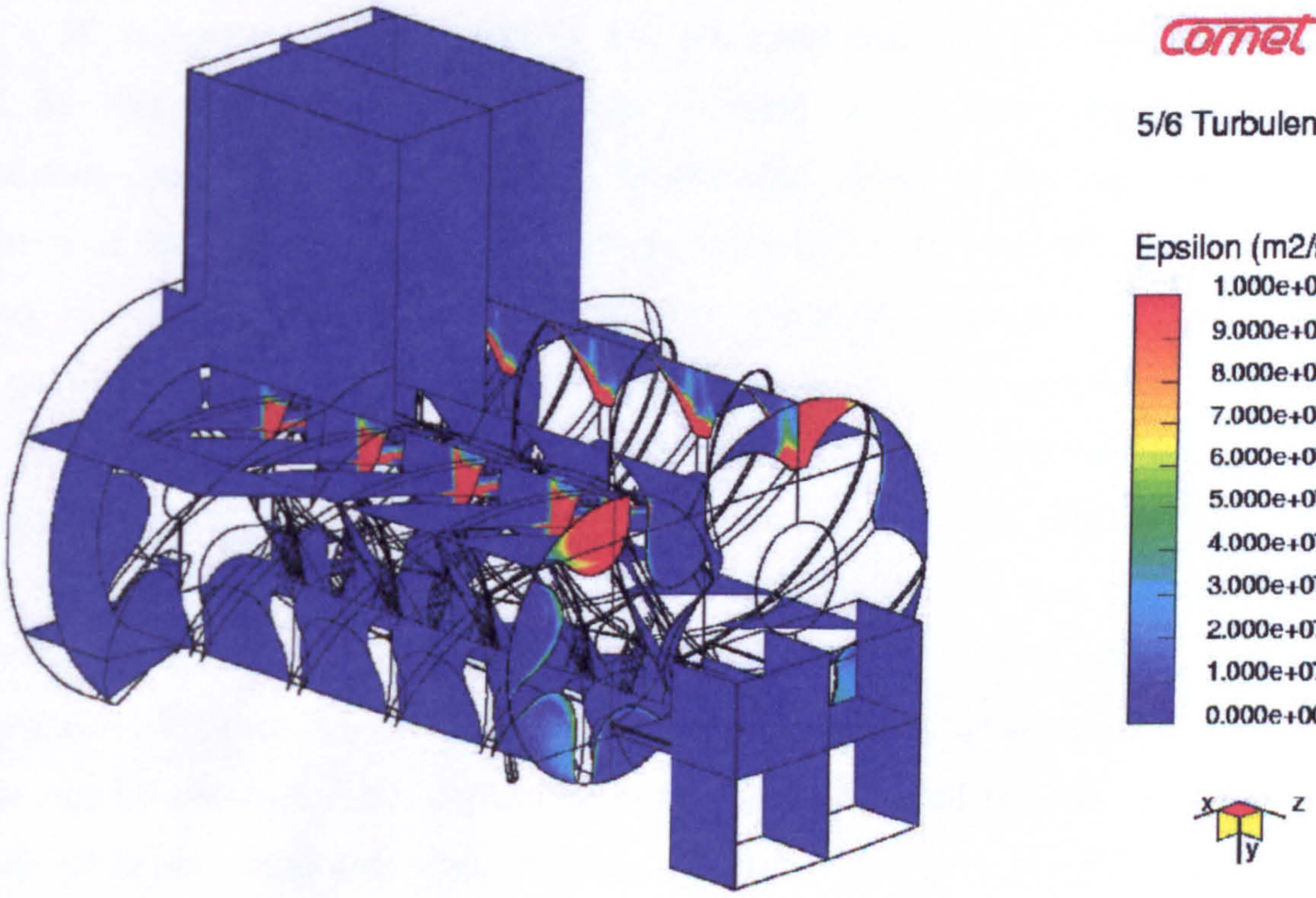

Figure 6-30 Dissipation rate within the screw compressor

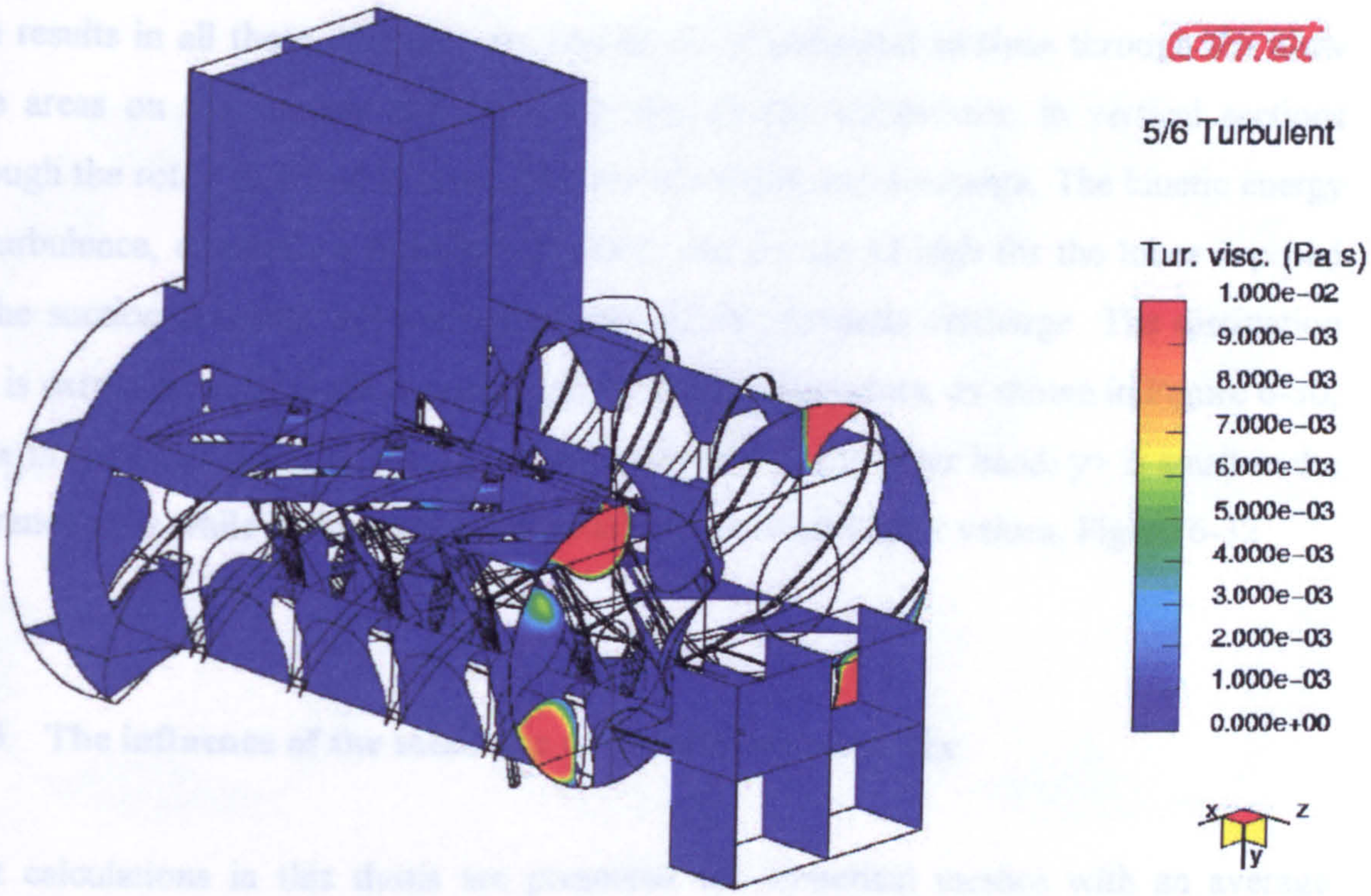

Figure 6-31 Turbulent viscosity within the screw compressor

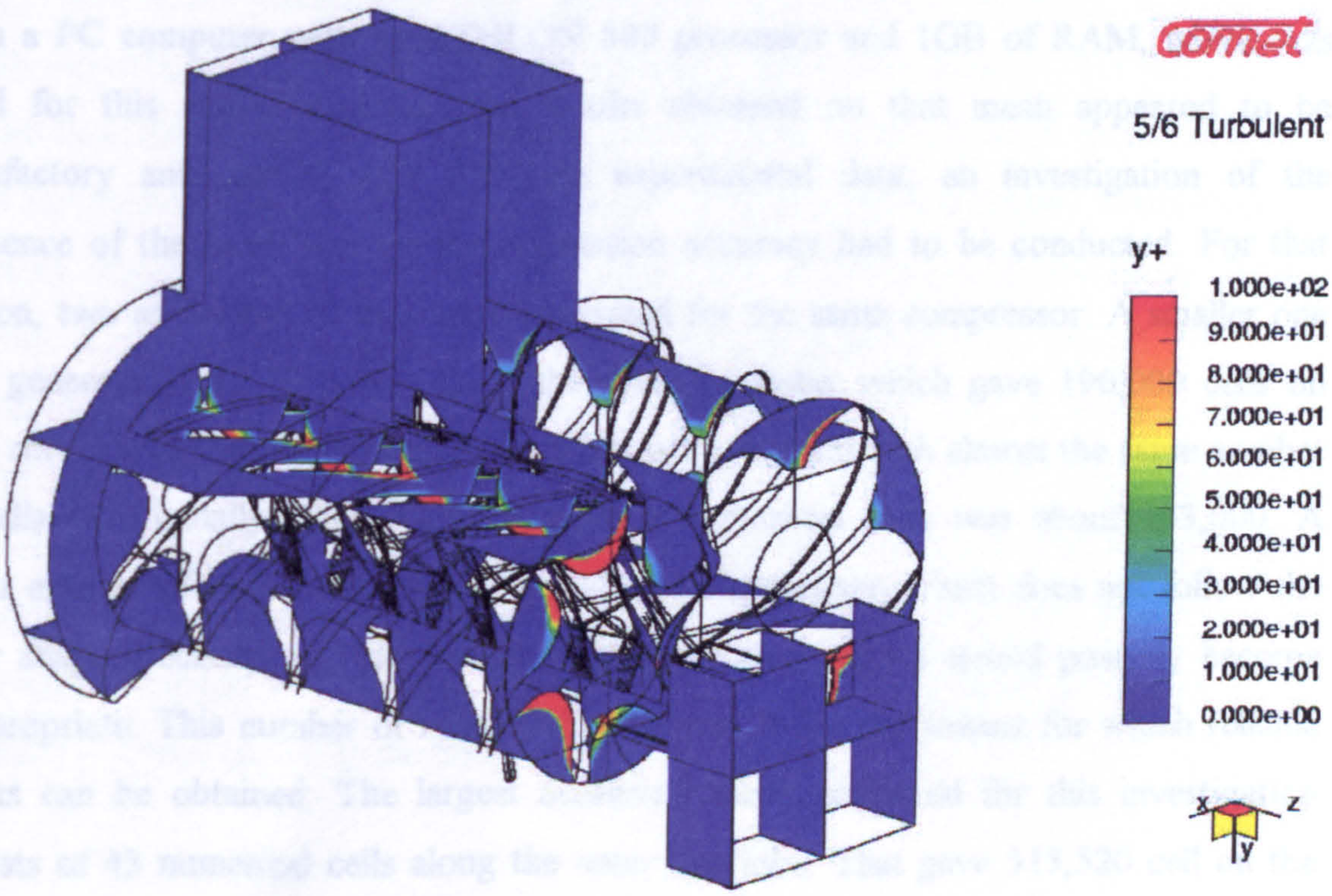

Figure 6-32 Dimensionless distances from the wall within the compressor

The results in all these diagrams are presented in horizontal sections through the blow hole areas on the suction and discharge side of the compressor, in vertical sections through the rotor axes and in cross sections at suction and discharge. The kinetic energy of turbulence, dissipation, turbulent viscosity and y+ are all high for the lobes exposed to the suction domains. All these gradually die out towards discharge. The dissipation rate is extremely high in the clearance gaps between the rotors, as shown in Figure 6-30, while in the other domains it is significantly lower. On the other hand, y+ is small in the clearance gaps while in the main domains at suction it has higher values, Figure 6-32.

6.3.5 The influence of the mesh size on calculation accuracy

Most calculations in this thesis are presented for numerical meshes with an average number of 30 cells along one interlobe and a similar number of time steps selected for the rotor to rotate between two interlobe positions. The numerical mesh for the compressor in this example consists of about 450,000 cells of which About 322,000 numerical cells define the rotor domains. This was a convenient number of cells to use with a PC computer with an ATHLON 800 processor and 1GB of RAM, which was used for this study. Although the results obtained on that mesh appeared to be satisfactory and agreed well with the experimental data, an investigation of the influence of the mesh size on the calculation accuracy had to be conducted. For that reason, two additional meshes were generated for the same compressor. A smaller one was generated with 20 points along the rotor interlobe, which gave 190,000 cells on both rotors while the other compressor parts were mapped with almost the same number of cells as originally. The overall number of numerical cells was about 353,000. A lower number of cells on the rotors would give a geometry, which does not follow the rotor shape precisely, and the interconnection between rotors would possibly become inappropriate. This number of numerical cells is probably the lowest for which reliable results can be obtained. The largest numerical mesh generated for this investigation consists of 45 numerical cells along the rotor interlobe. That gave 515,520 cell on the rotors and 637,000 cells for the entire compressor domain. This was the biggest numerical mesh that could be rested on the available computer without swapping. These three numerical meshes are presented in Figure 6-33 in the cross section perpendicular to the rotor axes.

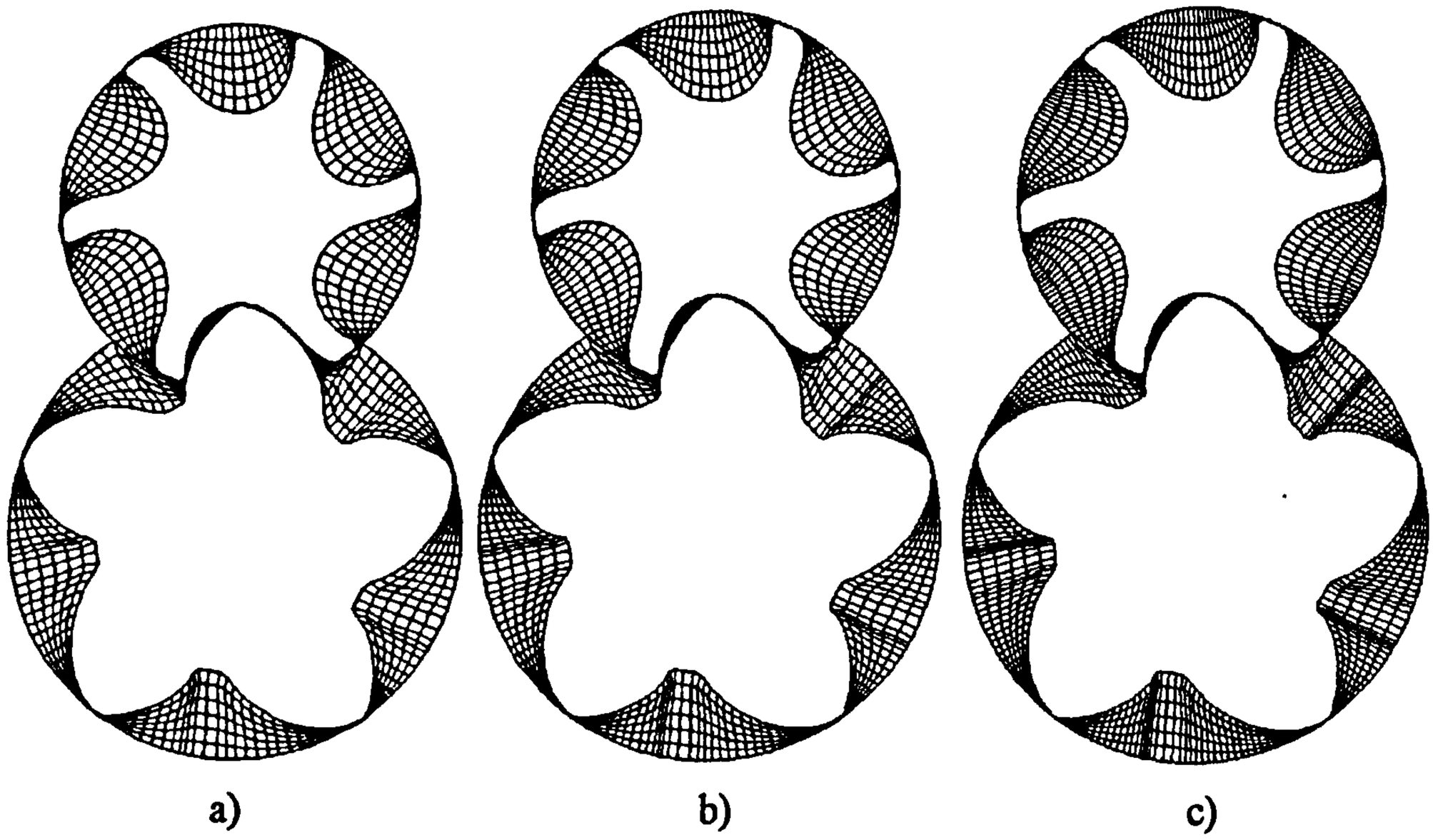

Figure 6-33 Three different mesh sizes for the same compressor

a)189,144; b)322,560; c)512,520

The results of the calculations are presented in Figure 6-34 in the form of a pressure-angle diagram, and in Figure 6-36 as a discharge flow-angle diagram. The first diagram shows how the calculated working pressures for all three investigated mesh sizes agree with the measurements. The lowest number of cells gives the highest pressure in the working chamber and vice versa. As a result of that, the consumed power is changed slightly, from 42 kW obtained with the smallest mesh to slightly less then 41 kW for the largest mesh. The difference between the two is less then 3%. This situation is shown in Figure 6-35. The diagram shows the largest difference within the cycle in the discharge area of the compressor. Some difference is also visible in the middle area of the diagram which seems to be a consequence of the leakage flows obtained on smaller meshes between the rotors. In that area, the mesh is probably too coarse to capture all the oscillations which appear in the flow.

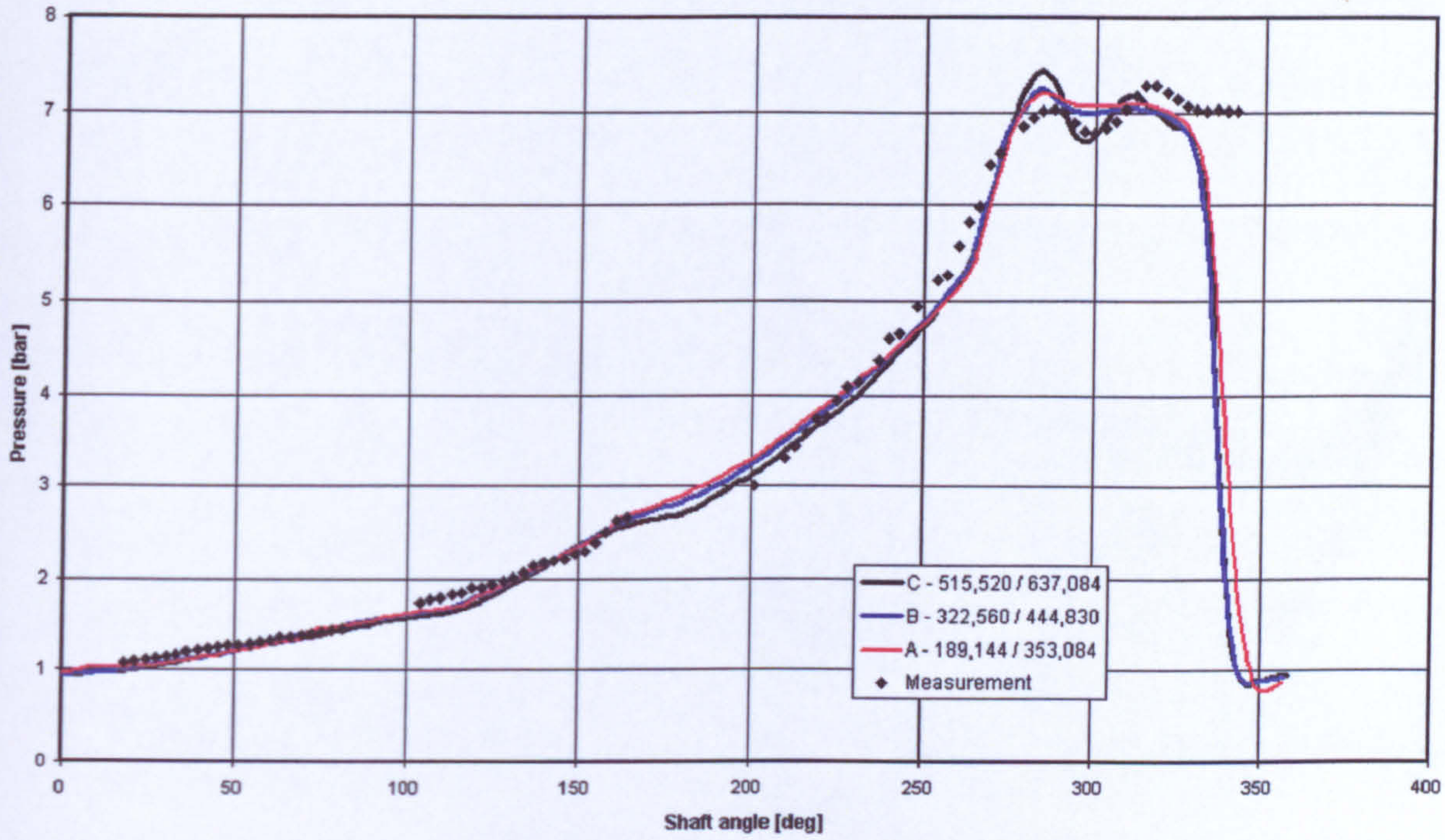

Figure 6-34 P-alpha diagrams for three different mesh sizes

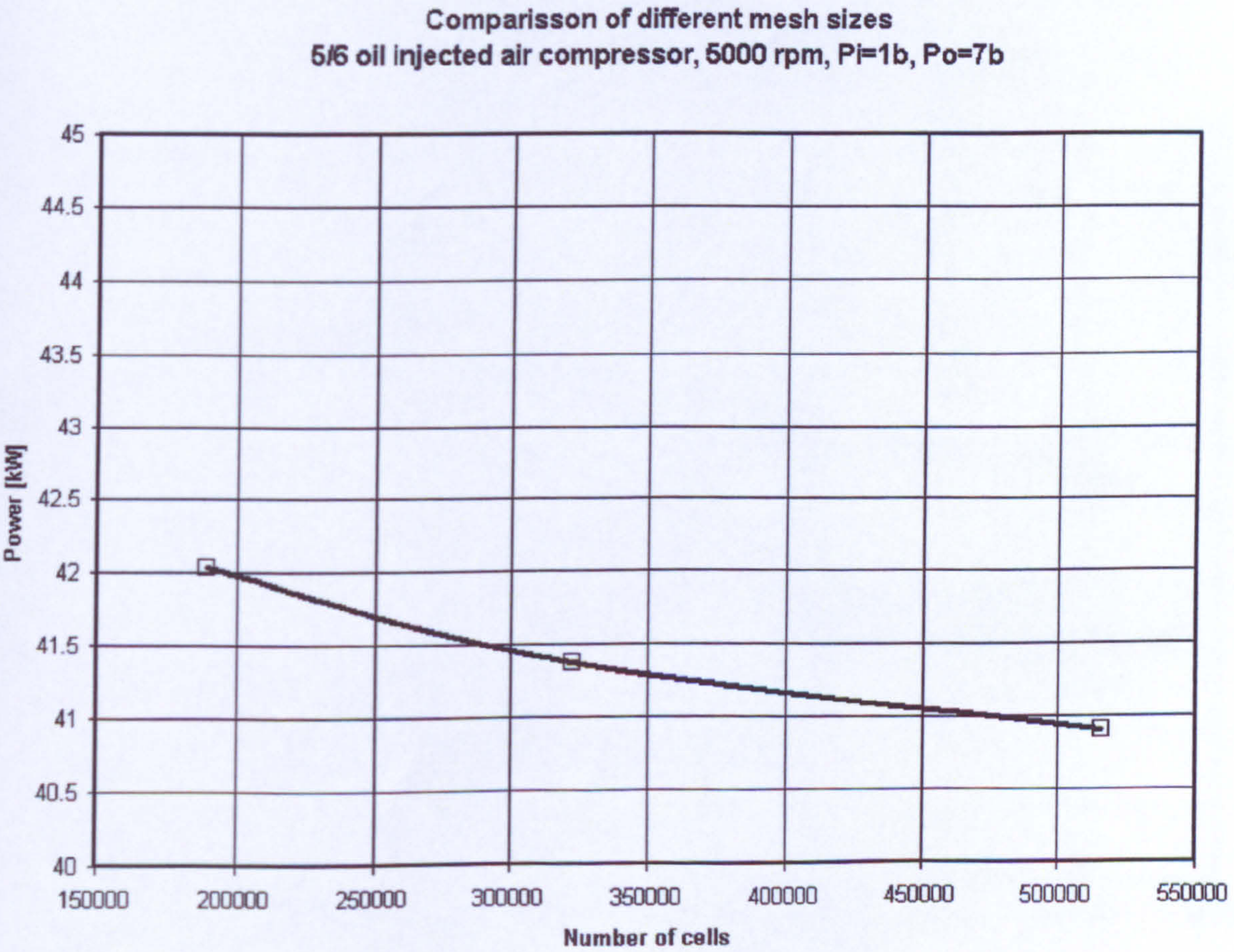

Figure 6-35 Compressor power calculated with three different mesh sizes

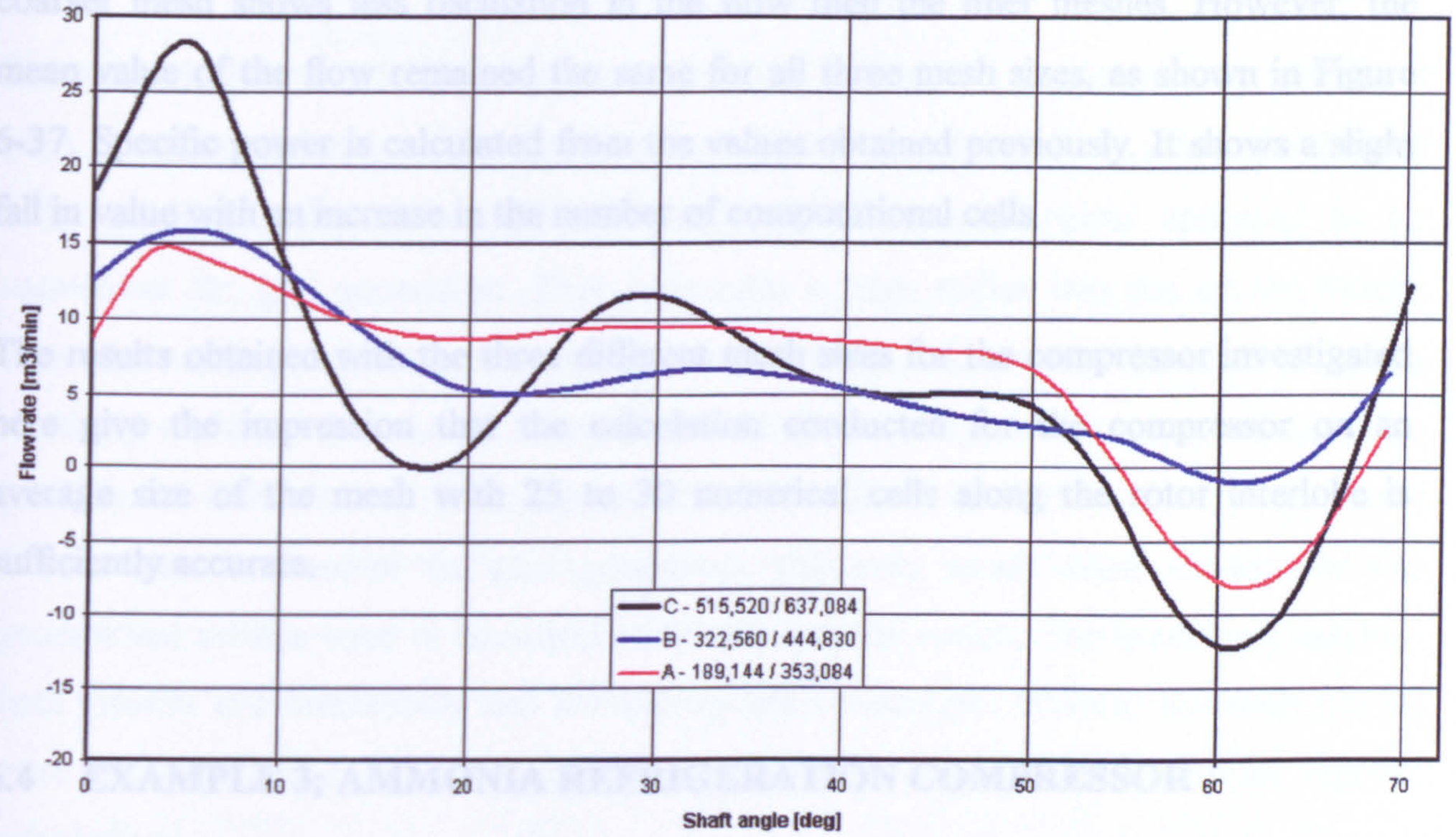

Figure 6-36 Discharge flow rates for different mesh sizes

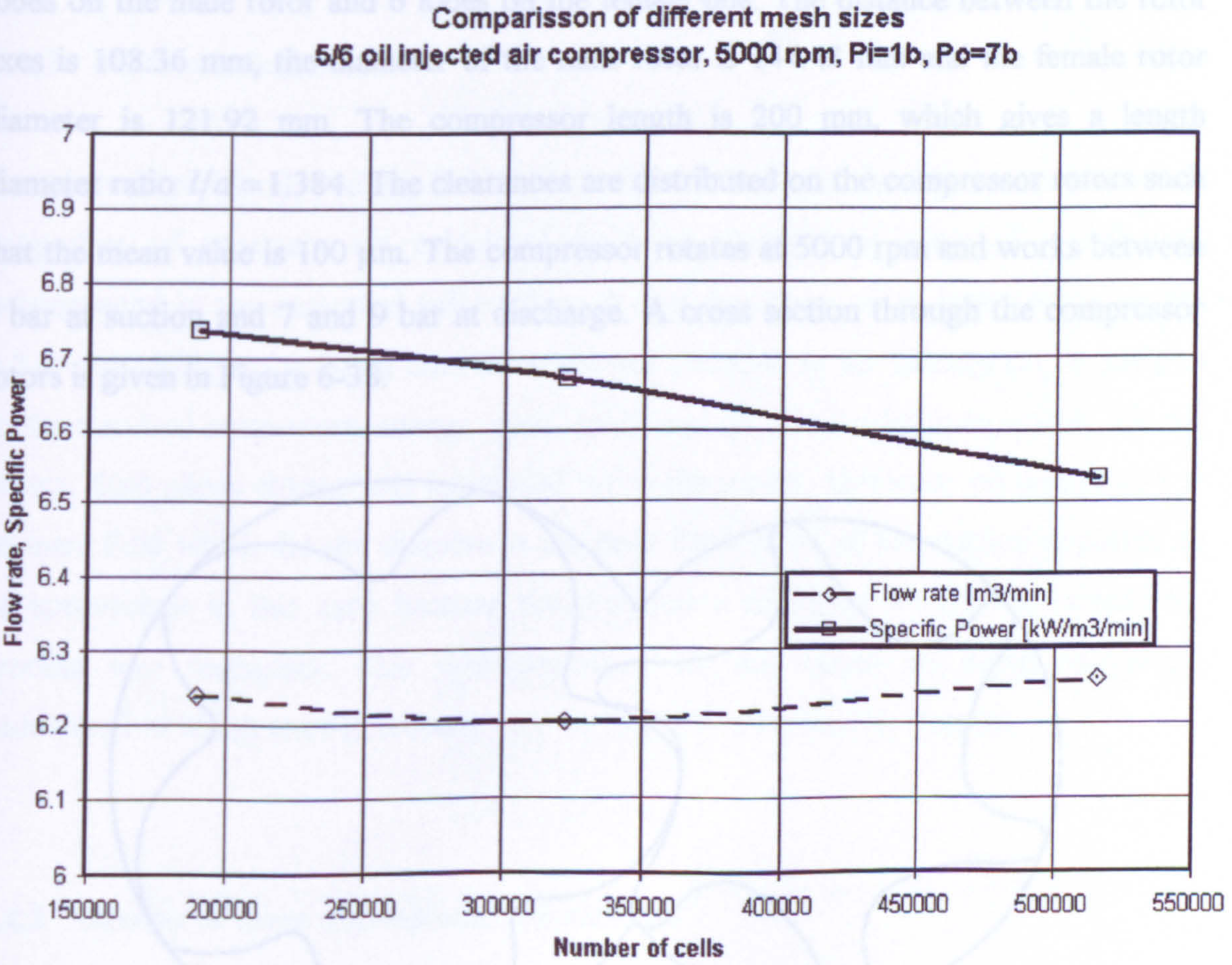

Figure 6-37 Integral flow rate and Specific power obtained with different mesh sizes

Discharge flow diagrams as function of rotation angle are given in Figure 6-36. The coarser mesh shows less oscillation in the flow then the finer meshes. However, the mean value of the flow remained the same for all three mesh sizes, as shown in Figure 6-37. Specific power is calculated from the values obtained previously. It shows a slight fall in value with an increase in the number of computational cells.

The results obtained with the three different mesh sizes for the compressor investigated here give the impression that the calculation conducted for the compressor on an average size of the mesh with 25 to 30 numerical cells along the rotor interlobe is sufficiently accurate.

6.4 EXAMPLE 3; AMMONIA REFRIGERATION COMPRESSOR

This example is given for the oil injected ammonia refrigeration compressor with 5 lobes on the male rotor and 6 lobes on the female one. The distance between the rotor axes is 108.36 mm, the diameter of the male rotor is 144.43 mm and the female rotor diameter is 121.92 mm. The compressor length is 200 mm, which gives a length diameter ratio $l/d = 1.384$. The clearances are distributed on the compressor rotors such that the mean value is 100 μm. The compressor rotates at 5000 rpm and works between 2 bar at suction and 7 and 9 bar at discharge. A cross section through the compressor rotors is given in Figure 6-38.

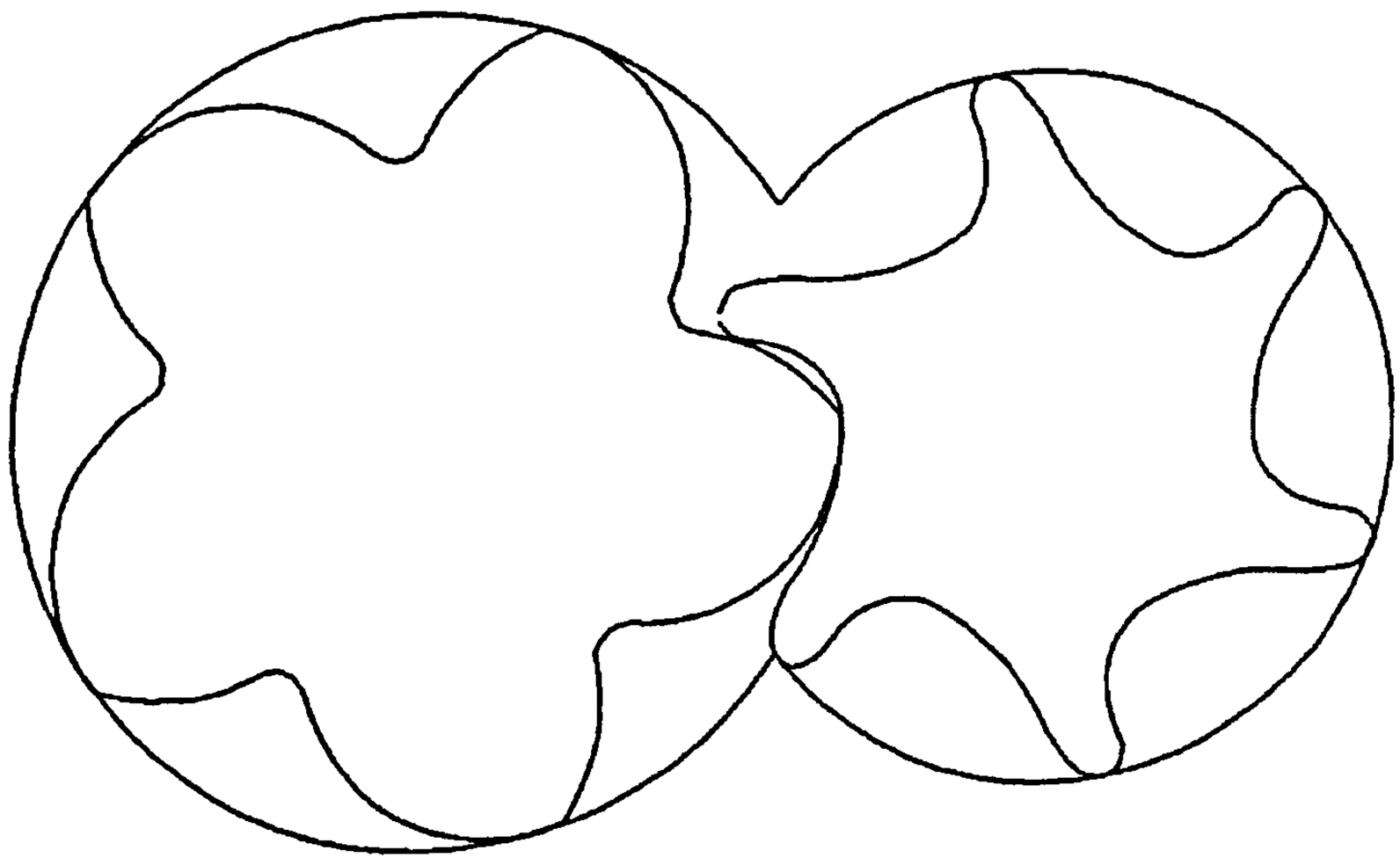

Figure 6-38 Cross section of the ammonia refrigeration compressor rotors

6.4.1 Grid generation

The numerical mesh of this compressor consists of 256,690 numerical cells generated with 20 computational points distributed along one interlobe. Such a low number of cells has been selected because the geometry of the compressor appeared to be convenient for grid generation. That is because a large radius was put on the female rotor tip, which gives less curvature of the rotor lobes. Additionally, the rotor lobes are relatively shallow which is the consequence of the profile generation method used for profiling of these rotors. It is explained in more detail by *Rinder* (1987). All these factors were convenient for grid generation with only small values needed for the geometrical criteria used in boundary adaptation on the rotors. The mesh was checked both visually and numerically and the appropriate connections between the mesh blocks were established. Only 20 time steps for one interlobe rotation were needed for reliable calculations.

6.4.2 Mathematical model

Ammonia is a natural working fluid with favourable features. In this example, the fluid properties of ammonia are calculated from an equation of state of a real fluid implemented in the numerical solver through user functions, as is explained in section 4.2.4. An equation for liquid concentration was included in the calculation, in addition to the standard momentum, energy, mass, space and oil concentration equations. By this means, fluid phase change was accounted for in the model. However, oil is regarded as an inert fluid which did not dissolve in the main fluid. Such an assumption appeared to be appropriate in this case because the production of liquid within the compressor process was negligible. This was confirmed by the values of liquid refrigerant concentration which were practically zero throughout the complete domain.

6.4.3 Results of three dimensional calculations

Results of the three dimensional calculation are presented in the form of velocity field, pressure distribution and oil concentration in two different cross sections, one normal to

the rotor axis and in another horizontal section through the blow hole area. Based on these, integral parameters are calculated for this compressor in the form of pressure, torque and delivered flow.

Figure 6-39 shows an axial section through the rotors of the oil injected ammonia compressor. The large white area on the left of the figure is the male rotor while the female rotor is crossed on the right. The section is taken through the high pressure blow hole area with the suction port at the top of the figure and the discharge opening at the bottom. The rotor profile allows a large blow hole area through which a substantial amount of fluid leaks back to the domain with a lower pressure. The pressure distribution is shown in this figure together with the velocity vectors. The oil injection port is positioned on the bottom right of the figure. The oil enters the compressor through that port at relatively high speed. High velocities indicate a substantial leakage in the blow hole. The discharge pressure in this case was 9 bar. In the figure, the values of the relative pressure are given. To obtain their absolute values, atmosphere pressure of 1 bar should be added.

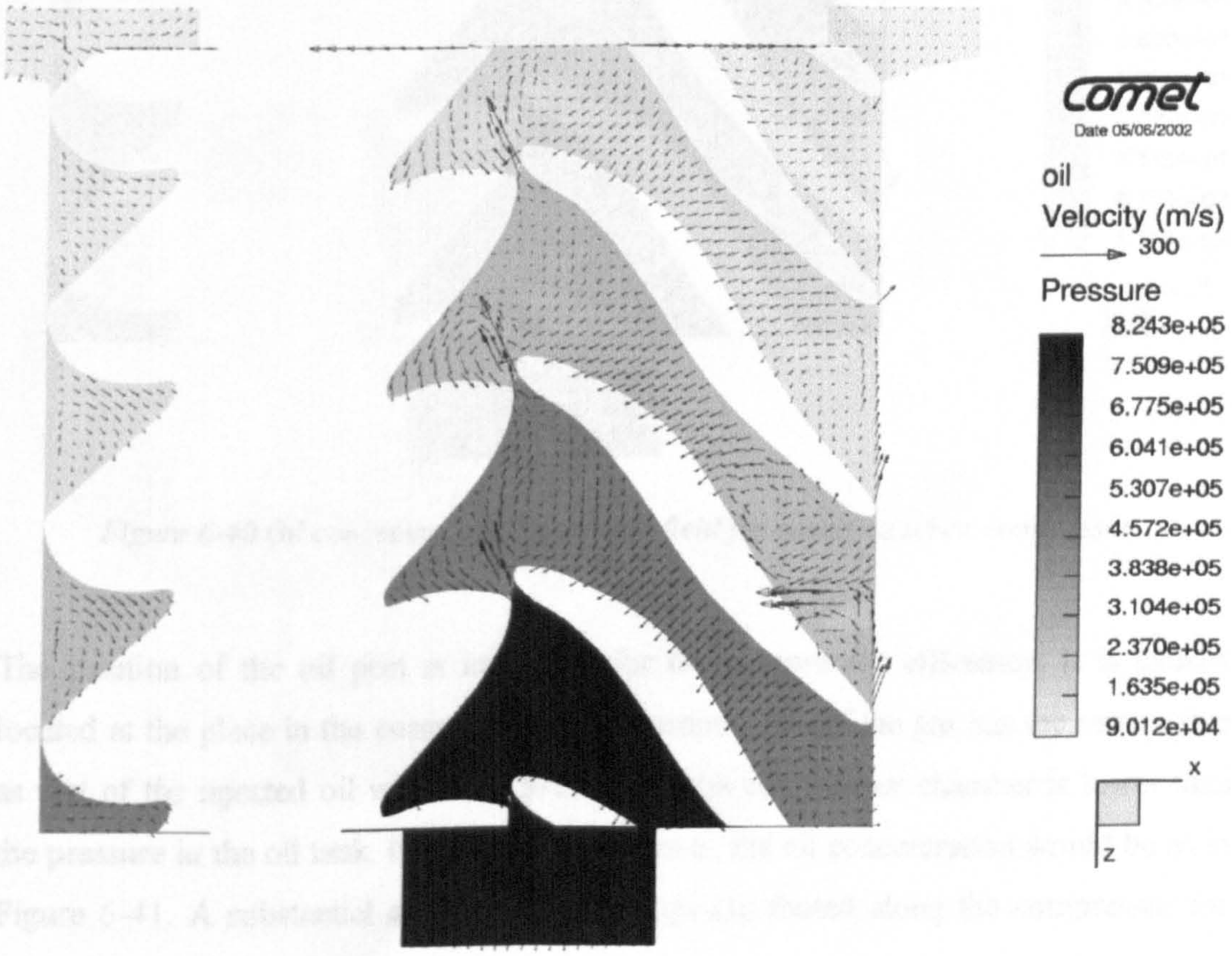

Figure 6-39 Pressure distribution and velocity field in the ammonia screw compressor

The oil concentration is presented in Figure 6-40, together with the velocity field. The dark shades on the bottom right of the figure indicate high concentration of oil at the injection point. Oil is distributed across the entire compressor with the higher concentration towards the discharge port. However, some oil together with gas leaks back to the domains with lower pressure through both the clearances and blow hole. This situation is attained when the oil injection port is positioned properly and is shown in Figure 6-41.

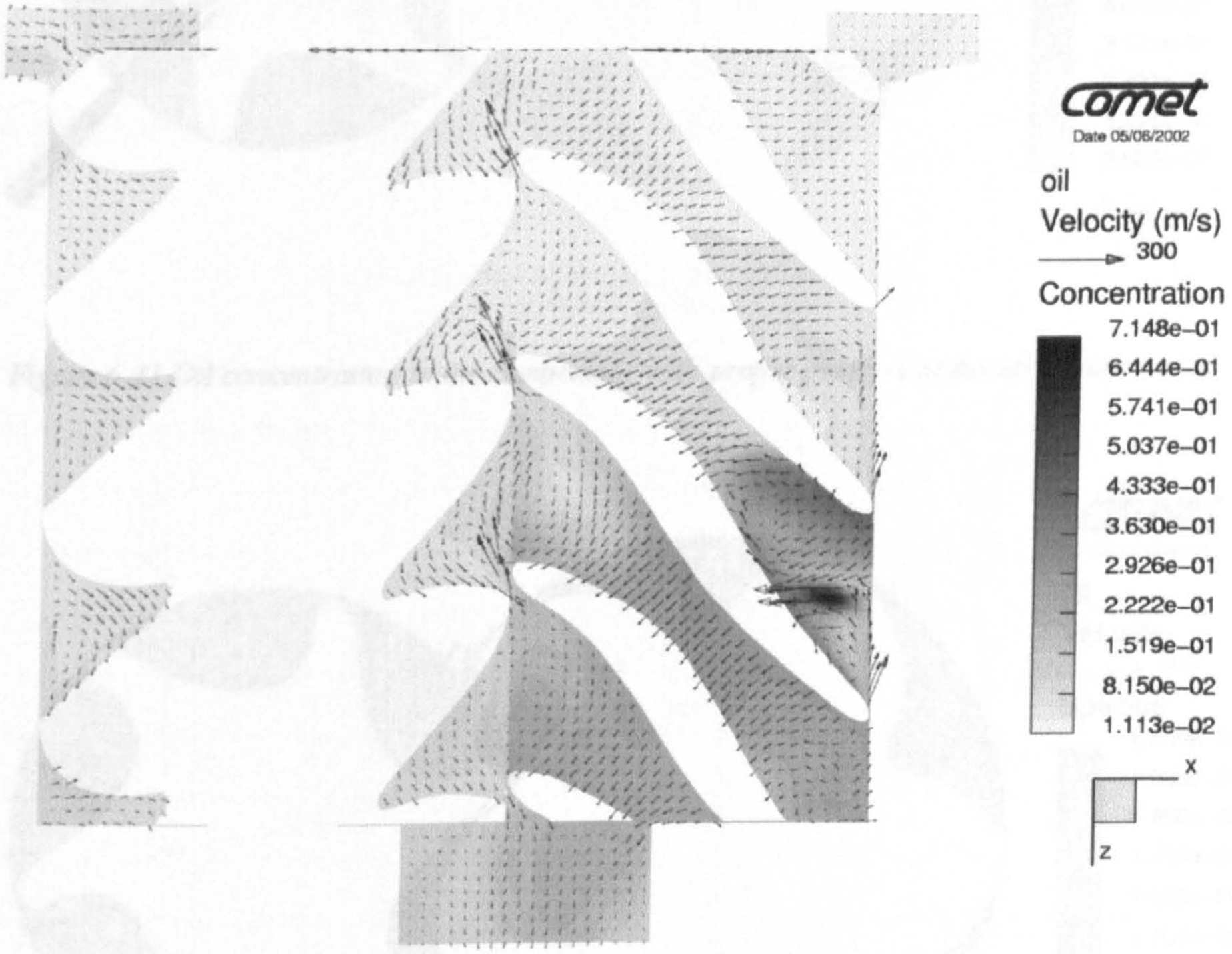

Figure 6-40 Oil concentration and velocity field for ammonia screw compressor

The position of the oil port is important for the compressor efficiency. It is usually located at the place in the compressor where temperature of the gas has the same value as that of the injected oil where the pressure in the compressor chamber is lower than the pressure in the oil tank. If these criteria are met, the oil concentration would be as in Figure 6-41. A substantial amount of oil is then distributed along the compressor for lubrication and cooling.

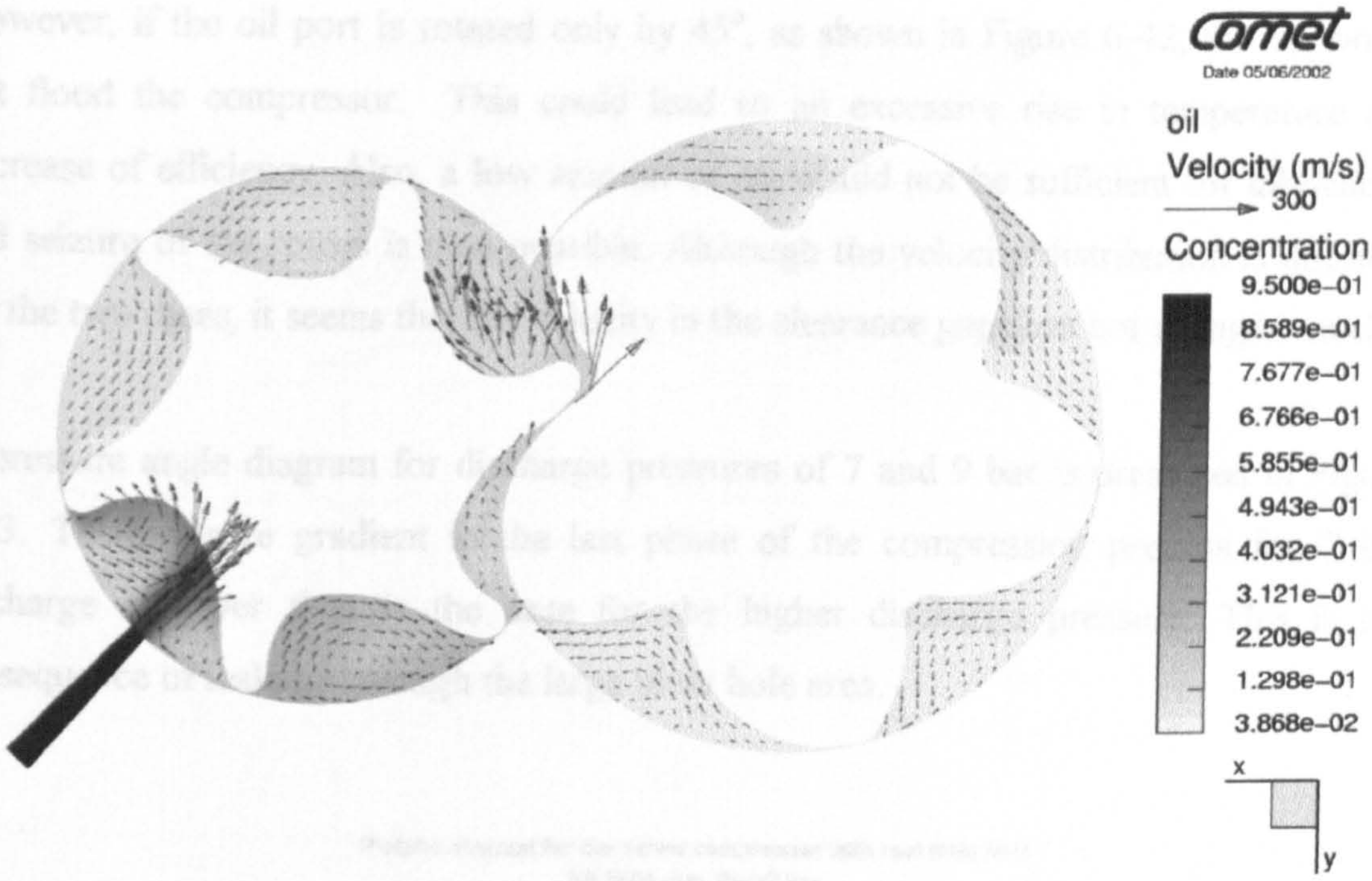

Figure 6-41 Oil concentration in the compressor with proper position of the oil injection port

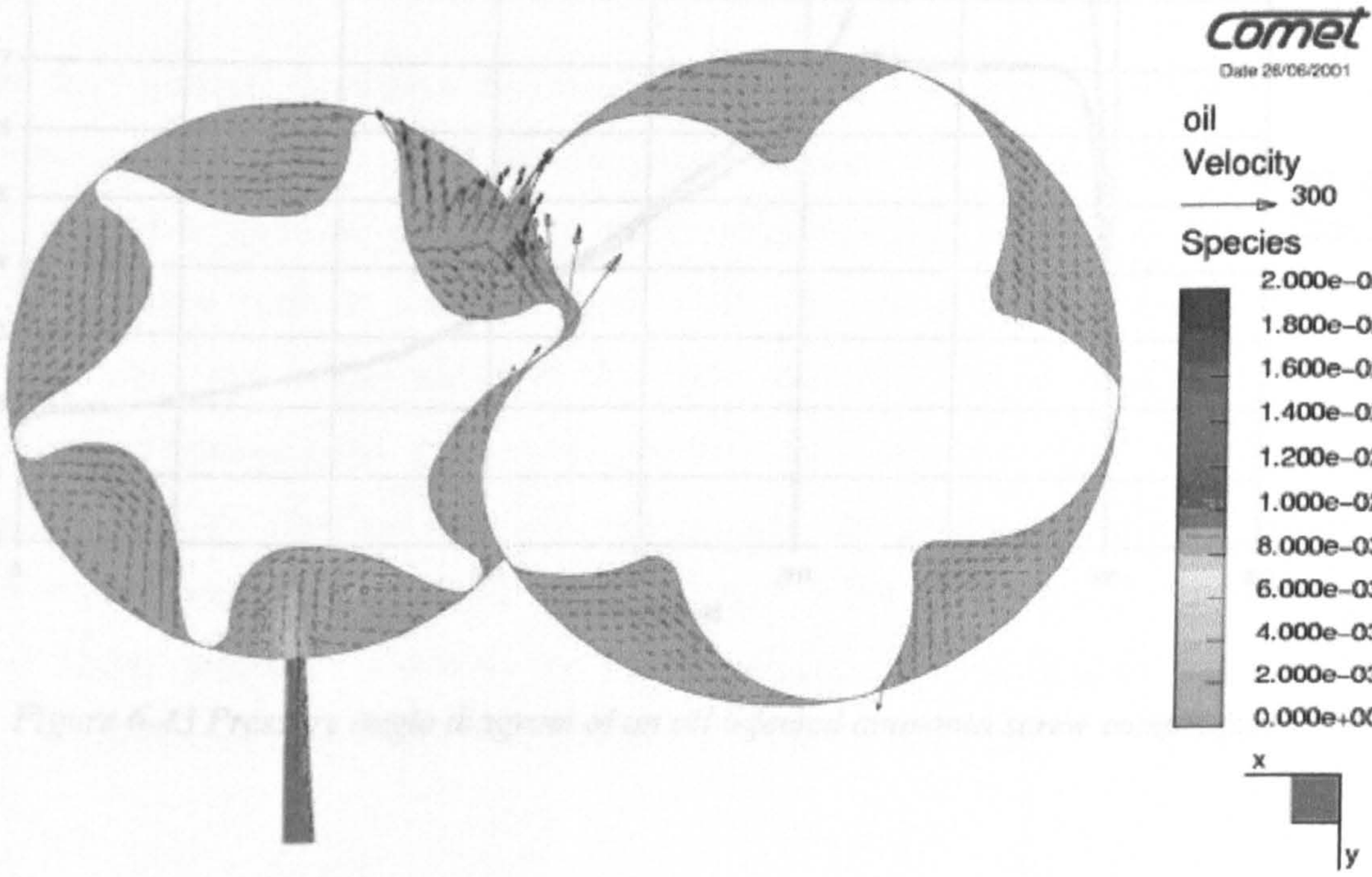

Figure 6-42 Oil concentration in the compressor with improper position of oil injection port

However, if the oil port is rotated only by 45°, as shown in Figure 6-42, the oil would not flood the compressor. This could lead to an excessive rise in temperature and decrease of efficiency. Also, a low amount of oil would not be sufficient for lubrication and seizure of the rotors is then possible. Although the velocity distribution is different for the two cases, it seems that the velocity in the clearance gaps has not changed much.

A pressure angle diagram for discharge pressures of 7 and 9 bar is presented in Figure 6-43. The pressure gradient in the last phase of the compression process for 7 bar discharge is lower than is the case for the higher discharge pressure. This is the consequence of leakage through the large blow hole area.

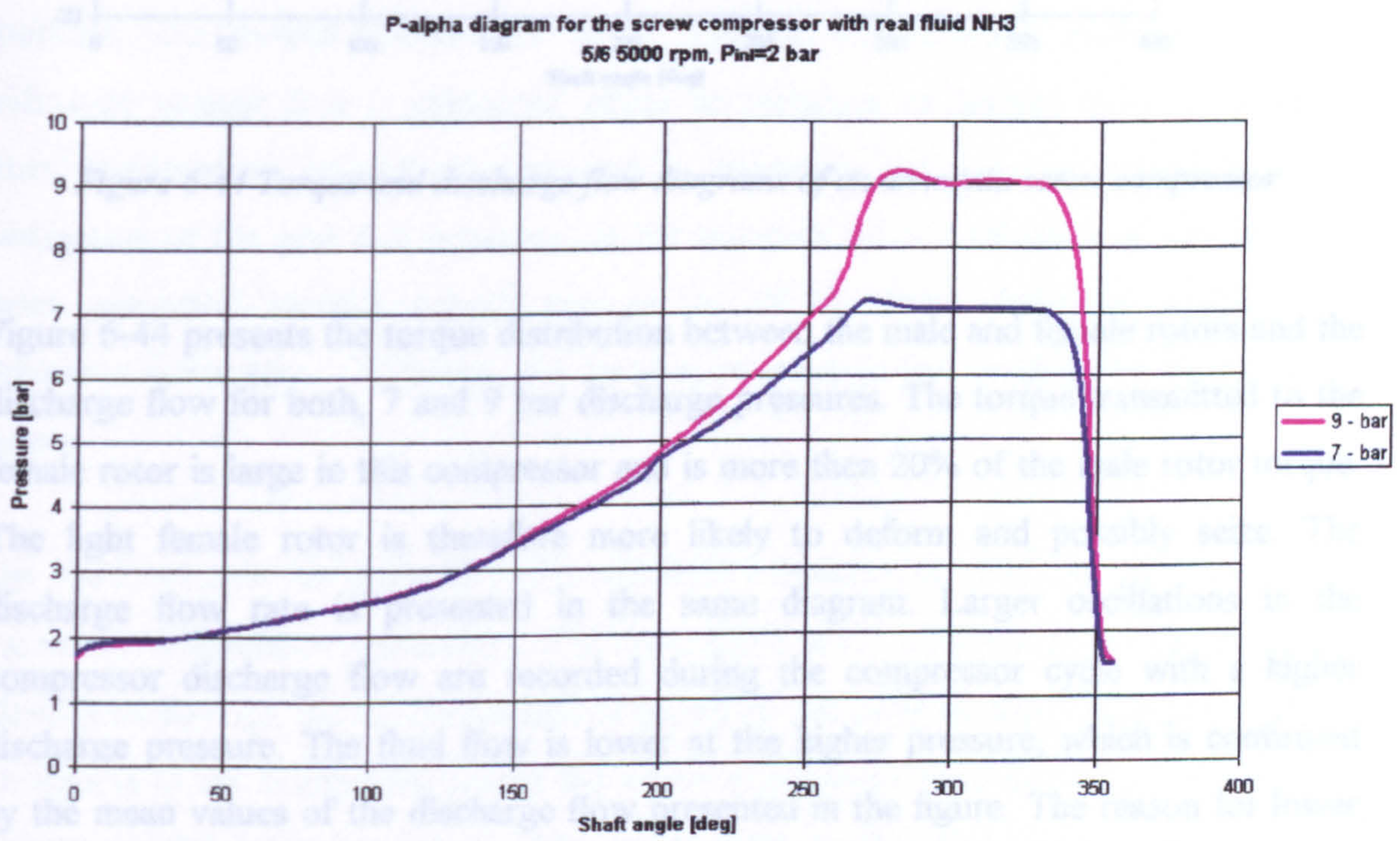

Figure 6-43 Pressure angle diagram of an oil injected ammonia screw compressor

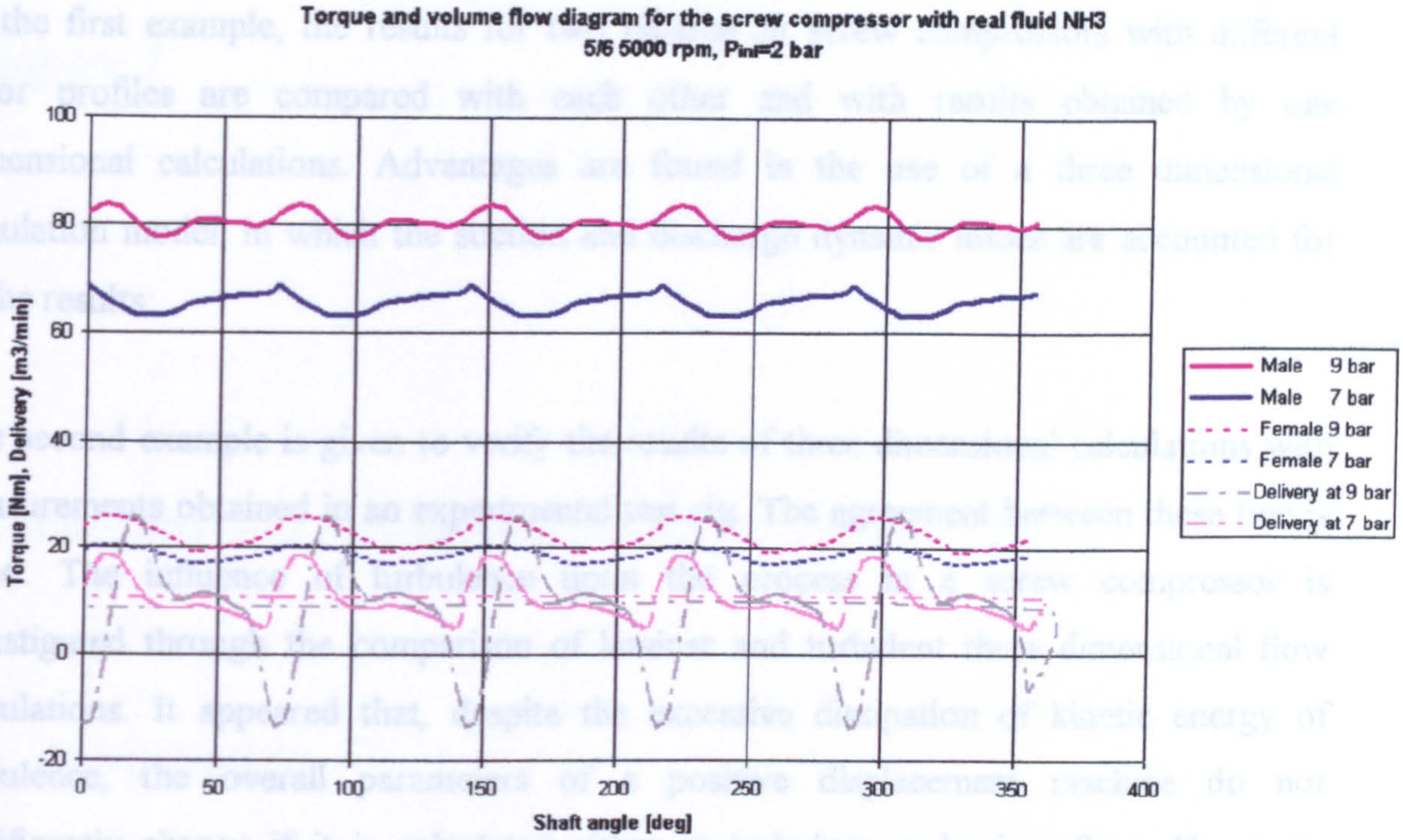

Figure 6-44 Torque and discharge flow diagrams of an ammonia screw compressor

Figure 6-44 presents the torque distribution between the male and female rotors and the discharge flow for both, 7 and 9 bar discharge pressures. The torque transmitted to the female rotor is large in this compressor and is more then 20% of the male rotor torque. The light female rotor is therefore more likely to deform and possibly seize. The discharge flow rate is presented in the same diagram. Larger oscillations in the compressor discharge flow are recorded during the compressor cycle with a higher discharge pressure. The fluid flow is lower at the higher pressure, which is confirmed by the mean values of the discharge flow presented in the figure. The reason for lower flow at higher pressures is due to the higher leakage flow resulting from the higher pressure difference through both the blow hole areas and clearances.

6.5 CLOSURE

In this chapter, three examples have been given in order to outline the scope of the applied mathematical model for three dimensional calculation of screw compressor fluid flow.

In the first example, the results for two oil-free air screw compressors with different rotor profiles are compared with each other and with results obtained by one dimensional calculations. Advantages are found in the use of a three dimensional simulation model, in which the suction and discharge dynamic losses are accounted for in the results.

The second example is given to verify the results of three dimensional calculations with measurements obtained in an experimental test rig. The agreement between these two is good. The influence of turbulence upon the process in a screw compressor is investigated through the comparison of laminar and turbulent three dimensional flow calculations. It appeared that, despite the excessive dissipation of kinetic energy of turbulence, the overall parameters of a positive displacement machine do not significantly change if it is calculated either as turbulent or laminar flow. However, further investigation of that phenomenon is necessary for a better understanding. Investigation of the grid size influence on the accuracy of 3-D calculations shows that coarser numerical meshes cannot capture all of the flow variations within the compressor accurately. However, the integral parameters are in all cases reasonably accurate.

In the third example the procedures for real fluid properties enabled fast calculation of the ammonia compressor parameters. The importance of the oil injection port position is outlined here through the oil distribution obtained by the three dimensional calculations. Such figures of oil distribution within the screw compressor have not ever been found anywhere in the open literature. This achievement is therefore a step forward in understanding screw compressor internal flows.

Chapter 7

Conclusions and Recommendations for Further Work

7.1 CONCLUSIONS

The following summarises the results of this study.

i) One-dimensional modelling of flow processes within screw compressors is insufficiently precise to enable the improvements to their design that would be possible from a more accurate estimate of the flow patterns within them. Accordingly a numerical method for three-dimensional simulation of working processes in these machines has been developed to meet this requirement.

ii) The key feature of this research has therefore been the development of a procedure to generate a numerical mesh suitable for three dimensional numerical calculation of screw compressor processes. Based on that, a computer program has been written in FORTRAN, which is suitable for all windows and UNIX oriented applications. It forms user friendly stand-alone interface which has been given the acronym SCORG (Screw COmpressor Rotor Geometry grid generation). SCORG automatically generates files which contain the node, cell and region specifications as well as user subroutines which enable flow and process simulations for an entire compressor to be obtained by attachment to any general CFD solver of the finite volume type.

iii) A number of novel features have been incorporated in SCORG to make it effective. Those most significant are:

a) Two novel procedures for establishing adequate point distribution on the system boundaries.
b) An effective grid generation procedure.
c) A means of maintaining inlet and discharge pressures constant at their desired final values, throughout the calculation procedure within the CFD code.
d) A fast thermodynamic property estimation procedure for real fluids.
e) A method for including two-phase flow and phase change effects during the compression process.

iv) The whole package has been tested on COMET, a commercial CFD solver, and complete process simulations obtained with it for an oil injected air compressor, an oil free air compressor and an oil injected refrigeration compressor.

v) The validity of the oil injected air compressor simulations was assessed by comparing estimates of the pressure field within the compressor and the various integral parameters derived from it such as torque, flow and volumetric and adiabatic efficiencies, with measured values obtained by the author. For the remaining cases, the simulations were compared with one-dimensional flow predictions for the same machine. Good agreement was obtained with all of them.

More significantly, the method of analysis derived in this thesis has brought illumination to flow characteristics, the effects of which hitherto could not be quantified or even understood qualitatively. For example, the effects of secondary flow in positive displacement screw machines, in which all processes are governed by large pressure gradients. This is especially true for flow into the inlet section where it can now be shown how the flow profile changes because of both the shape of entry port and the rotor profile. The later can lessen recirculation and thereby reduce admission losses. In addition, the manner in which oil or other fluids injected into the compressor are distributed within the machine, was previously wholly unknown and the best guess was to make the simplistic assumption that all liquid within the machine is in contact with the casing, even though this was known to be questionable. By use of the procedures

derived in this thesis, these effects, and how they vary during the different stages of compression, can all be demonstrated.

The results obtained so far are therefore highly encouraging but it must be stressed that the development of this means of three-dimensional flow analysis is only the first stage of what must constitute a long term programme which can bring many advantages to screw compressor design techniques and to achieve these further work is required.

7.2 RECOMMENDATIONS FOR FURTHER WORK

Firstly, more reliable validation of the modelling procedure is needed than comparison of measured and estimated pressure distribution in the compressor. A programme for measuring detailed flow patterns within such machines is therefore a necessary next step to determine the accuracy of flow predictions. The results of this may then be used to fine tune the predictive procedure. Laser Doppler anemometry and velocimetry appear to be the most promising methods for such evaluative procedures.

A major problem affecting the design of screw machines, which has not yet been considered, is that pressure and temperature changes within the screw machine working chamber can distort the rotors and housing and this produces an interactive effect on the fluid flow. Clearances are thereby caused to vary in the machine thus affecting both volumetric and adiabatic efficiencies and, in extreme cases, can even lead to seizure. The determination of such effects is beyond the scope of dimensionless or one-dimensional models. The next stage in improving the analysis of screw compressors should therefore be the development of numerical analysis of fluid and solid interactions within them. The boundary formation and grid generation techniques developed in this thesis can be used as a basis for evaluating such effects and, indeed, preliminary work in this field has already been begun by the author.

As the speed and capacity of computers continues to increase, the scope of their modelling can be extended even further, as is now being done for IC engines. A long term aim could thus be the development of virtual compressors that would include the

estimation, not only of performance, but also the prediction of noise levels due to sonic flow through micron sized gaps and other vibratory effects and how to suppress them.

For all these future possibilities, it is believed that the work carried out in this thesis will form a useful foundation on which to build.

References

Amosov P.E et al, 1977: Vintovie kompresornie mashinii - Spravochnik (Screw Compression Machines - Handbook), Mashinstroienie, Leningrad

Andreev P.A, 1961: Vintovie kompressornie mashinii (Screw Compression Machines), SUDPROM Leninngrad

Arbon I.M, 1994: The Design and Application of Rotary Twin-shaft Compressors in the Oil and Gas Process Industry, MEP London

Barker D.E, Lantz S.A, 1997: Automating Node and Element Assignments on Conforming Four-Sided Sections Defining a Domain for Mapping Quadrilateral Elements, Computers & Structures, Vol.62, No.2, 373-380

Batchelor G.K, 2000: An Introduction to Fluid Dynamics, Cambridge University Press, UK

Bird R.B, Stewart W.E, Lightfoot E.N, 1962: Transport Phenomena, Wiley, New York

Bradshaw P, 1994: Turbulence: The Chief Outstanding Difficulty of Our Subject, Experiments in fluids, Vol 16, 203-216

Buckingham E, 1963: Analytical Mechanics of Gears, Dover Publ, New York

Chawner J.R, Anderson D.A, 1991: Development of an Algebraic Grid Generation Method with Orthogonality and Clustering Control, Conference on Numerical Grid Generation in CFD and Related Fields at Barcelona, 107

Demirdžić I, Gosman A. D, Issa I. R, Perić M, 1987: A Calculation Procedure for Turbulent Flow in Complex Geometries, Comput. Fluids, 15, 251-273

Demirdžić I, Perić M, 1990: Finite Volume Method for Prediction of Fluid flow in Arbitrary Shaped Domains with Moving Boundaries, Int. J. Numerical Methods in Fluids Vol.10, 771

Demirdžić I, Issa I. R, Lilek Z, 1990: Solution Methods for Viscous Flows at all Speeds in Complex Domains, in P. Wesseling (ed.), Notes on Numerical Fluid Mechanics, Vol 29, Vieweg, Braunschweig

Demirdžić I, Kaludjerčić P, Stošić N, 1990: Računari u Inženjerstvu (Computers in Engineering), Svjetlost, Sarajevo

Demirdžić I, 1997: Numerička matematika, Svjetlost, Sarajevo

Demirdžić I, 1992: Mehanika fluida, Prvi dio-Teoretske osnove (Fluid Mechanics, Part one-Theoretical basis), Mašinski fakultet u Sarajevu, Sarajevo

Demirdžić I, Lilek Ž, Perić, M, 1993: A Collocated Finite Volume Method for Predicting Flows at All Speeds, Int. J Numerical Methods in Fluids, Vol. 16, 1029

Demirdžić I, Muzaferija S, 1995: Numerical Method for Coupled Fluid Flow, Heat Transfer and Stress Analysis Using Unstructured Moving Mesh with Cells of Arbitrary Topology, Comp. Methods Appl. Mech Eng, Vol.125 235-255

Demirdžić I, Ivanković A, 1996: Finite Volume Stress Analysis, Lecture notes for the course at Imperial College of Science, Technology & Medicine, University of London

Demirdžić I, Muzaferija S, 1997: Introduction to Computational Fluid Dynamics, Lecture notes for the course at Imperial College of Science, Technology & Medicine, University of London

Denton J.D, Dawes W.N, 1999: Computational Fluid Dynamics for Turbomachinery Design, Proceeding of Institution of mechanical Engineers, Vol.213, Part-C, 107-123

Denton J.D, Xu L, 1999: The Exploitation of Three-dimensional Flow in Turbomachinery Design, Proceeding of Institution of mechanical Engineers, Vol.213, Part-C, 125-137

Durst F, Pereira F.C.J, Scheurer G, 1985: Calculations and experimental investigation of the laminar unsteady flow in pipe extension, in Hirschel edition of Finite Approximation in Fluid Mechanics, Vieweg Brounnschweig, 43-55

Edström S.E, 1989: Quality Classes for screw Compressor Rotors, Proc IMechE Conference Development in Industrial Compressors, 83

Edström S.E, 1992: A Modern Way to Good Screw Compressors, International Compressor Engineering Conference At Purdue, 18

Eiseman P.R, 1985: Grid Generation for Fluid Mechanics Computations, Annuall Rev. Fluid Mech, Vol.17, 487-522

Eiseman P.R, 1991: Control Point Forms for Interactive Grid Manipulation, Computer Methods in Applied Mechanics and Engineering, Vol.91, 1151-1156

Eiseman P.R, 1992: Control Point Grid Generation, Computers Mathematical Applications, Vol.24, No.5/6, 57-67

Eiseman P.R, Hauser J, Thompson J.F, Waterhill N.P, 1994: (Ed.) Numerical Grid Generation in Computational Field Simulation and Related Fields, Proceedings of the 4th International Conference, Pineridge Press, Swansea Wales, UK

Ferziger J H, Perić, M, 1996: Computational Methods for Fluid Dynamics, Springer, Berlin

Field D.A, 2000: Qualitative Measures for Initial Meshes, International Journal for Numerical Methods in Engineering, Vol.47, 887-906

Fletcher C.A.J, 1991: Computational techniques for fluid dynamics, vol. I, Springer, Berlin

Fleming J.S, Tang Y, 1994: The Analysis of Leakage in a Twin Screw Compressor and its Application to Performance Improvement, Proc IMechE, Journal of Process Mechanical Engineering, Vol.209, 125

Fleming J.S, Tang Y, Cook G, 1998: The Twin Helical Screw Compressor, Part 1: Development, Applications and Competitive Position, Proc IMechE, Journal of Mechanical Engineering Science, Vol.212, p 355-367; Part 2: A Mathematical Model of the Working process, Proc IMechE, Journal of Mechanical Engineering Science, Vol.212, p 369-379

Fox R.W, McDonald A.T, 1982: Introduction to fluid mechanics, Wiley, New York

Fujiwara M, Osada Y, 1995: Performance Analysis of Oil Injected Screw Compressors and their Application, Int. J Refrig. Vol.18, 4

Golovintsov A. G et al, 1964: Rotacionii kompresorii (Rotary Compressors), Mashinostroenie, Moscow

Golub G.H, Van Loan C, 1990: Matrix Computations, John Hopkins Iniversity Press, Baltimore

Gordon W.J, 1969: Distributive lattices and the approximation of multivariate functions. Symposium on Approximation with Special Emphasis on Spline Functions, Academic Press, Madison, 223-277

Gordon W.J, Hall C.A, 1973: Construction of Curvilinear Coordinate Systems and Aplications to Mesh Generation, Int. J. Numer. Meth. Engineering, Vol.7, 461-477

Gordon W.J, Thiel L.C, 1982: Transfinite Mappings and Their Application to Grid Generation. In Thompson J.F (ed.): Numerical Grid generation, North Holland, 171-192

Gosman D.A, Watkins P.A, 1977: A computer prediction method for turbulent flow and heat transfer in piston/cylinder assemblies, Proceeding of 1st Symposium on Turbulent Shear Flows, The Pennsylvania State University, Pensylvania, p.523

Gosman D.A, Johnson J.R, 1978: Development of a predictive tool for in-cylinder gas motion in engines' SAE Paper 780315, 1978

Gosman D.A, 1984: Prediction of in-cylinder processes in reciprocating internal combustion engines, in Glowinski and Lions edition of Computing Methods in Applied Science and Engineering, Elsevier, Amsterdam, 604-629

Hanjalić K, 1970: Two-Dimensional Flow in an Axisymetric Channel, PhD Thesis, University of London

Hanjalić K, 1994: Advanced Turbulence Closure Models: A View on the Current Status and Future Prospects, Int. J. Heat & Fluid Flow, Vol 15, 178-203

Hanjalić K, Stošić N, 1994: Application of mathematical modeling of screw engines to the optimization of lobe profiles, Proc. VDI Tagung "Schraubenmaschinen 94" Dortmund VDI Berichte Nr. 1135

Hanjalić K, Stošić N, 1997: Development and Optimization of Screw Machines with a Simulation Model, Part II: Thermodynamic Performance Simulation and Design, ASME Transactions, Journal of Fluids Engineering, Vol.119, p 664

Holmes C.S, 1990: A Study of Screw Compressor Rotor Geometry Leading to a Method for Inter-Lobe Clearance Measurement, PhD Thesis, School of Engineering, Huddersfield Polytechnic, UK

Holmes C.S, 1994: Towards a Core Program for the Measurement of Screw Rotor Bodies by Co-ordinate Measuring Machine, Proc. VDI Tagung "Schraubenmaschinen 94", Dortmund VDI Berichte 1135

ICCM, 2001: COMET version 2.00 User manual, Hamburg, Germany

Kaludjerčić P, 1998: Numerička matematika-algoritamski pristup (Numerical Mathematics-Algoritmical Approach), Viša elektrotehnička škola, Beograd

Karki K.C, Patankar S.V, 1989: Pressure Based Calculation Procedure for Viscous Flows at All Speeds in Arbitrary Configurations, AIAA Journal, 27, 1167-1174

Kauder K, Harling H.B, 1994: Visualisierung der Ölverteilung in Schraubenkompressoren (Visualisation of Oil Effects in Screw Compressors), Proc. VDI Tagung "Schraubenmaschinen 94", Dortmund VDI Berichte 1135

Kauder K, Helpertz M, 1998: Einlauf- und Hybridschichten für Schraubenkompressoren (Run-in and Hybrid Coatings for Twin-Screw Compressors), Proc. VDI Tagung "Schraubenmaschinen 98", Dortmund VDI Berichte 1391

Kim J.H, Thompson J.F, 1990: 3-Dimensional Adaptive Grid generation on a Composite-Bloch Grid, AIAA Journal, Vol.28, Part.3, 470-477

Knupp P, Steinberg S, 1993: Fundamentals of Grid Generation, CRC Press, Boca Raton

Konka K-H, 1988: Schraubenkompressoren (Screw Compressors) VDI-Verlag, Duesseldorf

Kordulla W, Vinkour M, 1983: Efficient Computation of Volume in Flow Predictions, AIAA Journal, 21, 917-918

Kovačević A, Stošić N, Smith I. K, 1999: Development of CAD-CFD Interface for Screw Compressor Design, International Conference on Compressors and Their Systems, London, IMechE Proceedings, 757

Kovačević A, Stošić N, Smith I. K, 2000: The CFD Analysis of a Screw Compressor Suction, International Compressor Engineering Conference at Purdue, 909

Kovačević A, Stošić N, Smith I. K, 2000: Grid Aspects of Screw Compressor Flow Calculations, Proceesings of the ASME Advanced Energy Systems Division – 2000, Vol. 40, 83

Kovačević A, Stošić N, Smith I. K, 2001: CFD Analysis of a Screw Compressor Performance, International Conference on Compressors and Their Systems, London, IMechE Proceedings

Kovačević A, Stošić N, Smith I. K, 2001: Analysis of Screw Compressor Performance by means of 3-Dimensional Numerical Modelling, Seminar on Advances of CFD in Fluid Machinery Design, London, IMechE Proceedings

Lehtimaki R, 2000: An Algebraic Boundary Orthogonalization Procedure for Structured Grids, International Journal for Numerical Methods in Fluids, Vol. 32, 605-618

Lin W.L, Chen C.J, 1998: Automatic Grid Generation of Complex Geometries in Cartesian Co-ordinates, International Journal for Numerical methods in Fluids, Vol.28, No9, 1303-1324

Liou Y.C, Jeng Y.N, 1995: Algebraic Method Using Grid Combination, Numerical heat Transfer, Part B, Vol.28, 239-255

Liou Y.C, Jeng Y.N, 1995: Algebraic Method Using Grid Combination, Numerical heat Transfer, Part B, Vol.28, 257-276

*Liseikin V.D, 1991:*Techniques for Generating Three-dimensional Grids in Aerodynamics (review). Problems Atomic Sci. Technology. Ser. Math. Model. Psyh Process Vol.3, 31-45 (in Russian)

Liseikin V.D, 1996: Construction of Structured Adaptive Grids – a Review, Comp. Math. Math Phys, Vol.36, No.1, 1-32

Liseikin V.D, 1998: Algebraic Adaptation Based on Stretching Functions, Russian Journal for Numerical and Analytical Mathematical Modelling, Vol.13, No.4, 307-324

Liseikin V.D, 1999: Grid generation Methods, Springer-Verlag

Litvin F.L, 1956: Teoria zubchatiih zaceplenii (Theory of Gearing), Nauka Moscow, second edition 1968, also Gear Geometry and Applied Theory Prentice-Hill, Englewood Cliffs, NJ 1994

Lumley L.J, 1999: Engines - an introduction, Cambridge University press, UK

Lysholm A, 1942: A New Rotary Compressor, Proc. I.Mech.E. 150,11

Lysholm A, 1966: The Fundamentals of a New Screw Engine, ASME Paper No 66-GT-86

Lysholm A, 1967: US Patent 3,314,598

Margolis D.L, 1978: Analytical Modelling of Helical Screw Turbines for Performance Prediction, J.Engr.for Power Vol.100, No.3, 482

Marjanović Z, Stošić N, Hanjalić K, Kovačević A, 1988: Investigation Upon the Influence of the Gas Reality to the Mathematical Modelling of the Process in Refrigeration Screw Compressor, Klimatizacija, grijanje hladjenje Journal, Sarajevo, Bosnia & Herzegovina, Vol 4, 37-42

Meyers K, 1997: Creating the Right Environment for Compressor Bearings, Evolution, SKF Industrial Journal, Vol.4, 21

Moitra A, 1992: Two- and Three-Dimensional Grid Generation by an Algebraic Homotopy Procedure, AIAA Journal Vol.30, No.5, 1433

Muzaferija S, 1994: Adaptive Finite Volume Method for Flow Prediction Using Unstructured Meshes and Multigrid Approach, PhD Thesis, Imperial College of Science, Technology & Medicine, London

Nilson, 1952: US Patent 2,622,787

Oden J.T., 1972: Finite elements of non-linear continua, McGraw Hill, New York

O'Neill P.A, 1993: Industrial Compressors, Theory and Equipment, Butterworth-Heinemann, Oxford

Owen S.J, 1998: A Survey of Unstructured Mesh Generation Technology, published on web *http://www.andrew.cmu.edu/user/sowen/survey/index.html*

Owen S.J, Staten M.L, Cannan S.A, Saigal S, 1998: Quad-Morphing: Advanced Front Quad Meshing Using Triangle Transformations, *http://www.andrew.cmu.edu/user/sowen/qm/rt98quad.htm*

Patankar S.V, 1980: Numerical Heath Transfer and Fluid Flow, McGraw Hill, London

Perić, M, 1985: A Finite Volume Method for the Prediction of Three Dimensional Fluid Flow in Complex Ducts, PhD Thesis, Imperial College of Science, Technology & Medicine, London

Perić, M, 1990: Analysis of pressure-velocity coupling on non-orthogonal grids, Numerical Heat Transfer, Part B, 17, 63-82

Peng N, Xing Z, 1990: New Rotor Profile and its Performance Prediction of Screw Compressor, International Compressor Engineering Conference At Purdue, 18

Reynolds C. W, 1979: Thermodynamic Properties in SI: Graphs, Tables and Computational Equations for Forty substances, Department of Mechanical Engineering, Stanford University, California

Riemslagh K, Vierendeels J, Dick E, 1998: Two-dimensional Incompressible Navier-Stokes Calculations in Complex-shaped Moving Domains, Journal of Engineering mathematics, Vol.34, 57-73

Rinder L, 1979: Schraubenverdichter (Screw Compressors), Springer Verlag, New York

Rinder L, 1984: Schraubenverdichterläufer mit Evolventenflanken (Screw Compressor Rotor with Involute Lobes), Proc. VDI Tagung "Schraubenmaschinen 84" VDI Berichte Nr. 521 Düsseldorf

Rinder L, 1987: US Patent 4,643,654

Saha S, Basu B.C, 1991: Simple Algebraic Technique for Nearly Orthogonal Grid Generation, AIAA Journal, Vol.29, No.8, 1340

Samareh-Abolhassani J, Smith R.E, 1992: A Practical Approach to Algebraic Grid Adaption, Computers Mathematical Applications, Vol.24, No.5/6, 69-81

Sauls J, 1994: The Influence of Leakage on the Performance of Refrigerant Screw Compressors, Proc. VDI Tagung "Schraubenmaschinen 94", Dortmund VDI Berichte 1135

Sauls J, 1998: An Analytical Study of the Effects of Manufacturing on Screw Rotor Profiles and Rotor Pair Clearances, Proc. VDI Tagung "Schraubenmaschinen 98", Dortmund VDI Berichte 1391

Sakun I.A, 1960: Vintovie kompresorii (Screw Compressors), Mashinostroenie Leningrad

Shih T. I. P, Bailey R. T, Ngoyen H.L, Roelke R.J, 1991: Algebraic Grid Generation For Complex Geometries, International Journal for Numerical Methods in Fluids, Vol. 13, 1-31

Singh P.J, Onuschak A.D, 1984: A Comprehensive Computerized Method For Twin Screw Rotor Profile Generation and Analysis, Purdue Compressor Technology Conference 544

Singh P.J, Schwartz J.R, 1990: Exact Analytical Representation of Screw Compressor Rotor Geometry, International Compressor Engineering Conference At Purdue, 925

Smith G.D, 1985: Numerical Solution of Partial Differential Equations: Finite Difference Methods, 3rd edition, Claredon press, Oxford

Smith I.K, 1993: Development of the Trilateral Flash Cycle System, Part1: Fundamental Considerations, Proc Inst Mech Engineers, Vol 207, 179-194

Smith I.K, Da Silva, P.M.R, 1994: Development of the Trilateral Flash Cycle System, Part 2: Increasing Power Output with Working Fluid Mixtures, Proc Inst Mech Engineers, Vol 208, 135-144

Smith I. K, Stošić N, Aldis C. A, 1996: Development of the trilateral flash cycle system, Part 3: The design of high efficiency two-phase screw expanders, Proc IMechE, Journal of Power and Energy, Vol 210, p 75

Smith R.E, 1982: Algebraic Grid Generation, from Numerical Grid Generation, ed. By Thomson J.E, Elsevier Publishing Co, 137

Smith R.E, 1992: (Ed.) Proceedings of the Software Systems for Surface Modelling and Grid Generation Workshop, NASA Conference Publication 3143, Nasa Langley Research Centre, Hampton, VA

Smith R.E, Johnson L.J, 1996: Automatic Grid Generation and Flow Solution for Complex Geometries, AIAA Journal, Vol.34, No.6, 1120-1124

Soni B.K, 1992: Grid Generation for Internal Flow Configurations, Computers Mathematical Applications, Vol.24, No.5/6, 191-201

Soni B.K, Thompson J.F, Eiseman P.R, Hauser J, 1996: (Eds.) Numerical Grid Generation in Computational Filed Simulation, Proceedings of the 5th International Conference, MSU Publisher, Mississippi State, MS, USA

Sonneveld P, 1989: CGS, a fast Lanczos solver for Non-Symetric Linear Systems, SIAM Journal Scientific Stat. Computation, 10, 36-52

Sonntag E.R, Borgnakke C, 2001: Introduction to Engineering Thermodynamics, John Wiley & Sons, Inc, New York, USA

Spiegel M.R, 1968: Mathematical Handbook of Formulas and Tables, McGraw-Hill Book Company, New York

Steinthorsson E, Shih T. I. P, Roelke R. J, 1992: Enhancing Control of Grid Distribution In Algebraic Grid generation Generation, International Journal for Numerical Methods in Fluids, Vol. 15, 297-311

Stošić N, Hanjalić K, 1977: Contribution towards Modelling of Two-Stage Reciprocating Compressors, Int.J.Mech.Sci. 19, 439

Stošić N, 1982: Numerical Modelling of the Internal Unsteady Flow of Compressible Fluids, (in serbo-croatian) PhD thesis,

Stošić N, Hanjalić K, Koprivica J, Lovren N, Ivanović M, 1986: CAD of Screw Compressor Elements, Strojarstvo Journal Zagreb 28, 181

Stošić N, Kovačević A, Hanjalić K, Milutinović Lj, 1988: Mathematical Modelling of the Oil Influence upon the Working Cycle of Screw Compressors, International Compressor Engineering Conference at Purdue, 355

Stošić N, Hanjalić K, Kovačević A, Koprivica J, Marjanović Z, 1990: Mathematical Modelling and Experimental Investigation of refrigeration Screw Compressor Working Process, Strojarstvo Journal Zagreb 32, 17-25

Stošić N., Milutinović Lj., Hanjalić K. and Kovačević A, 1992: Investigation of the Influence of Oil Injection upon the Screw Compressor Working Process, Int.J.Refrig. 15,4,206

Stošić N., Hanjalić K., 1994: Development and optimisation of screw engine rotor pairs on the basis of computer modelling, Proc. XVII Conference on Compressor Engineering at Purdue, 55

Stošić N, 1996: Patent Application GB 9610289.2

Stošić N, Smith I. K. and Zagorac S, 1996: CFD Studies of Flow in Screw and Scroll Compressors, XIII Int. Conf on Compressor Engineering at Purdue

Stošić N, Hanjalić K, 1997: Development and Optimisation of Screw Machines with a Simulation Model, Part I: Profile Generation, ASME Transactions, Journal of Fluids Engineering, Vol.119, p 659

Stošić N, Smith I. K, Kovačević A, Aldis C. A, 1997: The Design of a Twin-screw Compressor Based on a New Profile, Journal of Engineering Design, Vol.8, 389

Stošić N, Kovačević A. and Smith I.K, 1998: Modelling of Screw Compressor Capacity Control, Proc. XIV Conference on Compressor Engineering at Purdue, 607

Stošić N. et al 1998: The Performance of a Screw Compressor with Involute Contact Rotors in a Low Viscosity Gas-Liquid Mixture Environment, Proc. VDI Tagung "Schraubenmaschinen 98", Dortmund VDI Berichte 1391

Stošić N, 1998: On Gearing of Helical Screw Compressor Rotors, Proc IMechE, Journal of Mechanical Engineering Science, Vol.212, 587

Stošić N, 1999: Recent Developments in Screw Compressors, International Conference on Compressors and their Systems, Transaction of ImechE, 3-13

Stošić N, Smith I.K, Kovačević A. and Venumadhav K, 2000: Retrofit 'N' Rotors for Efficient Oil-Flooded Screw Compressors, Proc. of 2000 International Compressor Engineering Conference at Purdue, West Lafayette, IN, USA, Vol.2, 917-924

Stošić N, 2001: Mathematical Modelling in Computer Aided Design of Screw Compressors, Lecture notes for Short Course at International Conference on Compressors and their Systems, London

Tang Y, Fleming J.S, 1992: Obtaining the Optimum Geometrical Parameters of a Refrigeration Helical Screw Compressor, International Compressor Engineering Conference at Purdue 213

Tang Y, Fleming J.S, 1994: Clearances between the Rotors of Helical Screw Compressors: Their determination, Optimisation and Thermodynamic Consequences, Proc IMechE, Journal of Process Mechanical Engineering, Vol.208, 155

Tang Y, 1994: Computer Aided Design of Twin Screw Compressors, PhD Thesis, University of Strathclyde, Glasgow, UK.

Thomas D.P and Lombard K.C, 1979: Geometric Conservation Law and its Application to Flow Computations on Moving Grids, AIAA Journal, 17, 1030-1037

Thompson J. E, 1984: Grid Generation Techniques in Computational fluid Dynamics, AIAA Journal, Vol.22, No.11, 1505-1523

Thompson J.E, Warsi Z.U.A, Martin C.W, 1985: Numerical Grid Generation – Foundations and Applications, Elsevier Science Publishing Co, also J.F. Thompson web edition 1997 (*http://www.erc.msstate.edu/education/gridbook*)

Thompson J.E, Waterhill N.P, 1993: Aspects of Numerical Grid Generation: Current Science and Art, AIAA Journal, Vol.93, 3539

Thompson J.E, 1996: A Reflection on Grid Generation in the 90's: Trends, Needs and Influence. In Soni B.K, Thompson J.F, Hauser J, Eiseman P.R (eds.): Numerical grid Generation in CFD, Mississippi State University, Vol.1, 1029-1110. Also published on web *2000, http://www.erc.msstate.edu/~joe/gridconf*

Thompson J.E, Soni B, Weatherrill N.P, 1999: Handbook of Grid generation, CRC Press

Trulio G.J, Trigger R.K, 1961: Numerical solution of the one-dimensional hydrodynamic equations in an arbitrary time-dependent coordinate system, University of California Lawrence Radiation Laboratory Report UCLR-6522

Tzabiras G, Vafiodau M, Nassos G, 1986: A Numerical Method for the Generation of 2-D Orthogonal Curvilinear Grids, International Conference on Numerical Grid generation in Computational Fluid Dynamics at Landshut, West Germany, 183

Van den Vorst H.A, Sonneveld P, 1990: CGSTAB, a more smoothly converging variant of CGS, Tech. Report 90-50, Delft University of Technology

Versteeg K.H, Malalasekera W, 1995: An Introduction to computational Fluid Dynamics – The Finite Volume Method, Longman Scientifica&Technology, UK

Vinokur M, 1983: On One-Dimensional Stretching Functions for Finite-Difference Calculations, Journal of Computational Physics, Vol.50, 215-234

Walas S.M, 1984: Phase Equilibria in Chemical Engineering, Butterworth Publishers, Stoneham, MA, USA

White F.M, 1986: Fluid Mechanics. NcGraw Hill, New York

Wilcox D.C, 1993: Turbulence modelling for CFD, DCW Industries, Inc. La Canada, California, USA

Xing Z, 2000: Screw Compressors: Theory, Design and Application, China Machine Press, Beijing (In Chinese)

Xing Z, Peng X, Shu P, 2001: Theoretical and Experimantal Study on Twin Screw Compressor, Proceedings of the 3rd ICTC, XI'AN Jiaotong University Press, China, pp 128

Xion Z. Dagang X, 1986: Study on Actual Profile Surface and Engaging Clearance of Screw Compressor Rotors, Purdue Compressor Technology Conference 239

Yang S.L, Shih T.I.P, 1986: An algebraic grid generation technique for time-varying two-dimensional spatial domains, Int. j. Numer. Methods fluids, Vol. 6, 291-304

Zenan X, 1984: The Dynamic Measurement and Mating Design of a Screw Compressor Rotor Pair, Purdue Compressor Technology Conference 314

Zhang L, Hamilton J.F, 1992: Main Geometric Characteristics of the Twin Screw Compressor, International Compressor Engineering Conference at Purdue 213

Zhou Q, 1998: A Simple Grid Generation Method, International Journal for Numerical Methods in Fluids, Vol. 26, 713-724

Zhu J, Rodi W, Schoenung B, : A Fast Method For Generating Smooth Grids,

Zienkiewicz O.C, Taylor R.L, 1991: The Finite Element Method – Vol. 2: Solid and Fluid Mechanics, McGraw Hill, New York

Appendix I

Profile Generation

The practice predominantly used for generating of screw compressor rotor profiles is to create primary profile curves on one of the real rotors and to generate a corresponding secondary profile curve on the other rotor using some appropriate conjugate action condition. Any curve can be used as a primary one, but traditionally the circle is the most commonly used. The skill required to produce rotors was, for decades, limited to the choice of a primary arc which would permit the derivation of an appropriate secondary profile.

The most popular rotor-to-rotor generated profiles are as follows;
The symmetric circular profile which consists of circles only.
The SRM asymmetric profile which employs a decentred circle on the low pressure side of the gate rotor.
It is followed by the SKBK profile introducing the same approach on the main rotor. In both cases, evolved curves were given analytically as epi- or hypocycloids.
The SRM "D" profile consists exclusively of circles, almost all of them eccentrically positioned on the main or gate rotor.
More recently, the circles have gradually been replaced by other curves, such as ellipses in the FuSheng profiles, parabolas in the Compair and Hitachi profiles and hyperbolae in the 'Hyper' profile. The hyperbola in the latest profile seems to be the replacement that gives the best ratio of the rotor displacement to seal line length.

Another method of generating curves from the screw rotor profile is to use some imaginary or 'non-physical' rotor. Since all gearing equations are independent of the coordinate system in which they are expressed, it is possible to define primary arcs as given curves using a coordinate system which is independent of both rotors. By this means, in many cases the defining equations may be simplified. In addition, the use of one coordinate system to define all the curves substantially simplifies the design process. Typically, the template is specified in a rotor independent coordinate system. The same is valid for a rotor of infinite radius which is a rack. From this, a secondary arc on some of the rotors is obtained by the procedure, which is called a 'rack

generation'. The first ever published patent on rack generation *Mensen* (1977) lacks practicality but conveniently uses the theory. *Rinder* (1987) and recently *Stošić* (1996) give a good basis for screw compressor rotor profile formed by the rack generation.

I.1 ENVELOPE METHOD: THE BASIS FOR ROTOR PROFILING

The envelope method is used here as a basis for generation of the screw compressor rotor profile. The method states that two surfaces are meshed if each generates or envelopes the other under a specified relative motion, as presented by *Litvin* (1998). This is becoming increasingly popular, and details of how it may be applied to screw compressor rotor profiles, have been given by *Stošić* (1998). Although the generation of screw compressor rotors can be regarded as a two-dimensional problem, a three-dimensional approach is given here as a general case. This gives more opportunities for tool profiling or other similar applications. *Andreev* (1961) and, more recently, *Xing* (2000), also use the envelope method for screw compressor rotor generation in their books on screw compressors. A similar approach was applied by *Tang* (1995).

Screw compressor rotors can be treated as helical gears with nonparallel and nonintersecting, or crossed axes which gives substantial benefits for some applications. However, here parallel axes will be assumed for the screw compressor rotors as presented in Figure A- 1.

In this figure, x_{01}, y_{01} and x_{02}, y_{02} are the point coordinates at the end rotor section in the coordinate systems fixed to the main and gate rotors. Rotation of the rotor shaft around the z axes is the common rotor movement in its bearings. While the main rotor rotates through angle θ, the gate rotor rotates through angle $\tau = r_{1w}/r_{2w}\theta = z_2/z_1\theta$, where r_w and z are the pitch circle radii and number of rotor lobes respectively. In addition external and internal rotor radii are: $r_{1e} = r_{1w} + r$ and $r_{1i} = r_{1w} - r_0$ and $r_{2i} = r_{2w} + r$ and $r_{2e} = r_{2w} + r_0$. The distance between the rotor axes is $C = r_{1w} + r_{2w}$. The constant p is the rotor lead given for unit rotor rotation angle. The indices *1* and *2* are related to the main and gate rotor respectively.

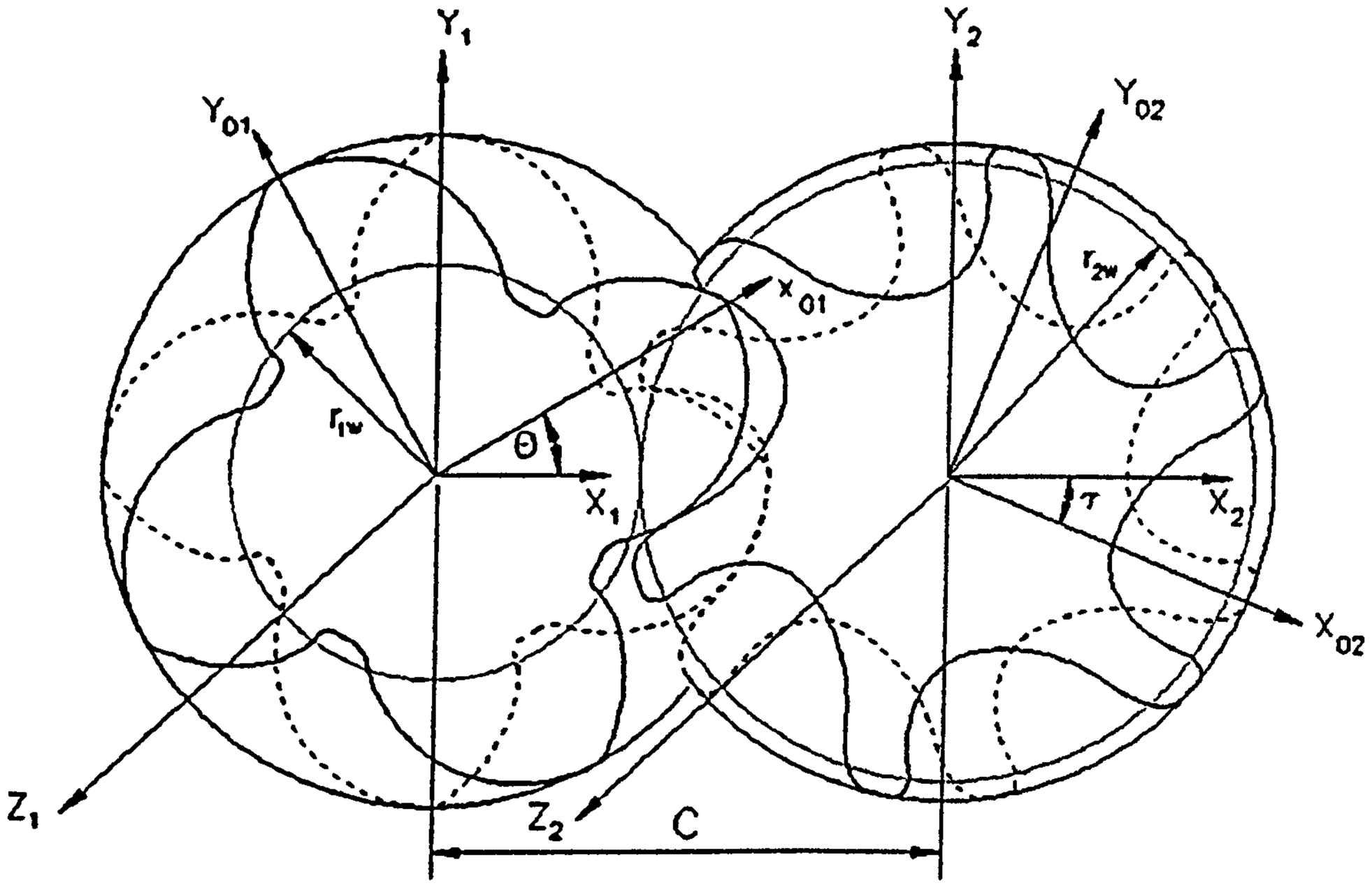

Figure A- 1 Screw compressor rotors with parallel shafts and their coordinate systems

Following *Litvin* (1998), the given profile $\mathbf{r}_1(t,\theta)$ should, in the meshing procedure, produce a family of generated profiles which are represented in the parametric form as $\mathbf{r}_2(t,\theta,\tau)$, where t is a profile parameter while θ and τ are motion parameters, rotation angles of the male and female rotor respectively.

The given profile is:

$$\mathbf{r}_1 = \mathbf{r}_1(t,\theta)=[x_1,y_1,z_1]= [x_{01}\cos\theta - y_{01}\sin\theta,\ x_{01}\sin\theta + y_{01}\cos\theta,\ p_1\theta], \tag{I-1}$$

$$\frac{\partial \mathbf{r}_1}{\partial t}= \left[\frac{\partial x_1}{\partial t},\frac{\partial y_1}{\partial t},0\right]= \left[\frac{\partial x_{01}}{\partial t}\cos\theta - \frac{\partial y_{01}}{\partial t}\sin\theta,\ \frac{\partial x_{01}}{\partial t}\sin\theta + \frac{\partial y_{01}}{\partial t}\cos\theta,\ 0\right], \tag{I-2}$$

$$\frac{\partial \mathbf{r}_1}{\partial \theta}= \left[\frac{\partial x_1}{\partial \theta},\frac{\partial y_1}{\partial \theta},\frac{\partial z_1}{\partial \theta}\right]=[-y_1,\ x_1,p_1]= [-x_{01}\sin\theta - y_{01}\cos\theta, x_{01}\cos\theta - y_{01}\cos\theta, p_1] \tag{I-3}$$

The generated profile is defined with its coordinates:

$$\begin{aligned}\mathbf{r}_2 = \quad & \mathbf{r}_2(t,\theta,\tau)=[x_2,y_2,z_2]=[x_1-C,\ y_1,z_1]= \\ & [x_{02}\cos\tau-y_{02}\sin\tau,\ x_{02}\sin\tau+y_{02}\cos\tau,\ p_2\tau],\end{aligned} \tag{I-4}$$

and its first derivative:

$$\begin{aligned}\frac{\partial\mathbf{r}_2}{\partial\tau} = \ & [-y_2,x_2,p_2]=[-y_1,x_1-C,p_2] \\ & [-x_{02}\sin\tau-y_{02}\cos\tau,\ x_{02}\cos\tau-y_{02}\sin\tau,\ p_2]\end{aligned} \tag{I-5}$$

The following envelope equation determines meshing between the profiles $\mathbf{r}_1$ and $\mathbf{r}_2$:

$$\left(\frac{\partial\mathbf{r}_1}{\partial t}\times\frac{\partial\mathbf{r}_1}{\partial\theta}\right)\cdot\frac{\partial\mathbf{r}_2}{\partial\tau}=0, \tag{I-6}$$

Previous equations make closed system of equations. If a generating profile *1* is defined by the parameter t, the envelope may be used to calculate another parameter θ, now a function of t, as a meshing condition to define a generated surface *2*, now the function of both t and θ. The cross product in the envelope equation represents a surface normal. The derivative $\frac{\partial\mathbf{r}_2}{\partial\tau}$ is the relative sliding velocity of two single points on the profiles *1* and *2* which together form the common tangential contact point of these two surfaces. Insertion of expressions (I-1) to (I-5) into an envelope condition (I-6) gives:

$$(p_1-p_2)\cdot\left(x_1\frac{\partial x_1}{\partial t}+y_1\frac{\partial y_1}{\partial t}\right)+p_1C\frac{\partial x_1}{\partial t}=0 \tag{I-7}$$

The above formula is the condition of meshing action for helical gears of uniform lead with parallel axes. The method can be used for synthesis purposes of screw compressor rotors, which are effectively helical gears with parallel axes.

I.1.1 Rack Generation Procedure

The centre distance of screw machine rotors with parallel axes is $C=r_{1w}+r_{2w}$. Rotors make a contact line between them with the meshing condition in the transverse plane, perpendicular to the rotor axes, equal to that of spur gears. Although the spur gear meshing condition fully defines helical screw rotors, it is more convenient to use the envelope method for parallel helical gears to get the required meshing condition.

The condition sufficient to obtain a solvable meshing condition (I-7) is to have known coordinates of one of the rotors, x_{01} and y_{01}, and their first derivatives, $\frac{\partial x_{01}}{\partial t}$ and $\frac{\partial y_{01}}{\partial t}$, or alternatively $\frac{dy_{01}}{dx_{01}}$.

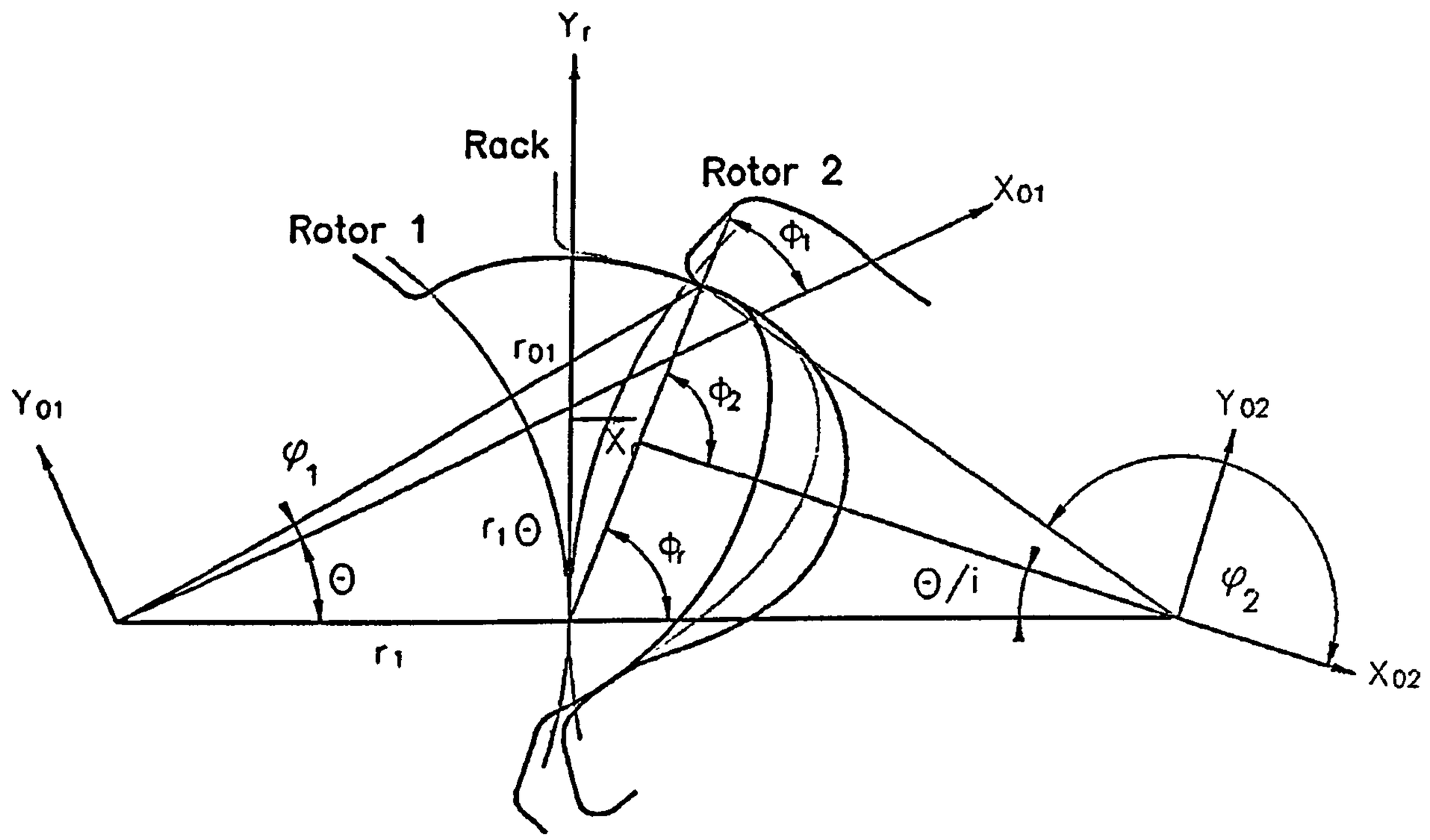

Figure A- 2 Position of the rack and rotors for rack generation procedure

The profile may be specified on either the main or gate rotor, or in sequence on both. If it is more convenient, the primary profile may also be defined as a rack as given in Figure A- 2.

The meshing condition given by (I-7) now becomes:

$$\frac{dy_{01}}{dx_{01}}\left(ky_{01}-\frac{C}{i}\sin\theta\right)+kx_{01}+\frac{C}{i}\cos\theta=0 \qquad \text{(I-8)}$$

where i=p_2/p_1 and k=1-1/i. This equation can be solved only numerically, similar to its original (I-7). Once obtained, the distribution of θ along the profile may be used to calculate the coordinate points of meshing rotor profiles, as well as to determine the sealing lines and paths of proximity between the two rotors. The rack coordinates may also be calculated from the same θ distribution.

Since for parallel axes $\tau=\theta i$, the coordinates of the meshing profile on the gate rotor in the transverse plane are:

$$\begin{aligned} x_{02} &= x_{01}\cos k\theta - y_{01}\sin k\theta - C\cos\frac{\theta}{i} \\ y_{02} &= x_{01}\sin k\theta + y_{01}\cos k\theta + C\sin\frac{\theta}{i} \end{aligned} \qquad \text{(I-9)}$$

The rack coordinates can be obtained uniquely if the rack-to-rotor gear ratio i tend to infinity:

$$\begin{aligned} x_{0r} &= x_{01}\cos\theta - y_{01}\sin\theta \\ y_{0r} &= x_{01}\sin\theta + y_{01}\cos\theta - r_1\theta \end{aligned} \qquad \text{(I-10)}$$

Conversely, if the gate rotor curves are given, generated curves will be placed on the gate rotor and similar equations with substituted indices will be used to generate the main rotor profile.

However, if the primary curves are given on the rack, their coordinates x_{0r} and y_{0r}, as well as their first derivatives, $\frac{\partial x_{0r}}{\partial t}$ and $\frac{\partial y_{0r}}{\partial t}$, or $\frac{dy_{0r}}{dx_{0r}}$ should be known. In that case, the curves on the male rotor are generated as:

$$x_{01} = x_{0r}\cos\theta - (y_{0r} - r_{1w})\sin\theta$$
$$y_{01} = x_{0r}\sin\theta + (y_{0r} - r_{1w})\cos\theta \qquad \text{(I-11)}$$

with the meshing condition in the form:

$$\frac{dy_{0r}}{dx_{0r}}(r_{1w}\theta - y_{0r}) - (r_{1w} - x_{0r}) = 0 \qquad \text{(I-12)}$$

The important feature of the meshing condition for the rack and rotor, given in the previous equation, is that the solution for θ is obtained directly without the need for a numerical iterative procedure.

Both, the numerical and direct solution of the meshing condition equations, presented here, enable the introduction of a variety of primary curves into the screw rotor profiling process. Further to that, the numerical derivation of primary arcs enables a general approach to be applied, in which only the coordinates of the primary curves are required for the solution and not necessarily their derivatives. In such a case, any analytical function and even a discrete point distribution can be used as a primary curve.

More about envelope meshing method and the rack generation procedure can be found in *Stošić* (1996), (1998) and (2001).

I.2 'N' ROTOR PROFILE

To overcome problems that arise from the rotor-to-rotor profiling procedure and to avoid a large blow-hole area on the rotors previously generated by the rack-to-rotor procedure, a special distribution of curves is applied to the rack. Such a rack is then used for profiling both the main and gate rotors. The method and its extensions were then used to create a number of different rotor profiles, *Stošić et al* (1986), and *Hanjalić and Stošić* (1993). One of the applications of the rack generation procedure protected by a patent is described by *Stošić* (1996).

The rotors presented in Figure A- 3 are generated from the procedure described above which is a combined rack and rotor generation method. It uses equation (2.1) to generate rotors from a rack with the meshing condition in the form of equation (2.2). All the curves on the 'N' profile are given in the form of a "general arc", $ax^p+by^q=1$. Straight lines, circles, parabolas, ellipses and hyperbolae are all easily described by selecting appropriate values for parameters a, b, p and q.

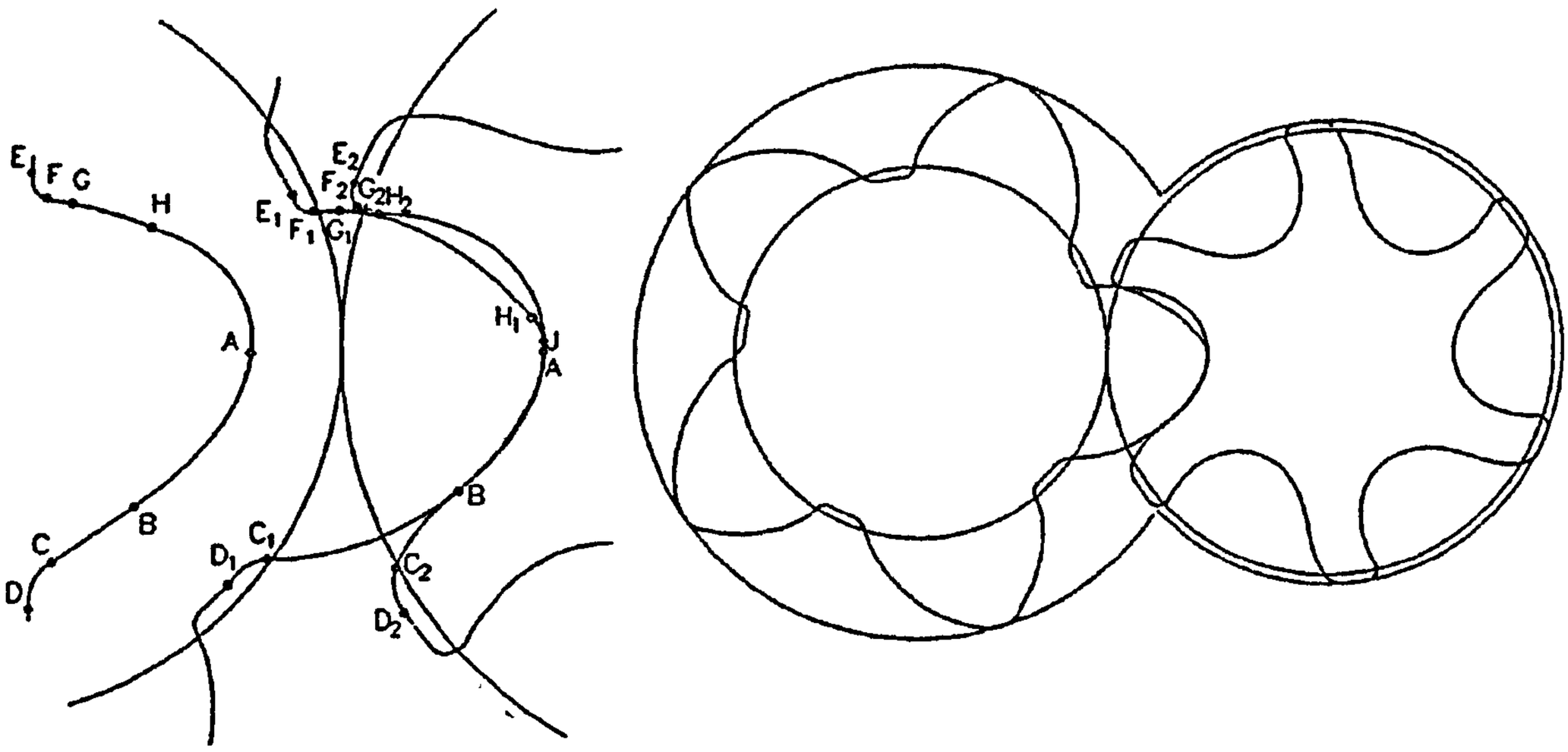

Figure A- 3 "N" Rotor profile

The "N" profile is defined from both the rack and rotors as follow:

- segment DE is a straight line on the rack,
- segment EF is a circular arc of radius r_4,
- segment FG is a straight line for the upper involute where $p=q=1$,
- segment GH on the rack is a meshing curve generated by the circular arc G_2H_2 on the gate rotor
- segment HJ on the rack is a meshing curve generated by the circular arc H_1J_1 of the radius r_2 on the main rotor
- segment JA is a circular arc of radius r on the rack,
- segment AB is an arc which can be any of following, circle, parabola, hyperbola or ellipse,
- segment BC is a straight line on the rack matching the involute on the rotor round lobe ,

- segment CD is a circular arc on the rack with radius r_3.

By means of these curves, a family of "N" rotors has been developed and built for compressors of various operations. In all cases, these obtained excellent performance results.

Appendix II

One-dimensional numerical analysis of the Screw Machine

The analysis of thermodynamic and flow processes in a screw machine is based on a mathematical model, represented by a set of equations which describe its physical behaviour. Analysing procedures can be categorised into three groups comprising one-, two- and three-dimensional methods.

One-dimensional methods assume that the working chamber of the machine is a control volume entrapped by two meshing rotors and a housing and that it cyclically repeats its shape and function with rotation of the male rotor as many times per revolution as there are interlobes on the male rotor. It is assumed in these methods that all thermodynamic values, such as temperature, pressure, density etc, are uniform within the specified control volume. In that case, only two general conservation laws are considered and modelled, namely the energy and mass continuity. Other phenomena, which happen within the control volume and on its boundaries, are modelled by a number of algebraic equations which describe leakage, inlet and outlet flow, oil injection etc, and the differential kinematic relations which describe the instantaneous operating volume and its change with the rotation angle or with time. A modern and powerful numerical model is suggested for use by *Stošić and Hanjalić* (1996). It has been incorporated into the computational code known as SCORPATH. This is an acronym for Screw **CO**mpressor **O**ptimal **R**otor **P**rofiling and **TH**ermodynamics. The software has been under continuous development since 1986. It has been verified in all aspects of its use through many years of application and development. Due to that, it can be used as the tool for preliminary evaluation during the development of the three-dimensional model, which is the scope of this thesis. The basic features of this mathematical model are presented in this appendix.

Two-dimensional methods are usually used to accompany one-dimensional modelling for phenomena that cannot be regarded as one-dimensional or that are more precisely simulated in a two-dimensional manner. Leakage and oil injection can be regarded as two dimensional processes.

Three-dimensional methods are based on the solution of the governing laws for a three-dimensional numerical mesh which closely describes real geometry. These models have less empirically simulated effects than the previous two.

II.1 ONE-DIMENSIONAL ANALYSIS

The working space (working chamber) of screw machine is a typical example of an open thermodynamic system in which the mass flow varies with time. The mathematical model of that system accounts for a number of effects which influence the final performance of the real machine. The working fluid can be any gas or mixture of liquid and gas for which the equation of state and relations for internal thermal energy and enthalpy are known. The model takes into account heat transfer between the gas and the body of screw machine and its rotors, leakage of the working medium within the machine, injection of oil or some other fluid to the working chamber and some other effects. The injection fluid can be any known liquid for which the gas solubility can be taken into account if required. The model is independent of the machine geometry specification, which means that any geometry can be accepted for analysis. However, in order to ensure efficient computation, the model has some assumptions. These are as follows: the fluid flow is assumed to be quasi-one-dimensional; the kinetic energy of the fluid is neglected in comparison with its internal energy; the flow of the gas or mixture through the suction or discharge ports is assumed to be isentropic, while the leakage flow is regarded as adiabatic. The computational domain is shown in Figure A- 4.

The conservation of internal energy is

$$\omega\left(\frac{dU}{d\theta}\right)=\dot{m}_{in}h_{in}-\dot{m}_{out}h_{out}+\dot{Q}-\omega p\frac{dV}{d\theta} \qquad \text{(II-1)}$$

where θ is angle of rotation of the main rotor, $h=h(\theta)$ is specific enthalpy, $\dot{m}=\dot{m}(\theta)$ is mass flow rate, $p=p(\theta)$ fluid pressure in the control volume, $\dot{Q}=\dot{Q}(\theta)$, heat transfer

between the fluid and the compressor surrounding, $\dot{V} = \dot{V}(\theta)$ local volume of the compressor working chamber, while $\omega = {d\theta}/{dt}$ represents angular velocity.

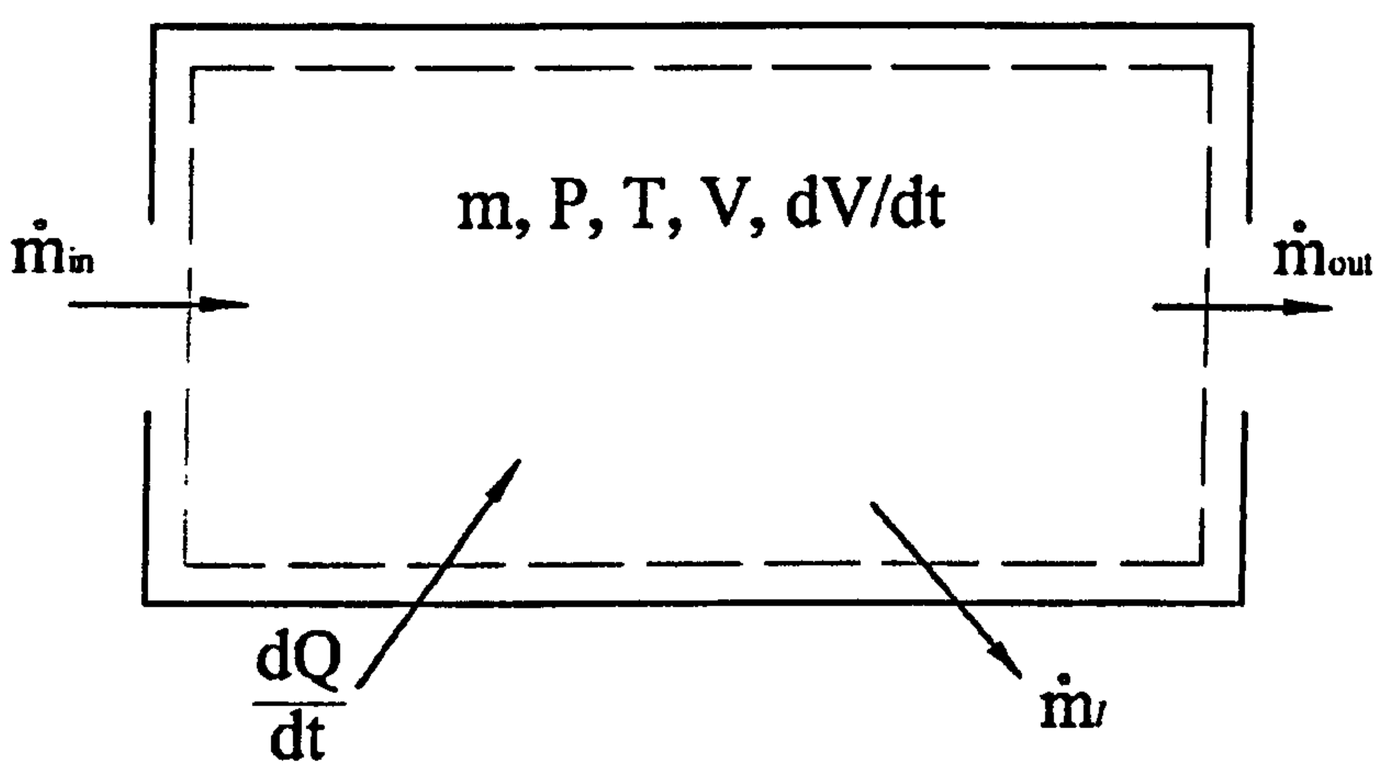

Figure A- 4 Screw compressor control volume for one-dimensional analysis

The total inflow (*in*) and outflow (*out*) enthalpies are:

$$\begin{aligned} \dot{m}_{in} h_{in} &= \dot{m}_{suc} h_{suc} + \dot{m}_{l,g} h_{l,g} + \dot{m}_{oil} h_{oil} \\ \dot{m}_{out} h_{out} &= \dot{m}_{dis} h_{dis} + \dot{m}_{l,l} h_{l,l} \end{aligned} \qquad \text{(II-2)}$$

where index *l,g* denotes leakage gain, *l,l* is the leakage loss, *suc*, *dis* and *oil* represent suction, discharge and oil parameters respectively.

The other terms on the right hand side of the energy equation (II-1) are also modelled. The heat exchange between the fluid and solid parts of the machine (rotors and housing) is accounted for through the heat transfer coefficient evaluated from the Nusselt number. The thermodynamic work supplied to the gas during the process of compression is represented by the term $p\frac{dV}{d\theta}$. This term is evaluated from the local pressure and local volume change rate. The latter is obtained from the relationships defining the screw kinematics, which yield the instantaneous working volume and its change with rotation angle.

The mass continuity equation is

$$\omega \frac{dm}{d\theta} = \dot{m}_{in} - \dot{m}_{out} \tag{II-3}$$

Similarly to (II-2) the inflow and outflow mass rates are:

$$\begin{aligned} \dot{m}_{in} &= \dot{m}_{suc} + \dot{m}_{l,g} + \dot{m}_{oil} \\ \dot{m}_{out} &= \dot{m}_{dis} + \dot{m}_{l,l} \end{aligned} \tag{II-4}$$

Each of the mass flow rates satisfies the continuity equation $\dot{m} = \rho w A$ where w denotes fluid velocity, ρ is fluid density and A is the flow cross-section area. The instantaneous density $\rho=\rho(\theta)$ is obtained from the instantaneous mass m and corresponding volume V as $\rho=m/V$.

The computation of the leakage flow is conducted on the assumption that the leakage process is essentially adiabatic Fanno-flow. A detailed description is given by *Stošić* (1996) and (2001). Injection of oil or other liquids for lubrication, cooling or sealing purposes, modifies substantially the thermodynamic process in a screw compressor. The method to take the injection fluid into account is described by *Stošić et al* (1990).

According to equation (II-1), the internal thermal energy of the gas-oil mixture is given as

$$U = (mu)_{gas} + (mu)_{oil} = (mu)_{gas} + (mcT)_{oil} \tag{II-5}$$

Since the internal energy can be expressed as a function of temperature and specific volume only, $u = f_1(T,V)$, similarly to the pressure $p = f_2(T,V)$, the procedure for calculation of pressure and temperature within the working chamber appears to be valid for both real and ideal fluids. This allows the calculation of a large variety of working fluids by means of a number of different software packages such as the Lee-Kessler equations, the IIR and NIST procedures.

The solution of the set of equations is performed numerically by employing the Runge-Kutta method which is of the 4th order, with appropriate initial and boundary conditions.

II.2 TWO-DIMENSIONAL EFFECTS

There are at least two phenomena that appear in screw compressor working processes which can be regarded as two dimensional. These are leakage flow and the heat transfer between the fluid and the solid body. These can be analysed in a two-dimensional manner and incorporated into the one-dimensional method.

An idealized clearance gap is assumed to be of rectangular shape in which case the mass flow of leaking fluid is expressed by the continuity equation $\dot{m}_l = \mu_l \rho_l w_l A_g$. There, ρ and $\dot{w}$ are density and the velocity of the leaking fluid respectively, $A_g = l_g \delta_g$ is the cross-sectional area of the clearance gaps, l_g is the length of the sealing line, δ_g the thickness of the leakage clearance also called the gap. $\mu=\mu(Re,Ma)$ is the discharge coefficient of the leakage flow.

However, the leakage clearance defined through δ_g usually is not constant. It changes along the sealing line and therefore the cross sectional area is not equal to an idealised rectangular path. The clearance δ_g becomes the function of the x and y coordinates of both the male and female rotors, which are, in the process of rotor generation, given as a function of the angle of rotation θ. More about this is given in *Stošić* (2001).

The oil-gas heat exchange is based on the temperature difference and the value of the Sauther mean droplet diameter. The temperature difference (3.29) is a function of the time constant k_t. The described approach is based on the assumption that the oil-droplet time constant τ is smaller than the time for which droplet travels through the gas before it hits the rotor or casing wall, or reaches the compressor discharge port. This means that heat exchange is completed within the droplet travelling time through the gas during compression. This prerequisite is fulfilled by appropriate atomisation of the injected oil which produces a sufficiently small droplet. It is achieved by the correct

selection of the nozzle angle, and, to some extent, the initial oil spray velocity. The separate computation of the droplet trajectory based on the solution of the droplet momentum equation for different droplet mean diameters and initial velocities, is usually done in two dimensions, in the cross section area of the screw compressor. For more details, refer to *Stošić et al* (1992).

II.3 COMPRESSOR INTEGRAL PARAMETERS

Numerical solution of the mathematical model of the physical process in the compressor provides the basis for more exact computation of all the desired integral bulk flow characteristics with a satisfactory degree of accuracy. In that respect, it is superior to a more empirical integral approach. The most important properties are the compressor mass flow $\dot{m}$ [kg/s], indicated power P_{ind} [kW], specific indicated power P_s [kJ/kg], volumetric efficiency η_v, adiabatic efficiency η_a, isothermal efficiency η_t and power utilization coefficient, indicated as efficiency η_i. These are directly calculated from the thermodynamic properties obtained within the working cycle and from the compressor theoretical displacement. The indicated work transferred to the screw rotors during the suction, expansion and discharge processes is represented by the area of the indicated *p-V* diagram generated from calculated values, *Stošić* (2001).

Appendix III

Turbulent Flow

Most engineering flows can only be regarded as mean flows calculated on an average basis, since small scale fluctuations of all flow quantities with high frequency are always present in both space and time. The flow is in fact in a particular state of continuous instability, which is called turbulence. Such flows are called turbulent flows.

Turbulent flows are well described by the governing differential equations presented in Section 3.2. However, their direct numerical simulation requires a mesh with spacing smaller than the length scale of the smallest turbulent eddies at which the energy is transformed to heat and time steps smaller than the smallest time scale of the turbulent fluctuations. Some calculations show that the average length scale of the smallest eddies in positive displacement machines is of the order of $10\mu m$ while their time scale is of the order of a couple of milliseconds, *Lumley* (1999). This requires calculating resources, which are not available at the present state of computer technology.

The alternatives are either, large eddy simulation, in which only the largest unsteady motions are resolved and the rest is modelled, or a solution of the Reynolds averaged Navier-Stokes equations, where all turbulent effects on the mean flow are modelled as functions of mean fluid flow quantities. These equations are also very time and space consuming to be applied.

The alternative to that are Reynolds averaged Navier-Stokes equations (RANS) obtained by using a statistical description of the turbulent motion formulated in terms of averaged quantities. The most popular is the Reynolds averaging for flows with constant density, whereby each dependent variable is expressed as a sum of its mean, or time-averaged value $\bar{\phi}$, and a fluctuating component ϕ'':

$$\phi = \bar{\phi} + \phi'' . \qquad \text{(III-1)}$$

The value $\bar{\phi}$ is averaged over the time interval, which is large enough, compared to the time scale of the turbulent fluctuations, but small with respect to the scale of other time dependant effects. For compressible flows a density-weighted, Favre averaging is used through the following definition:

$$\phi = \hat{\phi} + \phi', \qquad \text{(III-2)}$$

with the time averaged value $\hat{\phi} = \overline{\rho\phi} / \bar{\rho}$, and the fluctuating component calculated as $\overline{\rho\phi'} = 0$.

Applied to the governing equations of Section 3.2.1 the averaging procedure produces a set of additional unknowns in the equations of momentum, energy and species. These unknowns are fluctuating parts in the diffusive term of the equations, while other dependent variables are considered as averaged quantities. With this approach, the stress tensor $\mathbf{T}$ in the momentum equation is substituted with its effective value $\mathbf{T}^e=\mathbf{T}+\mathbf{T}^t$, the heat flux $\mathbf{q}_h$ in the energy equation is incorporated in the effective value $\mathbf{q}_h{}^e=\mathbf{q}_h+\mathbf{q}_h{}^t$, while the effective value of diffusive mass flux in the concentration equation becomes $\mathbf{q}_{ci}{}^e=\mathbf{q}_{ci}+\mathbf{q}_{ci}{}^t$. The averaged parts are the same as in the original equations while the fluctuating parts are defined as follows:

Turbulent momentum flux, known as Reynolds stress is: $\mathbf{T}^t = -\overline{\rho \mathbf{v}'\mathbf{v}'}$ (III-3)

Turbulent heat flux is $\mathbf{q}_h^t = -\overline{\rho e'\mathbf{v}'}$ (III-4)

Turbulent mass flux is $\mathbf{q}_{ci}^t = -\overline{\rho c_i'\mathbf{v}'}$ (III-5)

These new unknown values must be accompanied by a turbulence model which provides correlations of the fluctuations in terms of the mean quantities, in order to be incorporated into the governing equations of Section 3.2.1. The most popular group of turbulence models are eddy-viscosity models, which are based on the analogy between the turbulent and viscous diffusion. By this model, equations (III-3) to (III-5) become

$$\mathbf{T}^t = 2\mu_t \dot{\mathbf{D}} - \frac{2}{3}(\mu_t \operatorname{div}\mathbf{v} + \rho k)\mathbf{I},$$
$$\mathbf{q}_h^t = \kappa_t \operatorname{grad} T, \qquad \text{(III-6)}$$
$$\mathbf{q}_{ci}^t = \rho D_{i,t} \operatorname{grad} c_{wi}.$$

Similarly, the effect of turbulence is introduced through the turbulent diffusivity, viscosity and conductivity as given in (III-8). These are fluctuating parts of the effective diffusivity, viscosity and conductivity values:

$$D_{i,eff} = D_i + D_{i,t},$$
$$\mu_{eff} = \mu + \mu_t, \qquad \text{(III-7)}$$
$$\kappa_{eff} = \kappa + \kappa_t,$$

defined respectively in the next set of equations:

$$\rho D_{i,t} = \frac{\mu_t}{\sigma_{ci}}, \qquad \mu_t = \rho C_\mu \sqrt{k} L, \qquad \kappa_t = \frac{\mu_t C_p}{\sigma_T}. \qquad \text{(III-8)}$$

Here, σ_{ci}, C_μ, σ_T are empirical coefficients reasonably similar for all RANS turbulence models. They are usually C_μ =0.09, $\sigma_{ci} = \sigma_T$ =0.9. In the previous equation k is kinetic energy of turbulence and L is a length scale. Turbulent kinetic energy is defined as

$$k = \frac{1}{2}\overline{\mathbf{v}' \cdot \mathbf{v}'} \qquad \text{(III-9)}$$

Turbulent diffusivity and conductivity in (III-8) are directly estimated after the turbulent viscosity.

Many RANS models of turbulence are developed up to date which are suitable for different fluid flow situations. Only two of them are described here in some detail. These are the Zero-Equation model and the Standard k-ε two-equation model. More details on turbulence phenomenon can be found for example, in *Ferziger and Perić* (1995) and *Wilcox* (1993).

III.1 ZERO-EQUATION MODEL OF TURBULENCE

Turbulence is characterized by its kinetic energy k or by the turbulent velocity $q = \sqrt{2k}$, and length scale L. When this is substituted into equation (III-8), the turbulent viscosity for the zero-equation model can be written as:

$$\mu_t = C_\mu \rho q L \qquad \text{(III-10)}$$

The kinetic energy of turbulence in this model is determined from the mean velocity field using

$$q = L\frac{\partial v}{\partial y} \qquad \text{(III-11)}$$

where L is a prescribed function dependent on the coordinates. Accurate determination of L is difficult for the separated and three-dimensional flows and despite being simple, this model is not often used for engineering flow simulation.

III.2 K-ε MODEL OF TURBULENCE

The difficulty in prescribing the turbulence quantities suggests the use of differential equations for their calculation. Since the turbulent velocity and length scale are needed, a model based on two such equations is a good choice. In the majority of models, the equation of the turbulent kinetic energy k determines the velocity scale. The equation of the length scale is derived, taking into account that, for equilibrium turbulent flows, the dissipation ε, kinetic energy k and length ratio L are related by:

$$\varepsilon \approx \frac{k^{3/2}}{L} \qquad \text{(III-12)}$$

Partial differential equations for both kinetic energy and its dissipation can be derived from the Navier-Stokes equations. The final form of these equations is given here in their integral form:

$$\frac{d}{dt}\int_v \rho k dV + \int_s \rho k(\mathbf{v}-\mathbf{v}_s)\cdot d\mathbf{s} = \int_s \mathbf{q}_k \cdot d\mathbf{s} + \int_v (P-\rho\varepsilon)dV,$$
$$\frac{d}{dt}\int_v \rho \varepsilon dV + \int_s \rho\varepsilon(\mathbf{v}-\mathbf{v}_s)\cdot d\mathbf{s} = \int_s \mathbf{q}_\varepsilon \cdot d\mathbf{s} + \int_v (C_1 P\frac{\varepsilon}{k} - C_2\rho\frac{\varepsilon^2}{k} - C_3\rho\varepsilon\, grad\,\mathbf{v})dV \quad \text{(III-13)}$$

where k is the turbulent kinetic energy (III-9), ε is its dissipation, while P is production of turbulence energy given by:

$$P = \mathbf{T}^t : grad\,\mathbf{v} = 2\mu_t \dot{\mathbf{D}} : \dot{\mathbf{D}} - \frac{2}{3}(\mu_t div\,\mathbf{v} + \rho k) div\,\mathbf{v} \quad \text{(III-14)}$$

Diffusion fluxes in (III-13) are:

$$\mathbf{q}_k = \left(\mu + \frac{\mu_t}{\sigma_k}\right) grad\, k, \qquad \mathbf{q}_\varepsilon = \left(\mu + \frac{\mu_t}{\sigma_\varepsilon}\right) grad\,\varepsilon. \quad \text{(III-15)}$$

while the turbulent viscosity after implementing (III-12) reads:

$$\mu_t = C_\mu \rho \frac{k^2}{\varepsilon} \quad \text{(III-16)}$$

The constants in the k-ε model of turbulence are derived experimentally and they are: $C_\mu = 0.09$, $\sigma_k = 1$, $\sigma_\varepsilon = 1.3$, $C_1 = 1.44$, $C_2 = 1.92$, $C_3 = -0.33$.

Implementation of the k-ε model of turbulence is relatively simple. All equations of the model have the same form as the previously stated equations and only the viscosity is replaced by the effective viscosity (III-7). In addition, two equations for kinetic energy and its dissipation, have to be solved (III-13). However, these two equations are solved separately, after the main equations are solved and the momentum and pressure equations are balanced with the k and ε values from the previous iteration. The main reason for that is the 'stiffness' of the equations of turbulence model. Namely, the profiles of the turbulent kinetic energy and its dissipation contain more peaks then the main velocity profile which are difficult to capture. Therefore, either a finer grid for turbulence model equations than for the main equations or a local blending of numerical schemes of different order could be used. It is also useful to under-relax the iterative

method for these two quantities in order to avoid the negative values of k and ε, whose appearance can lead to the numerical instability.

Appendix IV

Wall Boundaries

There are two types of walls applied to a screw compressor: moving walls, if they bound the domain on the compressor rotors, and stationary walls in all other places. Boundary conditions on these walls are explicitly given for all equations in the numerical model. In the case of turbulent flow, which occurs in a screw compressor, dependent variables vary rapidly near the solid boundaries and a method, which can model near wall effects, has to be used. If the flow is laminar, then either Dirichlet boundary conditions, where the dependent variable is known on the boundary, or Neuman boundary conditions, where the flux of the dependent variable is given on the boundary, can be used.

Screw compressor walls are treated as 'no-slip walls', the case when viscous fluid sticks to the boundary wall.

Boundary conditions for the momentum equation are given through the known velocities on the wall, which represent the Dirichlet boundary condition. For boundaries on the rotors, velocities are calculated from the prescribed speed of rotation n of the male rotor as:

$$\omega_1 = \frac{2n\pi}{60}; \qquad \mathbf{v}_{1i} = \mathbf{r}_{1i}\,\omega_1$$
$$\omega_2 = -\omega_1 \frac{z_1}{z_2}; \qquad \mathbf{v}_{2i} = \mathbf{r}_{2i}\,\omega_2 \tag{IV-1}$$

Index *1* indicates the male rotor while the value *2* is related to the female rotor, z_1 and z_2 are the number of teeth on the rotors, $\mathbf{r}_{1i}$ and $\mathbf{r}_{2i}$ are radius vectors of the boundary points on the male and female rotors in the absolute coordinate system, respectively. ω_1 and ω_2 are the angular velocities on the male and female rotors respectively. For all stationary walls the wall velocity is equal to zero.

If the flow is turbulent and the numerical grid is too coarse to resolve large velocity variations in the near wall region, a special interpolation is necessary, which gives values of the shear stress more realistically. This interpolation is based on the wall functions, which rely on the existence of a logarithmic region in the velocity profile. The viscosity near the wall is replaced by the value μ_w determined from the universal logarithmic velocity profile as:

$$\mu_w = \frac{y^+}{u^+}\mu; \qquad u^+ = \begin{cases} y^+ & for \quad y^+ < y_v^+ \\ \frac{1}{\mathrm{K}}\ln(\mathcal{E}y^+) & for \quad y^+ \geq y_v^+ \end{cases} \qquad \text{(IV-2)}$$

where $\mathcal{E}$ is the wall roughness constant for logarithmic profile, K is he von Karman constant (K=0.41), y^+ is a dimensionless distance from the wall and y_v^+ is the viscous sub-layer thickness.

If the zero-equation turbulence model is applied, then

$$y^+ = \frac{1}{K}\frac{\mu+\mu_t}{\mu}. \qquad \text{(IV-3)}$$

For the k-ε model of turbulence this distance is:

$$y^+ = \frac{\rho\sqrt[4]{C_\mu}\sqrt{k_P}\delta_{nP}}{\mu}. \qquad \text{(IV-4)}$$

In the previous equation, k_P is the kinetic energy of turbulence at the centre of the boundary cell while σ_{nP} denotes the normal distance from the centre of the boundary cell to the wall.

The viscous sub-layer thickness is defined as the larger root of the non-linear equation

$$y_v^+ = \frac{1}{K}\ln\left(\mathcal{E}y_v^+\right) \qquad \text{(IV-5)}$$

The boundary condition for the continuity equation is the mass flux through the wall, which is equal to zero. This is the Neumann boundary condition which implies zero gradient of the pressure correction in the direction normal to the wall. Because of that, the pressure is always extrapolated from inside the solution domain.

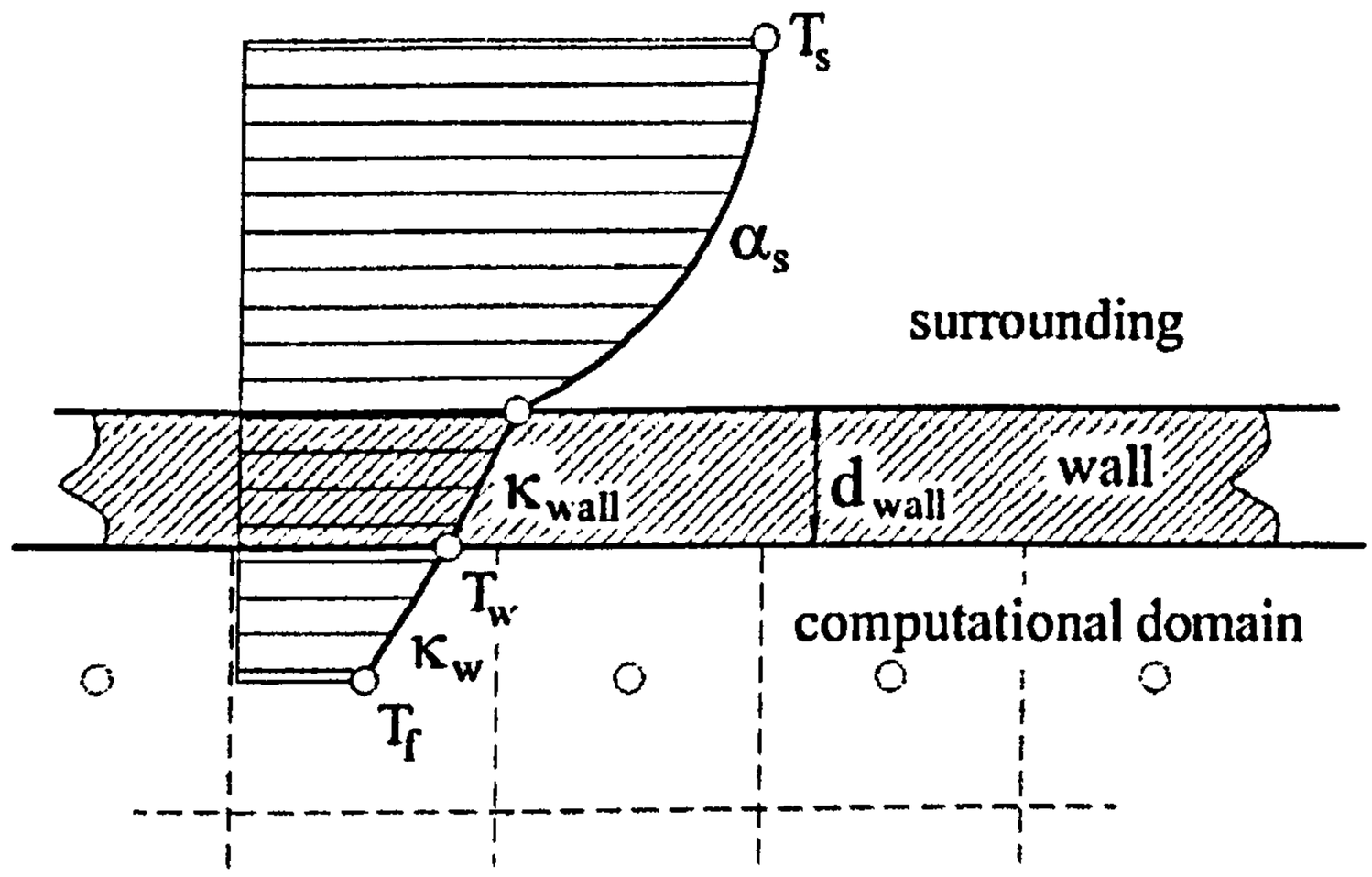

Figure A- 5 Wall thermal resistance

At the wall boundaries, Dirichlet, Neuman or mixed boundary conditions for the energy equation can be specified. There are no walls in the screw compressor that are adiabatic or on which the flux rate is exactly known. In such a situation, only Dirichlet boundary conditions on the wall are possible. However, sometimes the temperature on the wall is not exactly known but the temperature of the surrounding T_s is given. If the heat transfer coefficient between the surrounding and the wall can be estimated, the wall temperature T_W can be easily calculated from the surrounding temperature and the wall thermal resistance coefficient k_w. It is defined as

$$k_w = \frac{d_{wall}}{\kappa_{wall}} + \frac{1}{\alpha_s} \qquad \text{(IV-6)}$$

where the wall thickness d_{wall}, the thermal conductivity κ_{wall} and the heat transfer coefficient between the wall and the surrounding α_s are defined in Figure A- 5.

For turbulent flow, when the mesh is too coarse to resolve the large temperature variations in the near wall region, the interpolation based on the universal logarithmic temperature profile is applied. Realistic values of the heat flux can be obtained by use of the modified thermal conductivity in the near wall region on Figure A- 5, which has the following form:

$$\kappa_w = \begin{cases} \kappa & for \quad y^+ < y_T^+ \\ \dfrac{y^+}{u^+ + P_T} \dfrac{\mu C_p}{\sigma_T} & for \quad y^+ \geq y_T^+ \end{cases} \tag{IV-7}$$

where P_T is the viscous sub-layer resistance factor defined by the Prandtl number Pr and the turbulent Prandtl number σ_T as:

$$P_T = 9.24\left[\left(\frac{\mathrm{Pr}}{\sigma_T}\right)^{0.75} - 1\right]\left[1 + 0.28\exp\left(-0.007\frac{\mathrm{Pr}}{\sigma_T}\right)\right] \tag{IV-8}$$

The thermal sub-layer thickness y_T^+ is defined as the larger root of the non linear equation

$$\frac{\mathrm{Pr}}{\sigma_T} y_T^+ = \frac{1}{K}\ln\left(\varepsilon_T y_v^+\right) \tag{IV-9}$$

where ε_T is the wall roughness parameter in the logarithmic temperature profile.

The k-e turbulence model in conjunction with wall functions requires values of the production of turbulent kinetic energy and the dissipation rate of the turbulent kinetic energy to be given in a boundary cell. These two values are calculated from the logarithmic velocity profile. The diffusive flux of kinetic energy through the wall is assumed zero *Ferziger and Peric* (1995).

For the governing equations of the concentration of oil and liquid phases, Neuman boundary conditions with the diffusive flux through the wall set to zero are applied.

Appendix V

Finite Volume Discretisation of Equations

V.1 DISCRETISATION PRINCIPLES

The mathematical model for screw compressor fluid flow consists of continuity, momentum, energy, concentration, space and turbulence model equations. All of them can be written in the following general form:

$$\frac{d}{dt}\int_V \rho\phi dV + \sum_{j=1}^{n_f}\int_{S_j} \rho\phi(\mathbf{v}-\mathbf{v}_s)\cdot d\mathbf{s} = \sum_{j=1}^{n_f}\int_{S_j}\Gamma_\phi \operatorname{grad}\phi\cdot d\mathbf{s} + \left(\sum_{j=1}^{n_f}\int_{S_j}\mathbf{q}_{\phi S}\cdot ds + \int_V q_{\phi V}\cdot dV\right) \qquad \text{(V-1)}$$

These should be discretised prior to solving. Due to that, surface and volume integrals have to be replaced by quadrature approximations, spatial derivatives have to be replaced by some interpolation function, the time integration scheme has to be selected and the surface velocities $\mathbf{v}_s$ have to be determined. The result of discretisation is expressed in the form of a system of algebraic equations which then could be solved efficiently. Before the equations are discretised the volume of a numerical cell and a cell surface, which is generated in the space discretisation procedure, have to be known.

The volume of an arbitrary control volume (CV) is calculated using Gauss theorem

$$\int_V div\mathbf{r}\, dV = \int_S \mathbf{r}\cdot d\mathbf{s} \Rightarrow V_{P_0} = \frac{1}{3}\sum_{j=1}^{n_f}\mathbf{r}_j\cdot\mathbf{s}_j\,. \qquad \text{(V-2)}$$

In this equation $\mathbf{r}_j$ is the position vector of the cell face centre, $\mathbf{s}_j$ is a cell face surface vector and n_f is the number of the cell faces. The surface integral is approximated using a midpoint rule described later in the text.

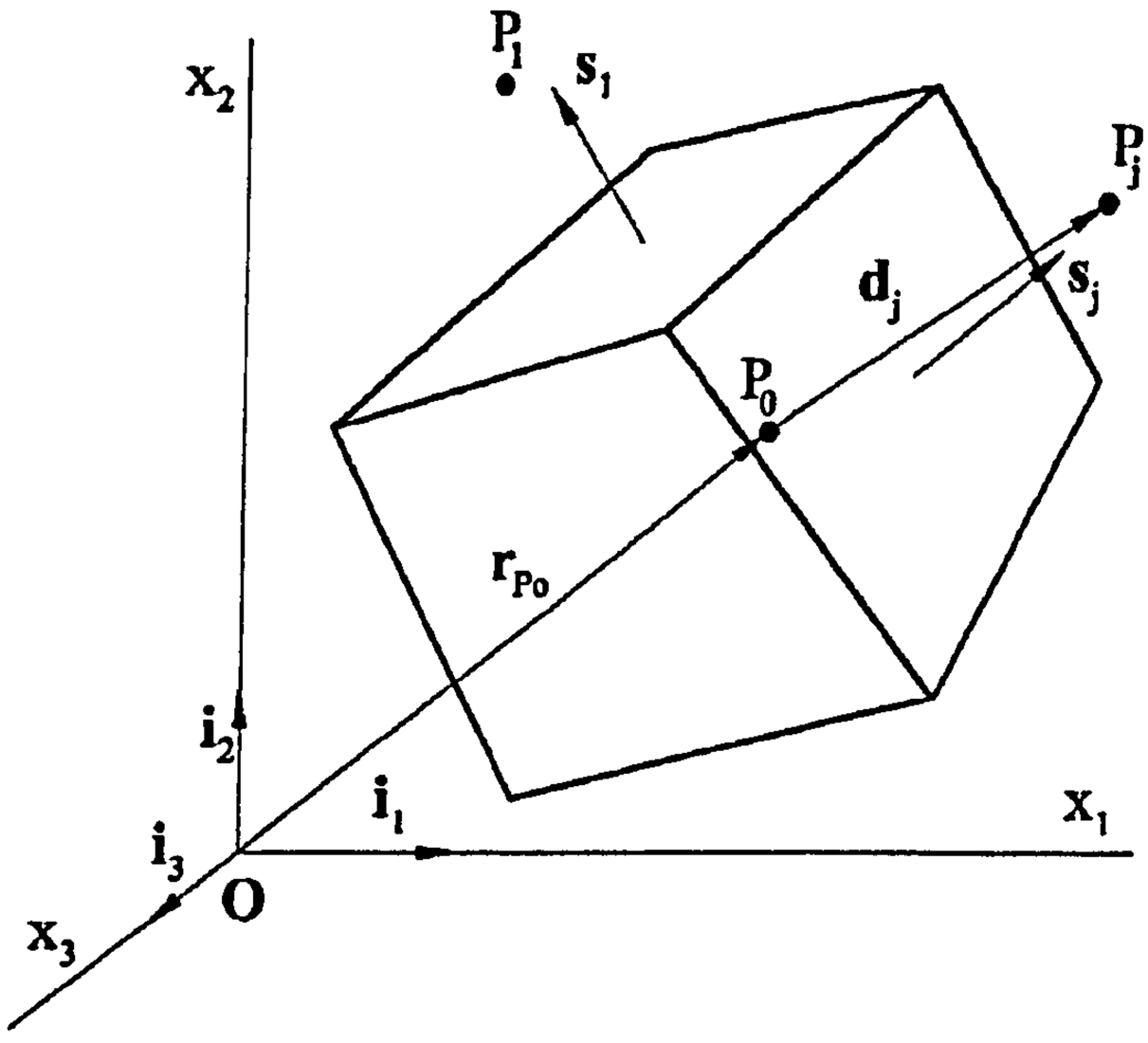

Figure A- 6 Notation applied to a hexahedral control volume

Since the edges of the CV are straight lines, the projections of the faces onto Cartesian coordinate surfaces are independent of the actual shape of the surface. These represent the Cartesian components of the surface vector, which are calculated by subdividing the cell face into triangles, for which surface vectors are easily computed;

$$s_j = \frac{1}{2}\sum_{i=3}^{n_j^v}\left[(\mathbf{r}_{i-1}-\mathbf{r}_1)\times(\mathbf{r}_i-\mathbf{r}_1)\right]. \qquad \text{(V-3)}$$

Here, n^v_j is the number of vertices in the cell-face j, and r_i is the position vector of the vertex i. The cell face area is independent of the choice of the common vertex $\mathbf{r}_1$.

Equation (4.62) consists of a number of integrals and gradients that also have to be approximated to obtain a system of algebraic equations. Both, the surface and volume integrals are approximated using a quadrature approximation. The simplest and the most frequently used is the midpoint rule approximation which is the product of the integrand at the centre of the integration domain and the surface or volume of the domain:

$$\int_{S_j}\mathbf{f}\cdot d\mathbf{s} \approx \mathbf{f}_j\cdot\mathbf{s}_j, \qquad \int_V f\,dV \approx f_{P_0}V_{P_0} \qquad \text{(V-4)}$$

where $\mathbf{f}$ and f are arbitrary vector and scalar respectively.

Although the variables and fluid properties are defined after discretisation at the computational nodes in the centre of CV, these quantities are often needed at locations other than the cell centres. In such a case, an interpolation based on the shape function is used. The simplest second-order linear approximation is used here.

$$\psi(\mathbf{r}) = \psi_{P_0} + (grad\psi)_{P_0} \cdot (\mathbf{r} - \mathbf{r}_{P_0}) \tag{V-5}$$

This equation applied to the cell face centre, in the symmetric form reads:

$$\psi_j = \frac{1}{2}(\psi_{P_0} + \psi_{Pj}) + \frac{1}{2}\left[(grad\psi)_{P_0} \cdot (\mathbf{r}_j - \mathbf{r}_{P_0}) + (grad\psi)_{P_j} \cdot (\mathbf{r}_j - \mathbf{r}_{P_j})\right] \tag{V-6}$$

The form of equation (V-6) ensures a unique approximation of the property at the centre of the cell face for CVs on both sides of the face. In this equation, $\mathbf{r}_j$ is the position vector of the cell face centre while P_o and P_j represent the centres of the calculating and neighbouring CV, Figure 4-2. The first term in this equation is a linear interpolation between the neighbouring cell centres, while the second term gives the correction for the cell nonorthogonality.

Since the variables are required at both the cell centres and the cell face centres, the gradients of the variables at these locations are also needed. Gauss theorem and the midpoint role integral approximation in the simple and efficient way obtain second order accuracy.

$$\int_V \text{grad}\,\psi\, dV = \int_S \psi\, d\mathbf{s} \Rightarrow \qquad (\text{grad}\,\psi)_{P_0} \approx \frac{1}{V_{P_0}} \sum_{j=1}^{n_f} \psi_j \mathbf{s}_j \tag{V-7}$$

Here, ψ_j is the value of variable ψ at the cell face centre.

The first term in the prototype equation (4.62) is different to the others because it contains an integration in time. If the equation is rearranged into the following form:

$$\frac{d\Psi}{dt} = F(\phi) \tag{V-8}$$

where

$$\Psi = \int_V \rho B_\phi \mathrm{d}V \approx \left(\rho B_\phi V\right)_{P_0} \quad \text{and} \qquad \phi = \phi(\mathbf{r}, t)$$

then the left side of this equation can be exactly integrated in time from t_{m-1} to $t_m = t_{m-1} + \delta t_m$. However, the mean value of the right hand side, which incorporates the convective and diffusive fluxes and source terms, is approximated over the interval δt_m. This is done through either the two-time-level Euler implicit scheme or the three-time-level implicit scheme. The first one is a first-order fully implicit approximation that requires less storage then the second one and poses no limitations on the time step size. Its implicit form means that the current value of F is used for calculation of the quantity Ψ at t_m time:

$$\Psi^m = \Psi^{m-1} + F^m \delta t_m \tag{V-9}$$

The three-time-level implicit scheme extends the time integrating domain for one more time step and in the case of constant time steps it reads:

$$\Psi^m = \Psi^{m-1} + \frac{2}{3} F^m \delta t_m + \frac{1}{3}\left(\Psi^{m-1} - \Psi^{m-2}\right). \tag{V-10}$$

It is accurate to the second order and is more stable than other schemes of the same accuracy. Switching to the Euler scheme, when accuracy is not essential, is easy. In this thesis only the two time level scheme would be applied for discretisation of dependent variables in time. More on this can be found in *Ferziger and Peric* (1995).

Solution of the prototype equation for the moving boundaries requires implementation of the space conservation law. The mesh movement is known in advance for both the fluid flow and the solid body as the function of the rotor rotation. The cell surface velocity $\mathbf{v}_s$, which exists in the prototype equation, is calculated in both cases when

either the two-time-levels or the three-time-levels scheme is used. In fact, the convective term in the prototype equation is a volume flux within the cell minus a volume flux through the faces. It is more convenient to express that term as the sum of fluxes than to calculate the surface velocity separately. In the Euler implicit scheme the volume fluxes through the faces are:

$$\frac{V_{P_0}^m - V_{P_0}^{m-1}}{\delta t_m} = \sum_{j=1}^{n_f} \int_{S_j} \mathbf{v}_s \cdot \mathbf{ds} = \sum_{j=1}^{n_f} \frac{\delta V_j^m}{\delta t_m} = \sum_{j=1}^{n_f} \dot{\delta V}_j^m \qquad \text{(V-11)}$$

while in the three-time-levels implicit scheme, the face volume fluxes are:

$$\frac{V_{P_0}^m - 4V_{P_0}^{m-1} + V_{P_0}^{m-2}}{\delta t_m} = \sum_{j=1}^{n_f} \int_{S_j} \mathbf{v}_s \cdot \mathbf{ds} = \sum_{j=1}^{n_f} \frac{\delta V_j^m}{\delta t_m} + \sum_{j=1}^{n_f} \frac{\delta V_j^m - \delta V_j^{m-1}}{2\delta t_m} \qquad \text{(V-12)}$$

The values $V_{P_0}^m, V_{P_0}^{m-1}, V_{P_0}^{m-2}$ are the volumes of the calculating cell at times t_m, t_{m-1} and t_{m-2} respectively and δV_j^m and δV_j^{m-1} are the volumes swept by the cell face s_j during the two consecutive time intervals δt_m. This is an arrangement which allows the volume fluxes at the cell faces to be calculated without knowing the value of the cell face velocity exactly. The swept volumes are easily calculated when the coordinates of the vertices are known throughout the working cycle.

The discretisation procedure for the four main terms in the prototype equation (4.62), namely the transient, convective, diffusive and source terms will be discussed briefly in the next paragraphs.

V.1.1 Transient Term

Transient rate of change is discretised through either the two-time-levels Euler discretisation (V-9) or the three-time-levels implicit discretisation scheme (V-10).

If the two-time-levels implicit Euler scheme is used for approximation of the transient term, it becomes:

$$\frac{\mathrm{d}}{\mathrm{d}t}\int_{\mathrm{V}} \rho B_{\phi} \mathrm{d}V \approx \frac{\left(\rho B_{\phi} V\right)_{\mathrm{P_0}} - \left(\rho B_{\phi} V\right)_{\mathrm{P_0}}^{m-1}}{\delta t_m} \qquad \text{(V-13)}$$

Assuming constant time steps, the transient term for the three-time-levels implicit scheme becomes:

$$\frac{\mathrm{d}}{\mathrm{d}t}\int_{\mathrm{V}} \rho B_{\phi} \mathrm{d}V \approx \frac{3\left(\rho B_{\phi} V\right)_{\mathrm{P_0}} - 4\left(\rho B_{\phi} V\right)_{\mathrm{P_0}}^{m-1} + \left(\rho B_{\phi} V\right)_{\mathrm{P_0}}^{m-2}}{\delta t_m}. \qquad \text{(V-14)}$$

The transient term has the same discretised form for all dependent variables in the fluid flow model where $B\phi$ stands for c_i, v_i, h, k, ε and the only difference appears for the momentum equation for solids.

V.1.2 Convective Flux

The convective flux of variable ϕ through the cell face j in the prototype equation (4.62) is a nonlinear term and, in order to be discretised, it must be linearized first. This is done by the Picard iteration approach which assumes that the mass flux is known for the calculation of the variable after which it is corrected by an iterative procedure until the iteration criterion is satisfied. The convective term then becomes:

$$C_{\mathrm{j}} = \int_{S\mathrm{j}} \rho\phi\left(\mathbf{v} - \mathbf{v}_s\right)\cdot \mathrm{d}\mathbf{s} \approx \dot{m}_{\mathrm{j}}\phi_{\mathrm{j}}^{\bullet}. \qquad \text{(V-15)}$$

The mass flux through the cell face $\dot{m}_{\mathrm{j}}$ is defined as:

$$\dot{m}_{\mathrm{j}} = \int_{S\mathrm{j}} \rho\left(\mathbf{v} - \mathbf{v}_s\right)\cdot \mathrm{d}\mathbf{s} \approx \rho_{\mathrm{j}}^{\bullet}\left(\mathbf{v}_{\mathrm{j}}^{\bullet}\cdot\mathbf{s}_{\mathrm{j}} - \dot{V}_{\mathrm{j}}\right), \qquad \text{(V-16)}$$

where the density ρ_j^* and velocity $\mathbf{v}_j^*$ are calculated through the pressure correction procedure described in V.1.7.

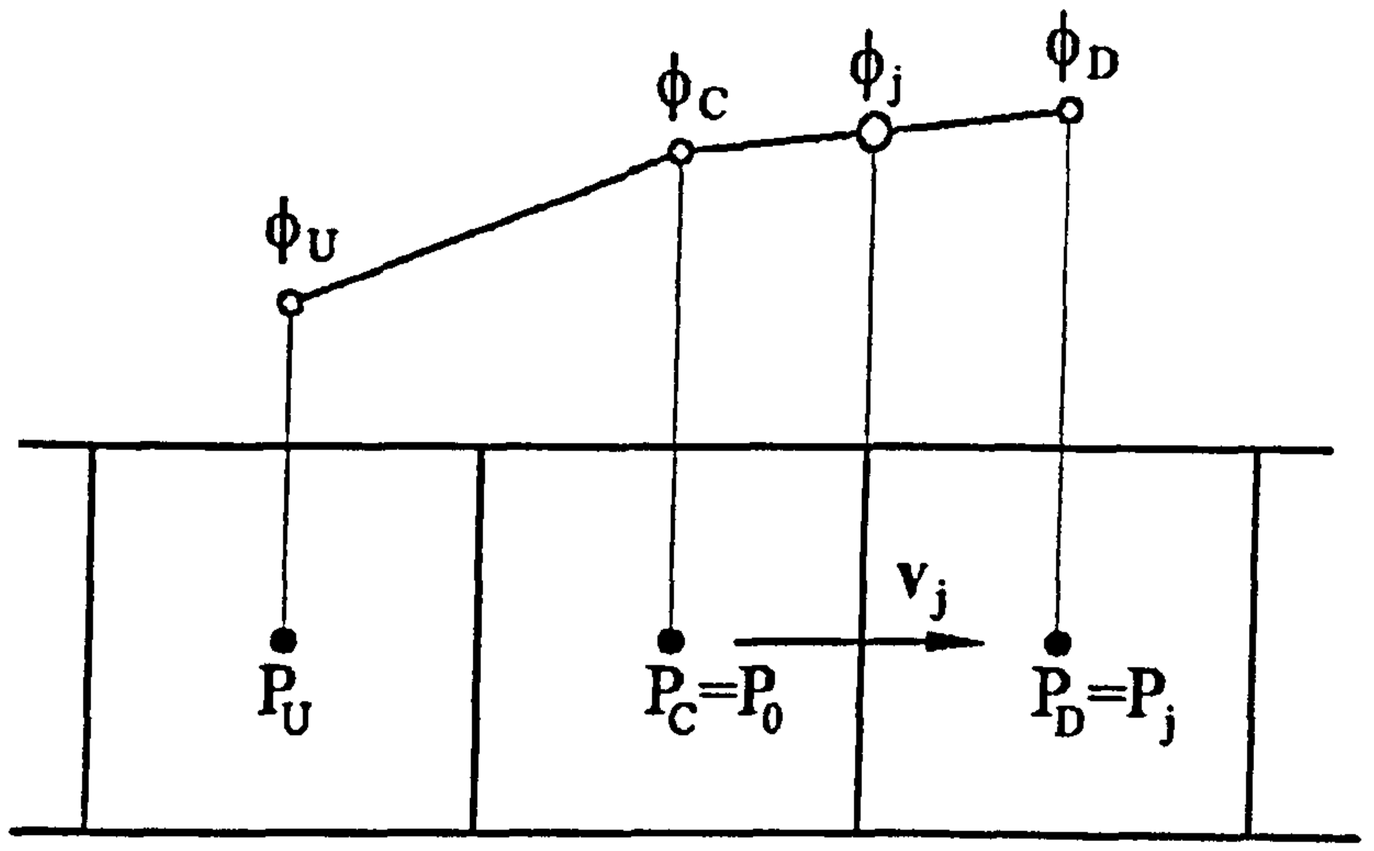

Figure A- 7 Upwind, central and downwind cell arrangement

There are several possibilities for calculation of the value at the cell face centre ϕ_j^* for equation (V-15). To explore them, variables in the centre of cells and at the cell face centre are defined according to Figure A- 6. A criterion to avoid non-physical oscillations is that the value in the central cell must be locally bounded between upstream and downstream values i.e. $\phi_U \le \phi_C \le \phi_D$ or $\phi_D \le \phi_C \le \phi_U$. Its value depends on the flow direction as it is presented in the previous figure.

The normalised variables at the end face α_j and at the centre of the cell α_C are calculated as

$$\alpha_j = \frac{\phi_j - \phi_U}{\phi_D - \phi_U}; \quad \alpha_C = \frac{\phi_C - \phi_U}{\phi_D - \phi_U}. \tag{V-17}$$

To visualise the criterion for the appearance of non-physical oscillations α_j is put on the ordinate of the diagram presented in Figure A- 8 while α_C is put on the abscissa. The normalised value α_j for each numerical cell falls in the hatched region of the upper triangle if $0 \le \alpha_c \le 1$ and otherwise lies on the line $\alpha_j=\alpha_C$ if the numerical solution is

bounded. The satisfaction of this criterion is especially important in cases when values of the physical property should not become negative, like density or concentration, or when they should not exceed unity, as concentration. However, many factors affect these conditions like, for example, the presence of sources in the equations. Three schemes are mentioned here for the solution of the convective flux.

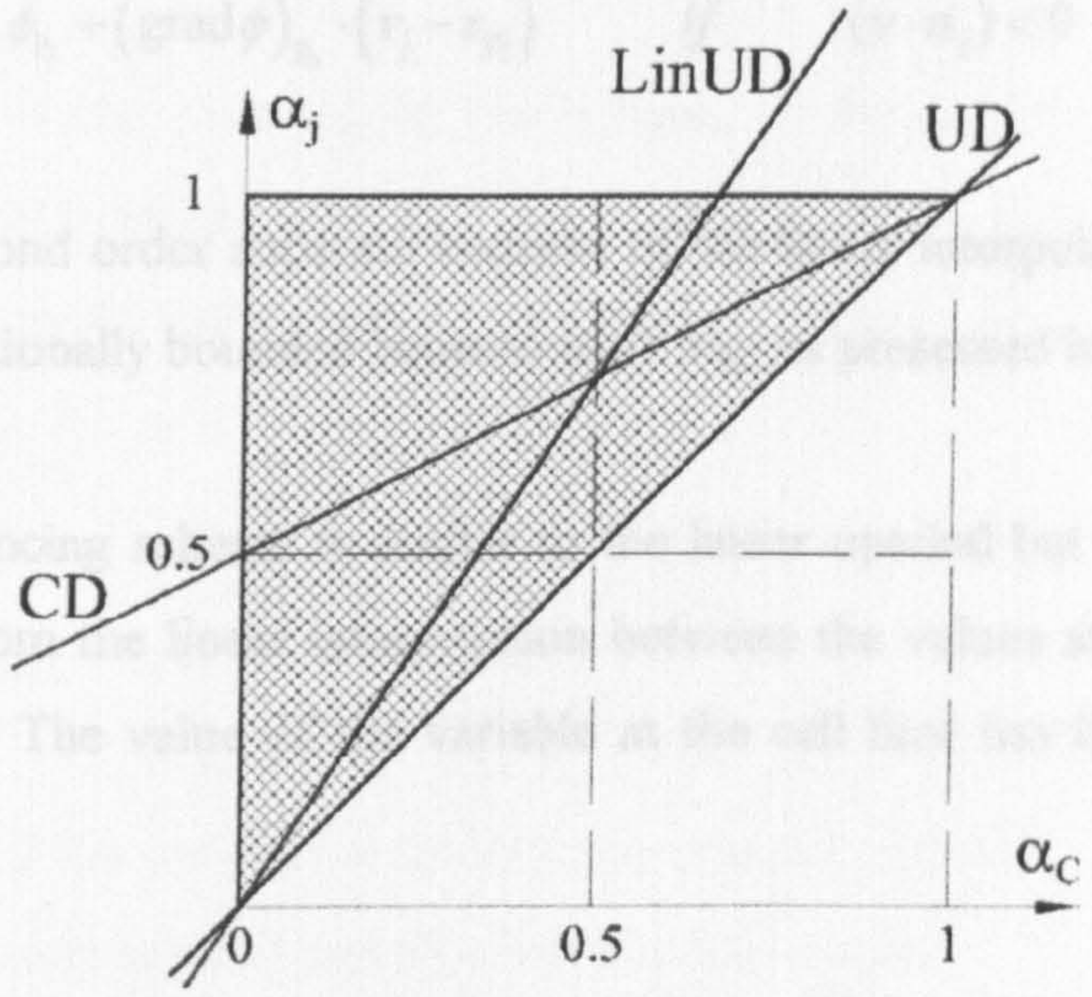

Figure A- 8 Normalised variable diagram NVD

– Upwind differencing is the scheme in which the value at the cell faces is equal to the value at the node upstream of the face. The value of the variable at the boundary ϕ_j^* is defined as:

$$\left(\phi_j^*\right)^{UD} = \begin{cases} \phi_{P_0} & if \quad (\mathbf{v}\cdot\mathbf{n}_j) > 0 \\ \phi_{P_j} & if \quad (\mathbf{v}\cdot\mathbf{n}_j) < 0 \end{cases} \tag{V-18}$$

Upwind differencing is the only approximation that satisfies the boundedness criterion because $\alpha_j=\alpha_C$ and it never leads to an oscillatory solution. However, it imposes numerical diffusion on the calculation and results in first order accuracy. The values ϕ_{P_0} and ϕ_{P_j} are specified for the computational point and centre of the neighbouring cell respectively.

– Linear upwind differencing corrects the upwind value by the gradient of the variable which accounts only for the upstream neighbours. The same rule as for the upwind differencing is applied. The cell face value is:

$$\left(\phi_j^*\right)^{LUD} = \begin{cases} \phi_{P_0} + \left(\text{grad}\phi\right)_{P_0}^* \cdot \left(\mathbf{r}_j - \mathbf{r}_{P_0}\right) & \text{if} \quad (\mathbf{v}\cdot\mathbf{n}_j) > 0 \\ \phi_{P_j} + \left(\text{grad}\phi\right)_{P_0}^* \cdot \left(\mathbf{r}_j - \mathbf{r}_{Pj}\right) & \text{if} \quad (\mathbf{v}\cdot\mathbf{n}_j) < 0 \end{cases} \qquad \text{(V-19)}$$

The scheme is second order accurate because of the linear interpolation between points but it is only conditionally bounded because $\alpha_j = 1.5\alpha_C$ as presented in Figure A- 8.

The central differencing scheme is similar to the linear upwind but the value at the cell face is obtained from the linear interpolation between the values at the calculating and neighbouring cells. The value of the variable at the cell face has the form of equation (V-6) and it reads:

$$\phi_j^{CD} = \frac{1}{2}\left(\phi_{P_0} + \phi_{Pj}\right) + \frac{1}{2}\left[\left(\text{grad}\phi\right)_{P_0} \cdot \left(\mathbf{r}_j - \mathbf{r}_{P_0}\right) + \left(\text{grad}\phi\right)_{P_j} \cdot \left(\mathbf{r}_j - \mathbf{r}_{P_j}\right)\right] \qquad \text{(V-20)}$$

Gradients in this equation are calculated from the values in both the central and neighbouring cell. The central differencing scheme is of second order of accuracy and, similar to the linear upwind, it can give unbounded and oscillatory solutions. This happens if the computational grid is too coarse. However, once the grid is sufficiently fine, the result converges faster than in other schemes.

There are also other schemes which combine these three basic ones and take advantage of each of them. For example, the *MINMOD* scheme is always of the second order of accuracy and it uses upwind differencing in the unbounded regions when $\alpha_C < 0$ and $\alpha_C > 1$, linear upwind in the region $0 < \alpha_C < 0.5$ and central differencing for $0.5 < \alpha_C < 1$. There are also some recent schemes, which are incorporated in commercial software, like that from *Przulj and Basara* (2001).

To prevent non-physical oscillations and wiggles, combination i.e. blending of the second order and the first order schemes is often used. It is based on the following formula:

$$\phi_j^* = \phi_j^{FO} + \gamma_\phi \left(\phi_j^{SO} - \phi_j^{FO} \right) \qquad \text{(V-21)}$$

where, ϕ_j^{FO} is the value obtained by the scheme of first order accuracy, while ϕ_j^{SO} represents the second order scheme. The blending factor γ_ϕ is a constant for the calculating domain but its value depends on the mesh quality.

V.1.3 Diffusive Flux

The diffusive flux of the variable ϕ through the internal cell face j is approximated by use of the mid point rule approximation of the surface integral.

$$D_j = \int_{S_j} \Gamma_\phi (\text{grad}\phi)_{P_0}^* \cdot \text{ds} \approx \Gamma_{\phi j} (\text{grad}\phi)_j^* \cdot \mathbf{s}_j \qquad \text{(V-22)}$$

In this equation $\Gamma_{\phi j}$ stands for diffusivity at the cell face centre obtained using (V-6). However, a second order approximation of the gradient from (V-7) cannot handle oscillations which have a period of twice the characteristic length of the numerical mesh and due to that, the third order dissipative term should be added to the interpolated value. More details about this one can be found in *Ferziger and Perić* (1995).

V.1.4 Source Terms

The source terms on the right hand side of the prototype equation (4.62) consist of two parts, namely the surface integral and the volume integral. They are discretised by means of the midpoint rule (V-4). As the result of discretisation, the surface integral over all the faces of the numerical cell becomes:

$$Q_{\phi S} = \int_S \mathbf{q}_{\phi S} \cdot \mathrm{d}\mathbf{s} \approx \sum_{j=1}^{n_f} \mathbf{q}_{\phi S} \cdot \mathbf{s}_j \qquad \text{(V-23)}$$

while the volume integral in the CV becomes:

$$Q_{\phi V} = \int_V q_{\phi V} \mathrm{d}V \approx \left(q_{\phi V}\right)_{\mathrm{P_0}} V_{\mathrm{P_0}} \qquad \text{(V-24)}$$

After all necessary values for the prototype equation (4.62) are set, the boundary and initial conditions must be implemented and the procedure for the pressure-velocity coupling has to be applied before the system of algebraic equations can be solved.

V.1.5 Boundary and Initial Conditions

Boundary conditions on the cell faces coinciding with the boundary of the solution domain have to be applied prior to solution of the system of algebraic equations. All boundaries of the screw compressor fluid flow through which it connects to the compressor solid parts are no-slip walls with either, known temperature or a temperature approximated by the earlier explained procedure. Due to that, a cell face flux ϕ_j^* becomes a boundary flux ϕ_B in all equations where boundary cell faces are considered. In such a case, the mass flux in the momentum equation at the boundary is zero, the heat flux through the boundary for energy equation is calculated from the wall temperature and the thermal conductivity in the near wall region (IV-7), while the concentration flux reads zero. Diffusive fluxes are also replaced with their boundary values.

Screw compressor flow is always in a transient state and a transient calculation is necessary, which in turn requires initial conditions to be prescribed for the dependent variables at each control volume of the computational domain. A proper estimation of these plays a significant role for efficiency and computational time to obtain consistent results. The calculation is regarded as complete if the solution for all the dependant variables is equal for the same relative position of the rotors in two consecutive cycles.

The initial values of the velocities in the momentum equation are set to zero in all the cells within the working chamber. The initial pressure is prescribed for the cells at the inlet and outlet receiver as the inlet and outlet pressure. For all other cells the initial values are calculated as a linear interpolation between these values with respect to the relative distance in the z direction as:

$$p_i^0 = p_{inl}^0 + \frac{z_i}{L}\left(p_{out}^0 - p_{inl}^0\right). \qquad \text{(V-25)}$$

z_i is the cell centre distance starting from the coordinate origin, while L is overall compressor length. This simple method to prescribe the initial values often gives a consistent final solution within 4 to 5 compressor cycles. The initial temperature is calculated in the same manner as the pressure, i.e. as the linear interpolation between the prescribed inlet and outlet temperatures T^0_{inl} and T^0_{out}. The density is then calculated from the equation of state. The concentration is also interpolated between the prescribed values at the inlet ρ^0_{inl} and the outlet ρ^0_{out} of the compressor similarly to other variables. Initial values of the kinetic energy and its dissipation rate are set at zero throughout the domain.

If the Euler implicit time integration is employed, these prescribed values at time t_0 are sufficient for the calculation. If, however, the three time level implicit scheme is used, the values at the time $t_{-1} = t_0 - \partial t_0$ should be given. They are set the same as values at time t_0.

V.1.6 Derived System of Algebraic Equations

If the discretisation methods and boundary conditions are implemented in the prototype equation (4.62) for all control volumes then the derived algebraic equation has the same form for all variables:

$$a_{\phi 0}\,\phi_{P_0} - \sum_{j=1}^{n_i} a_{\phi j}\,\phi_{P_j} = b_\phi\,, \tag{V-26}$$

where the index 0 determines the control volume in which the variable is calculated and the index j defines the neighbouring cells. The number n_i represents the internal cell faces between the calculating cell and the neighbouring cells. The right hand side contains all the terms for which the variables are known from either the previous iteration or the time step. All the coefficients, central $a_{\phi 0}$, neighbouring $a_{\phi j}$ and right hand side b_ϕ, are treated explicitly using the deferred correction approach to increase computational efficiency.

$$\begin{aligned}
a_{\phi j} &= \Gamma_{\phi j}\frac{\mathbf{s}_j\cdot\mathbf{s}_j}{\mathbf{d}_j\cdot\mathbf{s}_j} - \min(\dot{m}_j, 0),\\
a_{\phi 0} &= \sum_{j=1}^{n_f} a_{\phi j} + \frac{(\rho V)_{P_0}^{m-1}}{\delta t_m},\\
b_\phi &= \sum_{j=1}^{n_f}\Gamma_{\phi j}\left((\operatorname{grad}\phi)_j\cdot\mathbf{s}_j - \overline{\operatorname{grad}\phi}\cdot\mathbf{d}_j\frac{\mathbf{s}_j\cdot\mathbf{s}_j}{\mathbf{d}_j\cdot\mathbf{s}_j}\right) - \\
&\sum_{j=1}^{n_f}\frac{\gamma_\phi}{2}\dot{m}_j\left((\mathbf{r}_j-\mathbf{r}_{P_0})\cdot(\operatorname{grad}\phi)_{P_0} + (\mathbf{r}_j-\mathbf{r}_{P_0})\cdot(\operatorname{grad}\phi)_{P_j} + (\phi_{P_j}-\phi_{P_0})\frac{\dot{m}_j}{\operatorname{abs}(\dot{m}_j)}\right) + \\
&Q_{\phi S} + Q_{\phi V} + \sum_{B=1}^{n_B} a_{\phi B}\,\phi_B + \frac{(\rho V\phi)_{P_0}^{m-1}}{\delta t_m}.
\end{aligned} \tag{V-27}$$

$\mathbf{d}_j$ is a distance vector. It is effective if the mesh is non-orthogonal and then it is used to correct the cell face value. It is defined as the normal distance between the line connecting two neighbouring cell points and the cell face centre. n_B is the number of boundary faces surrounding the cell P_0. The coefficient $a_{\phi B}$ for the centre point at the boundary cell face is calculated similarly to the neighbouring coefficient $a_{\phi j}$, assuming the distance between the boundary point and the centre of the cell.

V.1.7 Pressure Calculation

As was mentioned in Chapter 5, pressure has no governing equation because it is not a conserved property. The method of calculation of the pressure and pressure gradient fields consists, in general, of three steps. The first one is to obtain the velocity and density fields from the momentum equation regardless of whether the continuity equation is satisfied. The second is a predictor stage in which a pressure correction is calculated to satisfy the continuity equation and the third one is a corrector stage in which new values of the velocity, pressure and density fields are calculated. The method is known as the SIMPLE algorithm.

The velocity through the cell face is calculated allowing a simple and reliable construction of the pressure correction equation. Therefore, it takes account of the pressure diffusion which is of third order accuracy:

$$\mathbf{v}_j^{\bullet} = \mathbf{v}_j - \overline{\left(\frac{V_{P_0}}{a_{v_0}}\right)}\left\{\frac{p_{P_j} - p_{P_0}}{|\mathbf{d}_j|} - \frac{\overline{\text{grad}p}\cdot\mathbf{d}_j}{|\mathbf{d}_j|}\right\}\frac{|\mathbf{d}_j|\mathbf{s}_j}{\mathbf{d}_j\cdot\mathbf{s}_j} \qquad \text{(V-28)}$$

The first term in this equation is the cell face velocity obtained by use of (V-6), while the rest is a third order pressure diffusion term. It acts as a correction of the interpolated velocity if oscillations in the pressure field are present. Otherwise it is negligible. This term vanishes if the pressure varies linearly or quadratically and in other cases it is proportional to the square of the mesh spacing. Therefore, it is reduced with the grid refinement together with other discretisation errors of the second order. The value a_{vo} in this term is the corresponding central coefficient of the momentum equation.

The value of the density at the centre of the cell face, because of stability, is usually calculated as a blend of the first and second order interpolation in the same manner as in (V-21). The value of the blending factor is usually high, $\gamma_r \approx 0.95$:

$$\rho_j^{\bullet} = \rho_j^{UD} + \gamma_\rho\left(\rho_j^{CD} - \rho_j^{UD}\right) \qquad \text{(V-29)}$$

T``he pressure correction equation in the form of a general algebraic equation (4.67) is now constructed to satisfy the momentum equation in which so-called predictor stage values $\mathbf{v}^{pred}$, p^{pred} and ρ^{pred} featuring in (V-28) and (V-29) also satisfy the continuity equation. If the Euler implicit time differencing scheme is employed the continuity equation can be written in a form convenient for further calculation:

$$\frac{(\rho V)_{P_0}-(\rho V)_{P_0}^{m-1}}{\delta t_m}+\sum_{j=1}^{n_f}\dot{m}_j=0 \qquad \text{(V-30)}$$

The pressure correction equation is now:

$$a_{P_0}\, p'_{P_0}-\sum_{j=1}^{n_f} a_{P_j}\, p'_{P_j}=b_{P_0}, \qquad \text{(V-31)}$$

with coefficients:

$$\begin{aligned}
a_{P_j} &= \rho_j^{*}\left(\frac{V_{P_0}}{a_{v_0}}\right)\frac{\mathbf{s}_j\cdot\mathbf{s}_j}{\mathbf{d}_j\cdot\mathbf{s}_j}-\left[(1-\gamma_\rho)\min(\mathbf{v}_j^{*}\cdot\mathbf{s}_j,0)+\frac{1}{2}\gamma_\rho\mathbf{v}_j^{*}\cdot\mathbf{s}_j\right]\left(\frac{\partial\rho}{\partial p}\right)_{P_j}\beta_p,\\
a_{P_0} &= \sum_{j=1}^{n_f}\hat{a}_{P_j}+\frac{V_{P_0}}{\delta t_m}\left(\frac{\partial\rho}{\partial p}\right)_{P_0}, \qquad \text{(V-32)}\\
b_{P_0} &= -\sum_{j=1}^{n_f}\dot{m}_j-\left((\rho V)_{P_0}-(\rho V)_{P_0}^{m-1}\right).
\end{aligned}$$

The central coefficient in (V-32) is obtained from 'conjugate' values $\hat{a}_{P_j}$ of the central coefficients at the neighbouring cells a_{P_j} if P_0 and P_j exchange their roles. The compressibility coefficient defined as $C_\rho=\partial\rho/\partial p$ is calculated in Section 4.2.4, while β_p is the under-relaxation factor for the pressure correction equation.

Finally, in the corrector stage, the velocity, pressure and density fields are corrected for the calculated value of pressure correction:

$$\mathbf{v}_{P_0} = \mathbf{v}_{P_0}^{pred} - \frac{1}{a_{v_0}} \sum_{j=1}^{n_f} p_j' \mathbf{s}_j,$$

$$p_{P_0} = p_{P_0}^{pred} + \beta_p p_{P_0}', \qquad \text{(V-33)}$$

$$\rho_{P_0} = \rho_{P_0}^{pred} + \left(\frac{\partial \rho}{\partial p}\right)_{P_0} \beta_p p_{P_0}'.$$

The mass fluxes which satisfy the continuity equation are calculated from the equation:

$$\dot{m}_j = \dot{m}_j^{pred} - a_{P_j} p_{P_j}' + \hat{a}_{P_j} p_{P_0}' \qquad \text{(V-34)}$$

and these are used for computation of the convective fluxes in the next iteration.

Since the boundary conditions of the momentum equation in the case of the screw compressor flow are prescribed velocities, which are Dirichlet boundary conditions, then the zero gradient boundary conditions on the pressure correction are applied.

The pressure correction equation adjusts itself automatically to the type of the flow. In the region of low Mach numbers the contribution of the density correction is small. In regions of high Mach number, contribution of the density correction becomes dominant and the equation becomes hyperbolic contrary to previous case when it was elliptic. This feature is very important for the screw compressor flows in which both low and high Mach number regions are presented. More about SIMPLE method and its implementation can be found in *Demirdžić et al.* (1993), *Karki and Patankar* (1989) or *Ferziger and Perić* (1995).

Appendix VI

SCORG

VI.1 INTRODUCTION

SCORG is stand-alone numerical CAD-CFD interface used to generate a screw compressor numerical mesh and to transfer it to a general finite volume numerical solver. The program is written in FORTRAN90 for DOS, WINDOWS or LINUX. The program generates a block structured hexahedral numerical grid for a screw compressor. It also prepares control parameters for a general CFD solver and user subroutines which enable calculation of screw compressor flow. The current version of the program was prepared for use with the numerical solver COMET.

VI.2 INSTALLATION

SCORG is provided on the attached CD-ROM. To install the software in DOS or WINDOWS, insert the CD ROM in the drive and copy the entire directory \SCORG\Windows to some destination on your local drive. Ensure that the directory and its contents are not Read-Only. To do that, in Windows 2000 or Windows 98, position the cursor above the directory name and highlight it. Then press the right mouse button and open Properties. The following screen should appear.

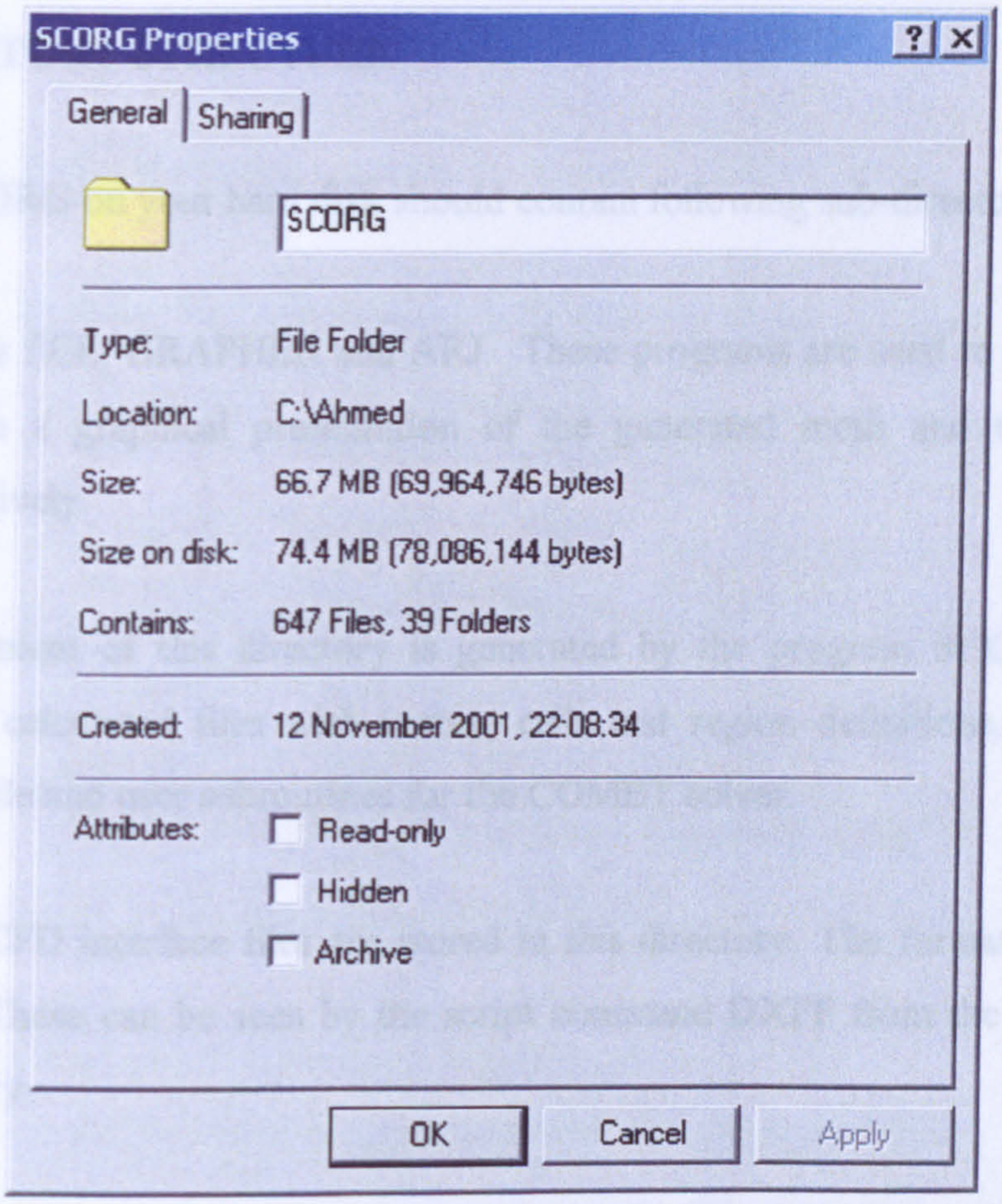

Figure A- 9 Properties of the SCORG directory

Be sure that the Read-only box of Attributes is unchecked and then press OK. The recommended working environment is the command prompt under Windows.

To run the program, go to the SCORG directory in the command prompt and type CALC followed by the ENTER button. The message that you need a licence will appear on the screen. Please send file REQUEST.LIC to the e-mail address: a.kovacevic@city.ac.uk.

If working under LINUX, the contents of the directory \SCORG\Linux should be copied on the local drive. The following procedure is same as for the windows version.

VI.3 DIRECTORY STRUCTURE

Directory SCORG on your hard disk should contain following sub-directories:

BIN - contains SEE, GRAPHER and ARJ. These programs are used to edit input data, to give a graphical presentation of the generated mesh and to archive files respectively.

DAT– the content of this directory is generated by the program SCORG. Here are stored calculated files with vertex, cells and region definitions, pre-processor script file and user subroutines for the COMET solver.

DXF - CAD-CFD interface files are stored in this directory. The format of the files is DXF. These can be seen by the script command DXFF from the SCORG main directory.

EXE - contains SCOG.EXE program, NODE.EXE and PORT.EXE programs.

INP - contains input data.

PLT - GRF and PLT files are stored in this directory. These are used by GRAPHER and VIEW to provide a graphical presentation of the numerical mesh created.

POS - RES???.DAT files generated by POST.F subroutine of the numerical solver should be stored in this directory. These are used by the post-processing program POST.EXE which calculates integral parameters and a p-alpha diagram.

SCO - user subroutines for CFD solver are stored in this directory.

TMP - Temporary files are stored in this directory. These are used for faster recalculation if required. The content of this directory can be cleaned up by script command CLEA from the SCORG main directory.

VI.4 SCRIPT COMMANDS

SCORG is controlled by script commands directly from its main directory. The commands are listed and explained in alphabetical order:

CALC - activates program SCORG placed in the directory EXE. Running this command all files from directories TEMP and DAT and their subdirectories are deleted.

CLEA - clean content of <DAT> and <TMP> directories.

DXFF [No] – generate a DXF file with a 2D numerical mesh in a cross section perpendicular to the rotor axis. [No] is integer >=1 which represents the number of the cross section in which the mesh is generated.

EDIT - edit input DATA. SEE editor is used from the directory <BIN>.

ERRB - display log file of Errors of Boundary distribution procedure.

ERRM- display log file of Errors in the grid generation procedure. It provides information of the position and number of irregular cells generated if any.

ERRP - display log file of irregular cells generated in the inlet and outlet ports.

HIST - display HISTORY file.

NEWI [F1] [F2] – New Input File. F1 and F2 are extensions of existing input files stored in the directory INP. These consist of three alphanumeric places, for example 56a. F1 indicates which file will be used. F2 indicates the file in which the current input file will be saved before being switched to the new one. NOTE: If F2 is not provided, then the input file, which was used, will not be saved and data may be lost.

PACK - copy content of the directory SCORG to floppy A:

POST - run post-processor file for calculation of integral parameters. These are calculated from RES???.DAT files in the directory POS.

RECA - reactivate without deleting files from directories DAT and TMP.

VIEW [N1] - view the distribution of boundary points in the cross section [N1]

VMES - view the distribution of internal grid points in the cross section [N1]

VPOR - view the grid distribution for inlet and outlet ports

VI.5 INPUT DATA FILES

The input data files for SCORG are as follows:

DAT.INP - contains basic features and control parameters for SCORG
RACK.INP - Coordinates of a rack
OIL.INP - physical properties of oil injected to the compressor
REAL.INP - coefficients for calculation of real fluids

These files are stored in the directory <INP>. To alter input data type EDIT in the SCORG main directory. The default editor is SEE.

The following is an example of the DAT.INP file. Further below is a description of the variables used.

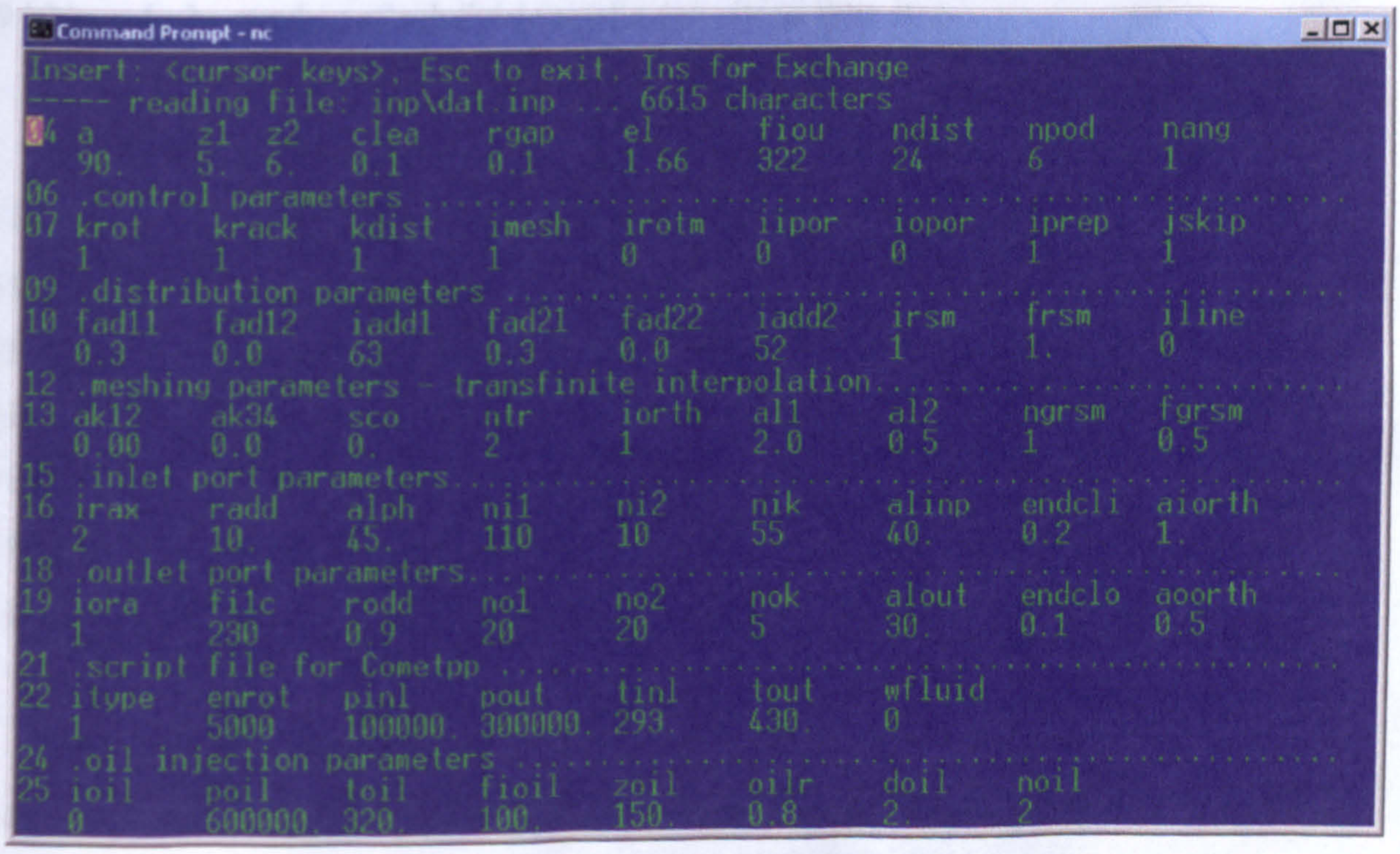

GENERAL data

1 a [mm] - rotors centre distance
2 z1,2 [ ] - number of teeth in the main and gate rotor
3 clea [mm] - clearance between rotors
4 rgap [mm] - radial clearance between rotor and housing

5 el	[ ]	- relative rotor length (l/d)	
6 fiou	[deg]	- overall (wrap) angle of the main rotor	
7 ndist	[ ]	- rotors	- number of divisions along the lobe
8 npod	[ ]	- rotors	- number of divisions in radial direction
9 nang	[ ]	- rotors	- number of divisions in z-direct. for each lobe

CONTROL parameters

1 krot	[ ]	- rotor calculation	1-generate	2-input	0-off
2 krack	[ ]	- rack calculation	1-on		0-off
3 kdist	[ ]	- boundary distribution	1-on		0-off
4 imesh	[ ]	- mesh calculation	1-transfinite	2-simple	0-off
5 irotm	[ ]	- rotor mesh calculation	1-transfinite	2-simple	0-off
6 iipor	[ ]	- inlet port calculation	1-transfinite	2-simple	0-off
7 iopor	[ ]	- outlet port calculation	1-transfinite	2-simple	0-off
8 iprep	[ ]	- generation of pre-processor input file		1-on	0-off
9 jskip	[ ]	- number of subdivisions of a calculated time step			

DISTRIBUTION parameters

1 fadd1	[<1]	- adaptation factor for the 1st criterion (fadd1+fadd2<1)			
2 fadd2	[<1]	- adaptation factor for the 2nd criterion (fadd1+fadd2<1)			
3 iadd1	[ ]	- adaptation criterions:	1-Angle;	2-Radius of curvature	
4 iadd2	[ ]	3-Polar dist;	4-Flatnes;	5-Cosin;	6-Sinus distribution
5 irsm	[ ]	- rack smoothing	1-on	0-off	
6 frsm	[=<1]	- rack smoothing factor			
7 iline	[ ]	- make a rotor mating line	1-on	0-off	

MESHING parameters

1 ak1-ak4	[ ]	- K-factors in Hermite bi-directional transfinite interpolation			
2 sco	[ ]	- smoothing coefficient (delta) 1.-cubic; 100.-linear			
3 ntr >imesh=1		- order of interpolation	1-one	2-two	3-three dimensional
ntr >imesh=3		- transformation constant	1-linear	2-quadratic	3-cubic
4 iorth	[ ]	- mesh orthogonalization	1-on		0-off
5 al1	[ ]	- coeff. 1 for mesh orth. - damping to the grid interior			
6 al2	[ ]	- coeff. 2 for mesh orth. - damping to the endpoints on boundary			

7 ngrsm [ ] - grid line smoothing - number of repetitions

9 fgrsm [<1] - smoothing coefficient for the grid lines smoothing

INLET port

1 irax [ ] - inlet port 1-axial, 2-both, 3-radial, 0-none;

2 radd [mm] - inlet port thicknes (addendum to outer radius)

3 alph [deg] - radial inlet port line angle

4 ni1 [ ] - inlet port - number of divisions along the circle

5 ni2 [ ] - inlet port - number of divisions in radial direction

6 nik [ ] - inlet port - number of divisions in z direction

7 alinp [mm] - length of the inlet port

8 endcli [mm] - inlet endface clearance

9 aiorth [ ] - orthogonalisation factor for inlet port and clearance

OUTLET port

1 iora [ ] - outlet port 1-axial, 2-both, 3-radial, 0-none;

2 fi1c [deg] - discharge port start angle (relative to the end of suction)

3 rodd [ ] - outlet radial port inner circle diameter (% of outer dia.)

4 no1 [ ] - outlet port - number of divisions along the circle

5 no2 [ ] - outlet port - number of divisions in radial direction

6 nok [ ] - outlet port - number of divisions in z direction

7 alout [mm] - length of the outlet port

8 endclo [mm] - outlet endface clearance

9 aoorth [ ] - orthogonalisation factor for outlet port and clearance

WORKING parameters (script file for COMET)

1 itype [ ] - Type of the machine 1-Compressor 2-Expander

2 enrot [rpm] - rotational speed of the main rotor (should be positive)

3 pinl [Pa] - compressor suction pressure

4 pout [Pa] - compressor discharge pressure

5 tinl [K] - compressor suctiuon temperature

6 tout [K] - compressor discharge temperature

7 wfluid [ ] - identification for working fluid

OIL parameters

1 ioil	[ ]	- Injection of oil: 1-Yes 0-No
2 poil	[Pa]	- Pressure in oil reservoir
3 toil	[K]	- Temperature in oil reservoir
4 foil	[deg]	- Angle of the oil injection port (0-90)
5 zoil	[mm]	- Axial position of the oil port
6 oilr	[ ]	- Oil/gas mass ratio (Applied to initial conditions)
7 doil	[mm]	- Dimension of the oil nozzle cross section (dia or a)
8 noil	[ ]	- Position of the oil port on: 1 - Male rotor, 2 - Female rotor

Identifications numbers for working fluids

00 - AIR

01 - AMONIA R-717

02 - R-134a

03 - R-113

04 - R-22

VI.6 OUTPUT FILES

The short description of the files produced by SCORG is given here. These files are stored in the directory <DAT> and its subdirectory <USERPROG>. The complete contents of these two directories should be copied in the working environment of a numerical solver.

PREP.DAT - COMET input script file. It reads the mesh in CometPP (pre-processor), it also defines boundaries, connections between blocks, control parameters and at the end it defines some postprocessor features.

VI.6.1 Cell files

Cells are defined by 8 nodes, 6 faces and 12 edges. The right hand rule is applied when cells are generated. All files containing cell definitions have the same format:

format (i6,8i8,i3)

while and the structure of files is:

cell_number V1 V2 V3 V4 V5 V6 V7 V8 Cell_type

The files in which the cell definition is stored are as follow:

ROTC.DAT - cell definition for rotors

INPC.DAT - cell definition for the inlet port

OUPC.DAT - cell definitions for the outlet port

VI.6.2 Vertex files

The data files which define node positions have the following format:

format (i6,3f12.7)

The structure of the lines is:

vertex_index X1 X2 X3,

where X1, X2 and X3 are coordinates of the vertex in the active coordinate system. In the case of the compressor numerical mesh, the active coordinate system is always a global Cartesian coordinate system. Files that contains vertex definitions are:

ROTV.DAT - definition of rotor vertices. This file is recalculated by the subroutine UMOVGR.F each time the new time step is calculated. It is recalculated from the vertex definition contained in file ROTVALL.DAT.

INPV.DAT - defines the nodes in the inlet port

OUPV.DAT - defines the nodes in the outlet port

ROTVALL.DAT - contains the definition of all the vertices in the rotor domains for all required time steps. This file is used as the source for recalculation of ROTV.DAT.

The data contained in this file have following format:

format (i6,2f12.7)

VI.6.3 Region files

Files in which regions are defined have the following format:

format (i6,4i8,i4)

Their structure is:

region_index V1 V2 V3 V4 Region_Type

Regions are bounding surfaces on blocks through which other blocks are connected or the boundary conditions are given. Files that contain definition of regions are:

ROTR.DAT - regions on the rotors
INPR.DAT - regions for the inlet port
OUPR.DAT - regions for the outlet port

VI.7 USER SUBROUTINES

A short description of the user subroutines is provided here. The user subroutines are used by COMET to enable calculation of screw compressor parameters. These are as follow:

UMOVGR.F - COMET subroutine for the control of the moving mesh. It reads file ROTVALL.DAT and recalculates vertices for a new time step. The new vertex positions are saved in ROTV.DAT file.

UCERBC.F - User boundary conditions for rotor domains

INITFI.F - Defines initial conditions throughout the calculated domain.

USEINP.F - Input file. Reads data, defines domains and performs first calculation of fluid properties.

TIMINT.F - Changes time step to accommodate required speed of rotation.

INUSER.F - Calculates density at the beginning of each time step.

DENSIT.F - Calculates properties of real fluids in all cells for each iteration.

ADDMASS.F - Calculates mass sources to be added to the boundary receivers in order to maintain constant pressure.

ENTSOU.F - Calculates the contribution to the energy equation.

SPESOU.F - Source terms in oil and liquid concentration equations.

POST.F - Postprocessor procedure that generates result files.

VI.8 CONTENT OF THE CD-ROM

VI.8.1 EXAMPLES

VI.8.1.1 1-Dry Compressor

VI.8.1.2 2-Oil Injected Air

VI.8.1.3 3-Ammonia oil injected

VI.8.1.4 4-R134a Screw expander

VI.8.2 PAPERS

VI.8.3 PRESENTATION

VI.8.4 SCORG

VI.8.4.1 Linux

VI.8.4.2 Windows

VI.8.5 THESIS

Thesis contains many DVD'S CD'S unable to copy.

If required please contact the University.